

ADVANCED STEEL CONSTRUCTION

An International Journal

Volume 14 Number 4

December 2018

CONTENTS

Technical Papers

Assessment of Design Requirements against Progressive Collapse in UFC 4-023-03: Numerical Simulation

H.H. Li, B.Y. Zhang and X.H. Cai

Experimental and Numerical Investigations on Skewed Plate-to-SHS X-Joints under Compression

Y. Chen, K. He, W.X. Zhang, B.C. Chen and J.G. Wei

Experimental Investigation into the Capacity of Cold-formed Screwed Steel Strap Bracing Connections

M. Zeynalian, A. Shelley, H.R. Ronagh and S. Hatami

Shear Lag Factors for Tension Angles with Unequal-Length Longitudinal Welds

J. K. Hsiao and S. Shrestha

Static and Kinematic Behaviour of a Foldable Truss Roof Structure

J.G. Cai, Z. Ye, X.Y. Wang, Y.X. Xu and J. Feng

Fatigue Life Assessment of Inclined Welded Joints in Steel Bridges Subjected to Combined Normal and Shear Stresses

Z.Y. Jie, Y.D. Li, X. Wei and P. Zhuge

Partial Interaction Shear Flow Forces in Simply Supported Composite Steel-Concrete Beams

Y. Zou, X.H. Zhou, J. Di and F.J. Qin

Seismic Behavior of Bolted Connections with Slot Bolt Holes at Ambient and Elevated Temperature

Z.X. Hou, C. Gong, Y. Zhang, Y.Z. Sun, J. Jiang and G.Q. Li

Safety Assessment of EUROCODE 3 Stability Design Rules for the Lateral-Torsional Buckling of Prismatic Beams

Luís Simões da Silva, Trayana Tankova, Liliana Marques, Carlos Rebelo and Andreas Taras

Behavior of Plastic Greenhouses under Symmetric Loading before and after Strengthening with Tension Ties

S.H. Lee, K.J. Shin and H.D. Lee

Interaction Curves for Concrete-filled L-shaped Multi-celled Steel Tube Sections under

Combined Biaxial Bending and Axial Force

G.S. Tong and X.G. Li

Announcements by IJASC:

Announcement for SDSS 2019

Copyright © 2018 by :

The Hong Kong Institute of Steel Construction

Website: <http://www.hkisc.org>

ISSN 1816-112X

Science Citation Index Expanded, Materials Science Citation Index and ISI Alerting

Cover: The MGM Mansion Roof in Macau, China. Designed by "Second-order Direct Analysis" without effective length.

e-copy of IJASC is free to download at "www.ascjournal.com" in internet and mobile apps.

ADVANCED STEEL CONSTRUCTION

VOL. 14, NO. 4 (2018)

ADVANCED STEEL CONSTRUCTION

an International Journal

ISSN 1816-112X

Volume 14 Number 4

December 2018



Editors-in-Chief

S.L. Chan, The Hong Kong Polytechnic University, Hong Kong

W.F. Chen, University of Hawaii at Manoa, USA

R. Zandonini, Trento University, Italy

ISSN 1816-112X

Science Citation Index Expanded,
Materials Science Citation Index
and ISI Alerting

EDITORS-IN-CHIEF

Asian Pacific, African and organizing Editor

S.L. Chan
*The Hong Kong Polytechnic Univ.,
Hong Kong*

American Editor

W.F. Chen
Univ. of Hawaii at Manoa, USA

European Editor

R. Zandonini
Trento Univ., Italy

ASSOCIATE EDITORS

Y.P. Liu
The Hong Kong Polytechnic Univ., Hong Kong

S.W. Liu
Sun Yat-Sen Univ., China

INTERNATIONAL EDITORIAL BOARD

F.G. Albermani
Central Queensland Univ., Australia

I. Burgess
Univ. of Sheffield, UK

F.S.K. Bijlaard
Delft Univ. of Technology, The Netherlands

R. Bjorhovde
The Bjorhovde Group, USA

M.A. Bradford
The Univ. of New South Wales, Australia

D. Camotim
Technical Univ. of Lisbon, Portugal

C.M. Chan
Hong Kong Univ. of Science & Technology, Hong Kong

T.H.T. Chan
Queensland Univ. of Technology, Australia

T.M. Chan
The Hong Kong Polytechnic Univ., Hong Kong

S.P. Chiew
Nanyang Technological Univ., Singapore

W.K. Chow
The Hong Kong Polytechnic Univ., Hong Kong

G.G. Deierlein
Stanford Univ., California, USA

L. Dezi
Univ. of Ancona, Italy

D. Dubina
The Politehnica Univ. of Timisoara, Romania

R. Greiner
Technical Univ. of Graz, Austria

L. Gardner
Imperial College of Science, Technology and Medicine, UK

Y. Goto
Nagoya Institute of Technology, Japan

L.H. Han
Tsinghua Univ. China

S. Herion
University of Karlsruhe, Germany

G.W.M. Ho
Ove Arup & Partners Hong Kong Ltd., Hong Kong

B.A. Izzuddin
*Imperial College of Science, Technology and
Medicine, UK*

J.P. Jaspart
Univ. of Liege, Belgium

S. A. Jayachandran
IIT Madras, Chennai, India

S.E. Kim
Sejong Univ., South Korea

S. Kitipornchai
The Univ. of Queensland, Australia

D. Lam
Univ. of Bradford, UK

H.F. Lam
City Univ. of Hong Kong, Hong Kong

G.Q. Li
Tongji Univ., China

J.Y.R. Liew
National Univ. of Singapore, Singapore

E.M. Lui
Syracuse Univ., USA

Y.L. Mo
Univ. of Houston, USA

J.P. Muzeau
CUST, Clermont Ferrand, France

D.A. Nethercot
*Imperial College of Science, Technology and
Medicine, UK*

Y.Q. Ni
The Hong Kong Polytechnic Univ., Hong Kong

D.J. Oehlers
The Univ. of Adelaide, Australia

J.L. Peng
Yunlin Univ. of Science & Technology, Taiwan

K. Rasmussen
The Univ. of Sydney, Australia

J.M. Rotter
The Univ. of Edinburgh, UK

C. Scawthorn
Scawthorn Porter Associates, USA

P. Schaumann
Univ. of Hannover, Germany

Y.J. Shi
Tsinghua Univ., China

G.P. Shu
Southeast Univ. China

L. Simões da Silva
*Department of Civil Engineering, University of
Coimbra, Portugal*

J.G. Teng
The Hong Kong Polytechnic Univ., Hong Kong

G.S. Tong
Zhejiang Univ., China

K.C. Tsai
National Taiwan Univ., Taiwan

C.M. Uang
Univ. of California, USA

B. Uy
University of Western Sydney, Australia

M. Veljkovic
Univ. of Lulea, Sweden

F. Wald
Czech Technical Univ. in Prague, Czech

Y.C. Wang
The Univ. of Manchester, UK

Y.L. Xu
The Hong Kong Polytechnic Univ., Hong Kong

D. White
Georgia Institute of Technology, USA

E. Yamaguchi
Kyushu Institute of Technology, Japan

Y.B. Yang
National Taiwan Univ., Taiwan

Y.Y. Yang
China Academy of Building Research, Beijing, China

B. Young
The Univ. of Hong Kong, Hong Kong

X.L. Zhao
Monash Univ., Australia

X.H. Zhou
Chongqing University, China

Z.H. Zhou
The Hong Kong Polytechnic Univ., Hong Kong

S.Y. Zhu
The Hong Kong Polytechnic Univ., Hong Kong

R.D. Ziemian
Bucknell Univ., USA

General Information

Advanced Steel Construction, an international journal

Aims and scope

The International Journal of Advanced Steel Construction provides a platform for the publication and rapid dissemination of original and up-to-date research and technological developments in steel construction, design and analysis. Scope of research papers published in this journal includes but is not limited to theoretical and experimental research on elements, assemblages, systems, material, design philosophy and codification, standards, fabrication, projects of innovative nature and computer techniques. The journal is specifically tailored to channel the exchange of technological know-how between researchers and practitioners. Contributions from all aspects related to the recent developments of advanced steel construction are welcome.

Instructions to authors

Submission of the manuscript.

Authors may submit on-line at www.hkisc.org

Asian Pacific, African and organizing editor : Professor S.L. Chan, Email: ceslchan@polyu.edu.hk
American editor : Professor W.F. Chen, Email: waifah@hawaii.edu
European editor : Professor R. Zandonini, Email: riccardo_zandonini@ing.unitn.it

All manuscripts submitted to the journal are recommended to accompany with a list of four potential reviewers suggested by the author(s). This list should include the complete name, address, telephone and fax numbers, email address, and at least five keywords that identify the expertise of each reviewer. This scheme will improve the process of review.

Style of manuscript

General. Author(s) should provide full postal and email addresses and fax number for correspondence. The manuscript including abstract, keywords, references, figures and tables should be in English with pages numbered and typed with double line spacing on single side of A4 or letter-sized paper. The front page of the article should contain:

- a) a short title (reflecting the content of the paper);
- b) all the name(s) and postal and email addresses of author(s) specifying the author to whom correspondence and proofs should be sent;
- c) an abstract of 100-200 words; and
- d) 5 to 8 keywords.

The paper must contain an introduction and a conclusion. The length of paper should not exceed 25 journal pages (approximately 15,000 words equivalents).

Tables and figures. Tables and figures including photographs should be typed, numbered consecutively in Arabic numerals and with short titles. They should be referred in the text as Figure 1, Table 2, etc. Originally drawn figures and photographs should be provided in a form suitable for photographic reproduction and reduction in the journal.

Mathematical expressions and units. The Systeme Internationale (SI) should be followed whenever possible. The numbers identifying the displayed mathematical expression should be referred to in the text as Eq. 1, Eq. 2.

References. References to published literature should be referred in the text, in the order of citation with Arabic numerals, by the last name(s) of the author(s) (e.g. Zandonini and Zanon [3]) or if more than three authors (e.g. Zandonini et al. [4]). References should be in English with occasional allowance of 1-2 exceptional references in local languages and reflect the current state-of-technology. Journal titles should be abbreviated in the style of the Word List of Scientific Periodicals. References should be cited in the following style [1, 2, 3].

Journal: [1] Chen, W.F. and Kishi, N., "Semi-rigid Steel Beam-to-column Connections, Data Base and Modelling", Journal of Structural Engineering, ASCE, 1989, Vol. 115, No. 1, pp. 105-119.

Book: [2] Chan, S.L. and Chui, P.P.T., "Non-linear Static and Cyclic Analysis of Semi-rigid Steel Frames", Elsevier Science, 2000.

Proceedings: [3] Zandonini, R. and Zanon, P., "Experimental Analysis of Steel Beams with Semi-rigid Joints", Proceedings of International Conference on Advances in Steel Structures, Hong Kong, 1996, Vol. 1, pp. 356-364.

Proofs. Proof will be sent to the corresponding author to correct any typesetting errors. Alternations to the original manuscript at this stage will not be accepted. Proofs should be returned within 48 hours of receipt on-line.

Copyright. Submission of an article to "Advanced Steel Construction" implies that it presents the original and unpublished work, and not under consideration for publication nor published elsewhere. On acceptance of a manuscript submitted, the copyright thereof is transferred to the publisher by the Transfer of Copyright Agreement and upon the acceptance of publication for the papers, the corresponding author must sign the form for Transfer of Copyright.

Permission. Quoting from this journal is granted provided that the customary acknowledgement is given to the source.

Page charge and Reprints. There will be no page charges if the length of paper is within the limit of 25 journal pages. A total of 30 free offprints will be supplied free of charge to the corresponding author. Purchasing orders for additional offprints can be made on order forms which will be sent to the authors. These instructions can be obtained at the Hong Kong Institute of Steel Construction, Journal website: <http://www.hkisc.org>

The International Journal of Advanced Steel Construction is published quarterly by learnt society, The Hong Kong Institute of Steel Construction, c/o Department of Civil & Environmental Engineering, The Hong Kong Polytechnic University, Hung Hom, Kowloon, Hong Kong.

Disclaimer. No responsibility is assumed for any injury and / or damage to persons or property as a matter of products liability, negligence or otherwise, or from any use or operation of any methods, products, instructions or ideas contained in the material herein.

Subscription inquiries and change of address. Address all subscription inquiries and correspondence to Member Records, IJASC. Notify an address change as soon as possible. All communications should include both old and new addresses with zip codes and be accompanied by a mailing label from a recent issue. Allow six weeks for all changes to become effective.

The Hong Kong Institute of Steel Construction

HKISC
c/o Department of Civil and Environmental Engineering,
The Hong Kong Polytechnic University,
Hung Hom, Kowloon, Hong Kong, China.
Tel: 852- 2766 6047 Fax: 852- 2334 6389
Email: ceslchan@polyu.edu.hk Website: <http://www.hkisc.org/>
ISSN 1816-112X

Science Citation Index Expanded, Materials Science Citation Index and ISI Alerting

Copyright © 2018 by:

The Hong Kong Institute of Steel Construction.



ISSN 1816-112X

Science Citation Index Expanded,
Materials Science Citation Index and
ISI Alerting

EDITORS-IN-CHIEF

Asian Pacific, African and organizing Editor

S.L. Chan
*The Hong Kong Polytechnic Univ.,
Hong Kong*
Email: ceslchan@polyu.edu.hk

American Editor

W.F. Chen
Univ. of Hawaii at Manoa, USA
Email: waifah@hawaii.edu

European Editor

R. Zandonini
Trento Univ., Italy
Email: riccardo.zandonini@ing.unitn.it

Advanced Steel Construction

an international journal

VOLUME 14 NUMBER 4

DECEMBER 2018

Technical Papers

- Assessment of Design Requirements against Progressive Collapse 514
in UFC 4-023-03: Numerical Simulation
H.H. Li, B.Y. Zhang and X.H. Cai
- Experimental and Numerical Investigations on Skewed 539
Plate-to-SHS X-Joints under Compression
Y. Chen, K. He, W.X. Zhang, B.C. Chen and J.G. Wei
- Experimental Investigation into the Capacity of Cold-formed 562
Screwed Steel Strap Bracing Connections
M. Zeynalian, A. Shelley, H.R. Ronagh and S. Hatami
- Shear Lag Factors for Tension Angles with Unequal-Length 589
Longitudinal Welds
J. K. Hsiao and S. Shrestha
- Static and Kinematic Behaviour of a Foldable Truss Roof 606
Structure
J.G. Cai, Z. Ye, X.Y. Wang, Y.X. Xu and J. Feng
- Fatigue Life Assessment of Inclined Welded Joints in Steel 620
Bridges Subjected to Combined Normal and Shear Stresses
Z.Y. Jie, Y.D. Li, X. Wei and P. Zhuge
- Partial Interaction Shear Flow Forces in Simply Supported 634
Composite Steel-Concrete Beams
Y. Zou, X.H. Zhou, J. Di and F.J. Qin
- Seismic Behavior of Bolted Connections with Slot Bolt Holes at 651
Ambient and Elevated Temperature
Z.X. Hou, C. Gong, Y. Zhang, Y.Z. Sun, J. Jiang and G.Q. Li
- Safety Assessment of EUROCODE 3 Stability Design Rules for 668
the Lateral-Torsional Buckling of Prismatic Beams
*Luís Simões da Silva, Trayana Tankova, Liliana Marques,
Carlos Rebelo and Andreas Taras*
- Behavior of Plastic Greenhouses under Symmetric Loading 694
before and after Strengthening with Tension Ties
S.H. Lee, K.J. Shin and H.D. Lee
- Interaction Curves for Concrete-filled L-shaped Multi-celled Steel 710
Tube Sections under Combined Biaxial Bending and Axial Force
G.S. Tong and X.G. Li

Announcements by IJASC :

Announcement for SDSS 2019

ASSESSMENT OF DESIGN REQUIREMENTS AGAINST PROGRESSIVE COLLAPSE IN UFC 4-023-03: NUMERICAL SIMULATION

H.H. Li ^{1, 2, *}, B.Y. Zhang ^{1, 2} and X.H. Cai ³

¹ Key Lab of Structures Dynamic Behavior and Control of the Ministry of Education,
Harbin Institute of Technology, Harbin, 150090, China

² Key Lab of Smart Prevention and Mitigation of Civil Engineering Disasters of
the Ministry of Industry and Information Technology,
Harbin Institute of Technology, Harbin, 150090, China

³ Architectural Design and Research Institute of HIT
(Corresponding author: Email: lihonghao@hit.edu.cn)

Received: 18 November 2016; Revised: 15 July 2017; Accepted: 19 September 2017

ABSTRACT: Unified Facilities Criteria (UFC 4-023-03): Design of Buildings to Resist Progressive Collapse published by the Department of Defense is one of the few design provisions that have been used around the US which provide design requirements on the basis of conventional design philosophy to the designers and the owners of the buildings against progressive collapse. These requirements are evaluated using numerical models which have been shown to be able to reasonably capture the behaviors of the buildings under column loss scenarios. A large number of case studies are conducted using validated three-dimensional macro-based models for four prototype buildings with different size, different height, different seismic detailing and different structural layouts. The simulation results show that the tie force method (TFM) is effective in protecting steel framed buildings against progressive collapse and can significantly reduce overall deformations of the structures after sudden loss of a column. However, the method for calculating the dynamic increase factor (DIF) proposed in the document is deemed problematic and thus a new energy-based approach is proposed to assess the peak dynamic displacement (PDD). The proposed method is shown to be accurate and reasonably conservative.

Keywords: 3-D macro-model, numerical simulation, UFC 4-023-03, tie force method, dynamic increase factor, peak dynamic displacement, energy-based method

DOI: 10.18057/IJASC.2018.14.4.1

1. INTRODUCTION

Progressive collapse has become a popular research topic in the field of structural engineering since the partial collapse of Ronan Pointe Tower in England in 1968. Currently, many ongoing studies related to progressive collapse are being conducted by federal agencies, research institute and universities. The ultimate goal of progressive collapse studies is to develop design and retrofit strategies so that the structures are not vulnerable to progressive collapse when subjected to abnormal loading conditions.

Currently, ASCE 7-10 [1] is the only mainstream standard that addresses the issue of collapse in some detail in the United States. It specifies two design alternatives: 1) a direct design method, which either considers explicit conditions for analysis when specific members are no longer capable of supporting load (Alternate Path Method), or ensures sufficient local strength to resist possible failure induced by accidents or misuse; 2) indirect design method, which includes implicit considerations that would enhance resistance to collapse through provision of minimum levels of strength, continuity and ductility. The provisions to prevent collapse in the UFC 4-023-03 (DoD [2]) and General Services Administration progressive guidelines (GSA [3]) were based on a similar philosophy to that in ASCE 7-10 [1], albeit with more details. The GSA progressive guidelines

(GSA [3]) and UFC 4-023-03 (DoD [2]), in particular, specify the Alternate Path Method (APM) as one of several alternatives, and promote linear and nonlinear analysis techniques to check structural members in the alternate path structure. Both documents are geared towards blast hazards and their primary intent is to protect a building that has lost critical structural members to a blast. The design approaches in UFC 4-023-03 [2] vary according to the building occupancy. Although much research has been done to develop these provisions, their conservatism and effectiveness in protecting buildings from progressive collapse under column-loss scenarios still needs to be evaluated through experimentations and simulations. The UFC 4-023-03 [2], in particular, need refinement because they were modeled after seismic performance based design guidelines and have yet to be fully adapted for gravity-induce collapse situations.

In the UFC 4-023-03 [2], one of the techniques permitted for designing against collapse is the Tie Force Method (TFM). This is an indirect technique, permitted under certain occupancy conditions, in which structural robustness is assured by promoting structural continuity, ductility, and structural redundancy. Robustness is achieved by specifying the minimum amount of tensile forces and their locations that must be provided to 'tie' the structure together. The TFM procedure traces its origins to British engineers involved in the 1968 Ronan Point incident and is one of the earliest design strategies against progressive collapse. The UK Building Establishment (BRE) conducted quarter-scale testing to determine its effectiveness as early as 1970s (Moore [4]). A number of studies have been conducted in the past decade to evaluate the adequacy of TFM for progressive collapse. Abruzzo et al. [5] investigated the behavior of a reinforced concrete commercial building designed according to older version of UFC 4-203-03 [2] under column loss scenarios and claimed that the TFM specified in UFC 4-203-03 (DoD [6]) was inadequate to prevent progressive collapse. Li et al. [7] evaluated the effectiveness of TFM specified in the British Standard in resisting progressive collapse of reinforced concrete frame structures and proposed an improved TFM. Tohidi et al. [8] conducted similar studies for precast concrete cross wall structures. Main [9] showed the effectiveness of tie forces requirements specified by the latest version of UFC 4-023-03 (DoD [2]) in preventing progressive collapse of a 2 by 2 bay composite floor system using a macro-based finite element model. It was found that the requirements might become unconservative when the system carried large load and a new equation was proposed for the calculation of tie forces for collapse prevention. One common shortcoming of the above studies is that none of the models used in these studies were able to represent a full 3-D multi-story building.

Another concept promoted by the provisions is the dynamic increase factor (DIF), which is used to predict the dynamic behavior of a building using static analysis by simply magnifying its corresponding static loads by DIF. In older versions UFC 4-023-03 (DoD [6]) and GSA [10], DIF was taken as 2.0, based on the behavior of elastic systems. This number has been proved to be too conservative by several researchers (Ruth et al. [11], Foley et al. [12], Khandelwal and El-Tawil [13]), primarily because system response is inelastic and not elastic. A series of experimental and numerical studies have been conducted to evaluate the DIF recently, such as Liu [14], Yu et al. [15], Ali et al. [16], Liu et al. [17] and Liu et al. [18]. It was demonstrated in Liu et al. [18] that method for the calculation of DIF provided by UFC 4-023-03 (DoD [2]) was unsafe under large deformation conditions when catenary action played the key role in resisting progressive collapse. The effects of slabs were neglected in all of these studies. However, the experimental tests conducted by Qian and Li [19] showed that the slab system played a significant role in determining the dynamic performance of RC frame structure subjected to sudden loss of a column. Thus, it is necessary to consider the effects of the floor slabs when determining the DIF for a certain structural system.

In summary, both sets of provisions (TFM and DIF) in UFC 4-023-03 (DoD [2]) have not yet to be thoroughly evaluated using well calibrated full 3-D nonlinear models including floor slab systems. This study sheds light on addressing the gaps in knowledge identified above. In particular, nonlinear dynamic and nonlinear static analysis are performed to assess the effectiveness of TFM in protecting steel framed structures against progressive collapse and the accuracy of the equations for calculating the DIF provided by UFC 4-023-03 (DoD [2]) using three-dimensional macro-based models. Numerous cases studies are conducted for four prototype buildings with different size, height, seismic detailing and structural layouts. A novel energy-based approach, which could replace the dynamic impact factor when assessing peak dynamic displacement (PDD) using static analysis, is proposed and its accuracy is evaluated. The applicability of the proposed method is also discussed in this study.

2. PROTOTYPE STRUCTURES, MODELING APPROACHES, SIMULATION STEUP AND NAMING SCHEME

2.1 Prototype Structures

In order to ensure that the analytical results are generally applicable, four prototype steel framed buildings are selected for case studies. All of the 4 buildings utilize moment resisting frames as the primary lateral load resisting system and simple shear connections are used in the gravity system. The structural layouts of the four buildings are outlined in Figure 1. The building shown in Figure 1(a) is a ten-story office building designed by the National Institute of Standard and Technology (NIST) for the purpose of investigating the collapse behavior of the building subjected to sudden column loss and it is designated as NIST-10. This building is designed for Seattle, WA, and categorized as Seismic Design Category D. Design details can be found in Liang et al. [20], Khandelwal et al. [21], and Alashker et al. [22]. The other three buildings are actually a set of buildings selected from the SAC model buildings in FEMA-335C (FEMA [23]), which were designed for the purpose of investigating the seismic performance of moment-resisting frame structures. They were designed for the Boston area using pre-Northridge connection configurations. This set of buildings consists of a three-story, a nine-story, and a twenty-story building and are designated as SAC-3, SAC-9, and SAC-20, respectively (Figure 1(b), Figure 1(c), and Figure 1(d)). These configurations are chosen because they represent typical steel framed office buildings designed for low-seismic risk, to contrast with NIST-10, which represents common steel framed office buildings designed for high seismic risk. Design details of these three buildings can be found in Foley et al. [24] and Hoffman [25]. Standard beam-to-column welded connections (WUF) are used in these buildings, unlike the NIST building, in which reduced beam sections (RBS) were used in the moment frames. The floor composite floor of the NIST-10 building is comprised of a RC slab of thickness 82.5mm sitting on a steel deck with 76 mm depth and connected to the underlying steel beams via shear studs. Steel reinforcement mesh in the RC slab is 0.06 mm²/mm in both directions. The composite floor in the three SAC buildings are identical. The composite floor is comprised of a 76 mm thick RC slab sitting on a 51 mm tall 19 gauge steel deck. The composite floor is connected to the underlying steel beams using shear studs and 6x6-W1.4×1.4 welded wire mesh reinforcement is used in the RC slab. Thus, the four prototype structures can cover different structural layouts, types of connections, and heights.

2.2 Modeling Approaches

Three-dimensional macro-based models are used to represent the prototype buildings. The general modeling approach adopted in this study is to model all primary structural elements in the system, including the beams, columns, slab systems, and the connections between them. Since the focus of

the study is on nonlinear response, each element's representation permits inelastic response to occur including fracture and separation, where appropriate. To enable realistic simulations of collapse, interpenetration between the various components of each model is prohibited. Therefore, falling components can introduce impact forces on the components with which they come in contact. The simulations are conducted with a single damping parameter that resulted in mass proportional damping ratios that ranged from 2% to 5%, depending upon the initial dynamic properties of the simulation in question. The simulations are carried out using the explicit finite element code LS-DYNA (Hallquist [26]).

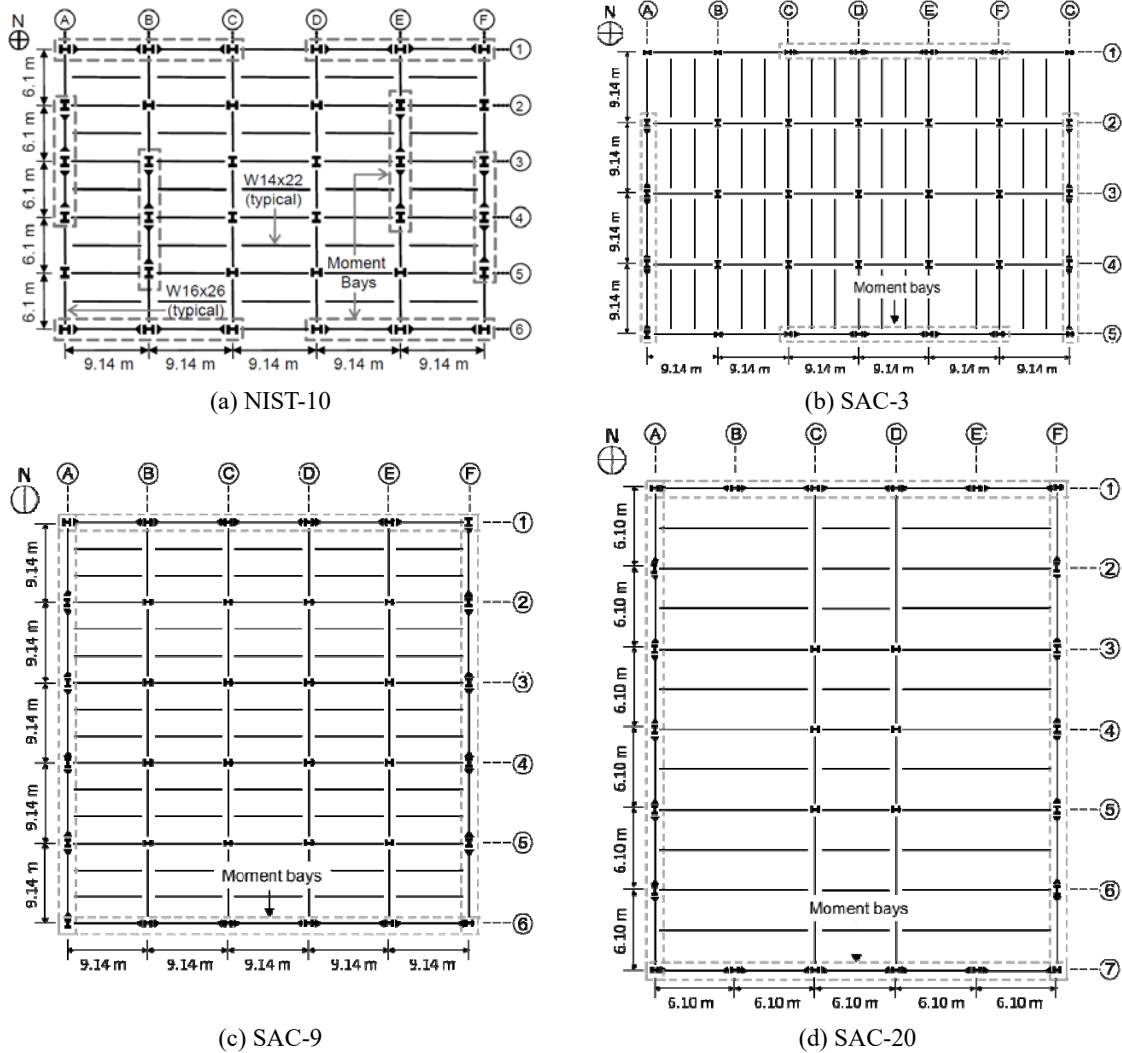


Figure 1. Structural Layouts of the Prototype Buildings

In these models, beams and columns are represented using a Hughes-Liu beam-column element formulation. The shear tab is modeled by a single beam element, which has integration points that correspond to the location of individual bolts, and a binding spring to represent contact between the beam and column flanges, as specified in Khandelwal and El-Tawil [27]. The binding spring had no tensile capacity and its compressive capacity and subsequent inelastic behavior are calibrated from detailed studies of the connection region. Unlike the macro model discussed in Khandelwal and El-Tawil [27], which represents the panel zone, the models used herein do not include such a detail to cut down on computational cost. The decision to do so was motivated by extensive preliminary studies that showed that the panel zone does not contribute significantly to the collapse response of the prototype building. A reduced model of the composite floor system is employed in this study.

The RC slab is modeled using fully integrated four-node, isotropic shell elements. A J2 plasticity model that can accommodate different tensile and compressive yield responses is used to model the RC slab. Since the steel deck can only develop resistance along the directions of the flutes, its effect is represented using bars element attached directly to the shell elements by sharing their nodes. The comparison between the responses of a composite floor system modeled using the modeling approach described previously (Alashker et al. [22]) and a detailed model (Sadek et al. [28]) showed that the proposed model was capable of representing the behavior of the composite floor system under column loss scenarios reasonably. The floor slab and the underlying steel beams are connected through rigid links. The links are intended to model the physical separation that exists between the center plane of the slab and that of the top beam flange, but cannot capture the inelastic behavior of the shear studs. The model for NIST-10 is designated as M2 in Alashker et al. [22] and Li and El-Tawil [29] but is designated as M2-NIST-10 under the naming scheme of this study. The models for the SAC buildings are designated as M2-SAC-3, M2-SAC-9, and M2-SAC-20, respectively. The 3-D overviews of the four models are shown in Figure 2.

Model M2-NIST-10 was extensively validated in previous studies (Alashker et al. [22] and Li and El-Tawil [29]) through comparisons to disparate experimental data and the results of more refined models and it was demonstrated that the 3-D macro-based model is accurate and reliable enough to represent the behavior of the structure under column loss scenarios. The details of modeling approaches and validation studies can be found in Alashker et al. [22] and Li and El-Tawil [29]. Since the same modeling approaches are employed for the other three buildings, confidence can be established in M2-SAC-3, M2-SAC-9, and M2-SAC-20.

2.3 Simulation Setup

All the models are exercised within an AMP setting and both nonlinear dynamic and nonlinear static procedures are implemented in this study. In the nonlinear dynamic analyses, the gravity loads are applied gradually within 5.0 seconds, followed by a wait period of 2.5 seconds in order to eliminate dynamic effects. After that, a column is removed by deleting it instantaneously. In the nonlinear static analyses, the column of interest is firstly removed, then the gravity loads are applied statically.

2.4 Naming Scheme

To facilitate the following discussion, the columns are designated as C-P-N-X. In this notation, C is the structural element type, i.e. columns. P is the position of the structural number described by the closest column lines in Figure 1. N is the story number and X is the notation of the building that the column belongs to, in which N10 represents the NIST-10 building, S3 represents the SAC-3 building, S9 represents the SAC-9 building, and S20 represents the SAC-20 building. For example, C-D6-5-N10 represents the column at the junction of column lines D and 6 in the 5th floor of the building NIST-10. C-C4-1-S9 represents the column junction of column lines C and 4 in the first floor of the building SAC-9.

3. EVALUATION OF TIE FORCE METHOD

Tie force method (TFM) is an indirect design approach advocated by UFC 4-023-03 (DoD [2]) with the objective of “enhancing continuity, ductility, and development of alternate load paths”. Two types of ties are required: horizontal ties and vertical ties, and both can be proportioned using methods provided in UFC 4-023-03 (DoD [2]). There are three types of horizontal ties that must be provided by the structural system: longitudinal, transverse, and peripheral. For framed structures,

the floor and roof system should carry the required longitudinal, transverse, and peripheral ties if the beams, girders and spandrels cannot be proven capable of carrying the tie force while undergoing a 0.20-rad rotation.

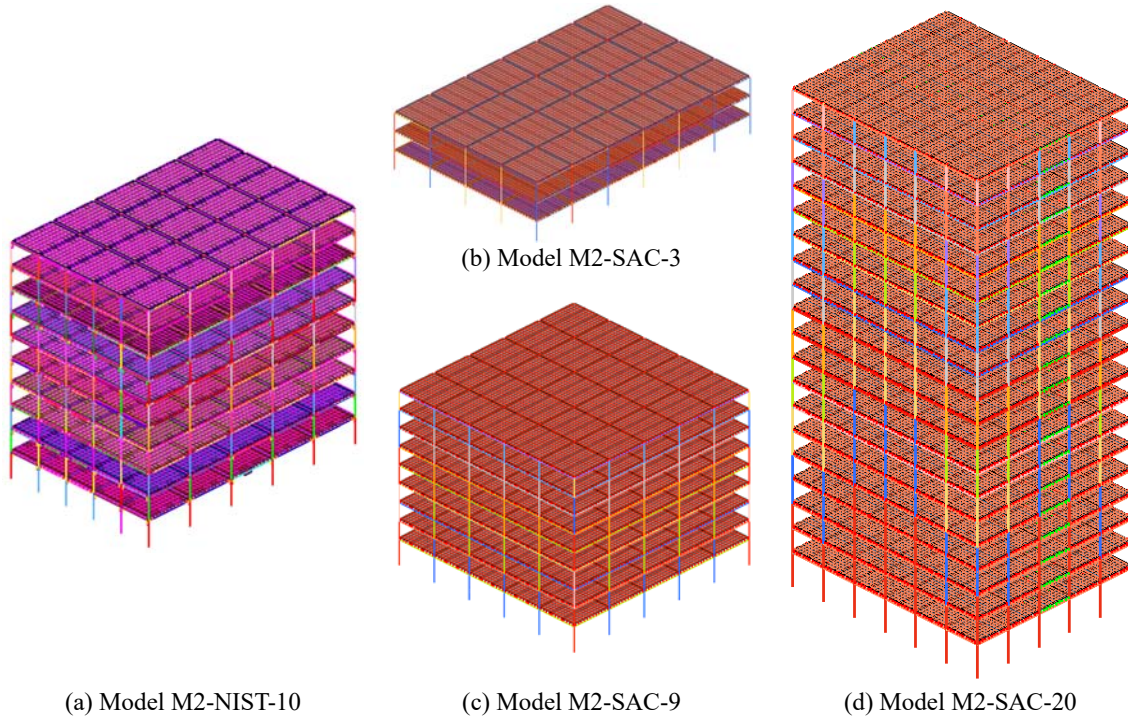


Figure 2. 3-D Overviews of the Models that are used in this Study

According to UFC 4-023-03 (DoD [2]), The required tie strength F_t in the longitudinal or transverse direction is:

$$F_t = 3W_F L_1 \quad (1)$$

Where

$W_F = 1.2D + 0.5L$ is the uniform floor load;

L_1 = greater of the distances between the centers of the columns, frames, or walls supporting any two adjacent floor spaces in the direction under consideration.

The rationality of the above equation can be shown through a simple analysis. The deformation of a frame structure subjected to loss of an interior column is shown in Figure 3(a). It is assumed that the maximum vertical displacement above the removed column reaches $0.2L$ given that the rotation limitation of beams is 0.20 rad according to UFC 4-023-03 (DoD [2]), where L is the span length of the frame structure. Under such deformation, plastic hinges should be formed at the ends of the beams and therefore the highlighted double span beam in Figure 3(a) can be modeled in the manner shown in Figure 3(b). By applying the equilibrium condition, the tie forces F_T can be calculated:

$$F_T = \frac{wL^2}{2} / 0.2L = 2.5wL \quad (2)$$

The coefficient of 2.5 in Eq. 2 is rounded up to 3.0 in the UFC 4-023-03 (DoD [2]).

The required peripheral ties, which are used for providing “adequate development or anchors at corners” (DoD [2]) and have to be placed within 1.0 m of the edge of a floor or roof, can be calculated as:

$$F_p = 6W_F L_1 L_p + 3W_C \quad (3)$$

Where

$L_p = 1.0$ m;

L_1 = The greater of the distances between the centers of the columns, frames or walls, at the perimeter of the building in the direction under consideration;

$W_c = 1.2 \times$ Dead load of cladding over the length of L_1 .

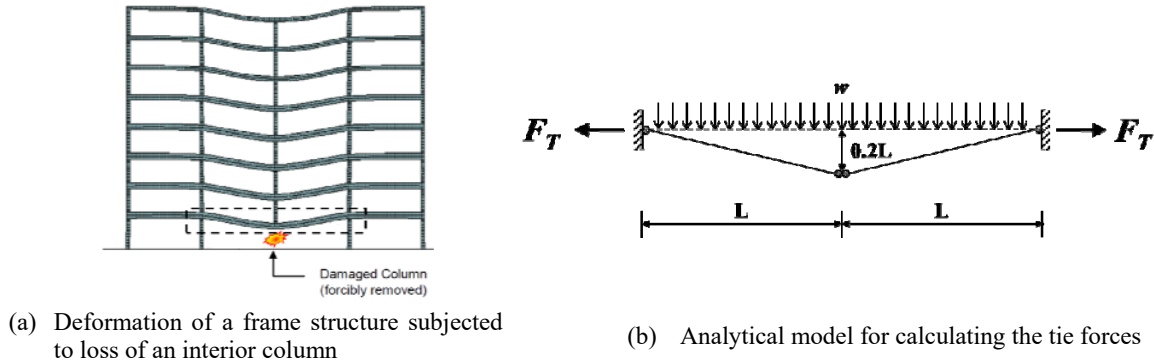


Figure 3. Simple Analysis of the Tie Force Method Equation

Similar with the longitudinal and transverse ties, the peripheral ties have to be carried by the floor and roof system unless the beams, girders, or spandrels could be shown to be capable of carrying the peripheral tie force while undergoing a 0.20-rad rotation.

According to ASCE 41-06: Seismic Rehabilitation of Existing Buildings (ASCE [30]), the plastic rotation angles for RBS connections and WUF connections cannot reach 0.20. Khandelwal and El-Tawil [27] also illustrated that the beam end rotations for these two types of connections cannot fulfill this requirement. Thus, the horizontal tie forces have to be carried by the slab systems. However, the welded wire reinforcement and the steel deck of the four prototype buildings cannot provide adequate horizontal ties required by Eq. 1 and Eq. 3. In order to develop the required tie forces in the slabs, reinforcing bars have to be added to the slabs in all of the four prototype buildings. The reinforcing bars used herein are ASTM grade 60 reinforcing steel with a minimum specified yield strength of 414 MPa. It is assumed that all of the required tie forces are carried by the reinforcing bars and no contribution from the steel deck and welded wire reinforcement is considered. The variation of models M2-X are developed. The model name is appended with ATF to signify that adequate tie forces are provided, e.g. M2-NIST-10-ATF, M2-SAC-3-ATF, M2-SAC-9-ATF, and M2-SAC-20-ATF. The variant models M2-X-ATF are identical to M2-X except the revised slab reinforcements. The reinforcing bars in the variant models are modeled using truss elements which are directly attached to the slabs. Similarly with the steel deck, these reinforcing bars is also assumed to be placed at the concrete centerline. This assumption is reasonable since the flexural behavior of the floor system is not as important as the tensile strength for collapse mitigation. The material property of the rebar is represented using a plastic-kinematic model and an elastic-perfectly plastic relationship is used to model the stress-strain response of the rebar. The elongation at fracture of the rebar used is based on Table 3 – 4 in Wight and MacGregor [31] and is listed in Table 1.

Table 1. Fracture Elongation of Rebar

Reinforcement type	Fracture elongation (%)
#4	9
#7	8
#8	8
#9	7
#10	7
#11	7

In order to investigate the role of the additional reinforcements in resisting progressive collapse, nonlinear dynamic analyses were performed using the original models (M2-X) and the models with adequate tie forces (M2-X-ATF) under various column loss scenarios. The responses (permanent deformation) between the models M2-X and M2-X-ATF subjected to similar collapse initiating events are compared. In all of the four prototype buildings, every possible single column loss case is considered in this study considering the symmetry of the structural framing plan.

3.1 NIST-10

Nine first floor column loss cases were investigated for NIST-10. Table 2 shows the comparison between the deflection of models M2-NIST-10 and M2-NIST-10-ATF at the location of the removed column in the various column loss cases. Progressive collapse, when it occurs, is designated as PC. Clearly, PC occurs in model M2-NIST-10 after interior gravity columns C-D5-1-N10 and C-E5-1-N10 are removed, but does not occur in any of the variant models M2-NIST-10-ATF, indicating that the added reinforcing bars prevent progressive collapse from happening. Adequate tie strength also reduced the overall deflection of the system significantly after loss of interior gravity column C-D4-1-N10 and exterior gravity column C-A5-1-N10. In neither of the cases, progressive collapse occurs to M2-NIST-10 but the displacement reaches 791 mm and 709 mm, respectively. The reduction is 48% and 40%, respectively. In all of the cases of removal of a gravity column which induces large deformation or progressive collapse in M2-NIST-10, the deformation given by M2-NIST-10-ATF is well below the maximum failure displacement, which is around 1300 mm as discussed in Alashker and El-Tawil [32]. Therefore, tie forces play a critical role in reducing system displacement when a gravity column is lost. However, when moment column(s) is (are) removed, the effect of the additional tie reinforcement is limited. The maximum difference between the displacements of M2-NIST-10 and M2-NIST-10-ATF is 11% and the minimum difference is only 3% after the structure lost one or two moment columns simultaneously. The reason is that the deformation of the structure subjected to loss of a moment column is so small that membrane action in the slabs is not mobilized. Moreover, the contribution of the additional reinforcement to composite action is also limited. Therefore, it is not surprising that the differences between the responses of M2-NIST-10 and M2-NIST-10-ATF under such column loss scenarios are small.

Table 2. Comparison between M2-NIST-10 and M2-NIST-10-ATF

Column lost	Column type	M2-NIST-10 (mm)	M2- NIST-10-ATF (mm)	Difference (%)
C-D4-1-N10	Interior gravity	791	536	48
C-D5-1-N10	Interior gravity	<i>PC^I</i>	576	NA
C-D6-1-N10	Exterior moment	82	74	11
C-E5-1-N10	Interior gravity	<i>PC^I</i>	535	NA
C-E6-1-N10	Exterior moment	29	28	4
C-D6-1-N10/ C-E6-1-N10	Exterior moment	457/348	417/317	10/10
C-A5-1-N10	Exterior gravity	709	506	40
C-F6-1-N10	Corner moment	47	43	9
C-E4-1-N10	Interior moment	69	66	5

PC^I: Progressive collapse

3.2 SAC Buildings

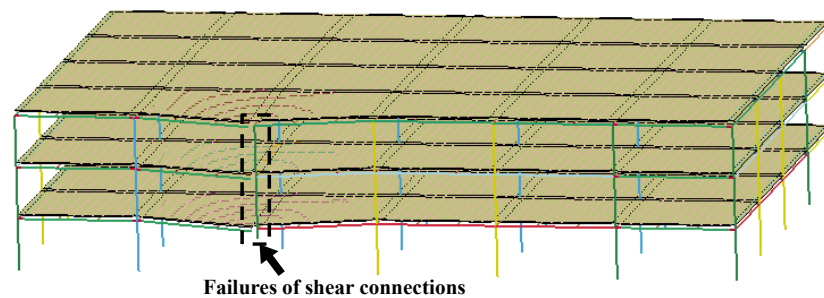
The same comparisons are made between models M2-SAC-X and M2-SAC-X-ATF and numerous column loss cases are conducted, including 12 column loss cases for SAC-3, 9 column loss cases for SAC-9, and 8 column loss cases for SAC-20. The simulation results are listed in Table 3 to Table 5. From Table 3 to Table 5 and similar trend was observed with those observed in NIST-10. The SAC buildings without adequate tie forces collapse after loss of a gravity column except loss of column C-C4-1-S20, in which the lost column has a small tributary area and the permanent deformation is 608 mm. Progressive collapse is prevented in all of the corresponding column loss cases conducted using model M2-SAC-X-ATF. The deformation obtained by M2-SAC-20-ATF after loss of column C-C4-1-S20 is 436 mm, which is 28% smaller than the one given by model M2-SAC-20. These results suggest that the additional reinforcement used for required tie forces contribute significantly to the system's collapse resistance after loss of a gravity column.

Table 3 demonstrates that the overall deflection of model M2-SAC-3 after loss of a moment column is much higher comparing with the other three buildings. In particular, the deformation of model M2-SAC-3 reaches as high as 648 mm after loss of the exterior moment column C-C5-1 of building SAC-3. This is because this particular column has only one moment connection on one side of the column. The shear connections connected to the other sides of the removed column fail immediately after loss of the column in both models M2-SAC-3 and M2-SAC-3-ATF. However, the deformation is reduced by 24% in model M2-SAC-3-ATF. The failure mechanisms of M2-SAC-3 and M2-SAC-3-ATF are shown in Figure 4. The reduction in the permanent deformation induced by the additional reinforcing bars ranges from 9% to 25% in the other moment column loss cases. For buildings SAC-9 and SAC-20, deformations given by both M2-SAC-X and M2-SAC-X-ATF after loss of moment columns are small. The reduction in deformation attributed to the reinforcing bars ranges from 3% and 12%.

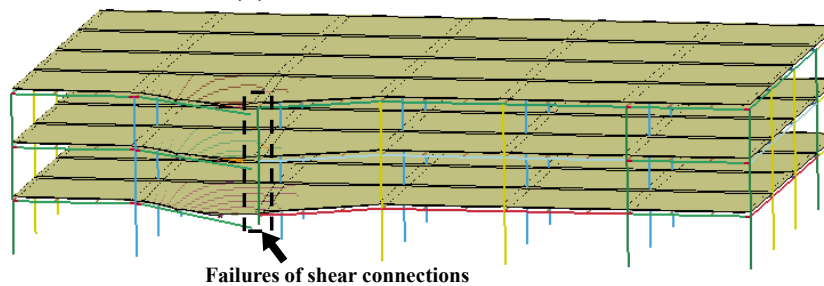
Table 3. Comparison between M2-SAC-3 and M2-SAC-3-ATF

Column lost	Column type	M2-SAC-3 (mm)	M2-SAC-3-ATF (mm)	Difference (%)
C-A3-1-S3	Exterior moment	113	97	14
C-A4-1-S3	Exterior moment	112	102	9
C-A5-1-S3	Corner moment	254	191	25
C-B3-1-S3	Interior gravity	<i>PC^I</i>	939	N/A
C-B4-1-S3	Interior gravity	<i>PC^I</i>	900	N/A
C-B5-1-S3	Exterior gravity	<i>PC^I</i>	1191	N/A
C-C3-1-S3	Interior gravity	<i>PC^I</i>	886	N/A
C-C4-1-S3	Interior gravity	<i>PC^I</i>	848	N/A
C-C5-1-S3	Exterior moment	648	495	24
C-D3-1-S3	Interior gravity	<i>PC^I</i>	885	N/A
C-D4-1-S3	Interior gravity	<i>PC^I</i>	828	N/A
C-D5-1-S3	Exterior moment	121	95	21

PC^I: Progressive collapse



(a) Failure model of M2-SAC-3-ATF



(b) Failure model of M2-SAC-3

Figure 4. Comparison between failure modes M2-SAC-3 vs. M2-SAC-3-ATF: loss of column C-C5-1

Table 4. Comparison between M2-SAC-9 and M2-SAC-9-ATF

Column lost	Column type	M2-SAC -3 (mm)	M2-SAC-3-ATF (mm)	Difference (%)
C-A4-1-S9	Exterior moment	29	27	7
C-A5-1-S9	Exterior moment	30	28	7
C-A6-1-S9	Corner moment	34	30	12
C-B4-1-S9	Interior gravity	<i>PC^I</i>	792	N/A
C-B5-1-S9	Interior gravity	<i>PC^I</i>	829	N/A
C-B6-1-S9	Exterior moment	43	40	7
C-C4-1-S9	Interior gravity	<i>PC^I</i>	864	N/A
C-C5-1-S9	Interior gravity	<i>PC^I</i>	864	N/A
C-C6-1-S9	Exterior moment	29	28	3

PC^I: Progressive collapse

In summary, from the comparisons described above, it can be concluded that the tie force method proposed in UFC 4-023-03 (DoD [2]) can effectively protect the steel special moment frame buildings against progressive collapse under column loss scenarios and is able to reduce the overall deflections of the structural systems significantly under large deformation conditions when catenary action developed by the ties plays a key role in resisting progressive collapse.

4. CALCULATION OF DYNAMIC INCREASE FACTOR

There are three procedures which are commonly used for the analysis of progressive building collapse: linear static, nonlinear static and nonlinear dynamic under the scheme of APM. Among these three procedures, linear static procedure is rarely used in the research of progressive building collapse because of the inaccuracy. Nonlinear dynamic analysis in conjunction with APM is widely viewed as the most comprehensive method. However, it requires extensive computational resources and is time consuming to perform such analyses. Thus, nonlinear static procedure might be a reasonable compromise between accuracy and computational time. One of the problems associated with nonlinear static procedure is that static procedures do not capture the dynamic nature of the column removal problem. One convenient way to do so is to apply a Dynamic Increase Factor (DIF) to the results of static models to account for the response magnification associated with dynamic behavior. The DIF can be defined as the ratio of the loads applied statically and dynamically when the structure is subjected to the same deformation demand. The DIF is used to amplify the gravity loads which are applied to the structure when nonlinear static procedure is implemented in order to estimate the dynamic peak displacement. In the latest version of UFC 4-023-03 (DoD [2]), the DIF for steel frame structures is specified as follows:

$$\Omega_N = 1.08 + \frac{0.76}{\theta_{pra}/\theta_y + 0.83} \quad (4)$$

Where θ_{pra} is the plastic rotation angle given in Table 5-6 of ASCE 41-06 (ASCE [29]) for the collapse prevention condition; and θ_y is the yield rotation according to Equation 5-1 in ASCE 41-06 (ASCE [20]).

Table 5. Comparison between M2-SAC-20 and M2-SAC-20-ATF

Column lost	Column type	M2-SAC-20 (mm)	M2-SAC-20-ATF (mm)	Difference (%)
C-A4-1-S20	Exterior moment	19	18	5
C-A5-1-S20	Exterior moment	20	19	5
C-A6-1-S20	Exterior moment	24	22	8
C-A7-1-S20	Corner moment	26	24	8
C-B7-1-S20	Exterior moment	11	10	9
C-C4-1-S20	Interior gravity	608	436	28
C-C5-1-S20	Interior gravity	<i>PC^I</i>	649	N/A
C-C7-1-S20	Exterior moment	18	17	6

PC^I: Progressive collapse

Table 6. Comparison between DIF_{DoD} , DIF_{NS} , and DIF_{real} : NIST-10 Building

Column lost	DIF_{DoD}	DIF_{NS}	DIF_{real}
C-D6-1-N10	1.32	1.40	1.49
C-E6-1-N10	1.32	1.96	1.46
C-F6-1-N10	1.32	1.85	1.45
C-D6-5-N10	1.32	1.25	1.50
C-E6-5-N10	1.32	1.97	1.48
C-F6-5-N10	1.32	1.78	1.48

Eq. 4 was obtained from curve fitting and thus lacks a theoretical basis. Furthermore, the three-dimensional models used to formulate the equation (McKay et al. [33]) did not include the slabs, which were shown in Li and El-Tawil [29] to contribute significantly to collapse response and should be considered as primary components according to UFC 4-023-03 (DoD [2]).

A series of cases studies in the context of APM are conducted in order to verify whether Eq. 4 is able to produce a reasonable value of DIF. The M2-X -ATF model is used in these simulations since UFC 4-023-03 (DoD [2]) require that “for elements with inadequate horizontal tie force capacity, the Alternate Path method cannot be used”. The following steps have to be performed to assess the DIF according to the procedures proposed in McKay et al. [33] and UFC 4-023-03 (DoD [2]):

- a. Nonlinear dynamic analysis is performed using the design gravity loads. The APM is employed and the peak dynamic displacement of the removed column is recorded.

- b. Using the same model in Step 1, a nonlinear static analysis is performed. Increased the gravity loads with a trial DIF are applied in the effective area of the removed column.
- c. Repeat step 2 until the deformation matches with the one computed in step 1.

The comparisons between the dynamic increase factors calculated according to Eq. 4 (DIF_{DoD}) and the DIFs obtained based on the simulation results of model M2-NIST-10-ATF (DIF_{real}) and M2-NIST-10-NS (DIF_{NS}) following the steps outlined above under various column loss scenarios are shown in Table 6. Model M2-NIST-10-NS is identical to M2-NIST-10 except the floor slabs are removed. Only moment column loss cases are considered because collapse will occur if a gravity column is removed from M2-NIST-10-NS. From Table 6, large differences between DIF_{DoD} and DIF_{real} can be seen, indicating that Eq. 4 fails to produce reasonable DIFs. The differences between DIF_{DoD} and DIF_{NS} are even larger although the models employed in UFC 4-023-03 (DoD [2]) to formulate the equation did not considered the effects of the slab system, either. For example, the differences between DIF_{NS} and DIF_{DoD} are 51%, 42% and 52% when moment columns C-E6-1-N10, C-F6-1-N10, and C-E6-5-N10 are removed, respectively. The comparisons between DIF_{DoD} and DIF_{NS} also reveal that the presence of the slabs is not the reason for such inaccuracy. Therefore, it can be concluded that as an empirical equation obtained from curve fitting and without any theoretical basis, Eq. 4 specified in UFC 4-023-03 (DoD [2]) for calculating DIF is problematic.

Another interesting observation from Table 6 is that the slabs have a significant impact on the values of DIFs based on the comparison between DIF_{NS} and DIF_{real} . It can be seen that the DIF_{real} are smaller than DIF_{NS} after loss of column C-E6 and C-F6 in the first and fifth floor and in the other two cases, DIF_{real} are smaller than DIF_{NS} . Therefore, removal of the slabs can overestimate or underestimate the value of DIF thus the slab floor system has to be considered if accurate DIF is aimed to be obtained.

Table 7 to Table 10 show the comparisons between DIF_{real} and DIF_{DoD} for the prototype buildings in various column loss cases. In these tables, a positive difference means UFC 4-023-03 (DoD [2]) underestimate the values of DIFs, and a negative difference means UFC 4-023-03 (DoD [2]) overestimate the values of DIFs. From these tables, a common trend for the four buildings is observed. It can be seen that the differences between DIF_{real} and DIF_{DoD} are remarkable, especially in the column loss cases when gravity columns are removed. For NIST-10 building, the difference ranges from 16% to 30% when a gravity column is removed. The deviations are around 40% for SAC-3 and SAC-9 and 30% for SAC-20 under single gravity column loss scenarios. Eq. 4 can estimate the DIFs reasonably after loss of moment columns, which induce relatively small deformations. Table 6 to Table 9 demonstrate that the differences between DIF_{real} and DIF_{DoD} are under 15% when the lost columns are in the moment resisting system. It also should be noted that the UFC method underestimated the DIF in most of the column loss conducted herein. Therefore, it can be concluded that the DIF specified in UFC 4-023-03 (DoD [2]) is inaccurate and unconservative.

Table 7. Comparison between DIF_{real} and DIF_{DoD} : NIST-10 Building

Column lost	DIF_{DoD}	DIF_{real}	Difference
C-A5-1-N10	1.32	1.72	30%
C-D4-1-N10	1.32	1.70	29%
C-D6-1-N10	1.32	1.49	13%
C-E4-1-N10	1.32	1.30	-2%
C-E5-1-N10	1.32	1.53	16%
C-E6-1-N10	1.32	1.46	11%
C-F6-1-N10	1.32	1.45	10%
C-A5-5-N10	1.32	1.64	24%
C-D4-5-N10	1.32	1.71	30%
C-D6-5-N10	1.32	1.50	14%
C-E4-5-N10	1.32	1.30	-2%
C-E5-5-N10	1.32	1.53	16%
C-E6-5-N10	1.32	1.48	12%
C-F6-5-N10	1.32	1.48	12%

Table 8. Comparison between DIF_{real} and DIF_{DoD} : SAC-3 building

Column lost	DIF_{DoD}	DIF_{real}	Difference (%)
C-A3-1-S3	1.38	1.48	7
C-A4-1-S3	1.38	1.49	8
C-A5-1-S3	1.38	1.45	5
C-B3-1-S3	1.28	1.85	45
C-B4-1-S3	1.28	1.82	42
C-B5-1-S3	1.28	1.82	42
C-C3-1-S3	1.28	1.85	48
C-C4-1-S3	1.28	1.84	44
C-C5-1-S3	1.38	1.39	1
C-D3-1-S3	1.28	1.87	46
C-D4-1-S3	1.28	1.85	45
C-D5-1-S3	1.38	1.52	10

Table 9. Comparison between DIF_{real} and DIF_{DoD} : SAC-9 Building

Column lost	DIF_{DoD}	DIF_{real}	Difference (%)
C-A4-1-S9	1.33	1.50	13
C-A5-1-S9	1.33	1.52	14
C-A6-1-S9	1.33	1.46	10
C-B4-1-S9	1.28	1.83	43
C-B5-1-S9	1.28	1.79	40
C-B6-1-S9	1.33	1.46	10
C-C4-1-S9	1.28	1.80	41
C-C5-1-S9	1.28	1.79	40
C-C6-1-S9	1.33	1.41	8

Table 10. Comparison between DIF_{real} and DIF_{DoD} : SAC-20 Building

Column lost	DIF_{DoD}	DIF_{real}	Difference (%)
C-A4-1-S20	1.30	1.42	9
C-A5-1-S20	1.30	1.38	6
C-A6-1-S20	1.30	1.40	8
C-A7-1-S20	1.30	1.27	-2
C-B7-1-S20	1.30	1.34	3
C-C4-1-S20	1.30	1.66	28
C-C5-1-S20	1.30	1.74	34
C-C7-1-S20	1.30	1.28	-2

On the other hand, it also reveals another two problems associated with Eq. 4: 1) θ_{pra}/θ_y is member dependent and not system dependent, and 2) certain members may be predominate in the DIF calculations. In other words, the members or connections with the smallest value of θ_{pra}/θ_y may associate with the same member section and structural layouts for the different column loss cases, and thus lead to the same DIF values. For example, an all of the column loss cases of NIST-10 building, the control member is the gravity beam in East-West direction. Such beams are considered primary members and not neglected in this study because they are not considered to be pinned at both ends and the flexural strength of the shear connection is not neglected and the value of θ_{pra}/θ_y for the member is the smallest among the primary structural component is the effective area of the removed column. Table 6 to Table 9 show that the actual value of DIF do depend on the type of the removed column.

5. ENERGY-BASED APPROACH FOR ASSESSING PEAK DYNAMIC DISPLACEMENT

The purpose of using DIF is to assess the peak dynamic displacement of a system under column loss scenarios through nonlinear static procedure. Since it has already been shown that the DIF specified in UFC 4-023-03 (DoD [2]) is not accurate nor conservative. It was discussed that the approach suffers from several critical drawbacks and that it is based on empirical data. To resolve this problem, a new approach for assessing PDD is proposed herein.

5.1 Energy-based Approach for Assessment of Peak Dynamic Displacement

To illustrate a general idea of the approach, a 4 slab-panel system with the mid-column removed as shown in Figure 5 is considered herein. It is assumed that the uniformly distributed load (UDL) that is applied to the system is w_0 . According to Izzundin et al. [34], if the column is removed suddenly, the external work done by the UDL when the PDD Δ_D is reached is:

$$W_{ext} = \alpha w_0 \Delta_D \quad (5)$$

where α is a work-related factor that depends on the gravity load distribution and when w is identical everywhere, it is a constant which depends on the deformed shape of the floor system.

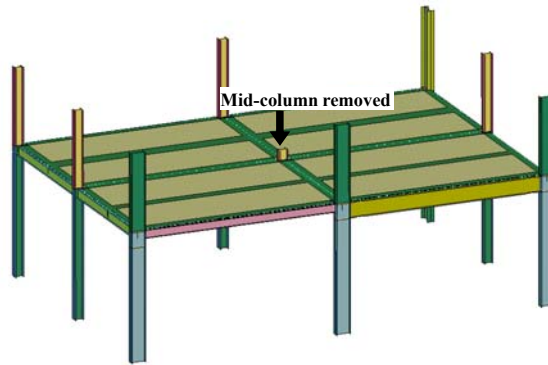


Figure 5. 4 slab-panel System with Mid-column Removed

Assume that the load-deflection response $w(\Delta)$ of the system obtained from a static push-down analysis is as shown in Figure 6(a). When the PDD of the system is reached, the internal energy stored in the system can be expressed as:

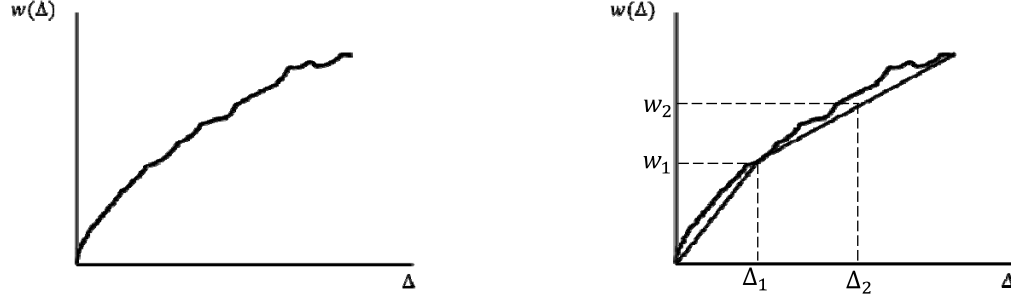
$$W_{int} = \int_0^{\Delta_D} \alpha w(\Delta) d\Delta \quad (6)$$

When the PDD is achieved, the kinematic energy stored in the system is zero. According to the law of energy conservation, an equality can be established, which is $W_{ext} = W_{int}$. It is reasonable to assume that the deformation modes of the system under dynamic and static loading conditions are the same. Therefore, the constant α can be eliminated. Thus,

$$w_0 \Delta_D = \int_0^{\Delta_D} w(\Delta) d\Delta \quad (7)$$

The PDD of the system can be expressed as:

$$\Delta_D = \frac{\int_0^{\Delta_D} w(\Delta) d\Delta}{w_0} \quad (8)$$



(a) Load-deflection curve obtained by static push-down (b) Bi-linear approximation of the load-deflection curve
Figure 6. Load-deflection Curve for the 4-slab Panel System

The relationship in Figure 6(a) can be approximated as a bi-linear relationship as shown in Figure 6(b). The assumption is reasonable since the force-displacement relationships obtained from a number of static push-down experimental tests conducted recently to test the robustness of bolted connections, semi-rigid connections and rigid connections under column loss scenarios (Li et al. [35], Guo et al. [36], Yang and Tan [37], Guo et al. [38], Weigland and Berman [39], and Wang et al. [40]) could be simplified as bi-linear without losing too much critical information. As shown in Figure 6(b), the bi-linear relationship can be defined by w_1 , w_2 and their corresponding displacement Δ_1 and Δ_2 . w_1 is the UDL when the system reaches its elastic stage since the initial stage of the force-displacement relationship in a static push-down test should be linear as shown in the progressive collapse tests mentioned above. On the other hand, w_1 could be calculated based on the size of the cross section of the structural components, which should be larger than the factored loads which should be carried by the system. w_2 is greater than w_1 and $w_2 = \beta w_1$, in which $\beta > 1$. For simplicity, the factored design gravity load $w_0 = 1.2D + 0.5L$ required by UFC 4-023-03(DoD [2]) is used instead of w_1 and thus $w_2 = \beta w_0$. This assumption is reasonable because the quantitative difference between w_0 and w_1 should be within a reasonable range according to the Load and Resistance Factor Design method. The displacements corresponding to w_0 and βw_0 are Δ_{01} and Δ_{02} , respectively. Δ_D is deemed to be larger than Δ_{01} , which is obtained from the nonlinear static analysis without the application of the DIF, but not necessarily smaller than Δ_{02} . Thus, the approximated bi-linear force-displacement relationship $w(\Delta)$ of the structural system can be expressed as:

$$w(\Delta) = \begin{cases} \frac{w_0}{\Delta_{01}} \Delta, & \Delta \leq \Delta_{01} \\ \frac{w_0}{\Delta_{02} - \Delta_{01}} [(\beta - 1)\Delta + \Delta_{02} - \beta\Delta_{01}], & \Delta > \Delta_{01} \end{cases} \quad (9)$$

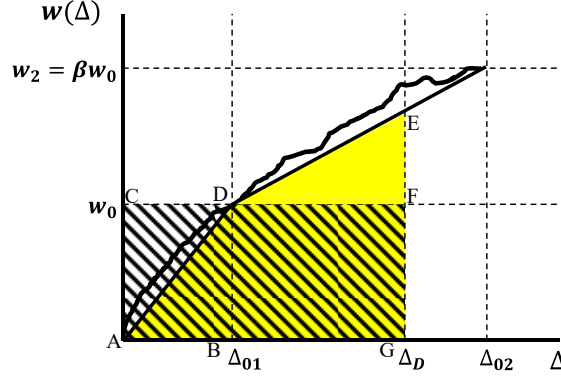


Figure 7. Energy-based Approach for Assessing Peak Dynamic Displacement Δ_D

An energy-based approach for assessment of PDD can be established based on this simplification. As shown in Figure 7, the hatched area represents the left-hand side of Eq. 7 and the shaded area represents the right-hand side of Eq. 7. To equate the hatched area to the shaded area, the area of the triangle ACD has to be equal to the area of the triangle DEF since triangle ABD and rectangular BDFG are shared by the hatched area and the shaded area. Thus,

$$\frac{1}{2}w_0\Delta_{01} = \frac{1}{2}[w(\Delta_D) - w_0](\Delta_D - \Delta_{01}) \quad (10)$$

By substituting Eq. 9 into Eq. 10,

$$\frac{1}{2}w_0\Delta_{01} = \frac{1}{2}\left\{\frac{w_0}{(\Delta_{02} - \Delta_{01})}[(\beta - 1)\Delta_D + \Delta_{02} - \beta\Delta_{01}] - w_0\right\}(\Delta_D - \Delta_{01}) \quad (11)$$

By solving this equation, the PDD can be obtained:

$$\Delta_D = \Delta_{01} + \sqrt{\frac{\Delta_{01}(\Delta_{02} - \Delta_{01})}{\beta - 1}} \quad (12)$$

Thus, the PDD can be estimated through a simple equation as long as Δ_{01} and Δ_{02} are acquired. The implementation of the proposed method requires the following steps:

- i. Conduct a nonlinear static analysis using APM with the application of the gravity load $w_0 = 1.2D + 0.5L$ and record the corresponding displacement Δ_{01} ;
- ii. Conduct another nonlinear static analysis using APM with the application of the gravity load βw_0 and record the corresponding displacement Δ_{02} ;
- iii. Use Eq. 12 to calculate the PDD of the system.

5.2 Verification of the Proposed Approach

In order to verify the accuracy of the proposed approach, a large number of case studies are conducted using the numerical models M2-X-ATF for all of the four prototype buildings. Nonlinear dynamic analyses are firstly performed to obtain the PDD for comparison purposes. Then nonlinear static analyses are conducted on the basis of the proposed approach and the method for the calculation of the DIF specified in UFC 4-023-03 (DoD [2]) under the same column loss scenarios. Table 11 to Table 14 show the comparisons between the normalized peak displacements obtained

by the two methods. “PDD” listed in these tables is nonlinear dynamic PDD and is used as reference in this section. Normalized peak displacement is defined as the ratio between the estimated PDD on the basis of the proposed method or UFC 4-023-03 (DoD [2]) (UFC method) to the PDD obtained from the nonlinear dynamic analyses. Based on a trial and error process, the value of β used in all of the case studies is set to 1.3. Considering the values of the DIFs are between 1.30 to 1.70 in most of the cases in this study as shown in Table 6 to Table 9, this number is reasonable.

Table 11. Comparison between the Normalized Peak Dynamic Displacements (NPDD) Obtained from the Proposed Method and the UFC Method: NIST-10 Building

Column lost	PDD ¹ (mm)	NPDD: Proposed method	NPDD: UFC method
C-A5-1-N10	644	1.02	0.69
C-D4-1-N10	660	1.05	0.69
C-D6-1-N10	114	1.16	0.76
C-E4-1-N10	101	1.33	0.90
C-E5-1-N10	664	1.07	0.71
C-E6-1-N10	43	1.27	0.84
C-F6-1-N10	59	1.24	0.83
C-A5-5-N10	652	1.05	0.70
C-D4-5-N10	685	1.03	0.67
C-D6-5-N10	149	1.09	0.72
C-E4-5-N10	167	1.21	0.86
C-E5-5-N10	684	1.07	0.70
C-E6-5-N10	53	1.28	0.84
C-F6-5-N10	72	1.23	0.81

¹PDD: peak dynamic displacement obtained from nonlinear dynamic analyses

Table 12. Comparison between the Normalized Peak Dynamic Displacements (NPDD) Obtained from the Proposed Method and the UFC Method: SAC-3 Building

Column lost	PDD ¹ (mm)	NPDD: Proposed method	NPDD: UFC method
C-A3-1-S3	124	1.17	0.84
C-A4-1-S3	129	1.14	0.84
C-A5-1-S3	229	1.12	0.83
C-B3-1-S3	989	1.11	0.70
C-B4-1-S3	967	1.13	0.72

C-B5-1-S3	1308	1.07	0.68
C-C3-1-S3	937	1.10	0.68
C-C4-1-S3	912	1.10	0.73
C-C5-1-S3	531	1.13	0.99
C-D3-1-S3	933	1.04	0.67
C-D4-1-S3	887	1.01	0.70
C-D5-1-S3	123	1.04	0.84

¹PDD: peak dynamic displacement obtained from nonlinear dynamic analyses

Table 13. Comparison between the Normalized Peak Dynamic Displacements (NPDD) Obtained from the Proposed Method and the UFC Method: SAC-9 Building

Column lost	PDD ¹ (mm)	NPDD: Proposed method	NPDD: UFC method
C-A4-1-S9	36	1.31	0.86
C-A5-1-S9	39	1.28	0.87
C-A6-1-S9	37	1.35	0.92
C-B4-1-S9	858	1.06	0.69
C-B5-1-S9	887	1.03	0.66
C-B6-1-S9	53	1.34	0.91
C-C4-1-S9	914	1.05	0.68
C-C5-1-S9	916	1.07	0.69
C-C6-1-S9	35	1.40	0.94

¹PDD: peak dynamic displacement obtained from nonlinear dynamic analyses

It can be seen from these tables that out of the 43 column loss cases considered herein, there are 42 cases in which the normalized peak displacements obtained on the basis of UFC method are smaller than 1.0, indicating that the UFC method underestimate the peak dynamic displacement in almost every single column loss case. The only exception is that the UFC method is overestimated the PDD by 3% when the SAC-20 building is subjected to loss of column C-A6-1-S20. The PDD of the NIST-10 building is underestimated by 30% by the UFC method when the building is subjected to loss of column C-D4-1-N10. In the case when column C-B5-1-S9 of SAC-9 building is removed, the PDD of the system is underestimated by 34%. The UFC PDD of the SAC-20 building is 31% smaller than the PDD evaluated by the nonlinear dynamic analysis when the building is subjected to loss of column C-A7-1-S20. In summary, based on the simulation results, the UFC method underestimates the PDD of the structural systems by a range of 1% to 34%, which means the vulnerability of the system is significantly underestimated and thus the UFC method is once again proved to be unsafe.

Table 14. Comparison between the Normalized Peak Dynamic Displacements (NPDD) Obtained from the Proposed Method and the UFC Method: SAC-20 Building

Column lost	PDD ¹ (mm)	NPDD: Proposed method	NPDD: UFC method
C-A4-1-S20	20	1.40	0.90
C-A5-1-S20	20	1.40	0.95
C-A6-1-S20	23	1.30	1.03
C-A7-1-S20	26	1.32	0.69
C-B7-1-S20	11	1.45	0.97
C-C4-1-S20	463	1.11	0.74
C-C5-1-S20	688	1.15	0.75
C-C7-1-S20	19	1.42	0.99

¹PDD: peak dynamic displacement obtained from nonlinear dynamic analyses

In contrast, the proposed approach shows reasonable accuracy and is fairly conservative. The normalized PDDs estimated by the proposed approach are between 1.01 and 1.45 according to Table 11 to Table 14. In the cases when the PDD is smaller than 100 mm, the proposed approach typically overestimates the PDD by 20% to 40%, such as the cases of loss of columns C-E6-1-N10, C-F6-1-N10, C-E6-5-N10, and C-F6-5-N10 of the NIST-10 building, loss of columns C-A4-1-S9, C-A5-1-S9, C-A6-1-S9, C-B6-1-S9, and C-C6-1-S9 of the SAC-9 building, loss of columns C-A4-1-S20, C-A5-1-S20, C-A6-1-S20, C-A7-1-S20, C-B7-1-S20, and C-C7-1-S20 of the SAC-20 buildings. These columns are all moment columns and loss of such columns is not critical for the system. However, for the column loss cases which result in large deformation (more than 100 mm), the proposed method is very accurate and does not overestimate the PDD in a significant manner. For example, the normalized PDD calculated using the proposed approach in the case of removal of column C-A5-1 of the NIST-10 building is 1.02, which means the PDD estimated on the basis of the proposed approach matches the PDD obtained from the nonlinear dynamic analysis. In this case, the PDD is 644 mm, as is shown in Table 11. Table 12 demonstrates that the normalized PDDs assessed on the basis of the proposed approach are all below 1.20 when SAC-3 building is subjected to various column loss scenarios. The PDD calculated according to the proposed approach is 3% to 7% larger than the corresponding nonlinear dynamic PDD under the loss of interior gravity columns of the SAC-9 building and the proposed method shows great accuracy in these cases. For the other column loss cases, the difference between the PDDs evaluated by implementing the proposed approach and the dynamic nonlinear procedure ranges from 10% and 17%.

In summary, the proposed simplified energy-based method can estimate the PDD of the steel framed structures accurately and is reasonably conservative. It is also worthwhile to mention that the column loss cases considered herein incorporate different beam-column connection types, including the shear connection, WUF moment connections and RBS moment connections, and unlike the UFC method, the accuracy of the proposed method is not significantly influenced by the connection type. Therefore, the proposed method can be generally applied to the design of steel framed buildings with various connection types against progressive collapse.

5.3 Suitability of the Proposed Approach for Design Office Environment

From the accuracy perspective, the PDD evaluated using the proposed approach has been shown to be more accurate comparing with the one calculated using the equation provided by UFC 4-023-03 (DoD [2]) in this study. On the other hand, as is mentioned earlier, the proposed approach is generally applicable to the steel framed structures with various types of beam-to-column connections, such as shear connections, WUF connections and RBS connections. Thirdly, the only calculation which needs to be done by hand in the proposed approach is the utilization of Eq. 12. However, the UFC method requires more hand calculations to determine the values of θ_{pra} and θ_y for the primary structural components.

Actually, the dynamic increase factor is no longer needed because by using the proposed method, the PDD can be calculated directly. Therefore, the proposed method could be a reasonable replacement of application of DIF for the purpose of estimating the peak dynamic displacement and thus evaluating the damage of the structure after loss of columns through nonlinear static analysis.

However, the proposed approach will be less accurate than the approach proposed by Izzundin et al. [34] because the proposed approach is an approximation of their method. However, from the computational perspective, the proposed approach outperforms the method proposed by Izzundin et al. [34]. In their method, a series of nonlinear static analyses are needed in order to obtain the static load-deflection curve of the system and a fairly complicated trial-and-error process is needed to obtain the PDD since it is an unknown and it serves as the upper limit of the integration.

On the other hand, the proposed method requires at most 2 nonlinear static simulations using the same model under different loading conditions. Although this is more effort than a single nonlinear static run, it is certainly less effort than running a full dynamic simulation, with all of its complications in modeling and data processing. Many commercial software packages can now run nonlinear static simulations, tracking the inelastic response of frame elements and even shell elements. Therefore, conducting the requisite static simulations is certainly within the capabilities of most design offices at present, rendering the method practical and suitable for routine application.

6. CONCLUSIONS

Two design requirements in the UFC 4-023-03 (DoD [2]) published by the US Department of Defense were evaluated, including Tie Force Method and criteria for the calculation of the Dynamic Increase Factor. To ensure that the analytical results are generally applicable, three-dimensional macro-based models for a pool of 4 buildings with different heights, structural layouts and seismic detailing were created. The modeling approach has been extensively validated in previous research (Alashker et al. [22] and Li and El-Tawil [29]). It was found the original design of these structures did not satisfy the Tie Force criteria and thus the buildings were redesigned to ensure adequate tie strength by adding reinforcing bars to the slabs of the structures. The responses of all four structures under column loss scenarios before and after the re-design were then compared to evaluate the efficacy of the TFM procedure in UFC 4-023-03 (DoD [2]). The DIFs of the prototype structures were obtained from the numerical simulations and compared with the DIFs calculated according to the method specified in UFC 4-023-03 (DoD [2]). It was found the UFC method were neither accurate nor conservative. To address this deficiency, a new, energy-based approach for assessing the peak dynamic displacement was proposed, in which the simulation results of two separate nonlinear static analyses were needed to compute the peak dynamic displacement. Extensive case studies were then conducted to assess the characteristics of the new method and the following conclusions are drawn:

- The tie force method as implemented in UFC 4-023-03 (DoD [2]) can effectively protect the structures against progressive collapse under column loss scenarios. Ensuring adequate tie strength also reduces the overall deflection of the structural system significantly under large deformation conditions when catenary action plays a significant role in resisting progressive collapse although this effect is limited when the deformations are small.
- The method for the calculation of the dynamic increase factor for the steel framed structures specified in UFC 4-023-03 (DoD [2]) is neither accuracy nor conservative. The method is also unsafe because it may underestimate the peak dynamic displacement of a structure by 30% in some cases and thus significantly underestimate the vulnerability of the structure under column loss scenarios.
- The proposed energy-based approach for assessing the peak dynamic displacement of a structure after sudden column loss is reasonably accurate and conservative. It is also generally applicable to the steel framed structures with various types of beam-column connections. Although the proposed needs two separate nonlinear static analyses, its accuracy and simplicity make it attractive for use in a design office environment. Furthermore, considering the advantages of the proposed approach over the UFC method, it could be a reasonable replacement of application of DIF for the purpose of estimating the peak dynamic displacement and thus evaluating the damage of the structure after loss of columns through nonlinear static analysis.

ACKNOWLEDGEMENT

The presented work was supported by grants from the National Natural Science Foundation of China under Grant No. 51408152, Natural Science Foundation of Heilongjiang Province, China under Grant No. LC2016021, the Fundamental Research Funds for the Central Universities through grant HIT.NSRIF.2015098, China Postdoctoral Science Foundation through grant 2014M550194, and China Postdoctoral Science Foundation through grant 2015T80353. Any opinions, findings, conclusions, and recommendations expressed in this paper are those of the authors and do not necessarily reflect the views of the sponsors.

REFERENCES

- [1] ASCE 7-10, "Minimum Design Loads for Buildings and other Structures", American Society of Civil Engineers, 2013.
- [2] UFC 4-023-03, "Design of Buildings to Resist Progressive Collapse", Department of Defense, 2013.
- [3] GSA, "Alternate Path Analysis & Design guidelines for Progressive Collapse Resistance", U.S. General Service Administration, 2013.
- [4] Moore, D.B., "The UK and European Regulations for Accidental Actions", Proceedings of Workshop on Prevention of Progressive Collapse, National Institute of Building Sciences, 2002.
- [5] Abruzzo, J., Matta, A. and Panariello, G., "Study of Mitigation Strategies for Progressive Collapse of a Reinforced Concrete Commercial Building", Journal of Performance of Constructed Facilities, 2006, Vol. 20, No. 4, pp. 384-390.
- [6] UFC 4-023-03, "Design of Buildings to Resist Progressive Collapse", Department of Defense, 2005.
- [7] Li, Y., Lu, X., Guan, H. and Ye, L., "An Improved Tie Force Method for Progressive Collapse Resistance Design of Reinforced Concrete Frame Structures", Engineering Structures, 2011, Vol. 33, No. 10, pp. 2931-2942.

- [8] Tohidi, M., Yang, J. and Baniotopoulos, C., "Numerical Evaluation of Codified Design Methods for Progressive Collapse Resistance of Precast Concrete Cross Wall Structures", *Engineering Structures*, 2014, Vol. 76, pp. 177-186.
- [9] Main, J.A., "Composite Floor Systems under Column Loss: Collapse Resistance and Tie Force Requirements", *Journal of Structural Engineering*, 2014, Vol. 140, No. 8, A4014003.
- [10] GSA, "Progressive Collapse Analysis and Design Guidelines for New Federal Office Building and Major Modernization Project", U.S. General Service Administration, 2003.
- [11] Ruth, P., Marchand, K.A. and Williamson, E.B., "Static Equivalency in Progressive Collapse Alternate Path Analysis: Reducing Conservatism while Retaining Structural Integrity", *Journal of Performance of Constructed Facilities*, 2006, Vol. 20, No. 4, pp. 349-364.
- [12] Foley, C. M., Barnes, K. and Schneeman, C., "Quantifying and Enhancing Robustness in Steel Structures: Part 1 - Moment-Resisting Frames", *Engineering Journal*, American Institute of Steel Construction, 2008, 4th Quarter, pp. 267-286.
- [13] Khandelwal, K. and El-Tawil, S., "Pushdown Resistance as a Measure of Robustness in Progressive Collapse Analysis", *Engineering Structures*, 2011, Vol. 33, No. 9, pp. 2653-2661.
- [14] Liu, M., "A New Dynamic Increase Factor for Nonlinear Static Alternate Path Analysis of Building Frames Against Progressive Collapse", *Engineering Structures*, 2013, Vol. 48, pp. 666-673.
- [15] Yu, J., Rinder, T., Stolz, A., Tan, K.H. and Riedel, W., "Dynamic Progressive Collapse of an RC Assemblage Induced by Contact Detonation", *Journal of Structural Engineering*, 2014, Vol. 140, No. 6, A04014014.
- [16] Ali, K., Mohsen, G. and Farshad, M., "Assessment of Dynamic Effect of Steel Frame due to Sudden Middle Column Loss", *The Structural Design of Tall and Special Buildings*, 2014, No. 23, No. 5, pp. 390-402.
- [17] Liu, C., Tan, K.H. and Fung, T.C., "Investigations of Nonlinear Dynamic Performance of Top-and-Seat with Web Angle Connections subjected to Sudden Column Removal", *Engineering Structures*, 2015, Vol. 99, pp. 449-461.
- [18] Liu, C., Tan, K.H. and Fung, T. C., "Dynamic Behavior of Web Cleat Connections subjected to Sudden Column Removal Scenario", *Journal of Construction Steel Research*, 2013, Vol. 86, pp. 92-106.
- [19] Qian, K. and Li, B., "Quantification of Slab Influences on the Dynamic Performance of RC Frames against Progressive Collapse", *Journal of Performance of Constructed Facilities*, 2015, Vol. 29, No. 1, 04014029.
- [20] Liang, X., Shen, Q. and Ghosh, S.K., "Assessing Ability of Seismic Structural System to Withstand Progressive Collapse: Seismic Design and Progressive Collapse Analysis of Steel Frame Buildings", Rep. Prepared for SK Ghosh and Associates, 2006.
- [21] Khandelwal, K., El-Tawil, S., Kunnath, S.K. and Lew, H.S., "Macro-model Based Simulations of Progressive Collapse: Steel Frame Structures", *Journal of Structural Engineering*, 2008, Vol. 134, No. 7, pp. 1070-1078.
- [22] Alashker, Y., Li, H. and El-Tawil, S., "Approximations in Progressive Modeling", *Journal of Structural Engineering*, 2011, Vol. 137, No. 9, pp. 914-924.
- [23] FEMA 355C, "State of the Art Report on Systems Performance of Steel Moment Frames subjected to Earthquake Ground Shaking", Federal Emergency Management Agency, 2000.
- [24] Foley, C. M., Martin, K. and Schneeman, C., "Robustness in Structural Steel Framing Systems", Final Report Submitted to the American Institute of Steel Construction, Inc., 2007.
- [25] Hoffman, S.T., "Behavior and Performance of Steel Moment-Framed Buildings subjected to Dynamic Column Loss Scenarios", Master Thesis, University of Illinois at Urbana-Champaign, Urbana, Illinois, 2010.
- [26] Hallquist, J., "LS-DYNA Keyword User's Manual", Livermore Software Technology Corporation, Livermore, CA, Version 971, 2006.

- [27] Khandelwal, K. and El-Tawil, S., "Collapse Behavior of Steel Special Moment Resisting Frame Connections", *Journal of Structural Engineering*, 2007, Vol. 133, No. 5, pp. 646-655.
- [28] Sadek, F., El-Tawil, S. and Lew, H.S., "Robustness of Composite Floor System with Shear Connections: Modeling, Simulation and Evaluation", *Journal of Structural Engineering*, 2008, Vol. 134, No. 11, pp. 1717-1725.
- [29] Li, H. and El-Tawil, S., "Three-Dimensional Effects and Collapse Resistance Mechanisms in Steel Frame Buildings", *Journal of Structural Engineering*, 2014, Vol. 140, No. 8, A4014017
- [30] ASCE 41-06., "Seismic Rehabilitation of Existing Buildings", American Society of Civil Engineers, 2007.
- [31] Wight, J. and Macgregor, J., "Reinforced Concrete: Mechanics and Design (5th Edition)", Prentice Hall, 2008.
- [32] Alashker, Y. and El-Tawil, S., "A Design-oriented Model for the Collapse Resistance of Composite Floors Subjected to Column Loss", *Journal of Constructed Steel Research*, 2011, Vol. 67, No. 1, pp. 84-92.
- [33] McKay, A., Marchand, K. and Diaz, M., "Alternate Path Method in Progressive Collapse Analysis: Variation of Dynamic and Nonlinear Load Increase Factors", *Practice Periodical on Structural Design and Construction*, 2012, Vol. 17, No. 4, pp. 152-160.
- [34] Izzuddin, B.A., Vlassis, A.G., Elghazouli, A.Y. and Nethercot, D.A., "Progressive Collapse of Multi-Storey Buildings Due to Sudden Column Loss - Part I: Simplified Assessment Framework", *Engineering Structures*, 2008, Vol. 30, No. 5, pp. 1308-1318.
- [35] Li, L., Wang, W., Chen, Y. and Lu, Y., "Effect of Beam Web Bolt Arrangement on Catenary Behaviour of Moment Connections", *Journal of Constructional Steel Research*, 2015, Vol. 104, pp. 22-36.
- [36] Guo L., Gao, S. and Fu, F., "Structural Performance of Semi-Rigid Composite Frame under Column Loss", *Engineering Structures*, 2015, Vol. 95, pp. 112-126.
- [37] Yang, B. and Tan, K.H., "Experimental Tests of Different Types of Bolted Steel Beam-column Joints under a Central-column-removal Scenario", *Engineering Structures*, 2013, Vol. 54, pp. 112-130.
- [38] Guo, L., Gao, S., Fu, F. and Wang, Y., "Experimental Study and Numerical Analysis of Progressive Collapse Resistance of Composite Frames", *Journal of Constructional Steel Research*, 2013, Vol. 89, pp. 236-251.
- [39] Weigland, J. M. and Berman, J.W., "Integrity of Bolted Angle Connections Subjected to Simulated Column Removal", *Journal of Structural Engineering*, 2015, Vol. 142, No. 3, 04015165.
- [40] Wang, W., Fang, C., Qin, X., Chen, Y. and Li, L., "Performance of Practical Beam-to-SHS Column Connections against Progressive Collapse", *Engineering Structures*, 2016, Vol. 106, pp. 332-347.

EXPERIMENTAL AND NUMERICAL INVESTIGATIONS ON SKEWED PLATE-TO-SHS X-JOINTS UNDER COMPRESSION

Y. Chen ^{1,2,*}, K. He ¹, W.X. Zhang ^{3,*}, B.C. Chen ¹ and J.G. Wei ¹

¹ College of Civil Engineering, Fuzhou University, Fuzhou, China (350116)

² School of Urban Construction, Yangtze University, Jingzhou, China (434023)

³ The Key Laboratory of Urban Security and Disaster Engineering, Ministry of Education, Beijing University of Technology, Beijing 100124, China (100124)

*(Corresponding author: Email: kinkinging@163.com and zhwx@bjut.edu.cn)

Received: 20 November 2018; Revised: 22 July 2017; Accepted: 22 October 2017

ABSTRACT: Experimental and numerical investigations were conducted on skewed plate-to-SHS X-joints under compression. In order to research static behavior of skewed plate-to-SHS X-joints under compression, a total of ten specimens including orthogonal and skewed plate-to-SHS X-joints were tested. The failure modes, compression-displacement curves and strain intensity distribution curves of joints were presented in the paper. The effects of τ (The ratio of plate thickness to SHS chord thickness) and θ (skewed angle between plate and SHS chord axis) on the ultimate bearing capacity and ductility of X-joints were also studied. The corresponding finite element analysis (FEA) was also performed and calibrated against the test results. Therefore, an extensive parametric study was carried out to evaluate the effects of main geometric parameters (τ and θ) on the static behavior of skewed plate-to-SHS X-joints under compression. Results of these tests showed that as value of θ increased, ultimate bearing capacity of X-joints increased irregularly. As value of τ increased, the ultimate bearing capacity of X-joints increased significantly. Maximum strain intensity was located in the region of weld seam end between plate and SHS chord. As value of θ increased, ductility of joints with thin plates increased; ductility of joints with thick plates decreased. Except X-joints with $\theta=90^\circ$, coefficient of ductility of joints with thick plates were larger than that of joints with thin plates. In addition, the design equations were proposed for skewed plate-to-SHS X-joints under compression, which were shown to be accurate and reliable.

Keywords: Skewed plate-to-SHS X-joints, compression, static behavior, FEA, ultimate bearing capacity, design equation

DOI: 10.18057/IJASC.2018.14.4.2

1. INTRODUCTION

The cutting and welding of intersection lines are the key construction work of tower and truss. The diversity of number, angle and size of brace makes the intersection lines forming three dimensions. Complicated tower and truss structures often have braces and chord intersecting at skewed angles. Square Hollow section (SHS) chord with plates braces inclined to the longitudinal axis of the SHS chord have become common. There are some skewed plate-to-SHS joints in real engineering project, as shown in Figure 1. Although plate-to-SHS X-joints are often designed with a diverse range of geometries, research and design recommendations into the effect of skewed angle (θ) on static behavior of plate-to-SHS X-joints under compression have been limited, necessitating further research to fill a gap in the current design knowledge base. Though the influence of skewed angle for plate-to-CHS joints has been examined by Voth and Packer [1], the effect of skewed angle has not previously been examined for plate-to-SHS joints, which becomes the focus of the experimental and FEA study discussed herein.

Extensive studies have been performed in recent years on joints made of plate braces and tube chord intersecting at orthogonal angles. A numerical analysis and experimental study were performed to investigate the behavior and strength of tube-gusset joints subjected to axial brace force by Kim [2].

Ultimate strength formulas for each of the forces were proposed. Experimental and numerical investigations were carried out on gusset plate joints to the ends of circular hollow section (CHS) members by Saucedo and Packer et al. [3]. An investigation of block shear tear-out failure for gusset-plate welded joints in both very high strength tubes and structural steel hollow section was conducted by Ling and Zhao et al. [4]. The existing design rules were inadequate, and five possible modifications were examined. A modification of the effective net area and failure stress definitions was proposed. An investigation of shear lag failure for gusset-plate welded joints in very high strength tubes with a yield stress of 1350 MPa, and shear lag design for gusset-plate welded joints in both high strength tubes and regular structural steel hollow section was conducted by Ling and Zhao et al. [5]. Design rules were proposed for gusset-plate welded joints in all tubes. Slotted rectangular and square hollow structural section tension joints without welding at the end of the gusset plate for different weld length ratios, slot orientations, weld sizes and levels of corner strength compared to its flat segment were numerically investigated by Zhao and Huang et al. [6]. Behavior and strength of 600MPa CHS tube-gusset joints were experimentally and numerically investigated by Lee and Shin et al. [7]. Behavior of transverse or longitudinal X-type plate-to circular hollow section joints loaded under branch plate tension or compression was experimentally and numerically investigated Voth and Packer [8-9]. Partial design strength functions, determined through regression analysis, were proposed with lower-bound reduction factors. Jiao and Mashiri et al. [10] investigated the fatigue behavior of very high strength (VHS) steel tubes to steel plate T-joints under cyclic in-plane bending.

Current design guidelines for axially loaded plate-to-SHS X-joints include IIW design rules [11], AWS design rules [12], CIDECT Design Guide No. 3, 2nd Edition [13], Eurocode3 design of steel structures [14], and AISC Steel Design Guide No. 24 [15].

Some research has been conducted in recent years on the static and dynamic behaviour of hollow and concrete filled SHS joints with different configurations [16-22]. Literature review shows that there is little research on skewed plate-to-SHS X-joints under compression. The existing design specifications are only design for orthogonal plate-to-SHS X-joints. The aforementioned literatures were all conducted on orthogonal plate-to-tube joints fabricated with plate brace members welded to the hollow structural section chord members. Little research has been carried out on skewed plate-to-SHS X-joints under compression. This paper focuses on the strength and behavior of skewed plate-to-SHS X-joints under compression. The orthogonal plate-to-SHS X-joints under compression were also tested for comparison. The ultimate strengths, failure modes, joint displacements and strain distributions of skewed and orthogonal plate-to-SHS X-joints under compression are reported in this study. The effect of skewed angle of plate member on the ultimate strength and initial stiffness of all specimens was evaluated. The test and FEA results are compared with the design strengths calculated using the current design rules. The new design equations are also proposed for skewed plate-to-SHS X-joints under compression.

2. EXPERIMENTAL DESIGN

2.1 Test Specimens

A total of ten plate-to-SHS X-joints under compression including six skewed plate-to-SHS X-joints and four orthogonal plate-to-SHS X-joints were tested, as shown in Figure 2. Effects of skewed angle and skewed plate thickness on static behavior of plate-to-SHS X-joints under compression were experimentally investigated.

The length (L) and height (H) of all specimens were uniformly fabricated by 400 mm and 332 mm, respectively, for the purpose of comparison. The 10 mm thick steel end plates were welded at the end

of plate brace members for the loading and boundary conditions. The joint type and cross-section dimensions of all specimens defined as chord width (b_0), plate brace width (b_1), chord wall thickness (t_0), plate brace thickness (t_1) and skewed angle (θ) as well as geometric parameters $\beta=b_1/b_0$, $\tau=t_1/t_0$ and $2\gamma=b_0/t_0$ are summarized in Table 1, using the dimensions of all specimens as detailed in Figure 3.

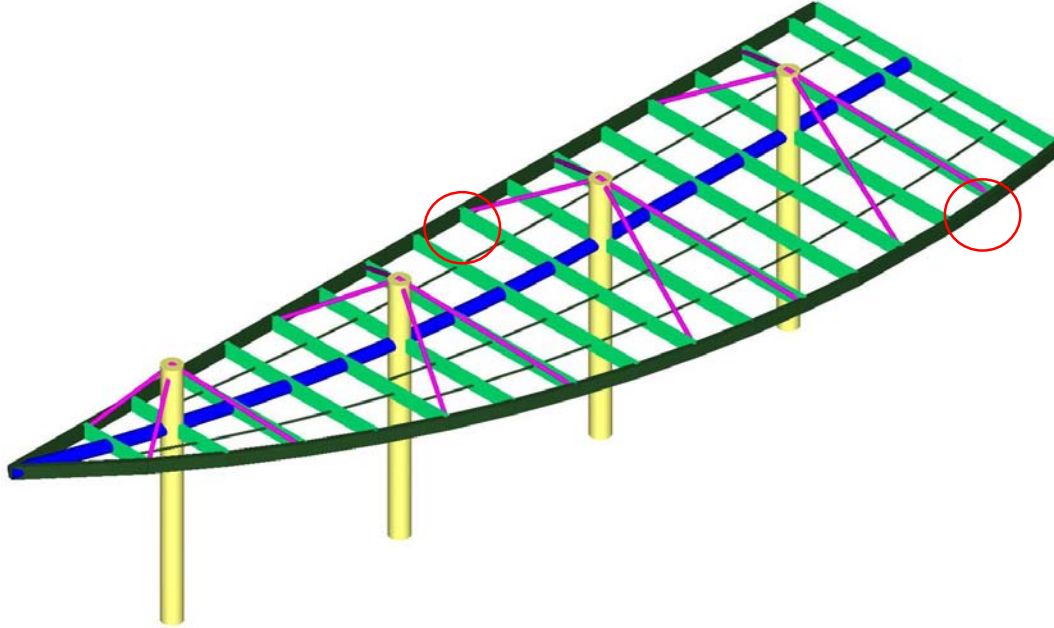


Figure 1. Skewed plate-to-SHS Joints in Real Engineering Project

Table 1. Geometric Parameters and Failure Modes of Plate-to-SHS X-joints

Number	SHS chord ($b_0 \times b_0 \times t_0$) (mm \times mm \times mm)	Plate brace ($b_1 \times h_1 \times t_1$) (mm \times mm \times mm)	θ ($^\circ$)	t_1 (mm)	τ	Failure mode
GXS400	$\square 120 \times 120 \times 5$	$-100 \times 100 \times 4$	0	4	0.8	Plate failure
GXS430	$\square 120 \times 120 \times 5$	$-100 \times 100 \times 4$	30	4	0.8	Plate failure
GXS445	$\square 120 \times 120 \times 5$	$-100 \times 100 \times 4$	45	4	0.8	Plate failure
GXS460	$\square 120 \times 120 \times 5$	$-100 \times 100 \times 4$	60	4	0.8	Plate failure
GXS490	$\square 120 \times 120 \times 5$	$-100 \times 100 \times 4$	90	4	0.8	Plate failure
GXS600	$\square 120 \times 120 \times 5$	$-100 \times 100 \times 6$	0	6	1.2	Tube-plate failure
GXS630	$\square 120 \times 120 \times 5$	$-100 \times 100 \times 6$	30	6	1.2	Tube-plate failure
GXS645	$\square 120 \times 120 \times 5$	$-100 \times 100 \times 6$	45	6	1.2	Tube-plate failure
GXS660	$\square 120 \times 120 \times 5$	$-100 \times 100 \times 6$	60	6	1.2	Plate failure
GXS690	$\square 120 \times 120 \times 5$	$-100 \times 100 \times 6$	90	6	1.2	Plate failure



Figure 2. Photos of Joint Specimens

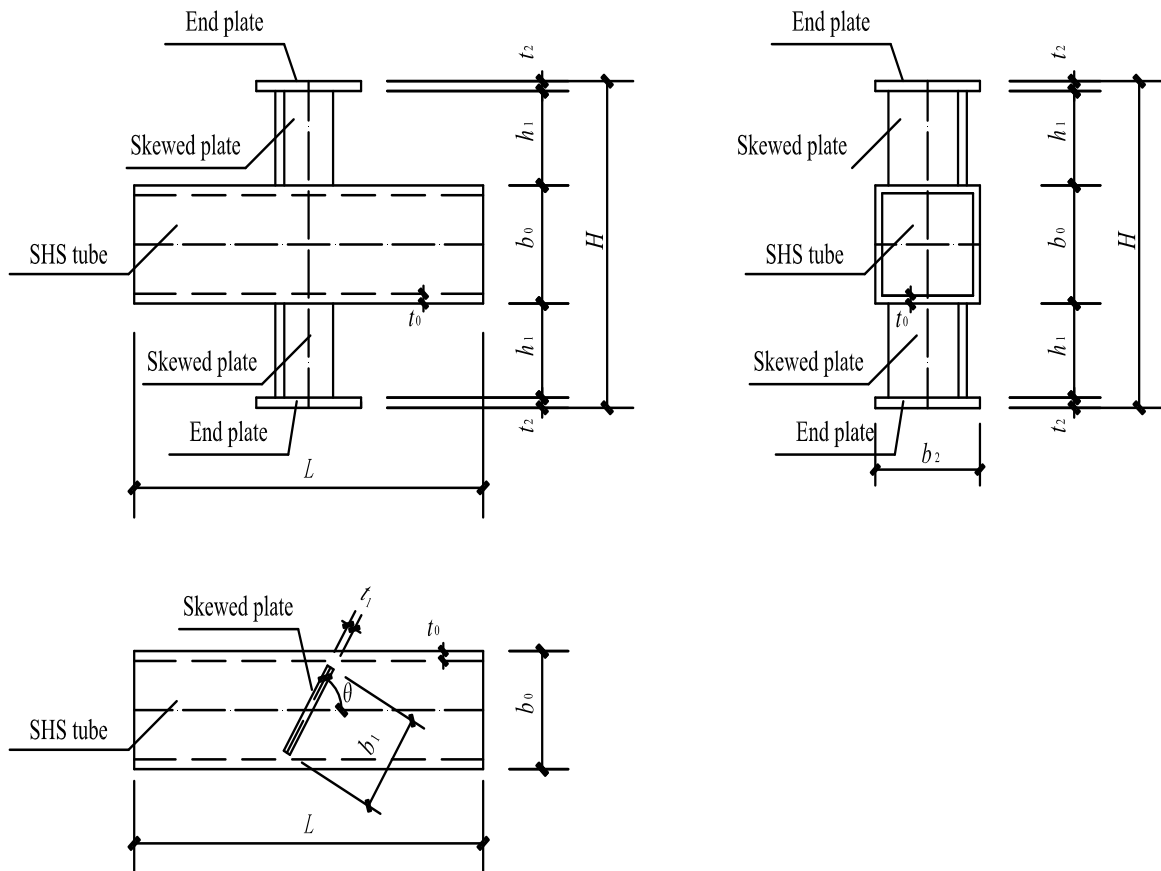


Figure 3. Detailed Schematic Drawings of Skewed Plate-to-SHS X-joints

The welds connecting brace and chord members were designed according to the American Welding Society (AWS D1.1/1.1M) Specification [12] and laid using shielded metal arc welding. The weld sizes in the test specimens are all greater than the larger value of $1.5t$ and 3 mm, where t is the thickness of thinner part between plate brace and chord members. The 4.0 mm and 4.5 mm electrodes of type E4304 with nominal 0.2% proof stress, tensile strength, and elongation of 390 MPa, 500 MPa, and 33%, respectively, were used for welding low carbon steel (Q235) specimens. All welds consisted of 2 to 3 runs of welding to guarantee that failure of specimens occurred in the plate brace or chord members rather than the welds.

2.2 Specimen Labelling

The specimens are labelled according to their joint type, joint configuration, cross-section type of chord, plate brace thickness and skewed angle. For example, the label ‘GXS645’ defines the following X-joint:

- The first letter ‘G’ denotes gusset plate.
- The second letter ‘X’ denotes X-joint.
- The third letter ‘S’ denotes square hollow section chord.
- The first number ‘6’ indicates the plate have the nominal thickness (t_1) of 6 mm.
- The second numbers ‘45’ indicates the skewed angle between plate and SHS chord axis is 45° .

The chord member of all specimens is square hollow section of SHS120×120×5, which having the nominal overall width (b_0) of 120 mm, and the nominal wall thickness (t_0) of 5 mm.

2.3 Material Properties

All specimens were fabricated by using Chinese Standard Q235 steel (nominal yield stress $f_y = 235$ MPa). Tensile coupon tests were conducted to determine the mechanical properties of low carbon steel square tubes. The coupons were taken from the center face of square tubes and plates in the longitudinal direction, which were prepared and tested based on the recommendations of Chinese Code of Metallic Materials (GB/T 228-2002) [23]. The tensile coupon tests were conducted by using a 250kN capacity MTS displacement controlled testing machine. The strain gauges and extensometer were positioned to measure the longitudinal strains of each specimen. A data acquisition system was used to record the load and strain at regular intervals during the tests. Through the uni-axial tensile test on standard specimens, which is shown in Figure 4, the material properties for the ten specimens listed in Table 2 are measured, and they are the fundamentals in numerical study. The material properties obtained from the tensile coupon tests are summarized in Table 2, including the elastic modulus (E), tensile yield stress (f_y), ultimate tensile stress (f_u), and elongation after fracture (ϵ_f).

Table 2. Result of Material Characteristic Test

Specimen	f_y (Mpa)	f_u (Mpa)	f_y/f_u	ϵ_f (%)	E (GPa)
□120×120×5	278	411	0.68	28	208
-100×100×4	317	409	0.78	31	211
-100×100×6	309	425	0.73	35	209



Figure 4. Steel Material Uni-axial Tensile Test

2.4 Test Procedure

All specimens were installed in the same test rig, as shown in Figure 5. During the experimental tests, an axial compressive load is applied at the end of the plate brace. The reaction frame and supports were connected to the strong floor firmly by anchor bolts. The 1000 kN capacity hydraulic jack was used to apply the compression to the plate brace members of test specimens and monitored by the load cell, which was positioned concentrically between the hydraulic jack and the reaction frame. Two steel end plates were welded at the end of plate braces members in order to generate symmetrical compression in the two plate braces. So far, ultimate bearing capacity equations were limited to orthogonal angel joints. The estimated ultimate bearing capacities of joints were considered as the value of the ultimate bearing capacity calculated according to IIW standard [11].



Figure 5. Test Rig

2.5 Measurement Plan

The test plan consists of two parts: (1) Arrangement of strain gauges at the intersection of joints with complex stress. (2) Arrangement of displacement transducers.

Since the stress of each point at the intersection was quite complex, three-dimensional strain gauges were arranged on the face of the SHS chord flange and at the foot of the plate brace to test the strain intensity distribution. Considering the symmetry, seven strain gauges were arranged. Three strain gauges named T1-T3 were placed at the foot of plate brace, and three strain gauges named T4-T6 corresponding to T1-T3 were placed on the face of the SHS chord flange. T4 strain gauge was placed at the corner of plate. All the three-dimensional strain gauges were arranged 15mm away from the weld in order to decrease the influence of weld area on strain testing, as shown in Figure 6.

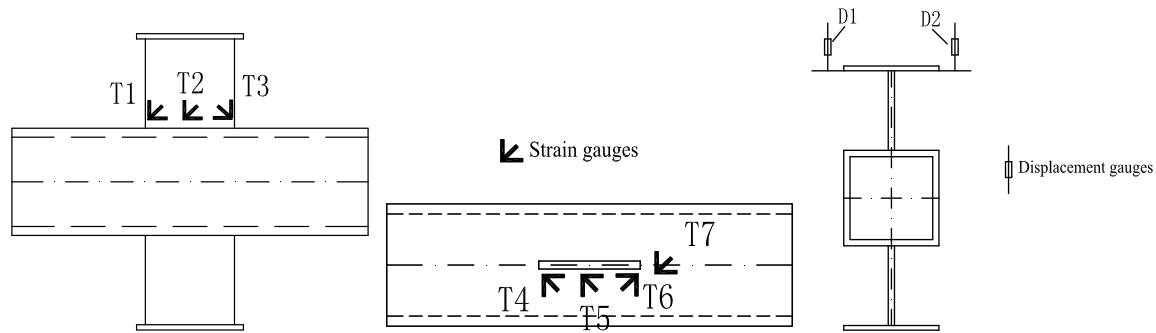


Figure 6. Arrangement of Strain and Displacement Gauges

3. TEST RESULTS

3.1 Failure Modes

Two types of failure modes, namely plate failure and tube-plate failure, were observed from the tests for different plate-to-SHS X-joints, as shown in Table 1.

When the load was small, the displacement of plate end and strains developed slowly as the load increased; then strains developed fast as the load approached the maximum with no obvious deformation of tube and plate; finally as the load reached the maximum, the plate suddenly buckled, at the same time the load fell down rapidly and the joints lost its bearing capacity. There was no visible deformation of chord tube during the loading process. Plate failure is the main failure mode in the tests, as shown in Figure 7.



Figure 7. Photo of Plate Failure Mode (GXS460)

The tube-plate failure mode occurred in specimens of GXS600, GXS630 and GXS645 in the tests. When the load was small, the displacement of plate end and strains developed slowly with the increase of the load, there was no visible deformation of the plates and tube chord. Then as the load approached the maximum, the displacement and strain developed rapidly and the plate appeared small deformation, but there was no visible deformation of the tube chord. Finally, the load reached the maximum, a small concave deformation appeared on the flange of the square tube, the plate buckled suddenly, and then the load fell down rapidly. The typical tube-plate failure mode of plate-to-SHS X-joints was shown in Figure 8.

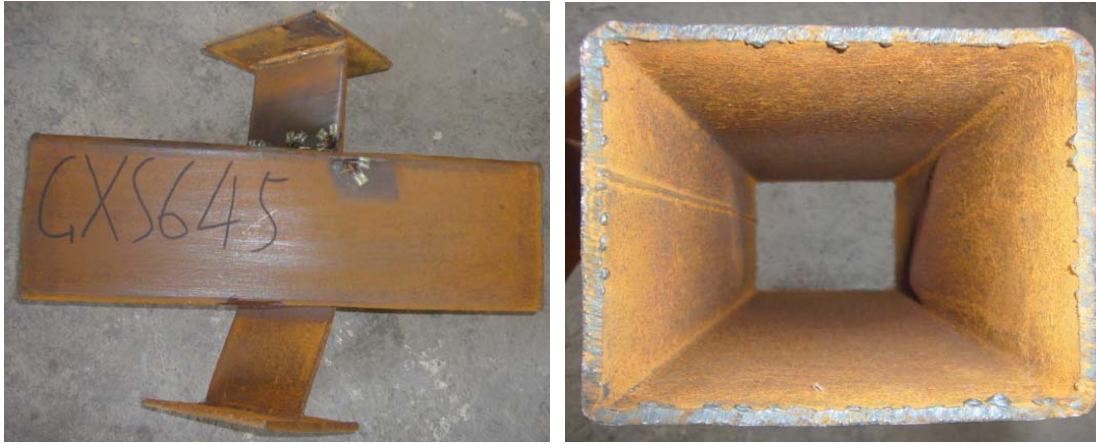


Figure 8. Photo of Tube-plate Failure (GXS645)

As shown in Table 1, when the thickness of plate was 4mm, that is, value of τ (0.8) was small, plate-to-SHS joints failed all due to the plate failure, and the failure mode of plate-to-SHS joints with thin plate was not affected by skewed angle; As the thickness of plate increased to 6 mm, that is, value of τ (1.2) was large, and tube-plate failure occurred in joints with small skewed angle θ (0° , 30° and 45°), the plate failure occurred in joints with large skewed angle θ (60° , 90°). So it is worth noting that skewed angle θ has an influence on the failure mode of plate-to-SHS X-joints with thick plate.

3.2 Load-displacement Curves

The curves of load-displacement of plate-to-SHS X-joints with plate thickness=4mm were plotted in Figure 9a, in which the work stage of the joints under compression consisted of elastic stage, elastic-plastic stage and failure stage. When the thickness of plate was 4mm, that is, the ultimate bearing capacity of plate-to-SHS X-joints with $\theta=45^\circ$ was the largest; Comparing the maximum value of X-axis in each curve, the largest ultimate displacement occurred when $\theta=0^\circ$, while the smallest ultimate displacement occurred when $\theta=60^\circ$. It is clear that the ductility of plate-to-SHS X-joints with thin plate was poor except the joints with $\theta=0^\circ$. In terms of the slope of the initial period of each curve in Figure 9a, the initial compressive stiffness of the joints with $\theta=60^\circ$ was the largest, but that of the joints with $\theta=0^\circ$ was the smallest.

The curves of load-displacement of plate-to-SHS X-joints with plate thickness=6mm were shown in Figure 9b, in which the work stages of the joints under compression consisted of elastic stage, elastic-plastic stage and failure stage. The ultimate bearing capacity of the joints with $\theta=90^\circ$ was the largest, while that of the joints with $\theta=30^\circ$ was the smallest, the ultimate bearing capacity of the joints with $\theta=0^\circ$, 45° and 60° was similar to each other. When the thickness of plate was 6 mm, as value of θ increased, the ultimate displacement decreased and the ductility became worse, but the axial compressive stiffness increased.

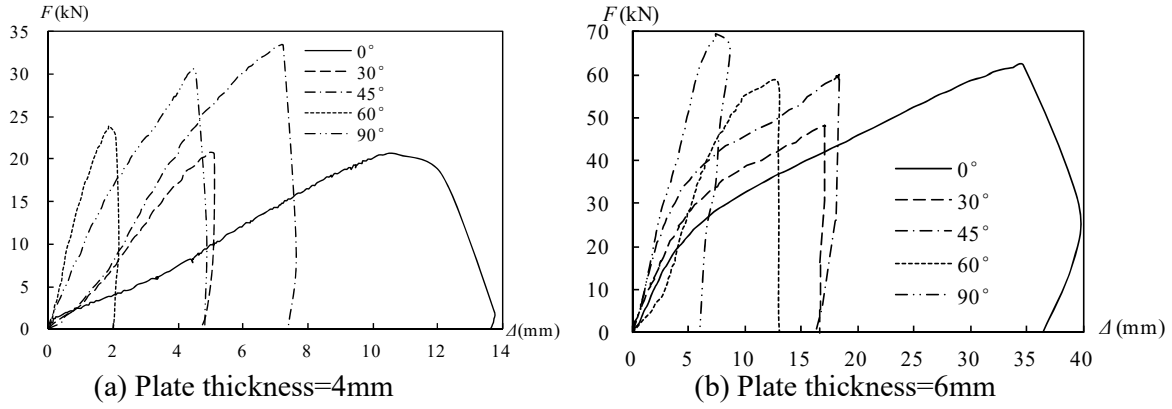


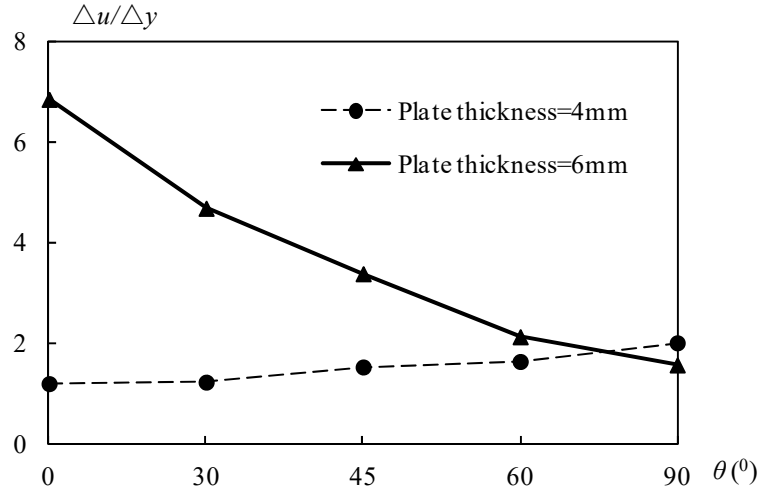
Figure 9. Load-displacement Curves

3.3 Ductility Analysis

The static and dynamic performance of joints is affected directly by the ductility. Good ductility can make the stress redistribution and facilitate energy dissipation. The better ductility of joints, the more obvious displacement will be presented before failure. Obvious signs of destruction make sure that the structure works safely and is advantageous for the improvement of the applicability and safety of the structure, which can also reduce the damage of structural failure. The ductility coefficient is used to evaluate the ductility of skewed plate-to-SHS X-joints, which is generally calculated from the ratio of the ultimate displacement to the yield displacement (Δ_u/Δ_y). The statistical results of ductility of skewed plate-to-SHS X-joints are shown in Table 3 and Figure 10.

Table 3. Ductility of Plate-to-SHS X-joints

Number	$\theta (^{\circ})$	Δ_y (mm)	Δ_u (mm)	Δ_u/Δ_y
GXS400	0	9.03	10.81	1.20
GXS430	30	4.18	5.13	1.23
GXS445	45	4.73	7.22	1.53
GXS460	60	1.15	1.89	1.64
GXS490	90	2.27	4.56	2.01
GXS600	0	5.07	34.70	6.84
GXS630	30	3.66	17.13	4.68
GXS645	45	4.78	18.31	3.83
GXS660	60	6.09	12.98	2.13
GXS690	90	5.54	8.71	1.57

Figure 10. Ductility Coefficient $\Delta u/\Delta y$ -skewed Angle θ Curves

It is shown that as value of θ increases, the ductility coefficient of joints with thin plates increases; the ductility coefficient of joints with thick plates decreases. Except joints with $\theta=90^\circ$, ductility coefficient of joints with thick plates is larger than that of joints with thin plates.

3.4 Load-strain Intensity Curve

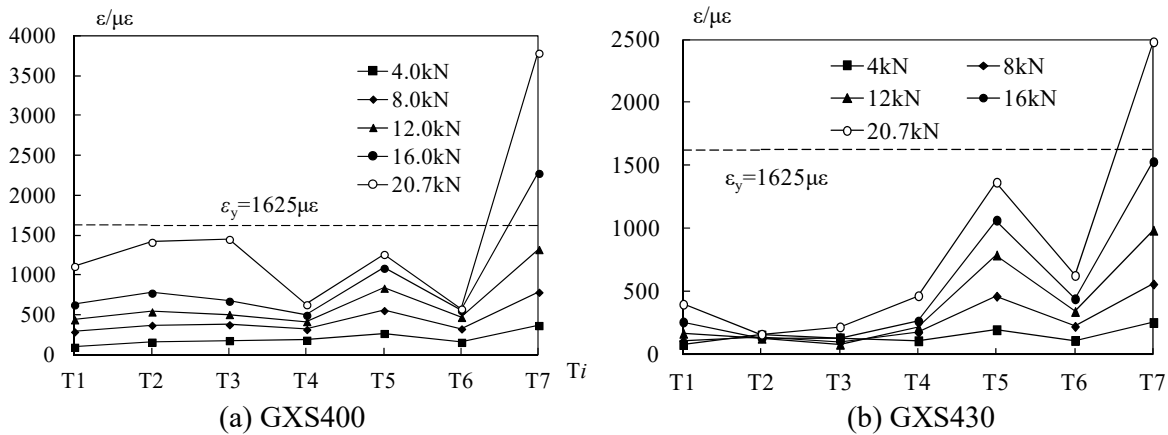
Strain variations and distribution are derived from the data of strain measuring points, and failure mechanism of joints under compression was studied. Arrangement of strain gauges at the intersection of joints is shown in Figure 6.

Expression of strain intensity is as follows:

$$\varepsilon_i = \frac{\sqrt{2}}{3} \sqrt{(\varepsilon_1 - \varepsilon_2)^2 + (\varepsilon_2 - \varepsilon_3)^2 + (\varepsilon_3 - \varepsilon_1)^2} \quad (1)$$

ε_1 , ε_2 and ε_3 are the first, secondary and third principal strains, respectively.

The curves of load-strain-intensity of joint specimens are plotted in Figure 11. The horizontal axis represents the number of measuring points (the number of strain gauge measuring points are shown in Figure 6), and the vertical axis represents the strain intensity.



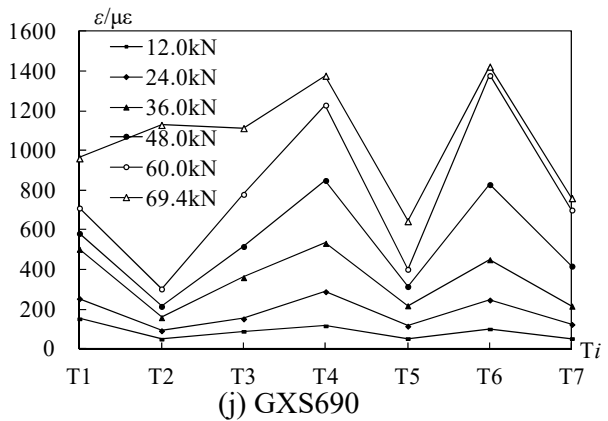
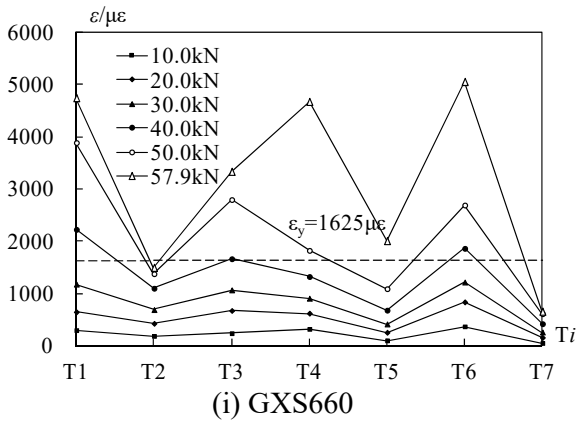
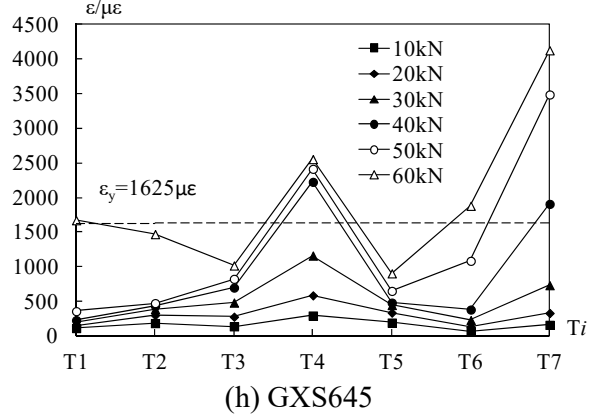
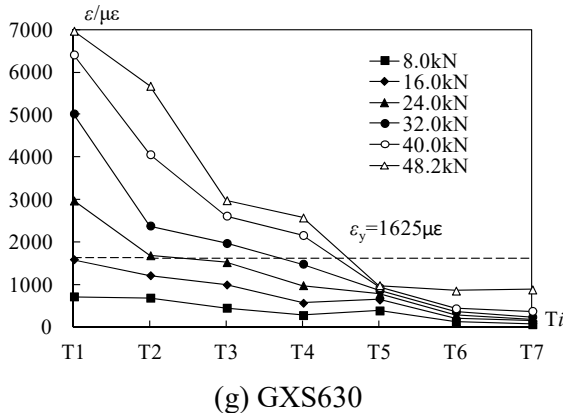
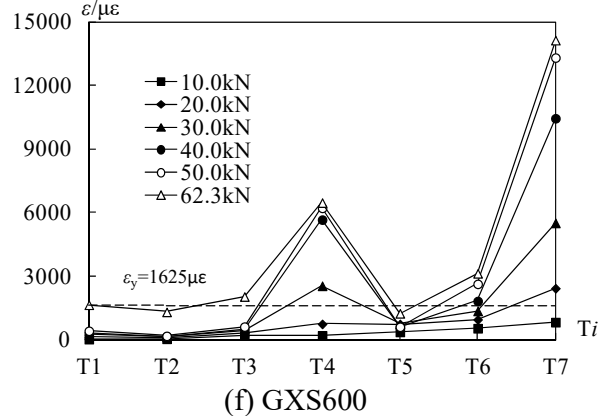
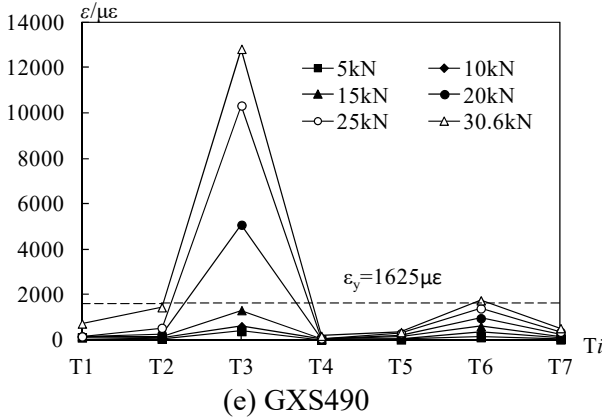
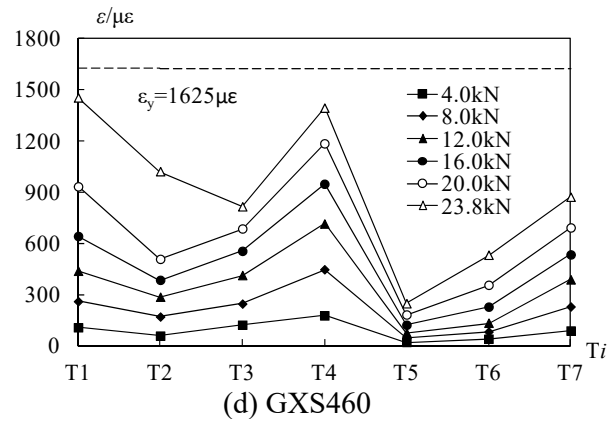
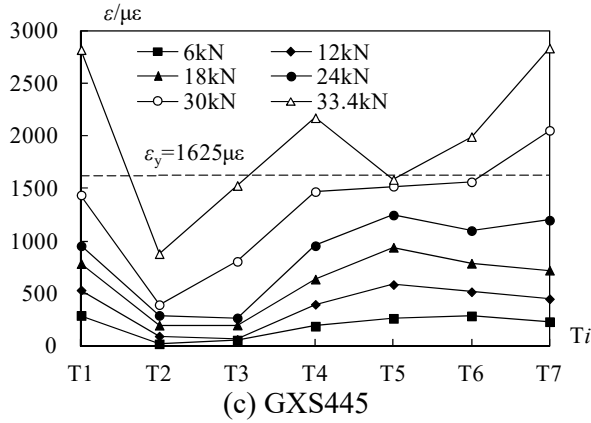


Figure 11. Strain intensity distribution curves

When the load was small, strain intensity varied uniformly along with the load. As the load increased, the distribution of strain intensity was non-uniform and the stress was redistributed in the region of joints at the late stage, stress concentration appeared at the end of the weld seams and joints failure because of plate buckling and SHS tube concave deformation. The statistics of the distribution and location of maximum strain intensity of plate-to-SHS X-joints are shown in Table 4. The maximum strain intensity of plate-to-SHS X-joints all occurred at the end of the weld seams.

Table 4. Strain Intensity of Joints

Number	$\theta(^{\circ})$	Failure Mode	Point of maximum strain	Points Location
GXS400	0	Plate failure	T7	Tube wall near weld end
GXS430	30	Plate failure	T7	Tube wall near weld end
GXS445	45	Plate failure	T1, T7	Tube-wall and plate bottom near weld end
GXS460	60	Plate failure	T1, T4	Tube-wall and plate bottom near weld end
GXS490	90	Plate failure	T3	Plate bottom near weld end
GXS600	0	Tube-plate failure	T7	Tube wall near weld end
GXS630	30	Tube-plate failure	T1	Plate bottom near weld end
GXS645	45	Tube-plate failure	T7	Tube wall near weld end
GXS660	60	Plate failure	T6	Tube wall near weld end
GXS690	90	Plate failure	T6	Tube wall near weld end

4. ULTIMATE BEARING CAPACITY

The evaluation of ultimate bearing capacity of plate-to-SHS X-joints under compression is shown in Table 5 and Figure 12. The value of θ represents the angle between plate plane and the axis of square steel tubes. The value of N_1^* and N_e represents the calculated ultimate bearing capacity by using CIDECT [13] and experimental ultimate bearing capacity of specimens, respectively. R_v represents the ratio of ultimate bearing capacity of skewed plate-to-SHS X-joints to ultimate bearing capacity of joints with $\theta=0^{\circ}$ when the other parameters are the same. So far, there is no formula to calculate the ultimate bearing capacity of the skewed plate-to-SHS X-joints in international standard or design guidelines. As a result, the theoretical ultimate capacities of the joints with $\theta=0^{\circ}$ and 90° obtained by using CIDECT [13] are given in Table 5. The load carrying capacity of joints under in-plane bending using Eurocode 3 can be calculated as follows:

Table 5. Ultimate Bearing Capacity of Joints

Number	$\theta(^{\circ})$	τ	$N_1^*(\text{kN})$	$N_e(\text{kN})$	N_e/N_1^*	R_v
GXS400	0	0.8	46.7	20.7	0.44	1.00
GXS430	30	0.8	—	20.7	—	1.00
GXS445	45	0.8	—	33.4	—	1.61
GXS460	60	0.8	—	23.8	—	1.15
GXS490	90	0.8	69.7	30.3	0.43	1.46
GXS600	0	1.2	46.3	62.3	1.35	1.00
GXS630	30	1.2	—	48.2	—	0.77
GXS645	45	1.2	—	60.0	—	0.96
GXS660	60	1.2	—	57.9	—	0.93
GXS690	90	1.2	69.7	69.4	1.00	1.11

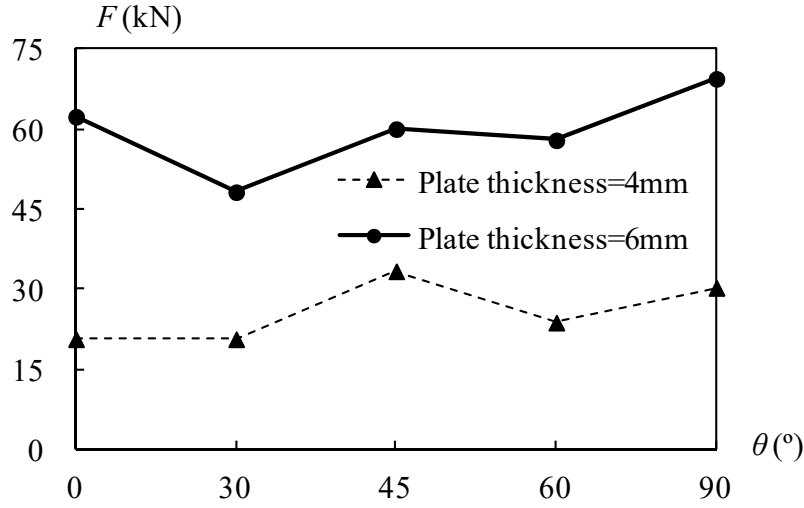


Figure 12. Ultimate Bearing Capacity-skewed Angle Curves

1) Transverse plate:**Chord face plastification** ($0.4 \leq \beta \leq 0.85$)

$$N_1^* = f_{y0} \cdot t_0^2 \cdot \frac{2 + 2.8 \cdot \beta}{\sqrt{1 - 0.9 \cdot \beta}} \cdot Q_f \quad (2)$$

Chord punching shear ($0.85b_0 \leq b_1 \leq b_0 - 2t$)

$$N_1^* = \frac{f_{y0} \cdot t_0}{\sqrt{3}} \cdot (2 \cdot t_1 + 2 \cdot b_{e,p}) \quad (3)$$

Chord side wall failure ($\beta \approx 1.0$)

$$N_1^* = f_{y0} \cdot t_0 \cdot (2 \cdot t_1 + 10 \cdot t_0) \cdot Q_f \quad (4)$$

2) Longitudinal plate:**Chord face plastification**

$$N_1^* = 2 \cdot f_{y0} \cdot t_0^2 \cdot \left(\beta + 2 \cdot \sqrt{1 - \frac{t_1}{b_0}} \right) \cdot Q_f \quad (5)$$

The experimental ultimate bearing capacity of plate-to-SHS X-joints with thin plates is far less than the calculated result of CIDECT, as shown in Table 5. It is obvious that the calculation of specification for plate-to-SHS X-joints with thin plates is unsafe. But the experimental ultimate bearing capacity of plate-to-SHS X-joints with thick plates was almost larger than the calculated result of CIDECT. CIDECT specification is very conservative to design the plate-to-SHS X-joints with thick plates. The ultimate bearing capacity of plate-to-SHS X-joints under compression shows an increasing trend as θ increases, as shown in Figure 12.

As shown in Figure 13, when value of τ is small, all values of R_v are larger than 1, the ultimate bearing capacity of plate-to-SHS X-joints has a obvious fluctuation along with the variation of the θ .

When value of τ is large, many values of R_v are less than 1, the ultimate bearing capacity of plate-to-SHS X-joints has an unobvious fluctuation along with the variation of the θ . All the height of black column is lower than that of the white with the same θ , which represents that θ has greater effect on the ultimate bearing capacity of plate-to-SHS X-joints with thin plates than on that of joints with thick plates.

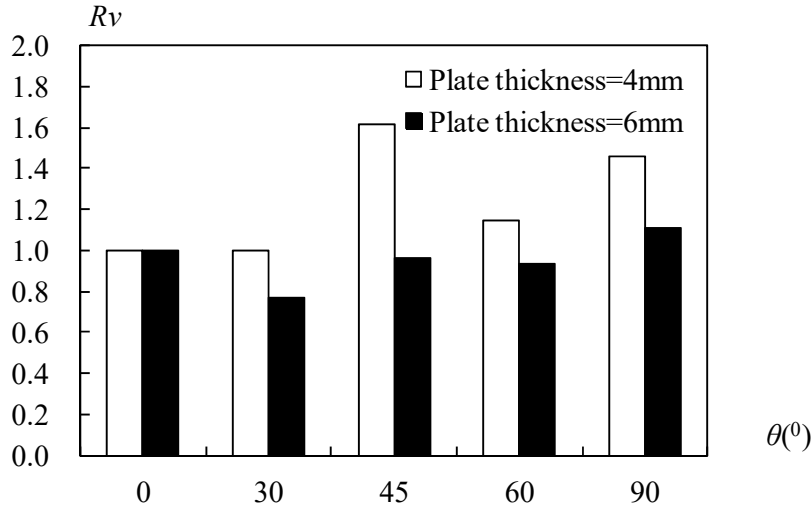


Figure 13. R_v - θ Curves

The effect of the relative thickness (τ) on the ultimate bearing capacity of plate-to-SHS X-joints is shown in Table 6. The ultimate bearing capacity of plate-to-SHS X-joints obviously increased when the thickness of plate increased from 4mm to 6mm, especially when θ was 0° , the maximum increment was 201.0%; then the second increment was 143.3% when θ was 60° ; increment was approximately about 130% when θ was 30° and 90° ; the minimum increment was about 80% when θ was 45° . As a result, the ultimate capacities of plate-to-SHS X-joints are influenced by value of θ and the relative thickness (τ) of plate.

Table 6. Effect of τ on the Ultimate Bearing Capacity of Joints

$\theta (^\circ)$	0	30	45	60	90
$\tau=0.8$	20.7	20.7	33.4	23.8	30.3
$\tau=1.2$	62.3	48.2	60.0	57.9	69.4
Δ	41.6	27.5	26.6	34.1	39.1
Amplification (%)	201.0	132.9	79.6	143.3	129.0

5. FINITE ELEMENT ANALYSIS

5.1 Finite Element Model

The general purpose finite element software ABAQUS was used for the nonlinear numerical investigation of the plate-to-SHS X-joints. The measured cross-section dimensions and material properties obtained from the tests were incorporated in the finite element model. Three-dimensional eight-node solid element with additional variables related to the incompatible modes (C3D8I) was used in this study. The incompatible mode eight-node brick element is an improved version of the C3D8-element. The welding seams were considered in the finite element model. The convergence studies were carried out to obtain the optimum finite element mesh density. The welding area along the joint interaction region are finely meshed to capture the high stress gradient, whereas the mesh size at the location away from the interest area is gradually coarse in order to save computing cost.

Both material and geometric nonlinearities have been taken into account in the finite element model. The bilinear material model based on the elastic modulus and post-yield tangential modulus of steel obtained from the tensile coupon tests is developed for the material modeling, while the Von-Mises yield criterion is applied which is normally used to estimate the yielding of the ductile materials. The typical finite element meshes of orthogonal and skewed plate-to-SHS X-joints are shown in Figure 14a-b, respectively.

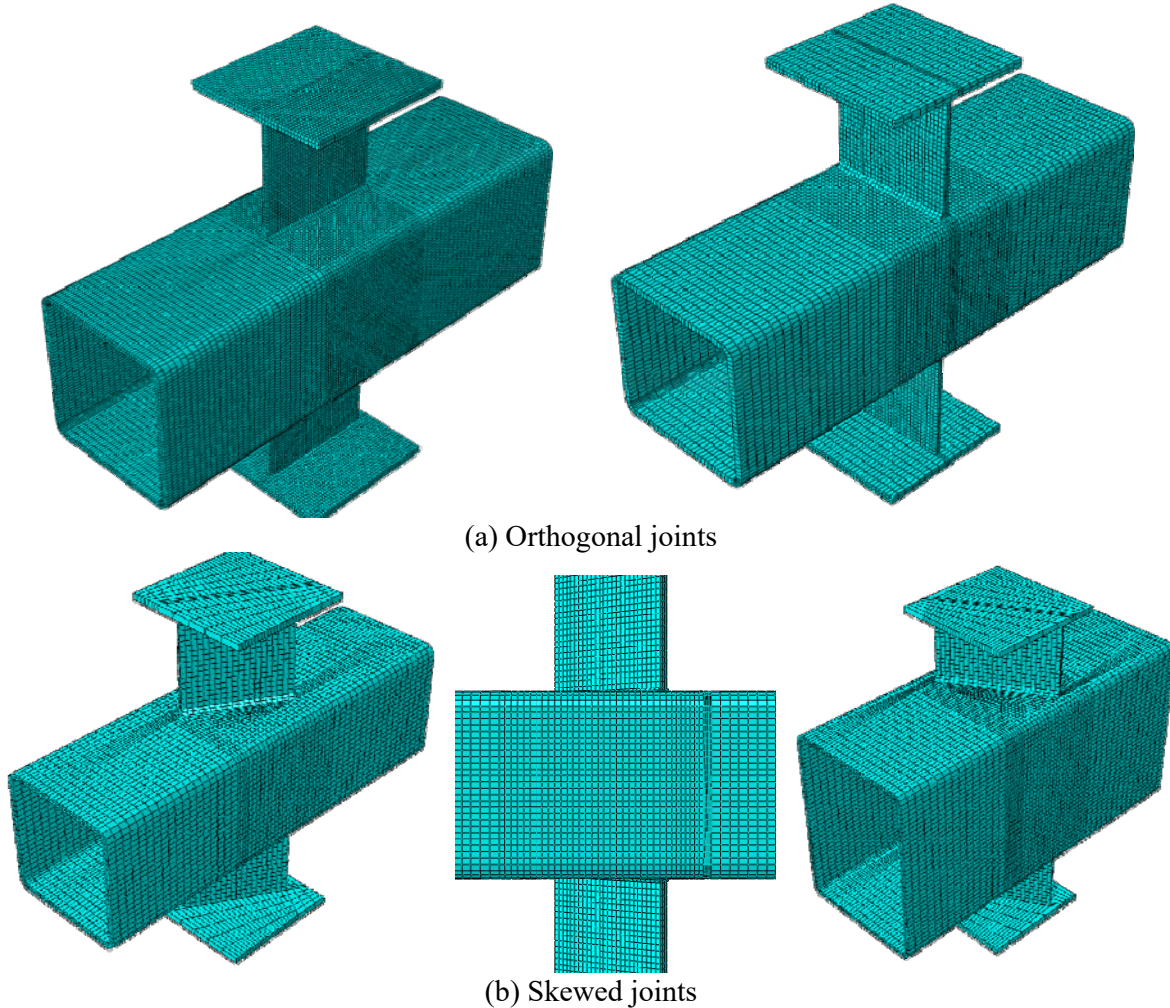


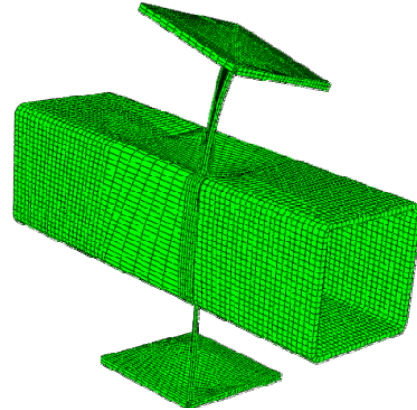
Figure 14. Meshes of Plate-to-SHS X-joints

5.2 Verification of Finite Element Model

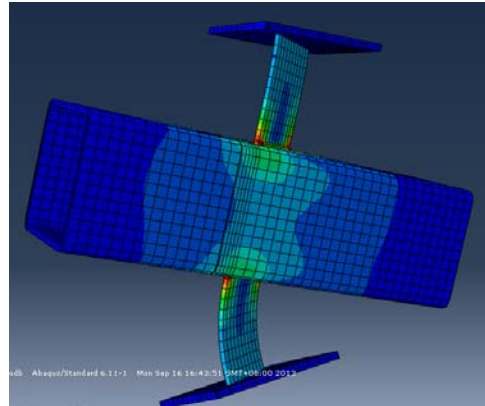
A comparison between the tests and FEA results was carried out to verify the finite element model. The ultimate capacities, failure modes and axial load-vertical displacement curves of the joints were investigated. The comparison of the load carrying capacity of all specimens obtained from the tests and finite element analysis is shown in Table 7. Good agreement between the tests and FEA results was achieved with the maximum difference of 10.50% and minimum difference of 4.76%. The typical failure modes of the joints observed in the experimental investigation were also verified by the finite element model, as shown in Figure 15. On the other hand, the axial load-vertical displacement curves obtained from the tests and finite element analysis were also compared in Figure 16. It is shown from the comparison that the FEA results generally agreed well with the test results. Therefore, it was demonstrated that the newly developed finite element model successfully predicted the structural behavior of the plate-to-SHS X-joints under compression.

Table 7. Comparison between the Ultimate Bearing Capacity in Tests and FEA Results

Number	Experimental value (kN)	FEA value (kN)	Deviation (%)
GXS400	20.7	21.9	5.80
GXS430	20.7	22.4	8.21
GXS445	33.4	35.6	6.59
GXS460	23.8	26.3	10.50
GXS490	30.6	32.6	6.54
GXS600	62.3	65.4	4.98
GXS630	48.2	52.1	8.09
GXS645	60.0	65.1	8.50
GXS660	57.9	63.8	10.13
GXS690	69.4	72.7	4.76



(a) GXS430



(b) GXS445

Figure 15. Failure Modes Comparison between Tests and FEA

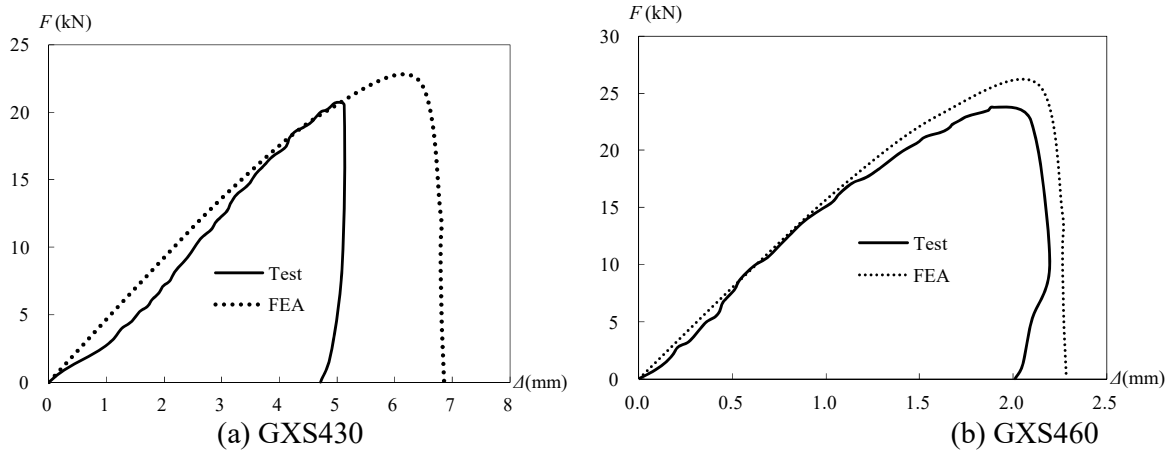


Figure 16. Comparison between Load-displacement Curves in Test and FEA Results for Typical Joints

5.3 Parametric Study

It is shown that the verified finite element model can accurately predict the strength and behavior of the plate-to-SHS X-joints. Therefore, an extensive parametric study was carried out to investigate the effects of main geometric parameters (θ and τ) on the plate-to-SHS X-joints. A total of 28 joints with different dimensional geometric parameters ($\theta=150-900$ and $\tau=0.4-1.0$) were analyzed in the parametric study, which were selected from the range of practical applications, as shown in Table 8. The square hollow section chord member of all specimens is taken to be $200 \times 200 \times 10$ (mm \times mm \times mm), which has the nominal overall depth (b_0) of 200mm and the nominal web thickness (t_0) of 10mm. The bilinear material model of steel including the elastic modulus (E) of 206 GPa, yield stress (f_y) of 235 MPa and the Poisson's ratio (ν) of 0.3 was used for the material modeling in the parametric study. The FEA results of the plate-to-SHS X-joints under compression in the parametric study are summarized in Table 8, which include the ultimate strengths (F_u) of X-joints.

Table 8. Results of Parametric Analysis

Numbers	τ	θ ($^\circ$)	F_u (kN)
X1	0.4	0	270.7
X2	0.4	15	280.7
X3	0.4	30	283.3
X4	0.4	45	285.2
X5	0.4	60	278.4
X6	0.4	75	282.7
X7	0.4	90	277.0
X8	0.6	0	300.8
X9	0.6	15	354.1
X10	0.6	30	375.8
X11	0.6	45	408.3
X12	0.6	60	418.1
X13	0.6	75	419.3
X14	0.6	90	409.3
X15	0.8	0	313.6
X16	0.8	15	376.5
X17	0.8	30	399.8

X18	0.8	45	446.0
X19	0.8	60	476.5
X20	0.8	75	500.3
X21	0.8	90	480.6
X22	1.0	0	323.6
X23	1.0	15	390.5
X24	1.0	30	415.6
X25	1.0	45	472.4
X26	1.0	60	513.6
X27	1.0	75	532.2
X28	1.0	90	544.4

For plate-to-SHS X-joints, the stresses at the end of welding seams step into the plastic range first. The stresses of the intersection region between plate and flange of chord gradually step into the plastic range with the increase of compression. The plasticity developed towards the flanges and webs of SHS chord at the intersection region between plates and chord. Eventually the plate end and chord at the joint intersection region is fully in plastic range at the ultimate limit state for small τ joints, as shown in Figure 17. Plate end and corner of chord at the joint intersection region is fully in plastic range at the ultimate limit state for large τ joints, as shown in Figure 18.

The effects of main geometric parameters (θ , τ) on the ultimate bearing capacity (F_u) of plate-to-SHS X-joints were also evaluated, as shown in Figure 19. It is demonstrated that the ultimate bearing capacity of plate-to-SHS X-joints increased with the increase of the τ value. The effect of τ on ultimate bearing capacity of X-joints with $\theta=0^\circ$ was unobvious. The ultimate bearing capacity of X-joints under compression increased with the increase of the θ value. The effect of θ on the ultimate bearing capacity of X-joints with $\tau=0.4$ was unobvious. The ultimate bearing capacity of plate-to-SHS X-joints with $\tau \geq 0.6$ significantly increased with the increase of the θ value.

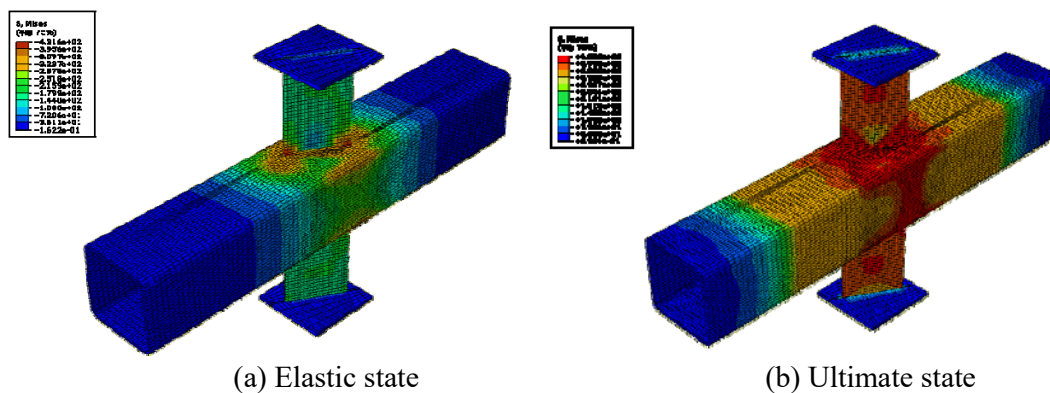
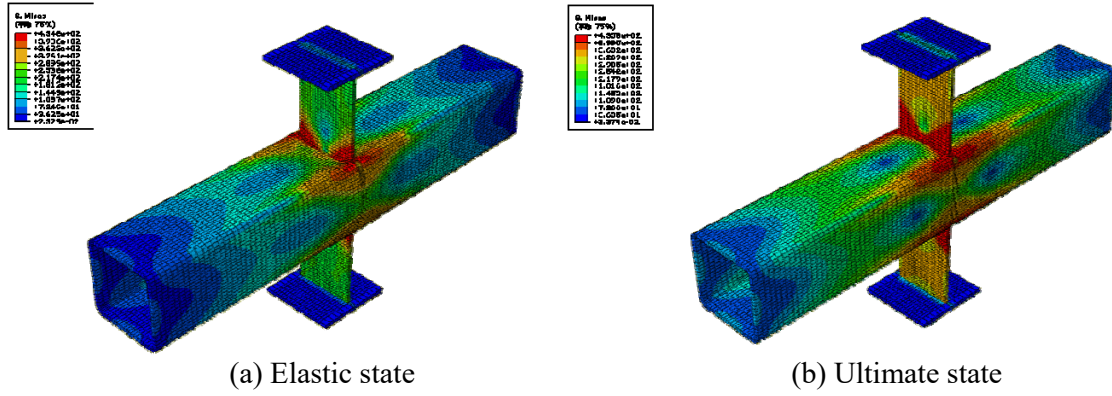
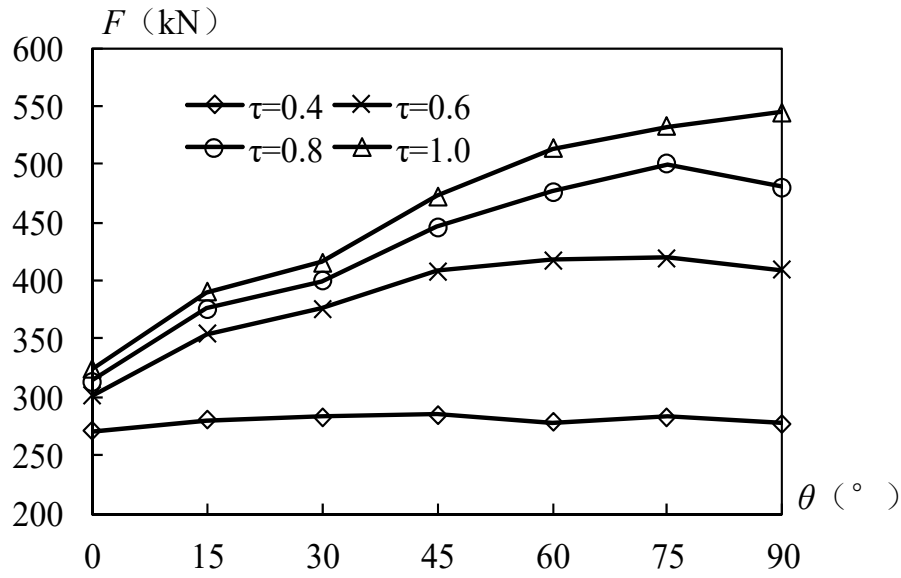


Figure 17. Plastic Development for Skewed Plate-to-SHS X-joints($\theta=30^\circ$, $\tau=0.6$)

Figure 18. Plastic Development for Skewed Plate-to-SHS X-joints($\theta=90^\circ$, $\tau=1.0$)Figure 19. F_u - θ Curves

6. PROPOSED DESIGN EQUATIONS

Based on the test and FEA results, the design equations were proposed by using the curve fitting technique for plate-to-SHS X-joints under compression. The proposed design equations were derived from the regression analysis by using Matlab. Skewed plate-to-SHS X-joints under compression can be calculated using the proposed design equations as follows:

For $\tau \geq 0.6$

$$F_u = 1.05 f_{y0} t_0 (t_1 + 5t_0) (1 + \sin \theta^{0.43\tau}) Q_f \quad (6)$$

For $\tau < 0.6$

$$F_u = 2.8 f_{y0} t_0^2 (\beta + 2 \sqrt{1 - \frac{t_1}{b_0}}) Q_f \quad (7)$$

F_u — Ultimate bearing capacity of skewed X-joints under compression;
 f_{y0} — Yield stress of SHS chord;
 b_0 — Width of SHS chord;
 t_0 — Thickness of SHS chord;
 t_1 — Thickness of plate;
 θ — Skewed angle between plate and chord axis;
 β — Ratio of plate width to chord width;
 τ — Ratio of plate thickness to chord thickness;
 Q_f — Parameter of chord stress

The ultimate bearing capacity of skewed plate-to SHS X-joints under compression calculated using the proposed design equations were compared with those obtained from the finite element analysis in the parametric study, as shown in Table 9. A good agreement was obtained with the mean value of proposed design strength-to-FEA result ratio of 0.88, and the corresponding coefficient of variation (COV) of 0.088 for skewed plate-to SHS X-joints under compression. Furthermore, the comparison of the ultimate strengths of skewed plate-to-SHS X-joints under compression calculated using the proposed design equations with the FEA results is clearly shown in Figure 20. It can be generally concluded from the comparison that the values of most proposed design strength-to-FEA result ratio are within the range of 0.8-0.9 and 0.9-1.0, which means the proposed design equations are more accurate and safe for designing of skewed plate-to SHS X-joints under compression.

Table 9. Statistics of Comparison between Proposed Design Equations Strengths and FEA Results

Specimen	Comparison	
A total of 28 X-joints	Max	0.99
	Min	0.67
	Mean	0.88
	COV	0.088

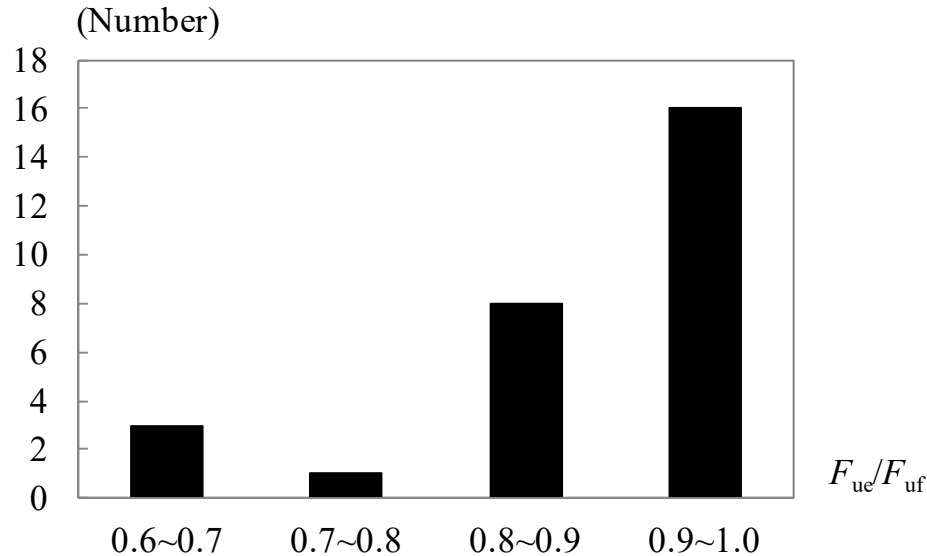


Figure 20. Number of FEA- F_{ue}/F_{uf} Curves

7. CONCLUSIONS

An experimental investigation was conducted in this study on the static behavior of skewed plate-to-SHS X-joints under compression. The joint strengths, failure modes, displacements and strain distributions of all specimens were reported. In addition, the corresponding finite element analysis was also performed and the validated finite element models were used for the parametric study to evaluate the effects of two main geometric parameters on the static behavior of skewed plate-to-SHS X-joints under compression. Based on the experimental and numerical investigations, the following conclusions can be drawn:

- (1) Plate failure and tube-plate failure were main two failure mode in the tests.
- (2) The maximum strain intensity of plate-to-SHS X-joints all occurred at the end of the weld seams.
- (3) The ultimate bearing capacity of plate-to-SHS X-joints under compression shows an increasing trend with the increase of skewed angle.
- (4) The ultimate bearing capacity of plate-to-SHS X-joints under compression increases significantly as the thickness of plate increases.
- (5) The proposed design equations were shown to be accurate and reliable for skewed plate-to-SHS X-joints under compression.

ACKNOWLEDGEMENTS

This research work was supported by the National Natural Science Foundation of China (No. 51478047 and No. 51778066) and Hubei Province Outstanding Youth Science Foundation of China (No. 2017CFA070).

NOTATION

F	Axial load
F_u	Ultimate bearing capacity of joints
Δ	Vertical displacement
θ	Skewed angle
L	Length of specimen
H	Height of specimen
b_0	Chord width
t_0	Chord thickness
b_1	Plate width
t_1	Plate thickness
τ	Plate to chord wall thickness ratio
β	Plate to chord width ratio
2γ	Chord width to wall thickness ratio
ε_i	Strain
ε_1	First principal strain
ε_2	Second principal strain
ε_3	Third principal strain
f_u	Ultimate tensile stress
f_y	Tensile yield stress
f_{y0}	Yield stress of the chord
f_{y1}	Yield stress of the brace
E	Elastic modulus
ν	Poisson's ratio

ε_f	Elongation after fracture
COV	Coefficient of variation
Δ_u	Ultimate displacement
Δ_y	Yield displacement
Δ_u/Δ_y	Ductility coefficient
N_1^*	Calculated ultimate bearing capacity by using CIDECT
N_e	Experimental ultimate bearing capacity
R_v	Ratio of ultimate bearing capacity of skewed plate-to-SHS X-joints to that of joints with $\theta=0^\circ$
Q_f	Parameter of chord stress

REFERENCES

- [1] Voth, A.P. and Packer, J.A., "Numerical Study and Design of Skewed X-type Branch Plate-to-circular Hollow Section Connections", *Journal of Constructional Steel Research*, 2012, Vol. 68, No. 1, pp. 1-10.
- [2] Kim, W.B., "Ultimate Strength of Tube-gusset Plate Connections Considering Eccentricity", *Engineering Structures*, 2001, Vol. 23, No. 11, pp. 1418-1426.
- [3] Saucedo, G.M., Packer, J.A. and Willibald, S., "Parametric Finite Element Study of Slotted End Connections to Circular Hollow Sections", *Engineering Structures*, 2006, Vol. 28, No. 14, pp. 1956-1971.
- [4] Ling, T.W., Zhao, X.L., Mahaidi, R.A. and Packer, J.A., "Investigation of Block Shear Tear-out Failure in Gusset-plate Welded Connections in Structural Steel Hollow Sections and Very High Strength Tubes", *Engineering Structures*, 2007, Vol. 29, No. 4, pp. 469-482.
- [5] Ling, T.W., Zhao, X.L., Mahaidi, R.A. and Packer, J.A., "Investigation of Shear Lag Failure in Gusset-plate Welded Structural Steel Hollow Section Connections", *Journal of Constructional Steel Research*, 2007, Vol. 63, No. 3, pp. 293-304.
- [6] Zhao, R.G., Huang, R.F., Khoo, H.A. and Cheng, J.J.R., "Parametric Finite Element Study on Slotted Rectangular and Square HSS Tension Connections", *Journal of Constructional Steel Research*, 2009, Vol. 65, No. 3, pp. 611-621.
- [7] Lee, H.D., Lee, J.M., Lee, S.H. and Shin, K.J., "Investigation of the Tube-gusset Connection in 600MPa Circular Hollow Section", *Procedia Engineering*, 2011, Vol. 14, No. 12, pp. 2124-2132.
- [8] Voth, A.P. and Packer, J.A., "Branch Plate-to-Circular Hollow Structural Section Connections. I: Experimental Investigation and Finite-element Modeling", *Journal of Structural Engineering*, 2012, Vol. 138, No. 8, pp. 995-1006.
- [9] Voth, A.P. and Packer, J.A., "Branch Plate-to-Circular Hollow Structural Section Connections. II: X-Type Parametric Numerical Study and Design", *Journal of Structural Engineering*, 2012, Vol. 138, No. 8, pp. 1007-1018.
- [10] Jiao, H., Mashiri, F. and Zhao, X.L., "Fatigue Behavior of Very High Strength (VHS) Circular Steel Tube to Plate T-joints under in-plane Bending", *Thin-Walled Structures*, 2013, Vol. 68, No. 10, pp. 106-112.
- [11] Hochanadel, Wayne P., "Static Design Procedure for Welded Hollow Section Joints: Recommendations", *Proceedings of International Institute of Welding (IIW) Overview*, Singapore, 2009, Vol. 3, pp. 126-140.
- [12] American Welding Society (AWS), "Structural Welding Code-steel. AWS D1.1/ 1.1M", Miami, USA, 2004.
- [13] Packer, J.A., Wardenier, J., Zhao, X.L. and Kurobane, Y., "Design Guide for Rectangular Hollow Section (RHS) Joints under Predominantly Static Loading", 2nd ed", CIDECT, 2009.
- [14] European Committee for Standardization., "Eurocode3 (EC3). Design of Steel Structures-Part 1-8: Design of Joints", Brussels, Belgium, 2005.

- [15] Packer, J.A., Sherman, D.R. and Lecce, M., "Steel Design Guide No. 24: Hollow Structural Section Connections", American Institute of Steel Construction (AISC), 2010.
- [16] Tong, L.W., Xu, G.W., Yan, D.Q. and Zhao, X.L., "Fatigue Tests and Design of Diamond Bird-beak SHS T-joints under Axial Loading in Brace", *Journal of Constructional Steel Research*, 2016, Vol. 118, No. 3, pp. 49-59.
- [17] Wang, W., Gu, Q., Ma, X.X. and Wang, J.J., "Axial Tensile Behavior and Strength of Welds for CHS Branches to SHS Chord Joints", *Journal of Constructional Steel Research*, 2015, Vol. 115, No. 12, pp. 303-315.
- [18] Chen, Y. and Chen, D.F., "Ultimate Capacities Formulae of Collar and Doubler Plates Reinforced SHS X-joints under in-plane Bending", *Thin-Walled Structures*, 2016, Vol. 99, No. 2, pp. 21-34.
- [19] Mashiri, F.R. and Zhao, X.L., "Square Hollow Section (SHS) T-joints with Concrete-filled Chords Subjected to in-plane Fatigue Loading in the Brace", *Thin-Walled Structures*, 2010, Vol. 48, No. 2, pp. 150-158.
- [20] Cheng, B., Qian, Q. and Zhao, X.L., "Stress Concentration Factors and Fatigue Behavior of Square Bird-beak SHS T-joints under Out-of-plane Bending", *Engineering Structures*, 2015, Vol. 99, No. 9, pp. 677-684.
- [21] Lie, S.T. and Yang, Z.M., "Fracture Assessment of Damaged Square Hollow Section (SHS) K-joint using BS7910:2005", *Engineering Fracture Mechanics*, 2009, Vol. 76, No. 9, pp. 1303-1319.
- [22] Shao, Y.B., "Static Strength of Collar-plate Reinforced Tubular T-joints under Axial Loading", *Steel and Composite Structures*, 2016, Vol. 21, No. 2, pp. 323-342.
- [23] Standardization Administration of The People's Republic of China., "Metallic Materials-Tensile Testing at Ambient Temperature", China Standards Press, 2002.

EXPERIMENTAL INVESTIGATION INTO THE CAPACITY OF COLD-FORMED SCREWED STEEL STRAP BRACING CONNECTIONS

M. Zeynalian ^{1,*}, A. Shelley ², H.R. Ronagh ³ and S. Hatami ⁴

¹ Assistant Professor, Department of Civil Engineering, The University of Isfahan, Iran

² Graduated Student, School of Civil Engineering, The University of Queensland, Australia

³ Professor, Institute for Infrastructure Engineering, Western Sydney University, Sydney, Australia

⁴ Assistant Professor, Department of Civil Engineering, Yasouj University, Iran

**(Corresponding author: Email: m.zeynalian@eng.ui.ac.ir)*

Received: 4 July 2017; Revised: 10 July 2017; Accepted: 19 October 2017

ABSTRACT: An experimental study on the behavior of cold formed steel (CFS) strap bracing connections is presented in this paper. 75 cold-formed steel strap bracing connections were examined. The connections maximum load capacity and the load-deformation behavior as well as the failure modes of the connections are investigated. The strap bracing connections included 0.55mm and 0.75mm cold-formed G550 steel and four different types of steel strap material. The connections behaviors are discussed and the design capacities calculated from different CFS design standards are compared to the experimental results of the connections. The results show that generally the monotonic tested connections capacities are lower than the cyclic capacities. Also, it is found that although the design provisions predict some of the behaviours of screwed connections, they are not fully suited to accurately predicting the ultimate behaviour of the strap bracing connections. Therefore, the recommended capacities for the strap bracing connections are based on the experimental results.

Keywords: Cold formed steel, strap bracing, connection, experimental study, screw

DOI: 10.18057/IJASC.2018.14.4.3

1. INTRODUCTION

The application of cold formed steel (CFS) in residential framing construction has become increasingly popular in housing industry in recent decades; and is now a highly competitive alternative to traditional framing due to its unique advantages such as being cost-effective, light-weight, and easy to work with. In order to design CFS structural system accurately, precise estimation of the potential failure modes and associated collapse load capacity is required. One of the most common CFS lateral resisting systems is X strap bracing (Kim et al. [1], Moghimi and Ronagh [2], Zeynalian and Ronagh [3-4]). In this system, straps are connected to the four exterior corners of the walls like an X, often with self-drilling metal screws.

Basically, connections are important components of any structure and are designed more conservatively than members. This is because usually the complexity of connections is more than members to analyze and design; and there are some discrepancies between analysis and actual behavior. In addition, in case of overloading, it is desirable to collapse an individual member rather than in connections, which may affect many members. Thus, improvement of the framing connections would increase the reliability of the structural performance of CFS framing system. This research study is aimed to conduct comparative evaluations for the optimization of one of the most currently in use screwed strap bracing connections in CFS housing industry as shown in Figure 1.



Figure 1. Screwed Strap Bracing to Wall Framing Connection

Four different strap materials were investigated in order to evaluate the number of screws required to obtain the maximum capacity of the connection. The capacities of the strap bracing connections given in this paper are based on the maximum, yield, and ultimate strengths found by analysis of the experimental data.

2. Failure Modes of Cold Formed Steel Connections

The screwed connections can fail in one mode or a combination of several modes (Yu and LaBoube [5]) and that these modes are typically edge tearing, bearing, tilting, pull-out, pull-over or by shear failure of the screw itself. Edge tearing occurs in screwed connections when the edge distance or spacing is too small. The tear starts from a screw hole and tears to the edge of the plate or to an adjacent screw hole. Hancock et al. [6] suggest that when the edge and spacing distances are large enough to avoid tear-out failure, bearing failure of the sheet could occur. Bearing failure often produces stretching of the hole on one side of the screw, while the sheet material is bunched together on the other side of the screw. Tilting failure usually occurs when two materials of the same thickness are connected, or when the thicker material is against the screw head. As the two sheets move over each other the screws can become tilted, and when the tilting angle becomes large, pull-out failure can occur. This type of failure is illustrated by Hancock [7] as shown in Figure 2.



Figure 2. Tilting Failure of Screwed Connections (Hancock [7])

Pull-out failure involves the screw(s) being ‘pulled out’ of the supporting sheet material under load, as a result of the axial tensile forces in the screws due to the rotated position of the screws relative to the direction of load in the connection (Rogers and Hancock [8]). This type of failure is often associated with tilting failure. Pull-over failure involves the connected sheet ‘pulling over’ the screw head. Pull-over is enhanced by cyclic loading conditions experienced in high wind areas and/or during seismic activity as this can reduce the tensile strength of the sheet.

Yielding of the gross cross-section of the sheet occurs when $A_n f_u > A_g f_y$, where A_n = net area of the cross section, f_u = ultimate strength of the sheet, A_g = gross area of the cross section, and f_y = yield

strength of the sheet (AS/NZS4600 [9]). This type of failure is ductile and can exhibit large deformations before ultimate failure of a sheet occurs. This ductile behavior is desirable in bracing systems in particular, where sudden brittle failure could be result in catastrophic failure of the overall structure. In contrast to gross cross-section failure, net section failure occurs when $A_n f_u < A_g f_y$, and failure is brittle. This type of failure can occur at lower loads than yielding of the gross cross section when the net area of the sheet is reduced by perforations or fastener holes. Screw shear failure occurs by shearing of the screw as the two sheets are pulled over each other. This failure is brittle, and can be catastrophic. Therefore when designing screwed connections it is desirable for one or more of the previously described failure modes to be more probable than screw shear.

3. Literature Review

Adham et al [10] tested six full-scale 2.4 x 2.4 m CFS strap shear walls under cyclic loads. They concluded that, upon preventing the buckling and connection failure at the design stage, the system will work more effectively in dissipating energy during the lateral cyclic displacement. Hatami et al. [11] investigated the performance of different strap bracing arrangements in CFS shear walls by means of cyclic loading of a total of ten full-scale walls. They assessed the failure modes of each system and the main factors contributing to the ductile response of the CFS walls to ensure that the diagonal straps yield and respond plastically with a significant drift. Fiorina et al. [12] conducted an experimental study on screw connections between wood and gypsum sheets and cold-formed steel stud profiles. They concluded that the sheathing type has a significant effect on the connections shear response. They also claimed that the connection test results yield reasonable prediction of the lateral response of steel shear walls. Rogers and Hancock [8] investigated the behavior of single overlap screwed specimens and also evaluated the existing design provisions with regard to the accuracy of the provisions in predicting both the capacity and failure mode of these connections. They found that none of their specimens failed in pure bending or tilting, but rather they all experienced a combination of the two modes. They stated that these combinations of failures were due to the very thin sheets used, and for some specimens the use of screws for which did not have thread which extended to the screw head. They found that when the thinner sheet is against the screw head, bearing failure becomes more likely. Lennon et al. [13] reported on a comparative investigation into the shear behavior of some mechanical connections in CFS frames. Five different mechanical fasteners were considered, including self-tapping screws which showed a low initial stiffness. They reported that the ductility of all screws samples tested was high because of the parent metal dragging on the screw threads in the large displacement range of response. Peterman et al. [14] reported an experimental study on hysteretic behavior of the screwed connection between CFS studs and sheathing subject to in-plane lateral demands. They reported that the connections have an important role for energy dissipation in wood sheathed CFS walls. They highlighted that the steel thickness impacts not only shear strength and stiffness, but also failure mode, ranging from highly ductile response to fastener shear.

The findings of the above review have provided indications of failure behaviors exhibited by test specimens and some of the factors which affect these behaviors. There are also criticisms on the strengths and weaknesses of the current design standards. The findings of this literature review will be taken into consideration when the results of the experimentation conducted for this research are evaluated.

4. Strap Bracing Connections

In strap braced CFS buildings, it is common to brace the wall framing with cross bracing at specified intervals throughout the buildings. These cross braces are constructed from steel strap and are connected to the wall framing systems generally using 10-16 wafer head screws (Buildex Co. [15]) which is shown in Figure 3. The currently in use strap bracing arrangement is shown in Figure 4 (Quickframe steel frames Pty Ltd. [16]).



Figure 3. Wafer Head Screw

This study is aimed to investigate the connection arrangement of screws required to adequately secure four different types of strap bracing to wall framing, and the capacities of these connections.

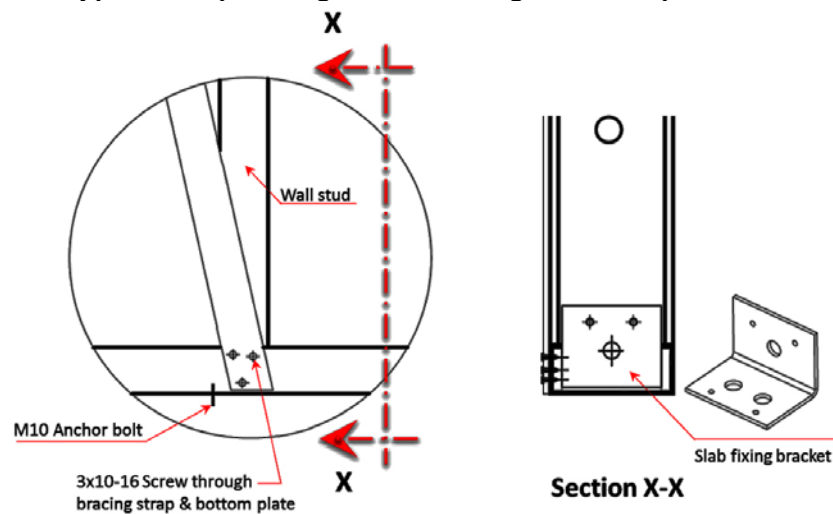


Figure 4. Strap Bracing Detail

The capacity of the connections can limit the ultimate capacity of the overall strap bracing system, particularly in the cases where the limiting failure occurs at the connection. The characteristic yield and ultimate strengths of a strap material determine the maximum potential capacity of the bracing system in which the strap is used; however when the capacity of the strap connection is lower than the ultimate strength of the strap, the connection reduces the ultimate strength of the overall bracing system and therefore reduces the amount of ductility that can occur before ultimate failure of the system occurs.

Strap bracing is designed to carry tensile loading only, so all specimens were tested in tension only. As cyclic loading is an important consideration in designing strap bracing, due to the nature of the lateral loads to which it can be subjected particularly during cyclonic and/or seismic activity, cyclic tests were conducted in addition to monotonic tests of each different specimen type. Hence, it was planned to examine the required screw arrangement to secure the different types of strap through a reliable series of experimental tests. Then, the results of the experimentation were discussed and compared with the design capacities calculated based on the cold-formed steel design guides and standards.

4.1 Materials

Two different most common in use thicknesses of G550 CFS sections for the connection tests were taken into account. The two material thicknesses are 0.55mm and 0.75mm, and will be referred to as types A and B, respectively. The material properties are given in Table 1. Also, four types of steel strap bracing material were considered in this research study (BlueScope Co. [17]). These materials were chosen, as they are materials which they either currently use or would consider using for the strap bracing. Axial tension tests were conducted on specimens of each type of strap to find out the mechanical characteristics of the straps as presented in Table 2. It is necessary to mention that G2 and G3 is represent the steel properties which are illustrated in Table 2 (BlueScope Co. [17]).

Table 1. G550 CFS Properties

Nominal Grade (MPa)	Elastic Modulus (GPa)	Yield Stress (f_y) (MPa)	Yield Strain (%)	Ultimate Stress (f_u) (MPa)	Ultimate Strain (%)	f_u/f_y
550	168.93	592.26	0.45	617.25	2.86	1.04

Table 2. Strap Bracing Material Properties

Strap Number	Description/Nominal Dimensions (mm*mm) [17]	Actual Width (mm)	Actual Thickness (mm)	Elastic Modulus (GPa)	Yield Stress (f_y) (MPa)	Yield Elongation (%)	Ultimate Stress (f_u) (MPa)	Ultimate Elongation (%)	f_u/f_y
1	Perforated G3 30*0.75	29.4	0.78	154	232	0.36	246	1.61	1.06
2	Solid G2 30*0.75	29.5	0.83	161	290	0.38	293	25.2	1.01
3	Perforated G2 30*0.75	29.5	0.74	133	270	0.40	271	4.07	1.00
4	Solid G2 40*1.0	40.1	0.96	150	298	0.40	302	22	1.01

Also, the strength property information provided by Buildex Co. [15] for these 10-16 screws is presented in Table 3.

Table 3. Properties for the 10-16 Screw

Gauge/TPI	Nominal Diameter	Head Diameter	Single Shear Strength	Axial Tensile Strength
10-16	4.8mm	9mm	5.2 kN	8.2kN

4.2 Screw Arrangements

The capacity of one screw was tested first with the type 2 solid strap. This estimate of the capacity of about 2.5kN per screw was then used to estimate the required number of screws for each strap. The nominal tension capacity of each strap bracing material was determined using Australian steel structures standard (AS/NZS4100 [18]) which deems that the nominal section capacity should be taken to be the lesser of $N_t = A_g f_y$; and $N_t = 0.85 k_t A_n f_u$ where N_t is the nominal section capacity in tension, A_g represents the gross area of the cross-section, f_y is the yield stress used in design, k_t = the correction factor, A_n = the net are of the strap and, and f_u is the ultimate stress. The nominal section capacity was then divided by the capacity per screw to estimate the number of screws required to prevent pull-out and obtain the maximum possible capacity of the strap bracing.

The optimal screw arrangements were based on two criteria. The first criterion was that the arrangement must conform to the spacing requirements of standard AS/NZS4600 [9]. The second criterion was that the arrangement should maximize the minimum net area for the possible failures that can occur through the holes in the strap. The second criterion was the reason for placing 2

individual screws along the strap before placing 2 screws together in a line perpendicular to the line of force as could be seen for the arrangements for more than 3 screws in the type 2 and 4 solid straps as illustrated in Figures 5 and 6, respectively; the net area at the connection could not be increased above the net area when failure occurs through only a single screw, and therefore this design was sufficient. LaBoube and Sokol [19] proved that the pattern of screws used has a very limited impact on the strength of a connection and therefore for this study more detailed connection design was not considered necessary.

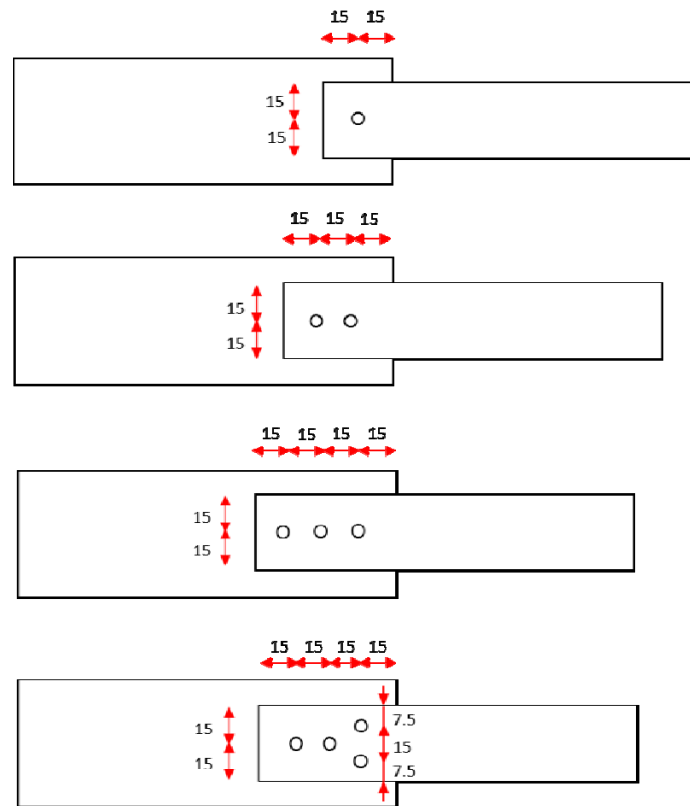


Figure 5. Screw Arrangements for Solid Type 2 Strap (All Dimensions are in mm)

The perforated straps were fastened using existing perforations where more than 1 screw was used in a connection. The end distance in the line of force from the center of the screw to the edge of the strap was always at least the $3d_f$ (diameter of screw) required by AS/NZS4600; however the spacing of screws and perpendicular edge distance was governed by the existing perforations. If the existing holes were not used, additional holes would have reduced the net section which would have weakened the connection more than if the existing 3mm holes were increased to 4.8mm holes by the screws. The patterns of the perforations in strap types 1 and 3 were the same and were illustrated in Figure 7.

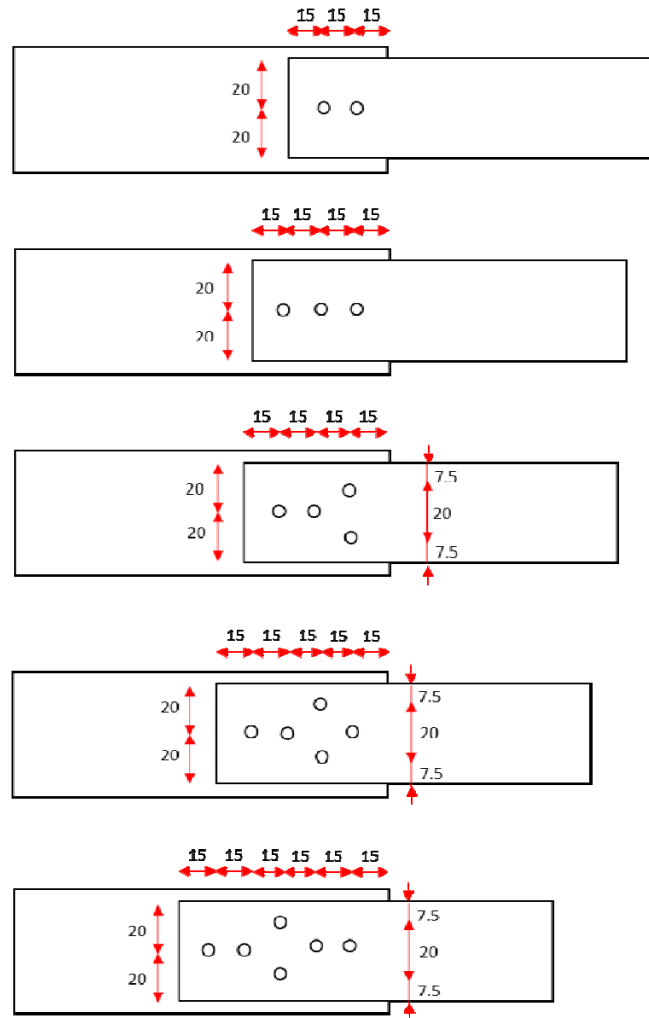


Figure 6. Screw Arrangements for Solid Type 4 Strap (All Dimensions are in mm)

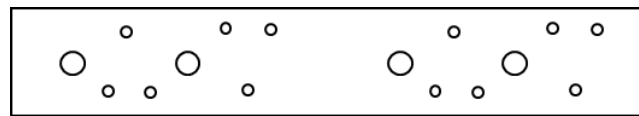


Figure 7. Perforations in Strap Types 1 and 3

5. EXPERIMENTAL PROGRAM

The program consisted of 75 specimens to investigate the structural performance of strap bracing connections. It is necessary to mention that this study is part of a major research project (Zeynalian and Ronagh [20], Zeynalian et al. [21]) that is concerned with structural performance of different currently in-use CFS structures. These specimens were tested in the structural laboratory of the School of Civil Engineering, the University of Queensland.



Figure 8. Testing Machine Set-up

The specimens were held in the grips of the testing machine at two ends: one of cold-formed steel, and the other of strap bracing. It worth to note that for specimen preparation, first, the flanges of the cold-formed steel C-section were cut into pieces of approximately 150mm in length. Then, the strap bracing materials were cut into lengths of approximately 150mm. After that, the screws were fastened in the chosen arrangements according to the currently in use fixing recommendations using a power screwdriver; and finally, the specimens were tightened into grips of the machine at both ends. The overall length of the specimen between the grips was 150mm. The specimens' name notation is illustrated in Figure 9.

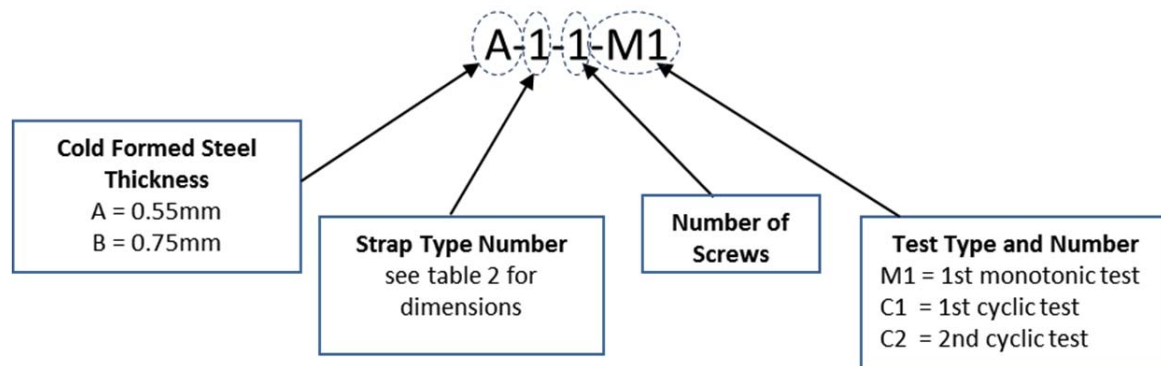


Figure 9. The Specimen Name Notation

Based on the recommendation of the ASTM Standard (ASTM-E2126-07 [22]) detailing test methods for cyclic load tests, one monotonic axial tension test to failure and two cyclic tests were conducted on each different specimen type. In monotonic test, the specimens were loaded to failure at a rate of 10mm/min until failure occurred, whereas in the cyclic tests, a loading regime which is demonstrated in Figure 10, was applied.

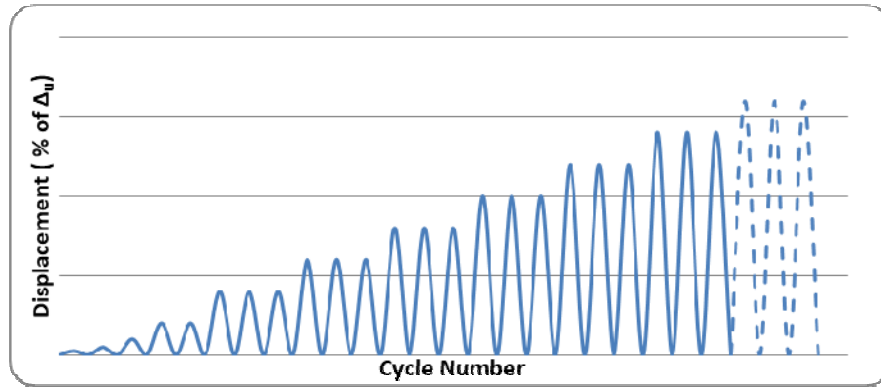


Figure 10. Cyclic Testing Extension Regime (ASTM-E2126-07 [22])

The cyclic loading regime, involved two stages of displacement patterns. The first stage involved single displacement cycles of 2.5%, 5% and 10%, and two cycles of 20% of the ultimate displacement found in the monotonic test. The second stage involved three cycles each of 20%, 40%, 60%, 80%, 100%, and 120% of the ultimate displacement until the specimen failed. The rate of extension was varied throughout the cyclic test to suit the capability of the testing machine. For the shorter extensions the rate of loading was between 1 and 10mm/min, while the greater extension cycles were conducted at between 15 and 25mm/min.

6. EXPERIMENTAL RESULTS

A load-extension graph was plotted for each monotonic test specimen in order to find the yield, maximum, and ultimate loads, and their corresponding extensions/displacements. An example of the load-extension graphs is shown in Figure 11. It is necessary to mention that the linear part of the curves is relatively small. That is because the curves represent the load-deformation of the whole connections, including the members and screw. Hence, the graphs imply the screw looseness and sliding as well, which lead to occurrence of nonlinearity in the graphs.

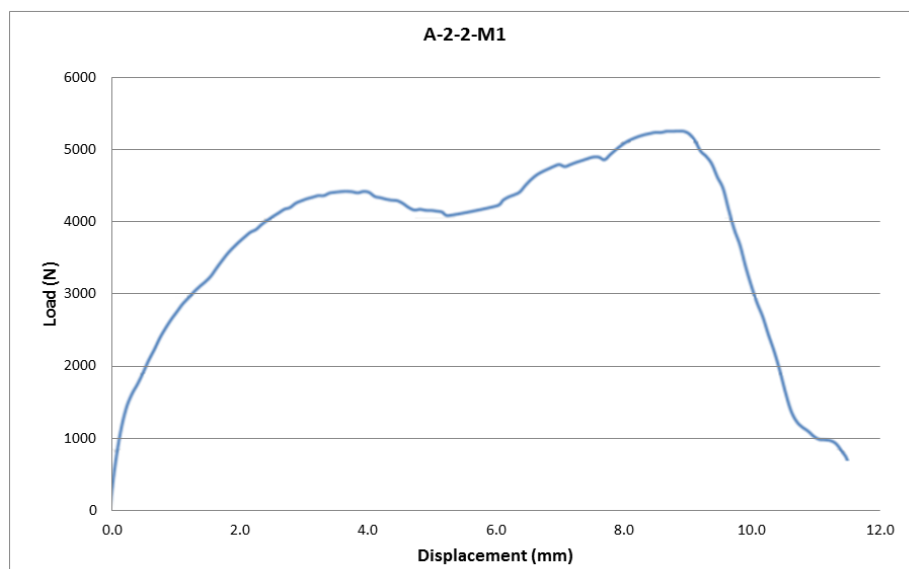


Figure 11. Load-extension Graph from Monotonic Test Results

The data from the cyclic test specimen results was first graphed in the load-extension form, referred to as a hysteresis curve, and from that curve an envelope curve was plotted by recording the maximum load for the first cycle of each phase of the cyclic loading. Examples of the hysteresis and envelope curves are shown in Figures 12 and 13, respectively.

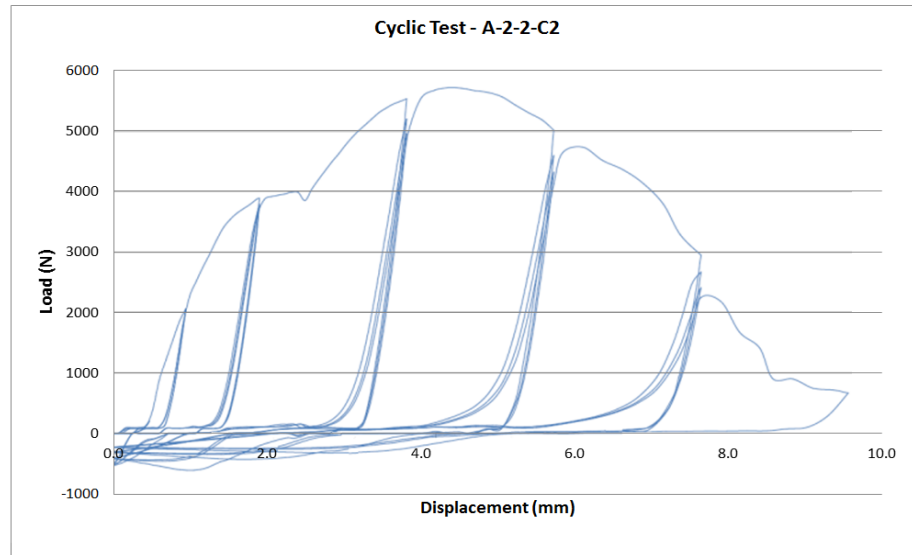


Figure 12. Example of Hysteresis Curve from Cyclic Test

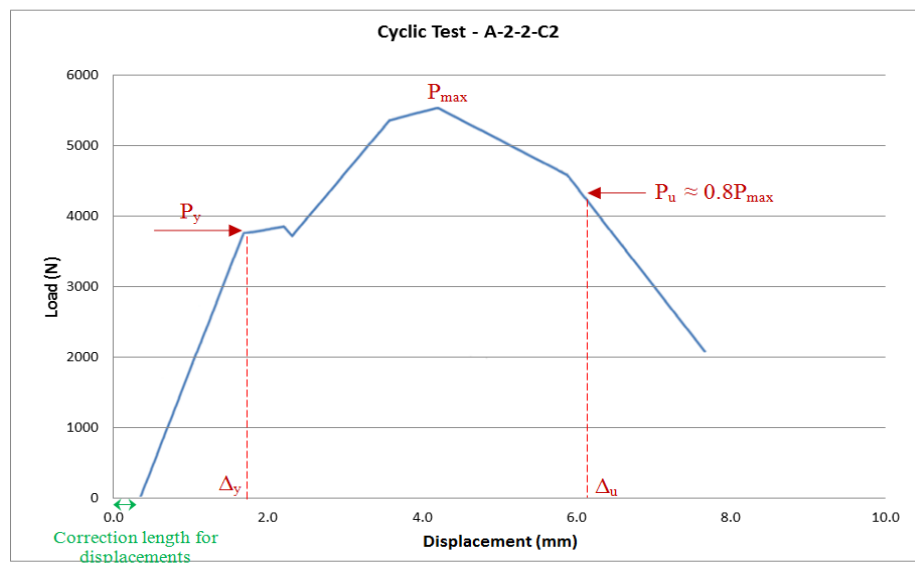


Figure 13. Example of Envelope Curve taken from Hysteresis

It should be mentioned that initially very small amounts of load were taken by the specimen over a certain length of extension. This is a result of the specimen straightening out and adjusting as it takes the load of the machine. To overcome the error which this may have caused in the calculation of the parameters, the extension length before the load on each specimen began to increase was taken away from the measured yield and ultimate displacements. The results of the monotonic and cyclic strap bracing tests are summarized in Tables 4, 5, and 6 on the following pages. The maximum load (P_{max}), yield load (P_y), ultimate load (P_u), and corresponding displacement at yield (Δ_y) and displacement at ultimate load (Δ_u) were found from the load-displacement graphs and

envelope curves for monotonic and cyclic tests respectively. According to ASTM Standard E2126 [22], Δ_u shall be an estimate of the maximum displacement at which the load in a primary cycle has not yet dropped below $P_u = 0.8 P_{max}$ as illustrated in Figure 13. The ductility factor R_μ , the yielding factor R_f , and the elastic shear stiffness K_e are also evaluated. The ductility factor is the ratio of displacement at the ultimate load to the displacement at the start of yield. Therefore, as the ductility factor increases, so does the ductile behavior exhibited by a specimen. The yielding factor R_f which is defined as the ratio of the maximum load (P_{max}) to $A_g F_y$, indicates whether a specimen should have yielded before the maximum load capacity of the connection was reached. If the yielding factor is less than one, no yielding has place, and in contrast if the yielding factor is above one, the specimen has exhibited yielding. The ASTM Standard E2126 defines the elastic shear stiffness K_e to be ‘the resistance to deformation of a connection in the elastic range before the first major event is achieved, which can be expressed as a slope measured by the ratio of resisted shear load to the corresponding displacement’. A major event as referred to by the ASTM Standard as the first limit state to occur, where a limit state is the point where there is a change in the behavior of the system. The limit states for these strap bracing connections are the yield limit state, the strength limit state and the failure limit state.

A discussion on the failure modes and trends exhibited in the monotonic tests and a similar discussion regarding any additional trends from the cyclic test results is presented here. This will be followed by an evaluation of the capacities of each strap to cold-formed steel connection and a comparison of these capacities for the monotonic and cyclic tests. Finally the calculated design capacities will be compared to the actual experimental capacities of the connections. It is necessary to mention that the notations for the failure modes observed during experimentation are:

- B = bearing
- T = tilting
- TR = tear-out
- PT = pull-out
- PR = pull-over
- NSF = net section failure
- (m) = moderate (≈ 1 -2mm bearing; $\leq 20^\circ$ tilting)
- (s) = severe (> 2 mm bearing; $> 20^\circ$ tilting)

Table 4. Monotonic Tests Results

		Specimen Name	P_{max} (N)	P_y (N)	Δ_y (mm)	P_u (N)	Δ_u (mm)	A_g (mm ²)	A_n (mm ²)	$A_g F_y$ (N)	$0.85 A_n F_u$ (N)	R_μ	R_f	K_e	Failure Mode
CFS Type A 0.55mm	Strap 1	A-1-1-M1	2472	2210	1.2	1980	3.1	22.9	16.2	5641.3	3199.7	2.58	0.44	3955	(m)B+(m)T+PT
		A-1-2-M1	4781	4130	3.8	3820	7.3	22.9	15.5	5641.3	3056.4	1.92	0.85	2854	(m)B+(s)T+PT
		A-1-3-M1	6084	4830	2	4860	6.9	22.9	15.5	5641.3	3056.4	3.45	1.08	9360	(m)T+NSF
	Strap 3	A-3-1-M1	2666	1990	1.3	2130	5.6	21.8	15.5	5915.9	3549.8	4.31	0.45	5332	(m)B+(s)T+PT
		A-3-2-M1	4769	3140	1.8	3820	6.7	21.8	15.5	5915.9	3557.0	3.72	0.81	2935	(m)B+(m)T+PT
		A-3-3-M1	6580	4900	3.2	5260	11.6	21.8	15.5	5915.9	3557.0	3.63	1.11	3290	(m)T+NSF
	Strap 2	A-2-1-M1	2820	2820	2.1	2260	5	24.5	20.5	7100.7	5105.8	2.38	0.40	3760	(s)B+(m)T+PT
		A-2-2-M1	5150	4355	3.32	4120	9.1	24.5	20.5	7100.7	5105.8	2.74	0.73	4120	(m)B+(s)T+PT
		A-2-3-M1	7000	7000	4.3	5600	7.2	24.5	20.5	7100.7	5105.8	1.67	0.99	8000	(m)B+(s)T+PT
		A-2-4-M1	7820	7226	6.15	6260	17.5	24.5	20.5	7100.7	5105.8	2.85	1.10	5586	NSF
	Strap 4	A-4-4-M1	10550	7120	4.8	8440	18.6	38.5	33.9	11625.8	8584.3	3.88	0.91	4220	(s)B+(s)T+PT
		A-4-5-M1	11570	7760	5.1	9260	20.9	38.5	33.9	11625.8	8584.3	4.10	1.00	3045	(s)B+(s)T+PT
		A-4-6-M1	13030	11090	5	10430	27.9	38.5	33.9	11625.8	8584.3	5.58	1.12	6949	NSF
CFS	Strap	B-1-1-M1	3801	2860	2.5	3040	6.3	22.9	16.2	5641.3	3199.7	2.52	0.67	2339	(m)B+(s)T+PT

Type B 0.75mm	1	B-1-2-M1	6250	2750	1	5000	9	22.9	15.5	5641.3	3056.4	9.00	1.11	3247	(s)TR+(s)T+PT
		B-1-3-M1	6760	5630	2.4	5410	6.9	22.9	15.5	5641.3	3056.4	2.88	1.20	6438	NSF
	Strap 3	B-3-1-M1	3350	3070	1.5	2680	6.2	21.8	15.5	5915.9	3549.8	4.13	0.57	3941	(s)B+(s)T+PT
		B-3-2-M1	6590	4240	2.6	5270	10.9	21.8	15.5	5915.9	3557.0	4.19	1.11	2897	(s)TR+(s)T+PT
		B-3-3-M1	6800	5610	2.5	5440	7.1	21.8	15.5	5915.9	3557.0	2.84	1.15	6974	NSF
	Strap 2	B-2-1-M1	3920	3078	2.2	3130	6.6	24.5	20.5	7100.7	5105.8	3.00	0.55	3834	(m)B+(s)T+PT
		B-2-2-M1	6280	5180	1.3	5020	8.9	24.5	20.	7100.7	5105.8	6.85	0.88	10253	(m)B+(s)T+PT
		B-2-3-M1	8050	7290	3.34	6440	11	24.5	20.5	7100.7	5105.8	3.29	1.13	10387	NSF
	Strap 4	B-4-2-M1	6420	3440	0.9	5140	6	38.5	33.9	11625.8	8584.3	6.67	0.55	3951	(m)B+(m)T+PT
		B-4-3-M1	9230	4810	1	7380	8.9	38.5	33.9	11625.8	8584.3	8.90	0.79	11538	(m)B+(s)T+PT
		B-4-4-M1	12670	10163	1.67	10140	10.7	38.5	33.9	11625.8	8584.3	6.41	1.09	10536	(m)T+NSF

The monotonic test results for all connections show a general trend of increasing capacity with the increasing number of screws. This is a trend which is commonly accepted for screwed connections and has been proven by prior research by LaBoube and Sokol [19]. The contribution of each screw decreased as the number of screws in the connection increased which was also proven in the research by LaBoube and Sokol. For the connection specimens that included fewer screws than were required for the strap to achieve its maximum possible capacity in tension, the modes of failure which were exhibited were combinations of bearing, tilting and pull-out. For each connection between a different strap type and cold-formed steel thickness, at least two connections using the same materials were tested with fewer screws than were required to achieve the maximum strap capacity. These connections were tested to evaluate: the failure modes that occurred when fewer screws were used, and the reduction in capacity as the number of screws is decreased. A load-extension graph from a specimen for which pull-out was the ultimate failure mode is shown in Figure 14. It shows straight that after the maximum load is reached the load begins to drop as the screw pulls out.

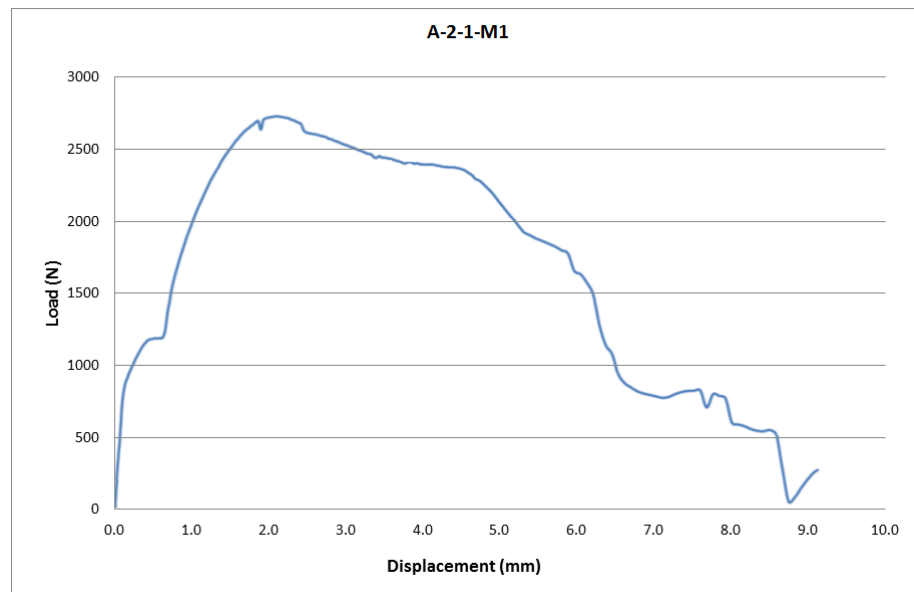


Figure 14. Load-extension Graph for a Pull-out Failure – Solid Strap

Figure 15 shows a load-extension for a perforated strap specimen which failed by pull-out. The initial yielding appears to occur in stages which can be attributed to the strap yielding at the different cross-sections along the strap due to the perforations. The load peaks which occur after the maximum load are due to the threads bearing on the cold-formed steel as they pull out one by one.

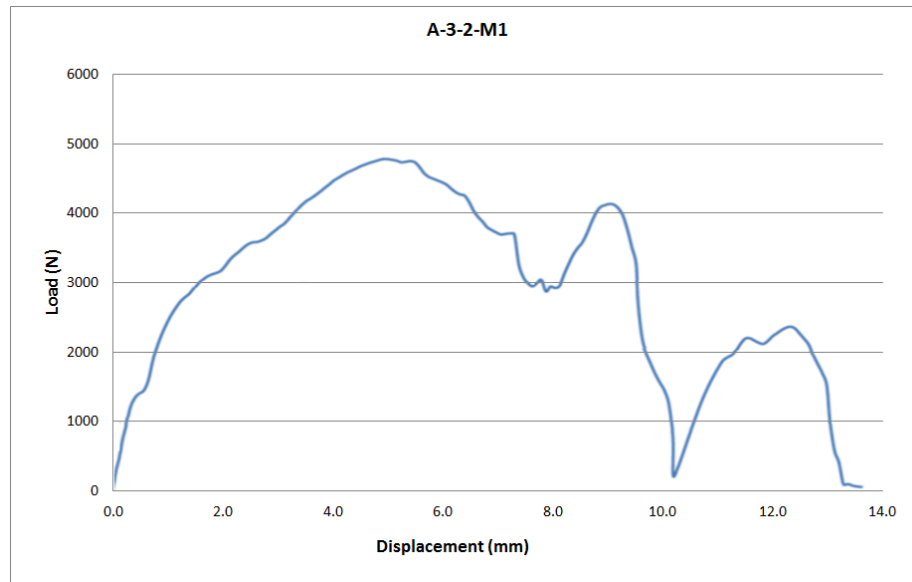


Figure 15. Load-extension Graph Pull-out Failure – Perforated Strap

In contrast to Figure 14 and Figure 15, Figure 16 is a load-extension plot for a specimen which failed by net section failure after yielding and significant ductile behavior had occurred.

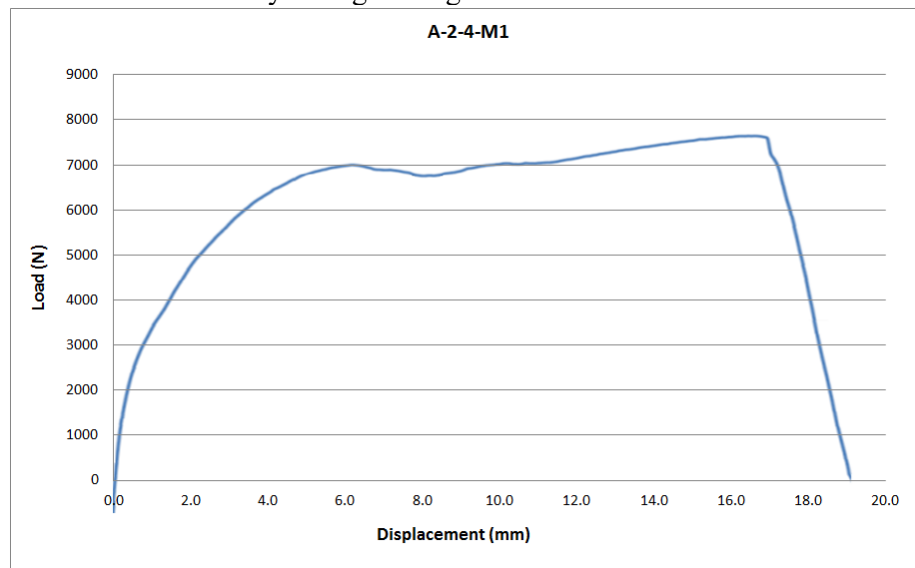
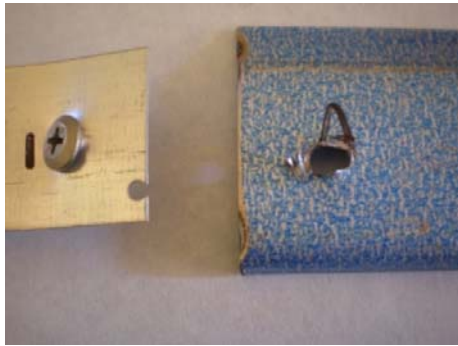
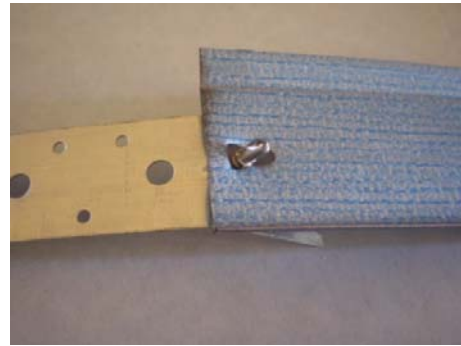


Figure 16. Load-extension Curve for a Net Section Failure – Solid Strap

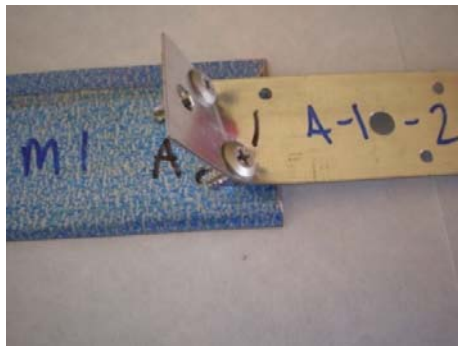
Some examples of different failure modes that occurred in the tested strap bracing specimens are shown in Figures 17 and 18, respectively, for some different specimens.



Bearing failure
Specimen A-1-1-M1



Bearing and Tilting failure
Specimen B-1-1-M1



Tilting failure
Specimen B-2-1-M1



Pull-out failure
Specimen A-1-2-M1

Figure 17. Examples of Different Failure Modes

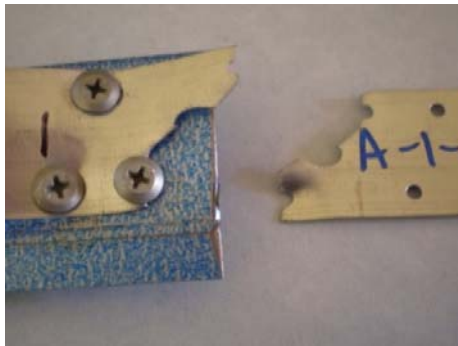
It should be noted that all of the specimens shown in Figure 17 ultimately failed by pull-out of the screws. An interesting combination of bearing, tilting, tear-out and pull-out was exhibited by the type 1 and 3 perforated straps connected to the type B 0.75mm cold-formed steel with 2 screws. Only these 2 specimens exhibited this behavior in the monotonic tests. One of them is shown in Figure 18.



Figure 18. Bearing, Tilting, Tear-out and Pull-out Failure: Specimen B-3-2-M1

When sufficient screws are used, it is expected that the strap will fail either by net section failure at the connection or for the perforated straps at the weakest cross-section of the strap; or by excessive yielding, depending on the properties of the material. The four types of strap material types tested to have ultimate stress to yield stress ratios between 0.94 and 1.01. These ratios reflect the closeness of values for the ultimate and yield stresses for these material and indicate that it is likely that net section failure will occur at loads which are near the yield point of a material. Some

specimens may experience significant ductile extension before the ultimate failure occurs, while for others the net section failure could be quite sudden once the required load is applied to the connection. When selecting a strap bracing material it is desirable to use a material which not only is strong enough to resist the required design loads on a structure, but which also exhibits significant ductile behavior before the ultimate behavior of the bracing system. For most of the monotonic test specimens the ductility factor increased with increasing number of screws. This was because the failure mode of the specimens was only net section failure for the maximum number of screws tested. The other specimens failed by various combinations of pull-out, bearing, and tilting which occurred at lower loads than the ultimate load for the strap material, therefore not allowing them to fully develop the maximum ductility that the strap material is capable of. Examples of the net section failure that occurred at the connections of the strap bracing materials are shown in Figures 19.



Net section failure
Perforated strap Specimen A-1-3-M1



Net section failure
Solid strap Specimen A-2-4-M1

Figure 19. Net Section Failure

When the perforated straps failed by net section failure, the failure always occurred at the same place in the perforation pattern of the straps as shown in Figure 20. This pattern in the strap has the lowest net area and therefore is the weakest part of the strap. The pattern repeats every 87mm and as a result there was only one repetition between the grips of the testing rig.

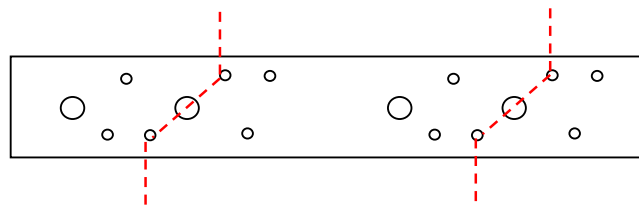


Figure 20. Perforated Strap Failure Location

An example of when the net section failure occurred away from the connection is shown in Figure 21. The weak area of the strap for this specimen was not near the connection, which resulted in the strap failure away from the connection.

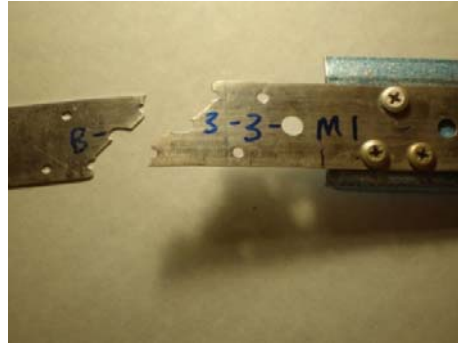


Figure 21. Net Section Failure away from the Connection: Specimen B-3-3-M1

For longer specimens of the perforated strap it would be expected that several of these weak areas at 87mm would elongate when the strap was loaded beyond the yield strength of the material. Both types of perforated straps had ductility ratios which were higher than that of the type 2 strap (which has similar dimensions) when connected to the 0.55mm cold-formed steel, but lower than the that of the type 2 strap when connected to the 0.75mm cold-formed steel.

Another parameter which was used to gauge the performance of the connection is the yielding factor R_f . Because the yield stresses of the strap materials are similar to the ultimate stresses, for most of the specimens which failed by combinations of bearing, tilting and pull-out, failure occurred before the material had begun to yield at all and therefore the yielding factors of these specimens is less than one. Also, the elastic shear stiffness K_e was calculated from the results of the strap bracing tests. Higher values of elastic shear stiffness indicate that a connection had a high stiffness and therefore more resistance to deformation during the elastic loading stage. In general, the solid strap materials exhibited higher elastic shear stiffness. The lower elastic shear stiffness of the perforated straps can be attributed to the yielding in the perforated straps at the narrower cross-sections of the strap material where there are significant perforations. These areas along the strap which have smaller cross sections yield at lower loads than the areas of the strap where there are fewer perforations. The perforations are intended to allow the strap material to deform with less resistance to load than if the strap was solid.

The thicker type B 0.75mm cold-formed steel connections had a higher capacity than the thinner cold-formed steel connections for all strap types except the type thicker and wider type 4 strap. The greater thickness increases the connections' capacity in bearing, tilting and pull-out according to the design provisions of AS/NZS4600 and therefore this result was expected. The reduction in capacity for the type 4 strap with the thicker cold-formed steel can be attributed to the reduction in the number of screws required for net-section failure to become the governing failure mode. For the 0.55mm cold-formed steel 6 screws are required while for the 0.75mm cold-formed steel only 4 screws are required to prevent the failure modes which occur when insufficient screws are used (bearing, tilting, pull-out, tear-out and pull-over). The reduction is relatively small (3%) and may also be due to specimen faults which occurred during assembly.

Table 5. Cyclic Test Results on CFS Type A (0.55 mm)

	Specimen Name	P _{max} (N)	P _y (N)	Δ _y (mm)	P _u (N)	Δ _u (mm)	A _g (mm ²)	A _n (mm ²)	A _g F _y (N)	0.85 A _n F _u (N)	R _μ	R _f	K _c	Failure Mode
Strap 1	A-1-1-C1	2856	1670	1.2	2285	5.5	22.9	16.2	5641	3200	4.58	0.51	1785	(m)B+(m)T+PT
	A-1-1-C2	3110	2119	1.65	2488	4.2	22.9	16.2	5641	3200	2.55	0.55	2145	(s)B+(m)T+PT
	A-1-2-C1	4379	3048	1.22	4379	6.2	22.9	15.5	5641	3056	5.08	0.78	5229	(m)B+(s)T+PT
	A-1-2-C2	5359	3727	2.36	4287	7.1	22.9	15.5	5641	3056	3.01	0.95	6496	(m)B+(m)T+PT
	A-1-3-C1	6532	3732	0.9	5226	6.6	22.9	15.5	5641	3056	7.33	1.16	4768	N5F
	A-1-3-C2	6068	5729	1.2	4854	3.8	22.9	15.5	5641	3056	3.17	1.08	4854	NSF
Strap 3	A-3-1-C1	2984	2063	1.8	2387	7.1	21.8	15.5	5916	3550	3.94	0.50	3226	(m)B+(m)T+PT
	A-3-1-C2	2838	2705	1.97	2270	7.4	21.8	15.5	5916	3550	3.76	0.48	3662	(m)B+(m)T+PT
	A-3-2-C1	5793	4571	1.5	4634	6.1	21.8	15.5	5916	3557	4.07	0.98	3049	(m)B+(m)T+PT
	A-3-2-C2	6088	5282	2.4	4071	6.7	21.8	15.5	5916	3557	2.79	1.03	5940	(s)B+(m)T+PT
	A-3-3-C1	6424	5522	2.2	5139	5.1	21.8	15.5	5916	3557	2.32	1.09	2495	NSF
	A-3-3-C2	6013	4203	1.1	4810	6.1	21.8	15.5	5916	3557	5.55	1.02	2559	(m)T+NSF
Strap 2	A-2-1-C1	3273	2856	2.2	2618	7.3	24.5	20.5	7101	5106	3.32	0.46	1657	(s)B+(s)T+PT
	A2-1-C2	3761	2340	0.9	3008	3.7	24.5	20.5	7101	5106	4.11	0.53	2180	(s)B+(s)T+PT
	A-2-2-C1	4996	4804	1.9	39%	6.6	24.5	20.5	7101	5106	3.47	0.70	6056	(m)B+(s)T+PT
	A-2-2-C2	5712	3983	1.9	4570	5.8	24.5	20.5	7101	5106	3.05	0.80	4080	(m)B+(s)T+PT
	A-2-3-C1	7528	6271	2.5	4570	11.5	24.5	20.5	7101	5106	4.60	1.06	6407	(m)B+(s)T+PT
	A-2-3-C2	7435	6936	1.9	5948	5.4	24.5	20.5	7101	5106	2.84	1.05	8038	(m)B+(s)T+PT
	A-2-4-C1	7922	7284	3.2	6338	9.4	24.5	20.5	7101	8584	2.94	1.12	7042	NSF
	A-2-4-C2	7770	4251	0.8	6216	8.1	24.5	20.5	7101	8584	10.13	1.09	6907	NSF
Strap 4	A-4-4-C1	10713	10704	3.9	8570	5.7	38.5	33.9	11626	8584	1.46	0.92	6593	(s)B+(s)T+PT
	A-4-4-C2	11152	10652	3.2	8922	5.9	38.5	33.9	11626	8584	1.84	0.96	7435	(s)B+(m)T+PT
	A-4-5-C1	11614	10388	2	9291	10.3	38.5	33.9	11626	8584	5.15	1.00	7834	(s)B+PT
	A-4-5-C2	12428	10533	2.5	9943	20.6	38.5	33.9	11626	8584	8.24	1.07	8527	(s)B+PT
	A-4-6-C1	13573	11358	1.6	10860	9	38.5	33.9	11626	8584	5.63	1.17	10858	NSF
	A-4-6-C2	13681	9583	1.6	10945	12	38.5	33.9	11626	8584	7.50	1.18	10945	(m)T+NSF

Table 6. Cyclic Test Results on CFS type B (0.75 mm)

	Specimen Name	P _{max} (N)	P _y (N)	Δ _y (mm)	P _u (N)	Δ _u (mm)	A _g (mm ²)	A _n (mm ²)	A _g F _y (N)	0.85 A _n F _u (N)	R _μ	R _f	K _c	Failure Mode
Strap 1	B-1-1-C1	3601	2390	0.7	2881	6.7	22.9	16.2	5641	3200	9.57	0.64	3893	(m)B+PR
	B-1-1-C2	3729	1626	0.7	2984	7	22.9	16.2	5641	3200	10.00	0.66	3551	(m)B+PR
	B-1-2-C1	6399	5324	2	5119	4.8	22.9	15.5	5641	3056	2.40	1.13	4654	(s)T+PT+TR
	B-1-2-C2	6362	5427	1.5	5089	6.3	22.9	15.5	5641	3056	4.20	1.13	7485	(s)B+(m)T+PT
	B-1-3-C1	6215	5076	1.6	4972	4.8	22.9	15.5	5641	3056	3.00	1.10	5524	NSF
	B-1-3-C2	6524	4390	1.2	5219	5.3	22.9	15.5	5641	3056	4.42	1.16	4745	NSF
Strap 3	B-3-1-C1	3705	2980	2.8	2964	7.1	21.8	15.5	5916	3550	2.54	0.63	1560	(s)B+(m)T+PT
	B-3-1-C2	3765	3277	2.6	3012	7.2	21.8	15.5	5916	3550	2.77	0.64	2215	(s)B+(s)T+PT
	B-3-2-C1	6581	6133	2.2	5265	6.9	21.8	15.5	5916	3557	3.14	1.11	5850	(m)B+(m)T+PT
	B-3-2-C2	6436	4503	1.6	5149	6.2	21.8	15.5	5916	3557	3.88	1.09	4291	(m)B+(m)T+NSF
	B-3-3-C1	6732	6505	2.5	5385	4.4	21.8	15.5	5916	3557	1.76	1.14	4371	NSF
	B-3-3-C2	6141	5321	1.2	4913	5.4	21.8	15.5	5916	3557	4.50	1.04	7018	NSF
Strap 2	B-2-1-C1	4082	2802	2.1	3265	6.7	24.5	20.5	7101	5106	3.19	0.57	3474	(m)T+PR
	B-2-1-C2	3877	2725	1.2	3101	7.4	24.5	20.5	7101	5106	6.17	0.55	4431	(s)T+PT
	B-2-2-C1	6618	6044	2.4	5294	8.5	24.5	20.5	7101	5106	3.54	0.93	6618	(m)B+(s)T+PT
	B-2-2-C2	6270	5701	1.8	5016	7.1	24.5	20.5	7101	5106	3.94	0.88	7600	(s)T+PT
	B-2-3-C1	7591	6092	1.2	6073	9.7	24.5	20.5	7101	5106	8.08	1.07	9201	(m)T+NSF
	B-2-3-C2	8301	7045	2.2	6641	13.6	24.5	20.5	7101	5106	6.18	1.17	10711	(m)T+NSF
Strap 4	B-4-2-C1	6730	3018	1.1	5384	6	38.5	33.9	11626	8584	5.45	0.58	2926	(m)T+PT
	B-4-2-C2	7036	4286	0.86	5629	6.85	38.5	33.9	11626	8584	7.97	0.61	4021	(m)T+PT
	B-4-3-C1	9924	8804	2.4	7939	6.7	38.5	33.9	11626	8584	2.79	0.85	7939	(m)B+(m)T+PT
	B-4-3-C2	9874	9185	2.3	7900	6.3	38.5	33.9	11626	8584	2.74	0.85	11285	(m)B+(m)T+PT
	B-4-4-C1	12956	11548	4.3	10364	15.2	38.5	33.9	11626	8584	3.53	1.11	6478	(m)T+NSF
	B-4-4-C2	13278	11208	2	10622	12.5	38.5	33.9	11626	8584	6.25	1.14	8852	(m)T+NSF

The cyclic test specimens exhibited similar failure modes to their corresponding monotonically tested specimens. As for the monotonically tested specimens, all the specimens with fewer screws (except Specimen A-3-2-C2) failed by combinations of bearing, tilting and eventual pull-out. There was one additional failure mode that occurred only in one of the type 2 solid strap and type B, 0.75mm cold-formed steel specimens, which was pull-over (see Figure 22). The strap curled up at the end and deformed around the hole before eventually pulling clear of the screw head. Pull over might be a result of the screw not having been fastened accurately, or there may some initial tearing at the hole in the strap due to imperfections in the strap caused during the assembly of the connection.



Figure 22. Pull-over Failure: Specimen B-2-1-C1

It should be noted that when considering the hysteresis curves for each specimen whilst the specimens were only subjected to positive extension, after plastic deformation began to take place in the specimen, residual strain occurred and so there was some small compression load on the specimen. When the specimen was returned to zero extension, the specimen had lengthened and therefore the stiffness of the specimens caused them to take the small compression loads. This behavior is shown in Figure 23.

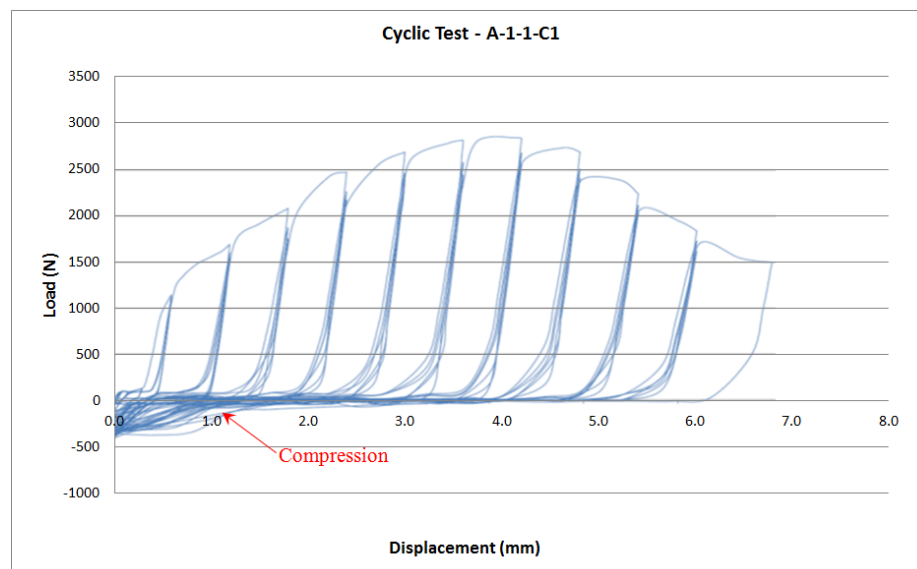


Figure 23. Compression Load in Cyclic Tests

The envelope of cyclic hysteresis curves showed similar relationships to the monotonic load-extension curves. The hysteresis curve presented in Figure 24 shows that the solid strap exhibited significant displacement before the ultimate load was reached.

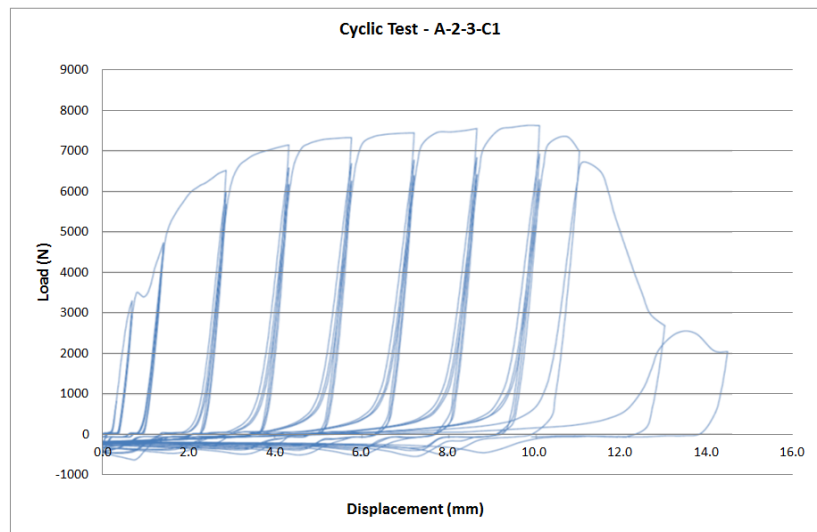


Figure 24. Hysteresis Curve for Solid Strap

In contrast Figure 25 shows that the load perforated strap dropped straight after yield as pull-out occurred. This behaviour was also shown in Figure 15 for a monotonic test on a perforated strap which failed by pull-out.

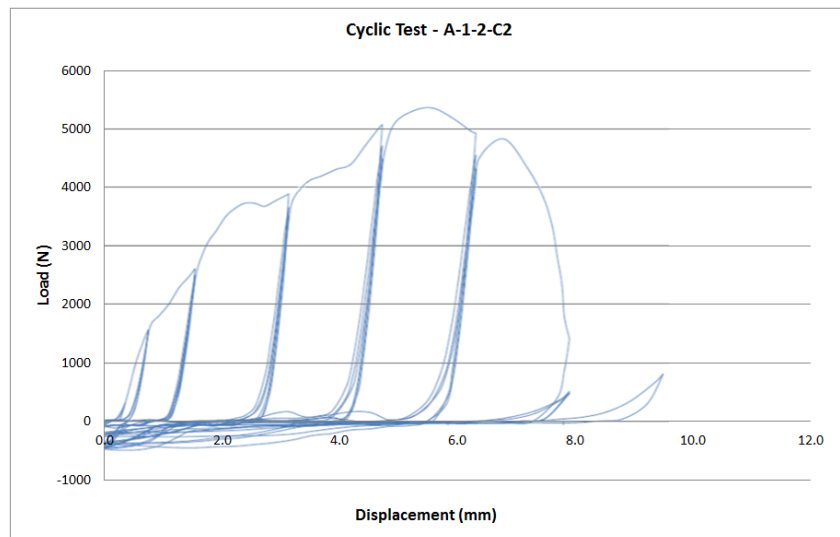


Figure 25. Hysteresis Curve for Perforated Strap

Table 7 presents a comparison between the monotonic and cyclic test results for the connections.

Table 7. Comparison of Monotonic and Cyclic Ultimate Loads (P_u)

		Number of Screws	P_u Monotonic Tests (N)	P_u Average of Cyclic Tests (N)	% Increase in P_u due to Cyclic Hardening
CFS Type A 0.55mm	Strap 1	1	1980	2387	0.21
		2	3820	4333	0.02
		3	4860	5040	0.04
	Strap 3	1	2130	2329	0.09
		2	3820	4353	0.25
		3	5260	4975	-0.05
	Strap 2	1	2260	2813	0.25
		2	4120	4283	0.04
		3	5600	5259	0.07
		4	6260	6277	0.00
	Strap 4	4	8440	8746	0.04
		5	9260	9617	0.04
		6	10430	10903	0.05
CFS Type B 0.75mm	Strap 1	1	3040	2933	-0.04
		2	5000	5104	0.02
		3	5410	5096	-0.06
	Strap 3	1	2680	2988	0.11
		2	5270	5207	-0.01
		3	5440	5149	-0.05
	Strap 2	1	3130	3183	0.02
		2	5020	5155	0.03
		3	6440	6357	-0.01
	Strap 4	2	5140	5507	0.07
		3	7380	7920	0.07
		4	10140	10493	0.04

A general trend which was exhibited by most of the strap bracing connections was that the maximum cyclic load for each connection was greater than the maximum monotonic load for the same connection type. This indicates that the strap bracing material underwent cyclic hardening as a result of the repeated loading which allowed the specimens to resist a slightly higher maximum load. There were a number of exceptions that occurred in the type 1 and 3 perforated strap connections, however this could be attributed to the variable nature of the perforated strap specimens, where there may have been more occurrences of the weaker perforation patterns in some specimens compared to the others. The cyclic hardening that did occur in specimens resulted in maximum load increases of less than 10% more than the maximum monotonic loads, which indicates that the hardening effect was small. The instances where the increase in load was significantly higher at around 20% were for connections with 1 or 2 screws in perforated strap material. The reason for this increase may be that there was some error involved in assembling the specimens, or because of the variability of the section of the perforated pattern which was included in each specimen.

In general the elastic shear stiffness was greater for the monotonic specimens for all strap types with the thicker 0.75mm cold-formed steel, and for the type 1 and 3 perforated straps with the 0.55mm cold-formed steel. The initial cycles in the cyclic tests appear to have reduced the stiffness of the specimens. The yielding factor R_f was similar for the monotonic and cyclic specimens; the specimens which experienced net section failure had exhibited some yielding leading up to failure and therefore had yielding factors which were above 1, and the specimens which failed in other modes generally had yielding factors which were less than 1.

Generally, the 0.75mm cold-formed steel increased the capacity of the strap bracing connections by 3-11% more than the 0.55mm cold-formed steel due to the increased anchorage of the connection. The maximum screw connections in the perforated straps had higher ductility ratios when connected to the 0.55mm cold-formed steel than the type 2 strap which had the same gross cross-sectional area (ignoring perforations), while in the 0.75mm cold-formed steel the opposite was true. However, for both the 0.75mm and the 0.55mm cold-formed steel connections the actual extension of the straps at ultimate strength was significantly higher for the type 2 solid strap material than both of the perforated strap materials.

Of the two perforated strap materials with the maximum number of screws: the type 3 strap had between 1% and 8% more capacity than the type 1 strap in the monotonic tests, and similar results for the cyclic tests. The type 3 strap also exhibited higher extensions at the ultimate load. In comparison to the perforated straps, the solid strap type 2 (of similar dimensions to the perforated straps) exhibited higher capacities which were approximately 18% more than those of the type 3 perforated straps in both thicknesses of cold formed steel. The type 2 strap also demonstrated greater extensions than the perforated straps at ultimate load.

The type 4 solid strap fastened with the maximum numbers of screws had ultimate capacities which were 67% and 57% higher than the ultimate capacities of the type 2 solid strap when connected to the 0.55mm and 0.75mm cold-formed steels, respectively. These increases in capacity are due to the significantly large cross-section of the type 4 strap. The type 4 straps demonstrated significantly higher extension at ultimate load in the 0.55mm cold-formed steel than of the type 2 solid strap, and similar extension in the 0.75mm cold-formed steel.

The slightly lower capacity and extension of the type 4 strap in the 0.75mm cold-formed steel compared to the 0.55mm cold-formed steel could possibly be increased by increasing the number of screws in the connection. However, net section would still be the limiting failure mode of the connection, and it is expected that the increases that could be obtained with extra screws would not be large, particularly with regards to the extension. Therefore the advantage of using fewer screws was deemed more efficient than the small increases that are to be gained in capacity. Finally the screw requirements and capacities of the connections are summarized below:

- The type 1 perforated strap bracing requires 3 screws in order to obtain the maximum capacity in the strap bracing system. When connected to the 0.55mm thick cold-formed steel (CFS) this connection has a capacity of 4.9kN, and when connected to 0.75mm CFS the capacity is 11% higher at 5.4kN.
- The type 3 perforated strap bracing requires 3 screws and has a capacity of 5.3kN when connected to 0.55mm CFS, and a capacity which is 3% higher when connected to 0.75mm CFS at 5.4kN.
- The type 2 solid strap bracing requires 4 screws in the pattern specified in Section 4.2. When connected to the 0.55mm CFS these connections have a capacity of 6.3kN, and a capacity which is 3% higher when connected to 0.75mm CFS.

- The type 4 solid strap bracing requires 6 screws when it is connected to 0.55mm CFS, and 4 screws when it is connected to 0.75mm CFS. The 4-screw connection to the 0.75mm CFS has 3% less capacity than the 6-screw connection to the 0.55mm CFS.

On the following, the capacities for the connections calculated based on the design codes (AS/NZS 4600 [9], AISI-S100 [23] and Eurocode3 [24]) will be compared with the capacities found from the experimental results.

Table 8. Strap Bracing Experimental Capacities Compared to Design Capacities from AS/NZS4600 (N)

		Screws number	Pu Monotonic Tests	Net-Section Tension Failure		Bearing Failure		Tear-out - strap		Pull-out		Pull-over		Limiting Factored Design Capacity	Related Failure Mode
				N _t	φ N _t	V _b	φ V _b	V _{fv}	φ V _{fv}	N _{ou}	φ N _{ou}	N _{ov}	φ N _{ov}		
CFS Type A 0.55mm	Strap 1	1	1980	1536	999	2317	1158	2714	1629	1385	693	2443	1221	693	PT
		2	3820	3764	2447	4633	2317	5429	3257	2770	1385	4886	2443	1385	PT
		3	4860	3596	2337	6950	3475	8143	4886	4155	2078	7329	3664	2078	PT
	Strap 3	1	2130	1699	1104	2317	1158	2997	1798	1385	693	2697	1349	693	PT
		2	3820	4176	2715	4633	2317	5994	3596	2770	1385	5395	2697	1385	PT
		3	5260	4185	2720	6950	3475	8991	5395	4155	2078	8092	4046	2078	PT
	Strap 2	1	2260	2443	1588	2317	1158	3648	2189	1385	693	3283	1642	693	PT
		2	4120	6007	3904	4633	2317	7296	4377	2770	1385	6566	3283	1385	PT
		3	5600	6007	3904	6950	3475	10944	6566	4155	2078	9849	4925	2078	PT
	Strap 4	4	6260	6007	3904	9267	4633	14591	8755	5540	2770	13132	6566	2770	PT
		4	8440	6007	3904	9267	4633	17165	10299	5540	2770	15448	7724	2770	PT
CFS Type B 0.75mm	Strap 1	5	9260	10099	6564	11584	5792	21456	12874	6926	3463	19310	9655	3463	PT
		6	10430	10099	6564	13900	6950	25747	15448	8311	4155	23172	11586	4155	PT
	Strap 3	1	3040	1536	999	2332	1166	2714	1629	1802	901	2443	1221	901	PT
		2	5000	3764	2447	4664	2332	5429	3257	3605	1802	4886	2443	1802	PT
		3	5410	3596	2337	6996	3498	8143	4886	5407	2704	7329	3664	2337	NSF
	Strap 3	1	2680	1699	1104	2543	1272	2997	1798	1802	901	2697	1349	901	PT
		2	5270	4176	2715	5086	2543	5994	3596	3605	1802	5395	2697	1802	PT
		3	5440	4185	2720	7630	3815	8991	5395	5407	2704	8092	4046	2704	PT
	Strap 2	1	3130	2443	1588	3152	1576	3648	2189	1802	901	3283	1642	901	PT
		2	5020	6007	3904	6303	3152	7296	4377	3605	1802	6566	3283	1802	PT
		3	6440	6007	3904	9455	4728	10944	6566	5407	2704	9849	4925	2704	PT
	Strap 4	2	5140	3022	1964	7041	3520	8582	5149	3605	1802	7724	3862	1802	PT
		3	7380	10099	6564	10561	5280	12874	7724	5407	2704	11586	5793	2704	PT
		4	10140	10099	6564	14081	7041	17165	10299	7209	3605	15448	7724	3605	PT

Table 9. Strap Bracing Experimental Capacities Compared to Design Capacities from the AISI-S100 [23] (N)

		Screws number	Pu Monotonic Tests	Bearing Failure		Tear-out - strap		Pull-out		Pull-over		Limiting Factored Design Capacity	Related Failure Mode
				V _b	φ V _b	V _{fv}	φ V _{fv}	N _{ou}	φ N _{ou}	N _{ov}	φ N _{ov}		
CFS Type A 0.55mm	Strap 1	1	1980	2317	1158	2714	1357	1385	693	2443	1221	693	PT
		2	3820	4633	2317	5429	2714	2770	1385	4886	2443	1385	PT
		3	4860	6950	3475	8143	4072	4155	2078	7329	3664	2078	PT
	Strap 3	1	2130	2317	1158	2997	1499	1385	693	2697	1349	693	PT
		2	3820	4633	2317	5994	2997	2770	1385	5395	2697	1385	PT
		3	5260	6950	3475	8991	4496	4155	2078	8092	4046	2078	PT
	Strap 2	1	2260	2317	1158	3648	1824	1385	693	3283	1642	693	PT
		2	4120	4633	2317	7296	3648	2770	1385	6566	3283	1385	PT
		3	5600	6950	3475	10944	5472	4155	2078	9849	4925	2078	PT
	Strap 4	4	6260	9267	4633	14591	7296	5540	2770	13132	6566	2770	PT
		4	8440	9267	4633	17165	8582	5540	2770	15448	7724	2770	PT
		5	9260	11584	5792	21456	10728	6926	3463	19310	9655	3463	PT
		6	10430	13900	6950	25747	12874	8311	4155	23172	11586	4155	PT

CFS Type B D 0.75mm	Strap 1	1	3040	2345	1173	2714	1357	1802	901	2443	1221	901	PT
		2	5000	4690	2345	5429	2714	3605	1802	4886	2443	1802	PT
		3	5410	7036	3518	8143	4072	5407	2704	7329	3664	2704	PT
	Strap 3	1	2680	2589	1295	2997	1499	1802	901	2697	1349	901	PT
		2	5270	5179	2589	5994	2997	3605	1802	5395	2697	1802	PT
		3	5440	7768	3884	8991	4496	5407	2704	8092	4046	2704	PT
	Strap 2	1	3130	3152	1576	3648	1824	1802	901	3283	1642	901	PT
		2	5020	6303	3152	7296	3648	3605	1802	6566	3283	1802	PT
		3	6440	9455	4728	10944	5472	5407	2704	9849	4925	2704	PT
	Strap 4	2	5140	7041	3520	8582	4291	3605	1802	7724	3862	1802	PT
		3	7380	10561	5280	12874	6437	5407	2704	11586	5793	2704	PT
		4	10140	14081	7041	17165	8582	7209	3605	15448	7724	3605	PT

Table 10. Strap Bracing Experimental Capacities Compared to Design Capacities from Eurocode3 [24] (N)

		Screws number	Pu Monotonic Tests	Net-Section Tension Failure		Bearing Failure		Pull-out		Pull-over				Limiting Design Capacity (not including cyclic pullover)	Related Failure Mode
				N _t	ϕ N _t	V _b	ϕ V _b	N _{ou}	ϕ N _{ou}	Static		Cyclic			
										N _{ov}	ϕ N _{ov}	N _{ov}	ϕ N _{ov}		
CFS Type A 0.55mm	Strap 1	1	1980	3764	3011	1824	1459	733	587	1629	1303	814	651	587	PT
		2	3820	3596	2877	3648	2919	1467	1173	1629	1303	814	651	1173	PT
		3	4860	3596	2877	5472	4378	2200	1760	1629	1303	814	651	1303	PR
	Strap 3	1	2130	4176	3341	2014	1611	733	587	1798	1439	899	719	587	PT
		2	3820	4185	3348	4028	3222	1467	1173	1798	1439	899	719	1173	PT
		3	5260	4185	3348	6042	4834	2200	1760	1798	1439	899	719	1439	PR
	Strap 2	1	2260	6007	4805	2451	1961	733	587	2189	1751	1094	875	587	PT
		2	4120	6007	4805	4903	3922	1467	1173	2189	1751	1094	875	1173	PT
		3	5600	6007	4805	7354	5883	2200	1760	2189	1751	1094	875	1751	PR
		4	6260	6007	4805	9805	7844	2933	2347	2189	1751	1094	875	1751	PR
	Strap 4	4	8440	10099	8079	11535	9228	2933	2347	2575	2060	1287	1030	2060	PR
		5	9260	10099	8079	14418	11535	3666	2933	2575	2060	1287	1030	2060	PR
		6	10430	10099	8079	17302	13842	4400	3520	2575	2060	1287	1030	2060	PR
CFS Type B 0.75mm	Strap 1	1	3040	3764	3011	1824	1459	954	763	1629	1303	814	651	763	PT
		2	5000	3596	2877	3648	2919	1908	1527	1629	1303	814	651	1303	PR
		3	5410	3596	2877	5472	4378	2863	2290	1629	1303	814	651	1303	PR
	Strap 3	1	2680	4176	3341	2014	1611	954	763	1798	1439	899	719	763	PT
		2	5270	4185	3348	4028	3222	1908	1527	1798	1439	899	719	1439	PR
		3	5440	4185	3348	6042	4834	2863	2290	1798	1439	899	719	1439	PR
	Strap 2	1	3130	6007	4805	2451	1961	954	763	2189	1751	1094	875	763	PT
		2	5020	6007	4805	4903	3922	1908	1527	2189	1751	1094	875	1527	PT
		3	6440	6007	4805	7354	5883	2863	2290	2189	1751	1094	875	1751	PR
	Strap 4	2	5140	10099	8079	5767	4614	1908	1527	2575	2060	1287	1030	1527	PT
		3	7380	10099	8079	8651	6921	2863	2290	2575	2060	1287	1030	2060	PR
		4	10140	10099	8079	11535	9228	3817	3053	2575	2060	1287	1030	2060	PR

It is necessary to mention that all edge distance and spacing requirements of the standards were satisfied except for in the perforated straps where there pre-existing perforations governed screw arrangements. Although the screws did increase the size of the holes from 3mm to 4.8mm, if the screws were not placed in the existing holes the net area would have been further reduced as there would be the pre-existing holes plus the additional screw holes. For the pattern of the pre-existing holes as was present in both of the perforated straps used for this study, there is no space to add holes for more than one individual screw where the extra holes will not decrease the net area of the strap and therefore weaken the strap.

The result tables show that the test specimen capacities exceed the nominal design capacities for all three of the standards considered. For the design calculations in this paper, the bearing and tilting capacities calculated for all three standards were assumed to increase directly with number of screws. That is, a connection with three screws is calculated to have the bearing capacity of one screw multiplied by three. Although this assumption was made, it is known that this is unconservative; however a more accurate relationship is not known. The design bearing capacities calculated by AS/NZS4600 and AISI are the same for most specimens, and the only differences vary by less than 3% for the strap types 1 and 2 connected to the 0.75mm cold-formed steel when AS/NZS includes a bearing capacity factor which applies to these specimens. Eurocode3 is less conservative and predicts significantly higher values (more than 50%) for factored bearing capacity. It is difficult to compare the design capacities with the experimental failure loads for this mode of failure as although many specimens exhibited bearing and tilting, it was never the ultimate failure mode. This makes hard to determine the load at which bearing first occurred. AS/NZS4600 and the AISI Specification specified factored bearing capacities for many of the tested specimens that were below the ultimate load capacity of the specimen. This is a true indication of the bearing and tilting behavior that had occurred in the specimens. The higher bearing values from Eurocode3 exceed the ultimate loads for some specimens which prove the standard is highly unconservative when predicting this type of failure mode capacity.

Similarly for pull-out and pull-over failures, a direct relationship was assumed between the number of screws and the design resistance to these failure modes. This also assumes the load is distributed evenly among the screws. The pull-over provisions are included from all three standards, however as there was only one case of pull-over which occurred in all of the monotonic and cyclic specimens tested, this design capacities as calculated for this failure mode are not discussed in detail here. For AS/NZS4600 and the AISI Specification the pull-over and pull-out capacities are calculated using the same equations and for the connections considered in this study, pull-out is the governing design capacity of the two for all cases. This is a true indication of the pull-out failures which occurred in most connections with insufficient screws for net section failure to occur. Eurocode3 conversely predicts more similar pull-over values as a result of its provisions' dependence on the pitch of the screw threads. Consequently, Table 10 shows that this standard often predicts that pull-over is the governing failure mode for the connections, which is inaccurate.

For net section tension failure, the unfactored capacities will be compared here but it should be noted that the AS/NZS4600 reduction factor of 0.65 is significantly more conservative than Eurocode3's factor of 0.8. The unfactored net section capacities predicted by AS/NZS4600 are reduced for single screwed connections, but for the remaining multiple screw connections, the capacities are the same as those given by Eurocode3. For the solid straps the standards accurately predict unfactored net section failure capacities which are greater than the ultimate capacities for the specimens which failed by eventual pull-out, and only slightly less than ultimate capacities which did fail by net section failure. The predicted capacities for the perforated straps are less accurate, particularly for the specimens which had two screws which was one less than the three required for net section failure to occur in all perforated strap specimens. The inaccuracy of these predictions can be attributed to the variable net section of the perforated straps.

Although these design provisions have some value in predicting some of the behaviors for screwed connections, there are some provisions which are not entirely suited to accurately predicting the ultimate behavior of the strap bracing connections tested for this research. Hancock [6] states that 'the provisions are intended for use when a sufficient number of test results is not available for the particular application, (and that) a higher degree of accuracy can be obtained by testing any particular application'. Therefore the recommended capacities for the strap bracing connections will be based on the experimental results.

As discussed earlier, the pattern of the screws was chosen in order to obtain satisfy the requirements of AS4100 provisions for the net section tension capacity of a member as best as possible with the given straps sizes and screw dimensions, but different patterns were not tested to completely optimize this design. This pattern selection was not further optimized because it was proven in by LaBoube and Sokol [19] that the effect of optimizing the pattern is very small in increasing the strength of the connection.

7. CONCLUSIONS AND RECOMMENDATIONS

The capacities of the screwed strap bracing connections are taken as the monotonic capacities found for each connection. These capacities were compared to the cyclic capacities of each connection and it was found that in general the cyclic capacities were higher than the monotonic values. Therefore it is a conservative approach to design wall bracing systems to the monotonic capacities. The required number of screws to obtain the maximum capacity of the strap materials, and the value of the ultimate load capacity of each connection based on monotonic tests are summarized in Table 11.

Table 11- Number of screws required, and the capacity of the connections for each type of strap bracing material based on monotonic tests

CFS Type	Strap Type	Number of Screws Required	P _u (kN)	Δ _u (mm)
Type A 0.55mm	Strap 1 G3 Perforated 30mm*0.75mm	3	4.86	6.9
	Strap 3 G2 Perforated 30mm*0.75mm	3	5.26	11.6
	Strap 2 G2 Solid 30mm*0.75mm	4	6.26	17.5
	Strap 4 G2 Solid 40mm*1.0mm	6	10.43	27.9
Type B 0.75mm	Strap 1 G3 Perforated 30mm*0.75mm	3	5.41	6.9
	Strap 3 G2 Perforated 30mm*0.75mm	3	5.44	7.1
	Strap 2 G2 Solid 30mm*0.75mm	3	6.44	11
	Strap 4 G2 Solid 40mm*1.0mm	4	10.14	10.7

According to the current research results, following conclusions can be made:

- The 0.75mm cold-formed steel increased the capacity of the strap bracing connections by 3-11% more than the 0.55mm cold-formed steel for the straps types 1, 2 and 3, due to the increased anchorage of the connection. The slight reduction in capacity of the type 4 strap can be attributed to the fewer screws used in the connections to 0.75mm cold-formed steel.
- For both the 0.75mm and the 0.55mm cold-formed steel connections the extension of the straps at ultimate strength was significantly higher for the type 2 solid strap material than both of the perforated strap materials.

- Of the two perforated strap materials which had the same dimensions: the type 3 G2 strap would be recommended for use rather than type 1 G3 strap due to its increased capacity and ductility.
- In comparison to the perforated straps the solid strap type 2 exhibited capacities which were higher than those of the type 3 perforated straps when connected to both thicknesses of cold formed steel. The type 2 strap also demonstrated greater extensions than the perforated straps at ultimate load.
- The type 4 solid strap fastened with the maximum numbers of screws had significantly higher capacities than the type 2 solid strap due to its greater cross-sectional area. The type 4 straps demonstrated significantly higher extension at ultimate load in the 0.55mm cold-formed steel than of the type 2 solid strap, and similar extension in the 0.75mm cold-formed steel. The lower extension of the type 4 strap connected to the 0.75mm cold-formed steel can be attributed to the lower number of screws used in this connection.
- Another strap type which would be worth consideration is solid G3 strap material. Although the perforated G3 strap (type 1) had less capacity than the perforated G2 strap, the strength properties of the G3 sheet material indicate that it is expected to have significantly different yield and ultimate strengths, which may result in more ductile behaviour than was exhibited by the solid G2 strap in this research as the G2 material has very similar yield and ultimate strengths. The perforations in the G3 strap tested for this study would have significantly affected the performance of the material, particularly in relation to the ultimate capacity of the material due to the reduction in net cross-sectional area. Therefore it is recommended that solid G3 strap material be tested and compared to the materials tested in this paper.
- The application of these particular strap types for the bracing systems will depend on the required capacity and ductility of the system. The solid straps exhibited higher extensions before their ultimate failure than the perforated straps, and therefore they may be preferred in areas where there is the potential for significant cyclonic or seismic events which may impose large deflections on the wall framing system.
- The limited area for the strap to be connected to the wall framing system may mean that it is not practical to use the number of screws recommended here. This could be a particular problem when using the thicker and wider type 4 strap material with 0.55mm cold-formed steel framing, as it requires 6 screws for adequate anchorage of the strap. Further investigation is recommended in order to quantify the maximum available area to which the straps can be fastened, and therefore the maximum number of screws which can be used to anchor the straps and satisfy the minimum edge and spacing requirements specified by AS/NZS4600.

REFERENCES

- [1] Kim, T.-W., Wilcoski, J., Foutch, D.A. and Lee, M.S., "Shake Table Tests of a Cold-formed Steel Shear Panel", *Engineering Structures*, 2006, Vol. 28, pp. 1462-1470.
- [2] Moghimi, H. and Ronagh, H.R., "Performance of Light-gauge Cold-formed Steel Strap-braced Stud Walls subjected to Cyclic Loading", *Engineering Structures*, 2009, Vol. 31, pp. 69-83.
- [3] Zeynalian, M. and Ronagh, H., "Experimental Study on Seismic Performance of Strap-braced Cold-formed Steel Shear Walls", *Advances in Structural Engineering*, 2013, Vol. 16, pp. 245-257.
- [4] Zeynalian, M. and Ronagh, H.R., "A Numerical Study on Seismic Performance of Strap-braced Cold-formed Steel Shear Walls", *Thin-Walled Structures*, 2012, Vol. 60, pp. 229-238.
- [5] Yu, W.-W. and LaBoube, R.A., "Cold-formed Steel Design", John Wiley & Sons, 2010.

- [6] Hancock, G.J., Murray, T. and Ellifrit, D.S., "Cold-formed Steel Structures to the AISI Specification", CRC Press, 2001.
- [7] Hancock, G.J., "Design of Cold-formed Steel Structures: To Australian/New Zealand Standard AS/NZS 4600", Australian Institute of Steel Construction, 1998.
- [8] Rogers, C.A. and Hancock, G.J., "Screwed Connection Tests of Thin G550 and G300 Sheet Steels", *Journal of Structural Engineering*, 1999, Vol. 125, pp. 128.
- [9] AS/NZS4600, "Cold-formed Steel Structures", Australian Building Codes Board, 2005.
- [10] Adham, S.A., Avanessian, V., Hart, G.C., Anderson, R., Elmlinger, W.J. and Gregory, J., "Shear Wall Resistance of Lightgauge Steel Stud Wall Systems", *Earthquake Spectra*, 1990, Vol. 6, pp. 1-14.
- [11] Hatami, S., Ronagh, H. and Ashari, M., "Behavior of Thin-strap-braced Cold-formed Steel Frames under Cyclic Loads", *Proceedings of Fifth International Conference on Thin-Walled Structures*, Queensland University of Technology, 2008, pp. 363-370.
- [12] Fiorino, L., Della Corte, G. and Landolfo, R., "Experimental Tests on Typical Screw Connections for Cold-formed Steel Housing", *Engineering Structures*, 2007, Vol. 29, pp. 1761-1773.
- [13] Lennon, R., Pedreschi, R. and Sinha, B., "Comparative Study of Some Mechanical Connections in Cold Formed Steel", *Construction and Building Materials*, 1999, Vol. 13, pp. 109-116.
- [14] Peterman, K.D., Nakata, N. and Schafer, B.W., "Hysteretic Characterization of Cold-formed Steel Stud-to-sheathing Connections", *Journal of Constructional Steel Research*, 2014, Vol. 101 pp. 254-264.
- [15] Buildex Co., "Self-Drilling Screws, Fasteners & Rivets", 2006, Victoria, Australia.
- [16] Quickframe Steel Frames Pty Ltd, "Steel Frame Fixing Manual", 2007, Australia.
- [17] BlueScope Co., "Complete Distribution Product Guide, Version 3", 2009, Australia.
- [18] AS/NZS4100, "Steel Structure, AS/NZS 4100", Australian Building Codes Board, 2012.
- [19] LaBoube, R. and Sokol, M., "Behavior of Screw Connections in Residential Construction", *Journal of Structural Engineering*, 2002, Vol. 128, pp. 115-118.
- [20] Zeynalian, M. and Ronagh, H.R. "An Experimental Investigation on the Lateral Behavior of Knee-braced Cold-formed Steel Shear Walls", *Thin-Walled Structures*, 2012, Vol. 51, pp. 64-75.
- [21] Zeynalian, M., Shelley, A. and Ronagh, H.R., "An Experimental Study into the Capacity of Cold-formed Steel Truss Connections", *Journal of Constructional Steel Research*, 2016, Vol. 127 pp. 176-186.
- [22] ASTM-E2126-07, "Standard Test Methods for Cyclic (reversed) Load Test for Shear Resistance of Walls for Buildings", 2007, USA.
- [23] AISI, "North American specification for the Design of Cold-formed Steel Structural Members", American Iron and Steel Institute, 2012, Washington, D.C.
- [24] Eurocode3, "Design of Steel Structures. Part 1-3, General Rules - Supplementary Rules for Cold-formed Members and Sheeting", European Committee for Standardization, 2001, Dublin.

SHEAR LAG FACTORS FOR TENSION ANGLES WITH UNEQUAL-LENGTH LONGITUDINAL WELDS

J. Kent Hsiao^{1,*} and Saurav Shrestha²

¹*Professor, Department of Civil and Environmental Engineering,
Southern Illinois University Carbondale, Carbondale, IL, USA*

²*Former Graduate Student, Department of Civil and Environmental Engineering,
Southern Illinois University Carbondale, Carbondale, IL, USA*

**(Corresponding author: Email: hsiao@engr.siu.edu)*

Received: 18 June 2017; Revised: 18 June 2017; Accepted: 19 October 2017

ABSTRACT: When a tension load is transmitted to some, but not all of the cross-sectional elements of a tension member, the tensile force is not uniformly distributed over the cross-sectional area of the tension member. The non-uniform stress distribution in the tension member is commonly referred to as the out-of-plane shear lag effect. The unequal-length longitudinal welds and the in-plane shear lag effect, however, are not addressed by the current American Institute of Steel Construction (AISC) Specification for the determination of the shear lag factors for tension members other than plates and Hollow Structural Sections (HSS). The purpose of this work is to propose a procedure for the computation of shear lag factors accounting for combined in-plane and out-of-plane shear lag effects on unequal-length longitudinal welded angles. The finite element method using three-dimensional solid elements and nonlinear static analyses accounting for combined material and geometric nonlinearities are conducted in this work to verify the accuracy of the proposed procedure.

Keywords: Angle sections, connections, finite element method, geometric nonlinearity, nonlinear analysis, shear lag, stress distribution, welds

DOI: 10.18057/IJASC.2018.14.4

1. INTRODUCTION

The provisions regarding shear lag effects in bolted tension members appeared in the 1978 American Institute of Steel Construction (AISC) Specification (Easterling and Gonzalez [1]; AISC [2]). The 1986 and 1989 AISC Specifications have extended the provisions to welded tension members (AISC [3]; AISC [4]). The 1993 and 1999 AISC Specifications expressed the shear lag provisions using the formula $U = 1 - (\bar{x} / L) \leq 0.9$ for the tension load transmitted only by longitudinal welds to a tension member other than a plate member, where U is the shear lag coefficient, \bar{x} is the connection eccentricity, and L is the length of the connection in the directions of loading (AISC [5]; AISC [6]). The upper limit of 0.9 has been removed in the 2005 and 2010 AISC Specifications (AISC [7]; AISC [8]).

The provisions specified in the current AISC Specification (AISC [8]) only address the out-of-plane shear lag effects for all tension members except plates while the in-plane shear lag effects have been neglected. When a tension load is transmitted to some, but not all of the cross-sectional elements of a tension member other than a plate member, the tensile force is not uniformly distributed over the cross-sectional area of the tension member. The non-uniform stress distribution in the tension member is commonly referred to as the out-of-plane shear lag effect.

Referring to the tension member shown in Figure 1, when the tension load is transmitted to some, but not all of the cross-sectional elements, the effective length of the welded connection is reduced to $L' = L - \bar{x}$, where \bar{x} is the connection eccentricity measured from the plane of the connection to

the member centroid and L is the length of the connection in the direction of loading. Since the reduction in the effective cross-sectional area is proportional to the reduction in the effective connection length, L' / L , the out-of-plane shear lag factor becomes (Geschwindner [9]):

$$U_{OE} = \frac{L'}{L} = \frac{L - \bar{x}}{L} = 1 - \frac{\bar{x}}{L} \quad (1)$$

Therefore, the value of the out-of-plane shear lag factor is influenced by the length of the connection and the geometry of the cross-section of the tension member.

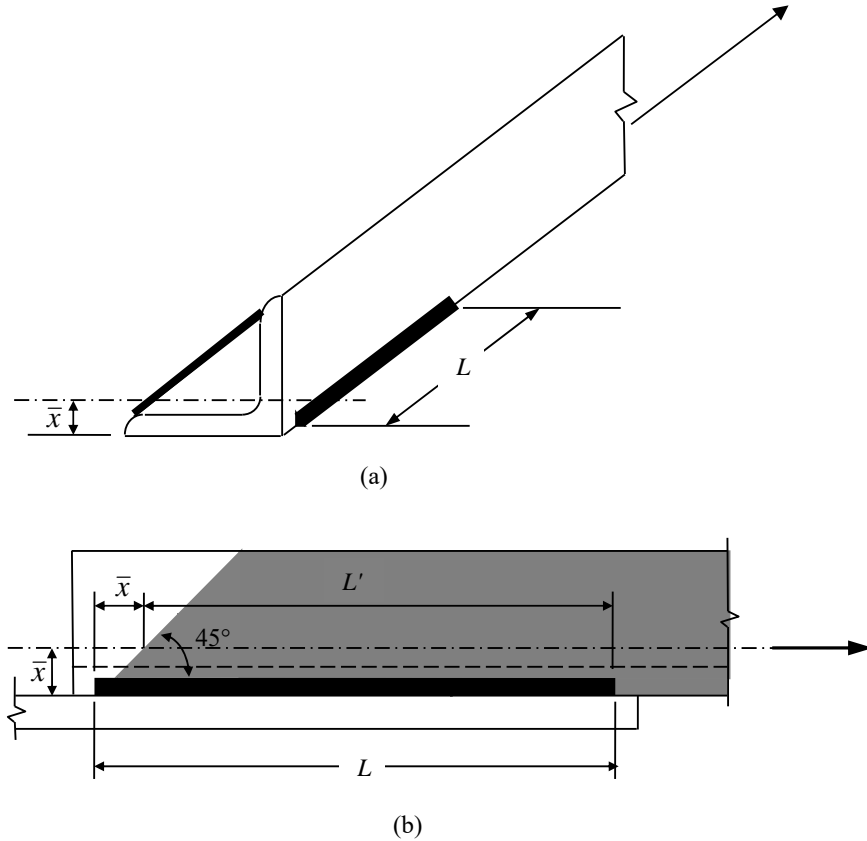


Figure 1. Out-of-Plane Shear Lag Effect on Welded Angle in Tension

In addition to the out-of-plane shear lag effect for unconnected (outstanding) element(s), the in-plane shear lag effect, U_{CE} , for connected element(s) was also recommended to be considered, as given in Eq. 2 (Fortney and Thornton [10]):

$$U_{CE} = \frac{1}{1 + \frac{1}{3} \left(\frac{w}{L} \right)^2} \quad (2)$$

where w = the distance between longitudinal welds and L = the length of weld.

The combined effect of the in-plane and out-of-plane shear lags can be approximately determined as the product of the two component effects as given in Eq. 3 (Fortney and Thornton [10]):

$$U = U_{CE}U_{OE} = \left(\frac{1}{1 + \frac{1}{3} \left(\frac{w}{L} \right)^2} \right) \left(1 - \frac{\bar{x}}{L} \right) \quad (3)$$

2. NEWLY PROPOSED PROCEDURE FOR THE COMPUTATION OF SHEAR LAG FACTORS

The following addresses a new computation procedure for shear lag factors for tension angles with unequal-length longitudinal fillet welds. Referring to Figure 2, when the width of the welded leg is shorter than the indented distance of the short weld length, [that is, $w \leq (L_1 - L_2)/2$], the out-of-plane shear lag effect on the out-of-plane leg can also be applied to the in-plane leg. Therefore, the in-plane shear lag effect, U_{CE} , for the connected leg can be computed using Eq. 4:

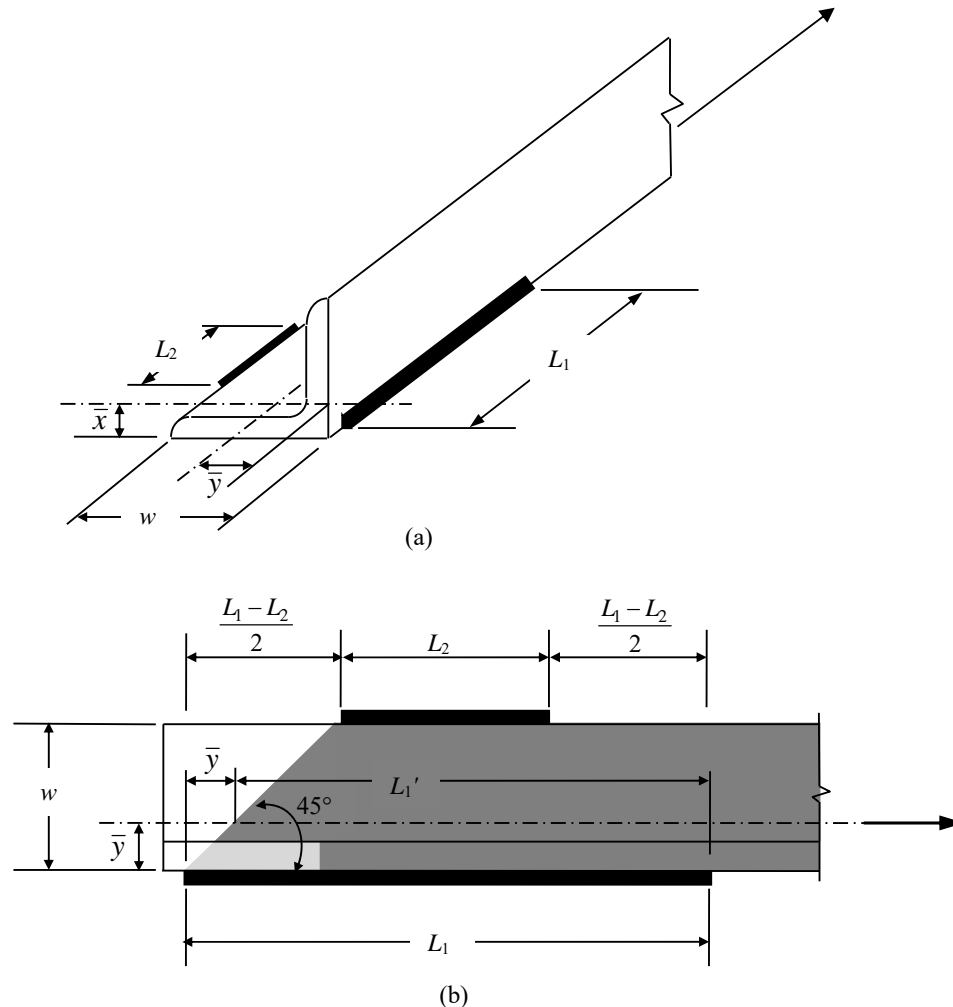


Figure 2. In-Plane Shear Lag Effect on a Tension Angle with Unequal-Length Welds

$$U_{CE} = \frac{L'_1}{L_1} = \frac{L_1 - \bar{y}}{L_1} = 1 - \frac{\bar{y}}{L_1} \quad (4)$$

The combined effect of the in-plane and out-of-plane shear lags can be approximately determined as the product of the two component effects, as given in Eq. 5:

$$U = U_{CE}U_{OE} = \left(1 - \frac{\bar{y}}{L_1}\right) \left(1 - \frac{\bar{x}}{L_1}\right) \quad (5)$$

where \bar{x} = the distance from the outer face of the connected leg to the centroid of the angle; \bar{y} = the distance from the outer face of the outstanding leg to the centroid of the angle; and L_1 = the length of the longer weld.

3. DESIGN PROCEDURE FOR A TENSION MEMBER TO A GUSSET PLATE CONNECTION

The following are the recommended criteria to be used for the design of a tension member to a gusset plate connection (Astaneh-Asl [11]) using longitudinal fillet welds:

- (1) The capacity of the welded connection is recommended to be at least equal to or greater than the axial tension yield capacity of the tension member calculated using a conservative expected yield stress of $1.1 R_y F_y$ in order to avoid brittle failure of the connections, where R_y is the ratio of the expected yield strength to the specified minimum yield strength of the grade of steel to be used [$R_y = 1.5$ for ASTM A36 steel channels (AISC [12])] and F_y is the specified minimum yield strength of the grade of steel to be used.
- (2) The yielding of the tension member shall occur before the yielding of the gusset plate in order to increase the global ductility of the entire frame:

$$R_y F_y A_g \leq F_y A_e \quad (6)$$

where A_g is the cross-sectional area of the tension member and A_e is the area of the Whitmore effective section of the gusset plate.

- (3) The design tensile strength for the tensile rupture in the net section of the tension member is recommended to be computed using the following equation (AISC [8]):

$$\phi_t P_n = \phi_t F_u A_n U \quad (7)$$

where $\phi_t = 0.75$; P_n = nominal tensile strength of the tension member; F_u = specified minimum tensile strength of the type of steel being used [$F_u = 58$ ksi (400 MPa) for ASTM A36 steel]; A_n = net area; and U = shear lag factor.

4. DESIGN EXAMPLE OF THE LONGITUDINAL WELDS BALANCED ABOUT THE NEUTRAL AXIS OF AN ANGLE IN TENSION

Use A36 steel, E70 electrodes to design the longitudinal side fillet welds to develop the full axial yield capacity of a 2L4×3× $\frac{3}{8}$ LLBB (with long legs back-to-back) tension member connected to a gusset plate. Assume that the tension member is subjected to cyclic loading which results in repeated stress variations; therefore, it is preferable to use two longitudinal welds of unequal length to ensure the welds' centroid will coincide with the centroid of the member so that the transmitted tensile forces will be balanced about the neutral axis of the tension angle (AISC [8]).

4.1 Design of the Unequal-Length Longitudinal Fillet Weld Connection to Balance the Tensile Forces about the Neutral Axis of the Tension Angle

The full axial yield capacity of a L4×3× $\frac{3}{8}$ tension member can be computed as follows:

$$1.1 R_y F_y A_g = 1.1 (1.5)(36 \text{ ksi})(2.49 \text{ in}^2) = 147.9 \text{ kips (658 kN)}$$

where $R_y = 1.5$ and $F_y = 36 \text{ ksi (248 MPa)}$ for A36 steel; A_g = the gross area of the tension member.

Assume that the gusset plate is thicker than the angle. In this case, since the material thickness of the thinner part joined is $\frac{3}{8}$ in. (10 mm), the minimum weld size = $\frac{3}{16}$ in. (5 mm) (AISC [8]). Also, since the thickness of the angle is $\frac{3}{8}$ in. (10 mm), the maximum weld size = $\frac{3}{8} - \frac{1}{16} = \frac{5}{16}$ in. (8 mm) (AISC [13]). With the minimum and maximum fillet weld sizes defined, one can use a size of $\frac{1}{4}$ in. (6 mm) for the fillet weld (since $\frac{3}{16} \leq \frac{1}{4} \leq \frac{5}{16}$, the weld size may be used). The design strength of the weld per inch can thus be computed as follows:

$$\phi t_e (0.60 F_{EXX}) = 0.75 [(0.707) (\frac{1}{4} \text{ in.})](0.60)(70 \text{ ksi}) = 5.568 \text{ kips/in. (0.975 kN/mm)}$$

where t_e = the effective throat of the fillet weld and F_{EXX} = the tensile strength of the weld metal ($F_{EXX} = 70 \text{ ksi}$ for E70 electrodes).

Therefore, the total required weld length can be computed as follows:

$$L_{total} = \frac{147.9 \text{ kips}}{5.568 \text{ kips/in.}} = 26.56 \text{ in. (675 mm)}$$

Referring to Figure 3(a), taking the moment about point A to determine the force P_2 and P_1 :

$$P_2 (4 \text{ in.}) = (147.9 \text{ kips}) (1.27 \text{ in.})$$

$$\text{From which, } P_2 = \frac{(147.9)(1.27)}{4} = 47.0 \text{ kips (209 kN), and } P_1 = 147.9 - 47.0 = 100.9 \text{ kips (449 kN)}$$

Therefore, the required weld length on the outstanding leg side, L_1 , and on the flat leg side, L_2 , can be computed respectively as follows:

$$L_1 = \frac{100.9}{5.568} = 18.12 \text{ in.} \approx 18.5 \text{ in. (470 mm)}$$

$$L_2 = \frac{47.0}{5.568} = 8.44 \text{ in.} \approx 8.5 \text{ in. (216 mm)}$$

The connection details of the unequal-length longitudinal fillet welds for the angle are shown in Figure 3(b). Note that fillet weld terminations should be located approximately one weld size from the edge of the connection to minimize notches in the base metal (AISC [8]).

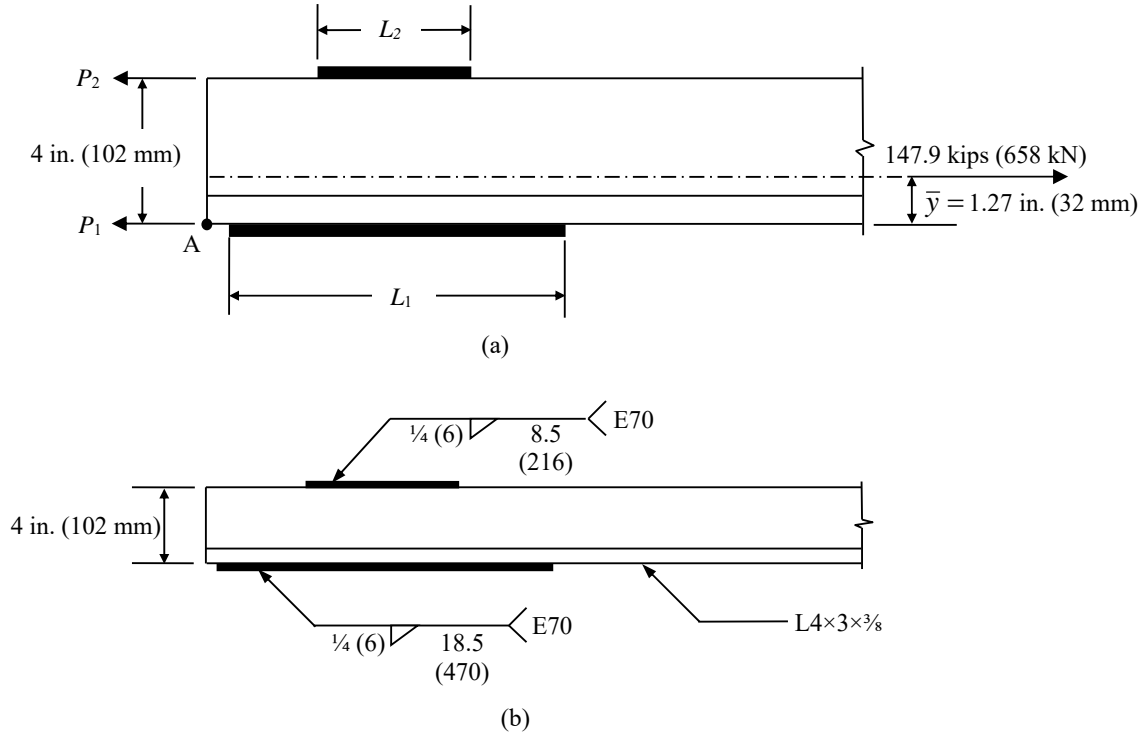


Figure 3. Unequal-Length Longitudinal Fillet Weld Connection for the L4×3× $\frac{3}{8}$ Tension Member

4.2 Design of the Gusset Plate

Using Eq. 6, one has:

$$1.5(36 \text{ ksi})(2)(2.49 \text{ in}^2) \leq (36 \text{ ksi})(A_e)$$

From which, the area of the Whitmore effective section, A_e , must be $\geq 7.47 \text{ in}^2$ (4819 mm²).

Note that in order to avoid the out-of-plane eccentricity effect on the gusset plate (due to one angle being connected to one side of the gusset plate), two L4×3× $\frac{3}{8}$ angles, with long legs back-to-back, are used as the tension member for this design example.

Referring to Figures 3 and 4, the effective width of the Whitmore section (Whitmore [14]) can be computed to be:

$$l_w = (8.5 \text{ in.})(\tan 30^\circ) + (18.5 \text{ in.})(\tan 30^\circ) + 4 \text{ in.} = 19.59 \text{ in. (498 mm)}$$

From which, the required thickness of the gusset plate can be computed to be:

$$t = \frac{A_e}{l_w} = \frac{7.47}{19.59} = 0.381 \text{ in. [use } 7/16 \text{ in. (11 mm)]}$$

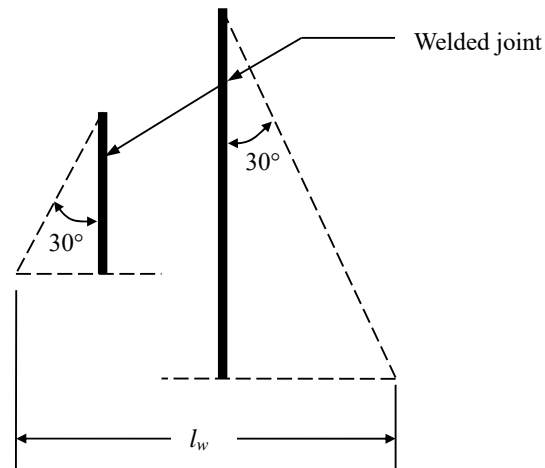
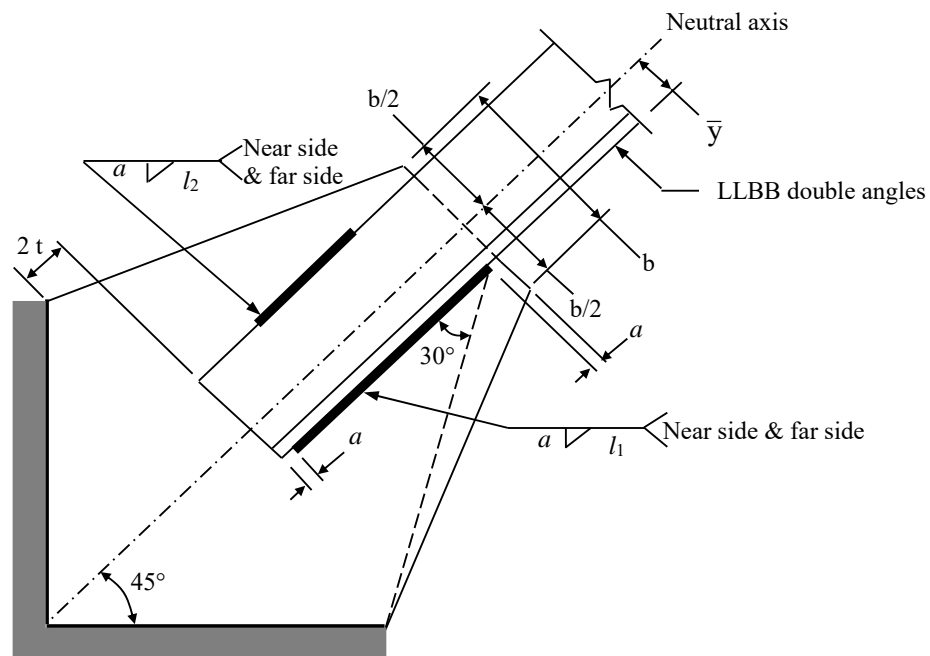


Figure 4. The Whitmore Section for Unequal-Length Welded Joints



Notes: t = Plate thickness; a = Weld size; l_1 = Long weld length; and l_2 = Short weld length

LLBB Double Angles	\bar{y} in. (mm)	b in. (mm)	t in. (mm)	a in. (mm)	l_1 in. (mm)	l_2 in. (mm)
2L4×3× ³ / ₈	1.27 (32)	6 (152)	⁷ / ₁₆ (11)	¹ / ₄ (6)	18.5 (470)	8.5 (216)
2L6×3½× ³ / ₈	2.02 (51)	8 (203)	⁷ / ₁₆ (11)	¹ / ₄ (6)	24.5 (622)	12.5 (318)
2L6×4× ⁹ / ₁₆	2 (51)	8 (203)	⁵ / ₈ (16)	³ / ₈ (10)	25.5 (648)	13 (330)

Figure 5. Unequal-Length Longitudinal Fillet Weld Connection Details for Double Angles

Following the procedure of this design example, the unequal-length longitudinal fillet weld connections for two additional double angles of different sizes ($2L6 \times 3\frac{1}{2} \times \frac{3}{8}$ and $2L6 \times 4 \times \frac{9}{16}$) are designed and summarized in Figure 5. Note that in order to ensure that the gusset plate can freely rotate when the double angles are subjected to compression forces, the distance from the end of the double angles to the line that connects the two re-entrant corners of the gusset plate is at least two times the thickness of the gusset plate (Astaneh-Asl [11]).

5. COMPUTATION OF SHEAR LAG FACTORS FOR TENSION ANGLES WITH UNEQUAL-LENGTH LONGITUDINAL FILLET WELD CONNECTIONS

5.1 The AISC Procedure

Since the unequal-length longitudinal welds and the in-plane shear lag effect are not addressed by the current AISC Specification (AISC [8]) for the determination of shear lag factors for tension members other than plates and Hollow Structural Sections (HSS), the following formula may be used for the computation of the U value for the given example, $2L4 \times 3 \times \frac{3}{8}$, shown in Figure 3.

$$U_{AISC} = U_{OE} = 1 - \frac{\bar{x}}{L}$$

The above formula results in three different U values, depending upon which of the follow three L values are used for this formula:

$$(1) \text{ For } L = l_1, U_{AISC(l_1)} = 1 - \frac{\bar{x}}{l_1} = 1 - \frac{0.775}{18.5} = 0.96$$

$$(2) \text{ For } L = \frac{l_1 + l_2}{2}, U_{AISC(ave)} = 1 - \frac{\bar{x}}{\left(\frac{l_1 + l_2}{2}\right)} = 1 - \frac{0.775}{13.5} = 0.94$$

$$(3) \text{ For } L = l_2, U_{AISC(l_2)} = 1 - \frac{\bar{x}}{l_2} = 1 - \frac{0.775}{8.5} = 0.91$$

Following the same procedure, the U values for two additional double angles of different sizes ($2L6 \times 3\frac{1}{2} \times \frac{3}{8}$ and $2L6 \times 4 \times \frac{9}{16}$ shown in Figure 5) are computed. All the results are summarized in Table 1.

5.2 The Fortney and Thornton Procedure

Fortney and Thornton [10] recommended that Eq. 3 be used for the computation of the U values for angles with unequal-length longitudinal welds. Also, $L = (l_1 + l_2)/2$ was recommended to be used for this formula. Using Eq. 3, the U value of the given example, $2L4 \times 3 \times \frac{3}{8}$, shown in Figure 3, can be computed to be:

$$U_{F\&T} = \left(\frac{1}{1 + \frac{1}{3} \left(\frac{w}{\left(\frac{l_1 + l_2}{2} \right)} \right)^2} \right) \left(1 - \frac{\bar{x}}{\left(\frac{l_1 + l_2}{2} \right)} \right) = \left(\frac{1}{1 + \frac{1}{3} \left(\frac{4}{13.5} \right)^2} \right) \left(1 - \frac{0.775}{13.5} \right) = 0.92$$

Following the same procedure, the U values for two additional double angles of different sizes ($2L6 \times 3\frac{1}{2} \times \frac{3}{8}$ and $2L6 \times 4 \times \frac{9}{16}$ shown in Figure 5) are computed. All the results are summarized in Table 2.

5.3 The New Procedure Proposed in this Paper

Eq. 5 is the newly proposed procedure that may also be used for the computation of the U values for angles with unequal-length longitudinal welds. Using Eq. 5, the U value of the given example, $2L4 \times 3 \times \frac{3}{8}$, shown in Figure 3 [in which $w = 4$ in. $\leq (L_1 - L_2)/2 = 5$ in.] can be computed to be:

$$U_{New} = U_{CE}U_{OE} = \left(1 - \frac{\bar{y}}{l_1} \right) \left(1 - \frac{\bar{x}}{l_1} \right) = \left(1 - \frac{1.27}{18.5} \right) \left(1 - \frac{0.775}{18.5} \right) = 0.89$$

Since both two additional double angles ($2L6 \times 3\frac{1}{2} \times \frac{3}{8}$ and $2L6 \times 4 \times \frac{9}{16}$) shown in Figure 5 satisfy the condition of $w \leq (L_1 - L_2)/2$, the U values for both of them can be computed using Eq. 5. The results are summarized in Table 3.

Table 1. Shear Lag Factors Derived from the AISC Specification

$U_{AISC} = U_{OE} = 1 - \frac{\bar{x}}{L}$			
LLBB Double Angles	$2L4 \times 3 \times \frac{3}{8}$	$2L6 \times 3\frac{1}{2} \times \frac{3}{8}$	$2L6 \times 4 \times \frac{9}{16}$
Shear lag factors $U_{AISC(l_1)}$	0.96	0.97	0.96
Shear lag factors $U_{AISC(avg)}$	0.94	0.96	0.95
Shear lag factors $U_{AISC(l_2)}$	0.91	0.94	0.92

Notes: $L = l_1$ for the computation of $U_{AISC(l_1)}$

$L = \frac{l_1 + l_2}{2}$ for the computation of $U_{AISC(avg)}$

$L = l_2$ for the computation of $U_{AISC(l_2)}$

Table 2. Shear Lag Factors Derived from Fortney and Thornton

$U_{F\&T} = U_{CE}U_{OE} = \left(\frac{1}{1 + \frac{1}{3} \left(\frac{w}{L} \right)^2} \right) \left(1 - \frac{\bar{x}}{L} \right)$			
LLBB Double Angles	2L4×3× ³ / ₈	2L6×3½× ³ / ₈	2L6×4× ⁹ / ₁₆
Shear lag factors $U_{F\&T}$	0.92	0.93	0.92

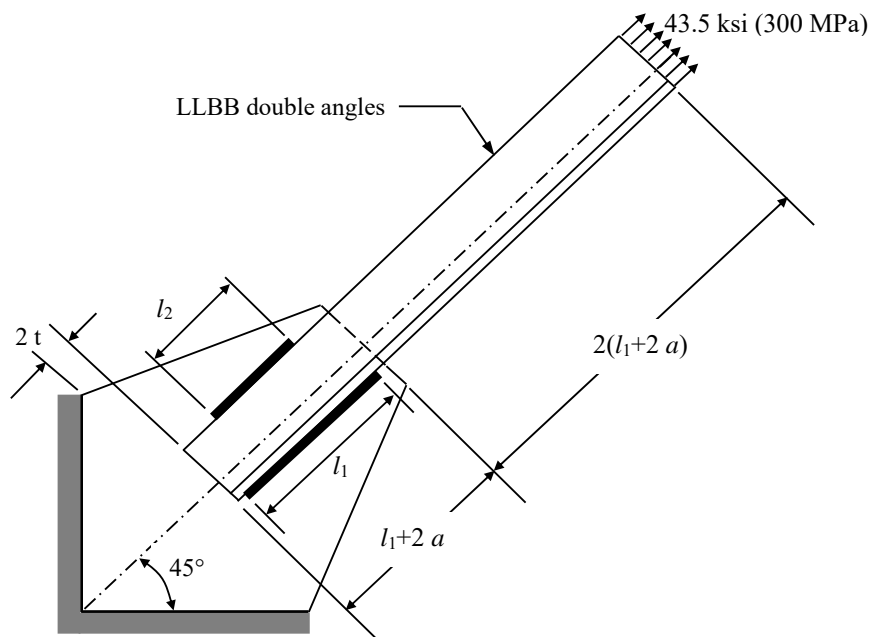
Note: $L = \frac{l_1 + l_2}{2}$ for the computation of $U_{F\&T}$

Table 3. Shear Lag Factors Derived from the Newly Proposed Formula

$U_{New} = U_{CE}U_{OE} = \left(1 - \frac{\bar{y}}{l_1} \right) \left(1 - \frac{\bar{x}}{l_1} \right)$			
LLBB Double Angles	2L4×3× ³ / ₈	2L6×3½× ³ / ₈	2L6×4× ⁹ / ₁₆
Shear lag factors U_{New}	0.89	0.89	0.89

6. COMPUTATION OF SHEAR LAG FACTORS USING THE FINITE ELEMENT METHOD

The finite element method using three-dimensional solid elements and nonlinear static analyses accounting for combined material and geometric nonlinearities are conducted in this work to verify the accuracy of the newly proposed procedure. Figure 6 illustrates the typical length of the tension angles and the applied tensile stress to be used for the construction of the computer models for the finite element analyses using the computer software NISA (NISA [15]).



Notes: t = Plate thickness; a = Weld size; l_1 = Long weld length; and l_2 = Short weld length

Figure 6. Typical Length of the Tension Angles and the Applied Tensile Stress at the 100th Time Step

The computer models for the finite element analyses are composed of numerous 8-node hexahedron and 6-node wedge elements. The material properties of the tension angles are: Modulus of elasticity = 29×10^6 psi (200,000 MPa) and Poisson's ratio = 0.3. The analyses account for material nonlinearities based on the elastic, piecewise linear hardening true stress-strain curve, as shown in Figure 7 (derived from Salmon and Johnson [16]) for the A36 steel for tension angles and the elastic, linear hardening, true stress-strain, as shown in Figure 8 (derived from the Lincoln Electric Company [17]) for the E7018 electrode for the longitudinal fillet welds. Therefore, the true stress of 68.73 ksi (474 MPa) and its corresponding strain of 0.1697, as shown in Figure 7, are derived from the engineering stress of 58 ksi (400 MPa) (which is the ultimate tensile stress of A36 steel) and its corresponding strain of 0.185.

A pseudo time of 100 has been used for the time span, which is equivalent to load increments or steps from zero to $\phi_t F_u$. Note that F_u is the ultimate tensile stress of the tension member. Also note that since the first-principal stress is related to fracturing (Cook and Young [18]), there is a critical time step at which the true maximum first-principal stress in the tension angles is closest to 68.73 ksi (474 MPa) (the true ultimate tensile stress). Assuming the i^{th} time step is the critical time step, the allowable applied tensile load at the free end of the tension angles can thus be determined as follows:

$$\text{Allowable applied tensile load} = \phi_t (F_u) (A_g) [(i^{\text{th}} \text{ time step}) / (100 \text{ time steps})] \quad (8)$$

Note that $\phi_t F_u = 0.75 \times 58 \text{ ksi} = 43.5 \text{ ksi}$ (300 MPa) for A36 steel is used as the applied tensile stress at the 100th time step as shown in Figure 6. Also, A_g is the gross area of the cross-section of the tension member.

Since $A_n = A_g$ for welded tension members, Eq. 9 is then derived from Eqs. 7 and 8:

$$U = (i^{\text{th}} \text{ time step}) / (100 \text{ time steps}) \quad (9)$$

where U is the shear lag factor and the i^{th} time step is the critical time step.

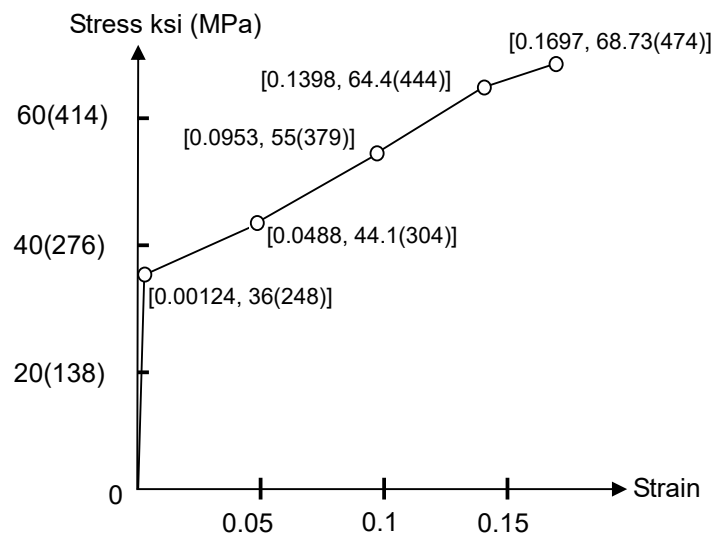


Figure 7. Elastic, Piecewise Linear Hardening, True Stress-Strain Curve for ASTM A36 Steel

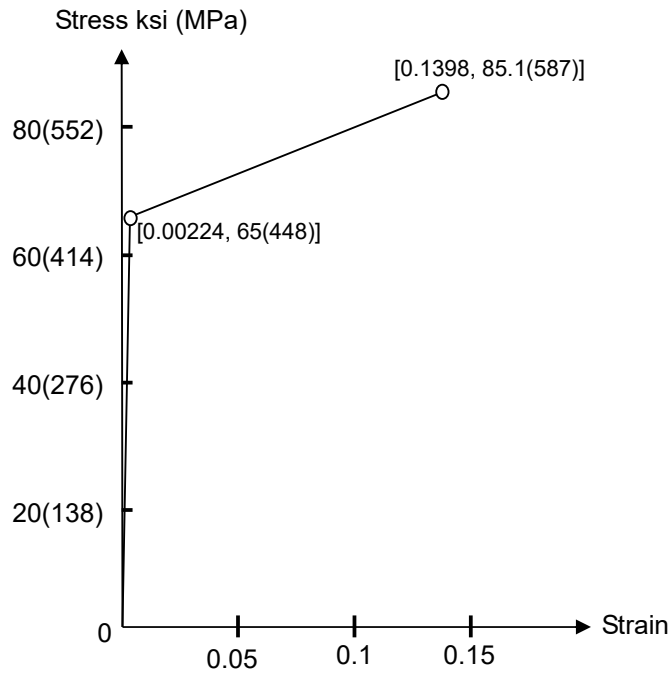


Figure 8. Elastic, Linear Hardening, True Stress-Strain Curve for E7018 Electrode

The results of the finite element analysis for the double angles $2L4 \times 3 \times \frac{3}{8}$ are shown in Figures 9, 10, 11, and 12. Figure 9 illustrates that at the 90th time step, the maximum first-principal stress reaches 68.84 ksi (475 MPa) [which is closest to the true ultimate tensile strength of 68.73 ksi (474 MPa)] at the cross-sectional area of the double angles close to the free end of the gusset plate. Therefore, the 90th time step is the critical time step for the $2L4 \times 3 \times \frac{3}{8}$ tension member. Furthermore, from Eq. 9, one has $U = 90/100 = 0.90$ for the $2L4 \times 3 \times \frac{3}{8}$ tension member. Figure 10 is a view from the side of the long weld, which illustrates the contour lines of the maximum shear stress distribution at the critical time step for the $2L4 \times 3 \times \frac{3}{8}$ tension member. The approximate 45° contour lines of the shear stress distribution at the end of the outstanding leg validate the out-of-plane shear lag effect on the outstanding leg shown in Figure 1. Figure 11 is an overhead view of the contour lines of the maximum shear stress distribution at the critical time step for the $2L4 \times 3 \times \frac{3}{8}$ tension member. The approximate 45° contour lines of the shear stress distribution at the end of the connected leg also validate the in-plane shear lag effect on the connected leg shown in Figure 2. Figure 12 illustrates the combined in-plane and out-of-plane shear lag effects on the tension angles.

The results of the finite element analysis for the two additional double angles of different sizes ($2L6 \times 3\frac{1}{2} \times \frac{3}{8}$ and $2L6 \times 4 \times \frac{9}{16}$ shown in Figure 5) are shown in Figures 13 and 14, respectively. Both the figures (Figures 13 and 14) illustrate that at the 90th time step, the maximum first-principal stress reaches a critical magnitude [which is closest to the true ultimate tensile strength of 68.73 ksi (474 MPa)] at the cross-sectional area of the double angles close to the free end of the gusset plate. Therefore, the 90th time step is the critical time step for the $2L6 \times 3\frac{1}{2} \times \frac{3}{8}$ and $2L6 \times 4 \times \frac{9}{16}$ tension members. The U values for all the double tension angles determined using the finite element analysis approach are summarized in Table 4.

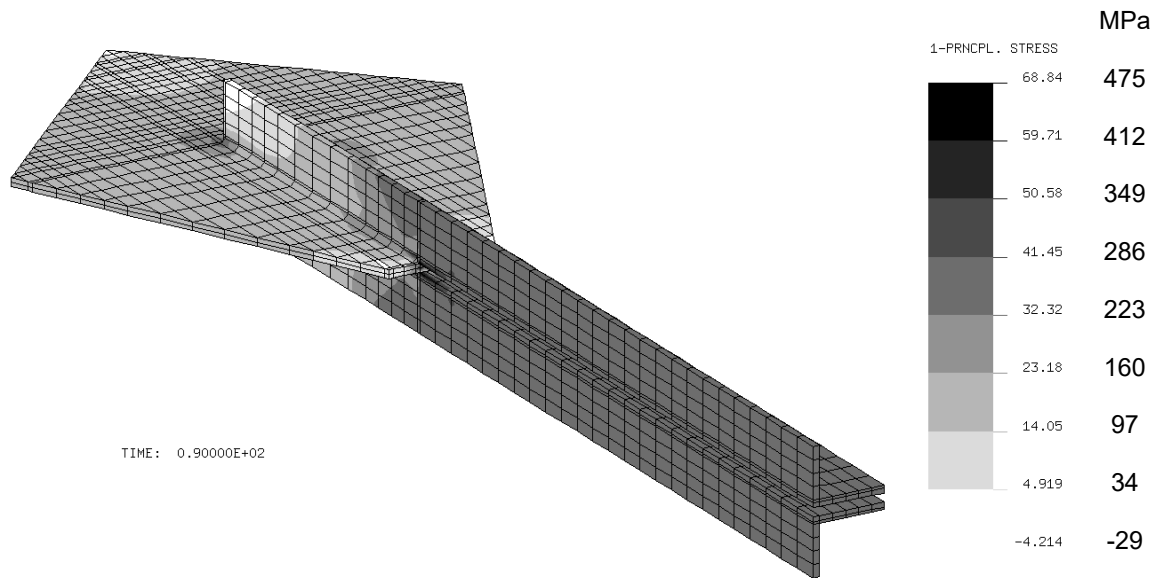


Figure 9. The First-Principal Stress Distribution at the Critical Time Step for the $2L4 \times 3 \times \frac{3}{8}$ Tension Member

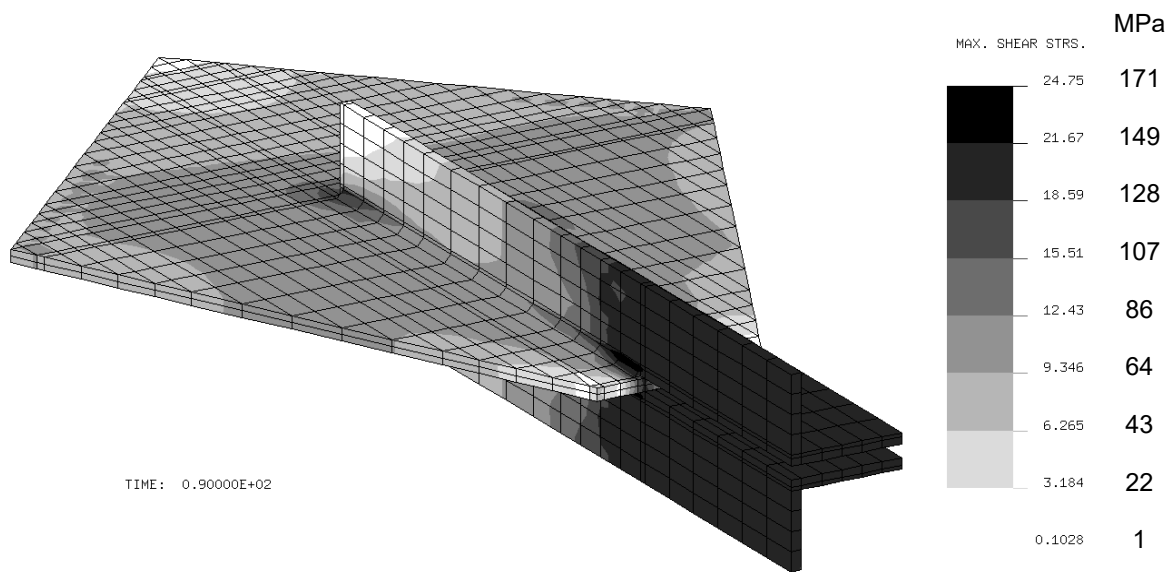


Figure 10. The Maximum Shear Stress Distribution at the Critical Time Step for the $2L4 \times 3 \times \frac{3}{8}$ Tension Member (a View from the Side of the Long Weld)

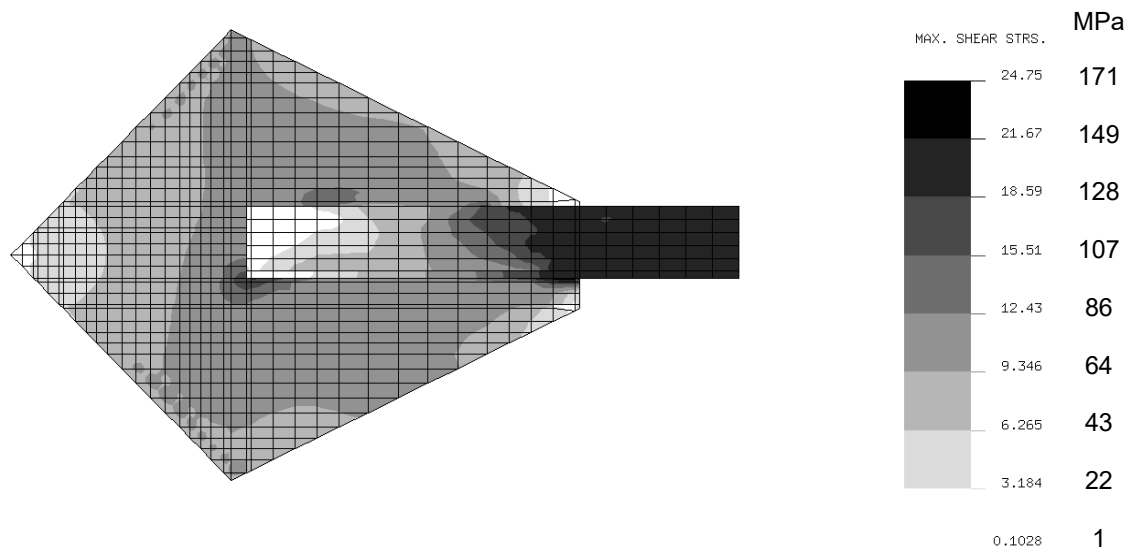


Figure 11. The Maximum Shear Stress Distribution at the Critical Time Step for the $2L4 \times 3 \times \frac{3}{8}$ Tension Member (an Overhead View)

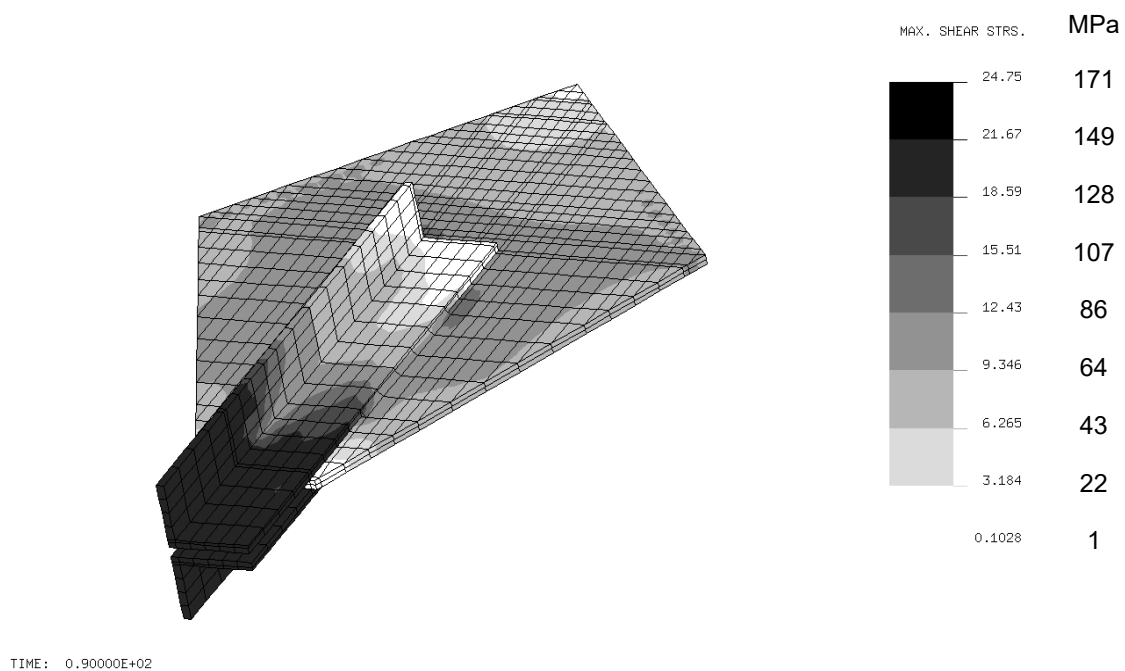


Figure 12. The Maximum Shear Stress Distribution at the Critical Time Step for the $2L4 \times 3 \times \frac{3}{8}$ Tension Member (a View from the Side of the Short Weld)

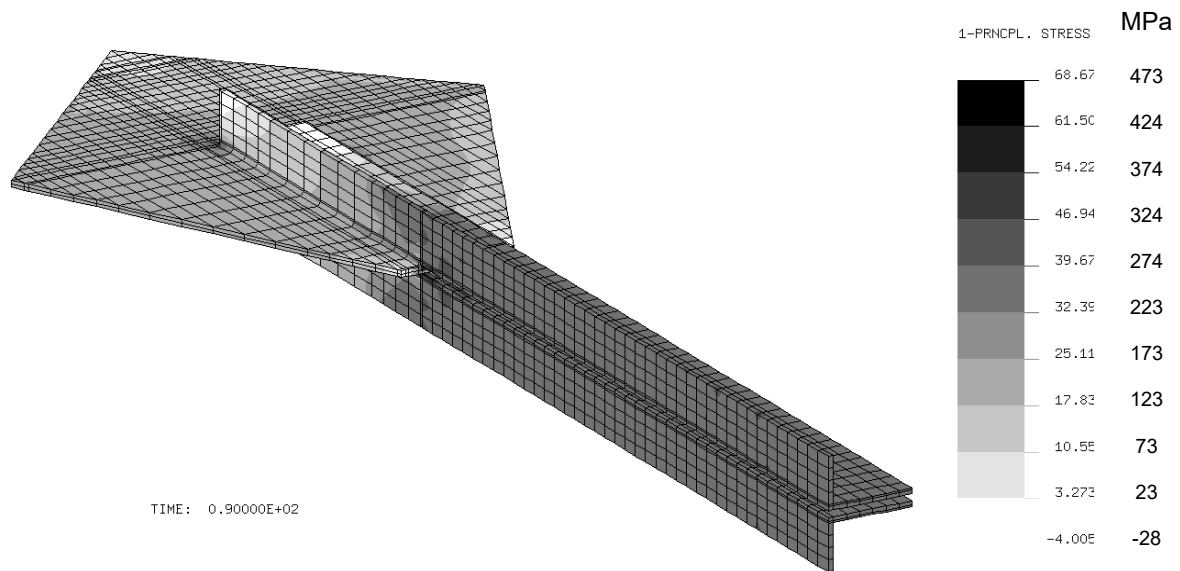


Figure 13. The First-Principal Stress Distribution at the Critical Time Step for the $2L6 \times 3\frac{1}{2} \times \frac{3}{8}$ Tension Member

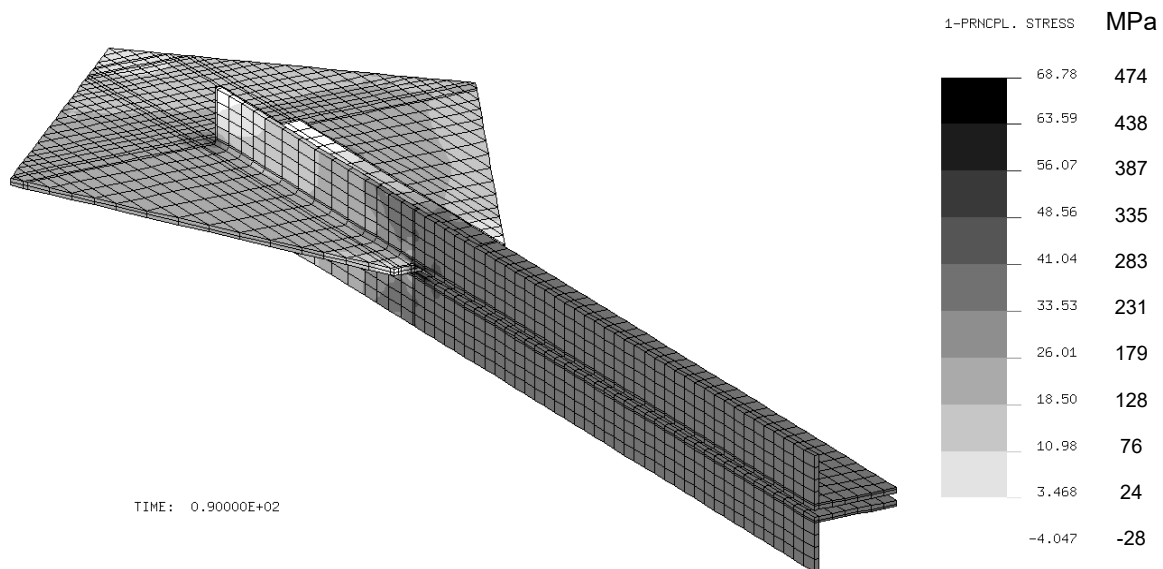
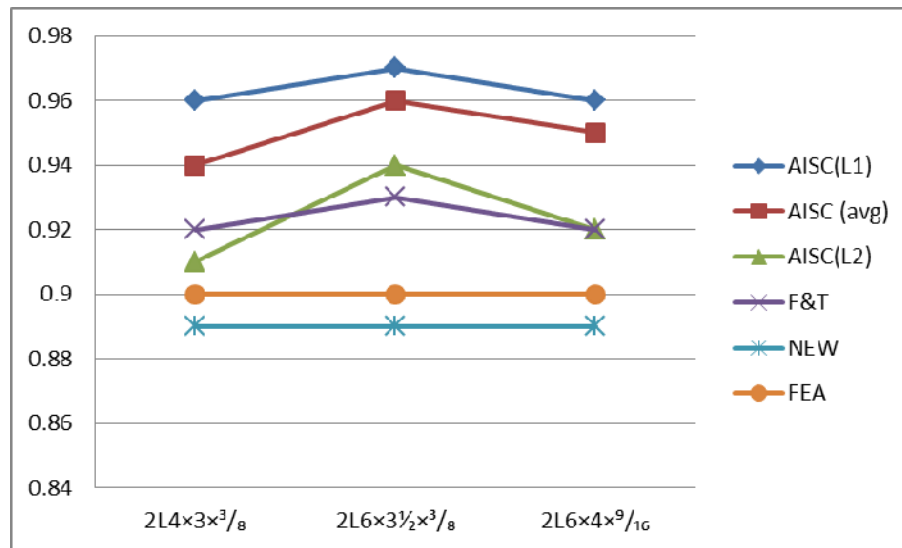


Figure 14. The First-Principal Stress Distribution at the Critical Time Step for the $2L6 \times 4 \times \frac{9}{16}$ Tension Member

Table 4. Shear Lag Factors Derived from the Finite Element Analysis Approach

LLBB Double Angles	$2L4 \times 3 \times^3/8$	$2L6 \times 3 \frac{1}{2} \times^3/8$	$2L6 \times 4 \times^9/16$
Shear lag factors U_{FEA}	0.90	0.90	0.90

A summary of the shear lag factors (U) determined using various approaches is graphically shown in Figure 15. This figure combines the results obtained from Tables 1 through 4. Figure 15 shows that among all the approaches, the newly proposed approach gives the results closest to those obtained using the Finite Element Analysis approach.

Figure 15. A Summary of the Shear Lag Factors (U) Determined Using Various Approaches

7. CONCLUSIONS

When a tension angle is subjected to cyclic loading, which results in repeated stress variations, it is preferable to use two longitudinal welds of unequal length to ensure the welds' centroid will coincide with the centroid of the angle so that the transmitted tensile forces will be balanced about the neutral axis of the angle. The unequal-length longitudinal welds, however, are not addressed by the current AISC Specification for the determination of the shear lag factor for tension members other than plates and Hollow Structural Sections (HSS). In addition, the current AISC Specification neglects the in-plane shear lag effect for the determination of the shear lag factors for tension members other than plates and HSS. A new procedure for the computation of shear lag factors accounting for combined in-plane and out-of-plane shear lag effects on unequal-length longitudinal welded angles is proposed in this work. The finite element method using three-dimensional solid elements and nonlinear static analyses accounting for combined material and geometric nonlinearities are conducted in this work to verify the accuracy of the proposed procedure. This work concludes that among all the approaches discussed in this paper, the newly proposed approach gives the results closest to those obtained using the Finite Element Analysis approach. However, the newly proposed approach can only be applied when $(l_1 - l_2)/2 \geq w$, where $(l_1 - l_2)/2$ is the indented length at both ends of the short weld, in which l_1 is the length of the long weld and l_2 is the length of the short weld, and w is the width of the in-plane welded leg of the angle.

REFERENCES

- [1] Easterling, W.S. and Gonzalez Giroux, L., "Shear Lag Effects in Steel Tension Members", Engineering Journal, American Institute of Steel Construction, 3rd Quarter, 1993, Vol. 30, pp. 77-89.
- [2] AISC, "Specification for the Design, Fabrication and Erection of Structural Steel for Buildings", American Institute of Steel Construction, Inc., Chicago, IL., 1978.
- [3] AISC, "Specification for Structural Steel Buildings-Load and Resistance Factor Design", American Institute of Steel Construction, Inc., Chicago, IL., 1986.
- [4] AISC, "Specification for Structural Steel Buildings-Allowable Stress Design and Plastic Design", American Institute of Steel Construction, Inc., Chicago, IL., 1989.
- [5] AISC, "LRFD Specification for Structural Steel Buildings", American Institute of Steel Construction, Inc., Chicago, IL., 1993.
- [6] AISC, "LRFD Specification for Structural Steel Buildings", American Institute of Steel Construction, Inc., Chicago, IL., 1999.
- [7] AISC, "Specification for Structural Steel Buildings", American Institute of Steel Construction, Inc., Chicago, IL., 2005.
- [8] AISC, "Specification for Structural Steel Buildings", American Institute of Steel Construction, Inc., Chicago, IL., 2010.
- [9] Geschwindner, L.F., "Unified Design of Steel Structures", John Wiley & Sons, Inc., Upper Hoboken, N.J., 2008.
- [10] Fortney, P.J. and Thornton, W.A., "Recommendations for Shear Lag Factors for Longitudinally-Welded Tension Members", Engineering Journal, American Institute of Steel Construction, 1st Quarter, 2012, pp. 11-32.
- [11] Astaneh-Asl, A., "Seismic Behavior and Design of Gusset Plates," Steel Tips Report, Structural Steel Educational Council, Moraga, CA., 1998.
- [12] AISC, "Seismic Provisions for Structural Steel Buildings", American Institute of Steel Construction, Inc., Chicago, IL., 2005.
- [13] AISC, "Steel Construction Manual", 14th Edition, American Institute of Steel Construction, Inc., Chicago, IL., 2011.
- [14] Whitmore, R.E., "Experimental Investigation of Stresses in Gusset Plates", Bulletin No. 16, Engineering Experiment Station, Univ. of Tennessee, TN., 1952.
- [15] NISA, "NISA User's Manual", the Cranes Software, Inc., Troy, MI, 2005.
- [16] Salmon, C.G., Johnson, J.E. and Malhas F.A., "Steel Structures, Design and Behavior", 5th Ed., Pearson Prentice Hall, Upper Saddle River, N.J., 2009.
- [17] The Lincoln Electric Company, "The Procedure Handbook of Arc Welding", 13th Ed., The Lincoln Electric Company, Cleveland, OH., 1994.
- [18] Cook, R.D. and Young, W.C., "Advanced Mechanics of Materials", Macmillan Publishing Company, New York, N.Y., 1985.

STATIC AND KINEMATIC BEHAVIOUR OF A FOLDABLE TRUSS ROOF STRUCTURE

J.G. Cai^{1,2*}, Z. Ye¹, X.Y. Wang¹, Y.X. Xu³ and J. Feng¹

¹ Key Laboratory of C & PC Structures of Ministry of Education, National Prestress Engineering Research Center, Southeast University, Nanjing 210096, China

² Key Laboratory of Electronic Equipment Structure Design of Ministry of Education, Xidian University, Xian 710126, China

³ Department of Mechanical Engineering, The University of Sheffield, Sheffield S10 2TN, UK

*(Corresponding author: Email: caijg_ren@hotmail.com / j.cai@seu.edu.cn)

Received: 18 June 2017; Revised: 18 June 2017; Accepted: 19 October 2017

ABSTRACT: In this paper, a type of foldable truss structure formed by four-bar linkages is firstly proposed as a retractable roof. Then the mechanical behavior of a fully closed roof system is studied. The results show that the member buckling has a great effect on the ultimate capacity of foldable truss structures. The failure load of the structure is smaller if buckling is considered. It is also found that the effect of imperfections on the failure load of the foldable structure is not significant. Furthermore, the stress variation during the folding is small. However, when initial imperfections are introduced, the maximal member stress during the motion increases greatly, which is almost close to yield stress.

Keywords: Foldable structure, four-bar linkage, moving process, mechanical behaviour, cables, imperfection

DOI: 10.18057/IJASC.2018.14.5

1. INTRODUCTION

Pantographic foldable structure, which uses scissor-like elements (SLEs) as basic structural elements, has many potential earthbound and aerospace industry applications [1]. In 1960s, the first of such structure has been designed and constructed by Spanish architect Piñero [2]. Substantial contributions to the general understanding of geometric and kinematic behavior of SLEs are due to Escrig [3, 4] and Escrig and Valcarcel [5]. They also applied this concept to the design of a swimming pool [6].

Zeigler firstly investigated the ‘snap-through’ phenomenon during the motion, which is caused by geometric incompatibilities between the SLEs [7]. Then the geometry design and structural response during the deployment of snap-through structures were thoroughly investigated by Gantes *et al.* [8], Gantes [9], Gantes and Konitopoulou [10]. Further studies of such deployable structures based on SLEs have been made by many other researchers. Shan presented an approach based on the concept of the standard stiffness method for the computer analysis of foldable structures [11]. Kaveh and Davaranl also developed an efficient computational method, incorporating the stiffness matrix of a SLE into a standard stiffness method [12]. Langbecker [13] formulated the foldability equation using a purely geometric approach, which then was used to analyze the kinematics and determine the foldability/deployability of translational, cylindrical, and spherical configurations. The kinematic of pantograph structures has also been studied by obtaining the null space of a constraint Jacobian matrix or the Screw theory [14, 15]. A scissor-hinged system consisting of several interconnected parallel linear SLEs was suggested as the supporting structure for membrane structures [16].

The elements of SLEs on the above study are straight bars. In the early 1990's, Hoberman invented a method for constructing loop assemblies consisting of a pair of identical angulated rods connected by a scissor hinge [17, 18]. In analogy to SLEs made from straight rods, angulated SLEs subtend a constant angle as their rods rotate while maintaining the end pivots on parallel lines. You and Pellegrino used the previous concept onto multi-angulated SLEs having more than one kink angle [19]. The cover elements and support conditions of the retractable roof structure based on angulated SLEs were also investigated by Kassabian *et al.* [20], Buhl and Jensen [21], and Jensen [22]. Furthermore, kinematics of Hoberman's Linkages was also studied using the Screw theory [23, 24]. Several other types of closed loop structures have been developed and studied [25-30].

Retractable roofs are structures that can transform from one configuration to another in order to provide a variable cover to the space underneath in response to changing conditions and/or functional requirements [31]. From a structural point of view, retractable roof structures have to be designed for two completely different loading conditions in the open and close situations. The structural design process is very complicated and requires successive iterations to achieve some balance between desired flexibility during deployment and higher stiffness in the open configuration [1, 10]. However when the foldable truss based on SLEs was used as a retractable roof structure, Chen *et al.* [32] suggested that there are still many unsolved problems such as high bending moment of member and low structural stiffness etc. The large bending moment will reduce the structural efficiency and low structural stiffness will lead to larger deflection. Moreover, Teall also observed that the deformation of the structure was quite large under self-weight in the experimental investigation of the structural behavior of a three layer foldable dome based on multi-angulated SLEs with a span of 2 m [33]. This leads to low stiffness of this structure that is unable to resist external loads. Recently, Mao and Luo investigated a few support conditions and structural forms to increase the structural stiffness [30].

In this paper, a foldable truss roof structure based on the four-bar linkage is introduced. An active cable and a passive cable are added between the diagonal joints of the four-bar linkage to control the deployment process and increase the structural stiffness. The mechanical behavior of the proposed system in the fully deployed configuration was then investigated and the role of cables was studied. Moreover, the moving process of the system was simulated using commercial software ABAQUS. The influence of the imperfection on the behavior in motion was also discussed.

2. GEOMETRICAL DESIGN

Plane linkages are member assemblies using revolute pairs or prismatic pairs. The simplest example of them is the planar four-bar linkage, which is widely used and works as the foundation of other planar linkages. The four-bar linkages in this paper is connected by revolute hinges only with a rotational degree-of-freedom perpendicular to the mechanism plane.

The foldable unit based on four-bar linkages, shown in Figure 1, is driven by telescopic rods, in which the four bars on the edge is neither foldable nor contractile while the diagonal bar can change its length as designed as a telescopic rod. Then at the foldable configuration, the structure is bunch-like and corresponding elements are parallel to each other. With the elongation of the telescopic rod, the structure is gradually unfolded and reaches its fully deployed state with the telescopic rods fully extended. In order to deploy the structures fully, the length of bars, 11 to 14, should satisfy the following equation as

$$l_1 + l_3 = l_2 + l_4 \quad (1)$$

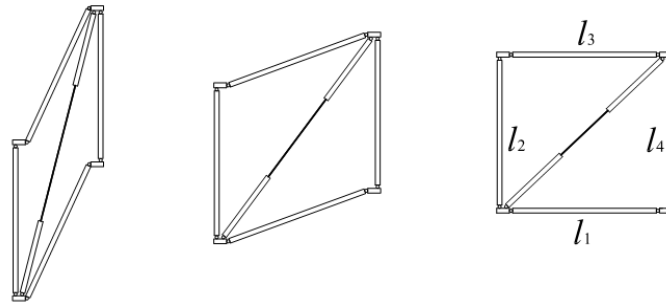


Figure 1. Foldable Units Driven by the Telescopic Rod

When this foldable unit is used to develop a deployable structure, large number of telescopic rods are required to drive the system, which makes it practically difficult for large deployable structures. Another method, based on the idea of active cables and passive cables [34], is proposed in this paper. In the foldable configuration, both the active cable and passive cable are slack as shown in Figure 2(a). During the deployment of the system, the distance between nodes A and C decreases progressively along with the shortening of the active cable. During the motion, the active cable is always in tension while the passive cable is slack. Subsequently, with the further shortening of the active cable, the passive cable turns to be tensional and thus the system movement is terminated as shown in Figure 2(c). If we keep stretching the active cable, no rigid-body displacement is produced but the whole system has been imposed with prestress shown in Figure 2(d).

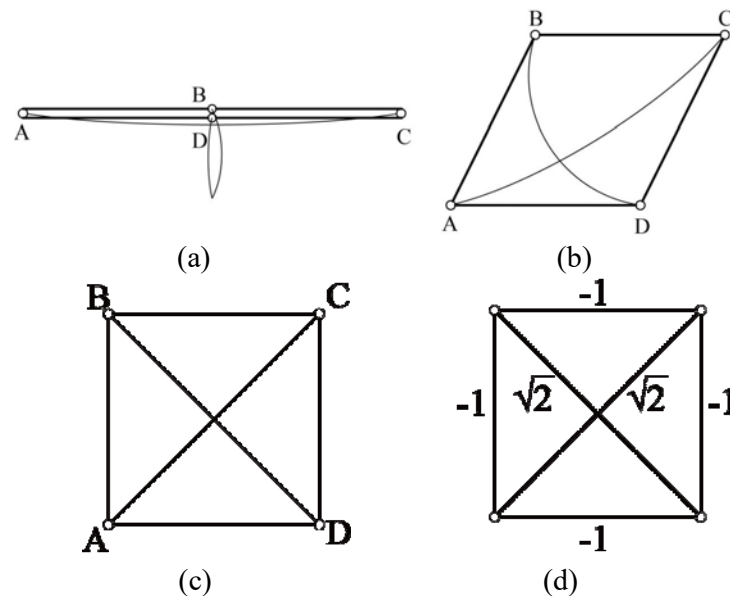


Figure 2. Foldable Units Driven by Cables

Due to its advantages of light weight, large rigidity, high integrity and well seismic performance, the space grid structure is widely used in various long-span structures. A spatial foldable unit, which is developed by the planar foldable unit based on four-bar linkages shown in Figure 2, will be used to form a foldable space truss structure in this paper. The moving progress of the spatial foldable unit is shown in Figure 3. If we consider each plane in this unit as a bar, then the unit can be considered as a four-bar linkage.

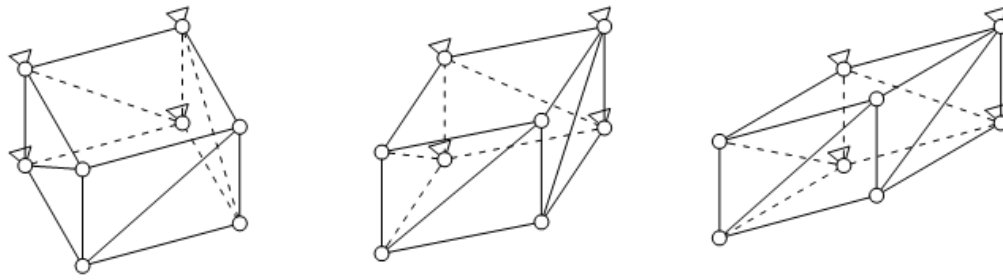


Figure 3. Moving Progress of the Spatial Foldable Unit

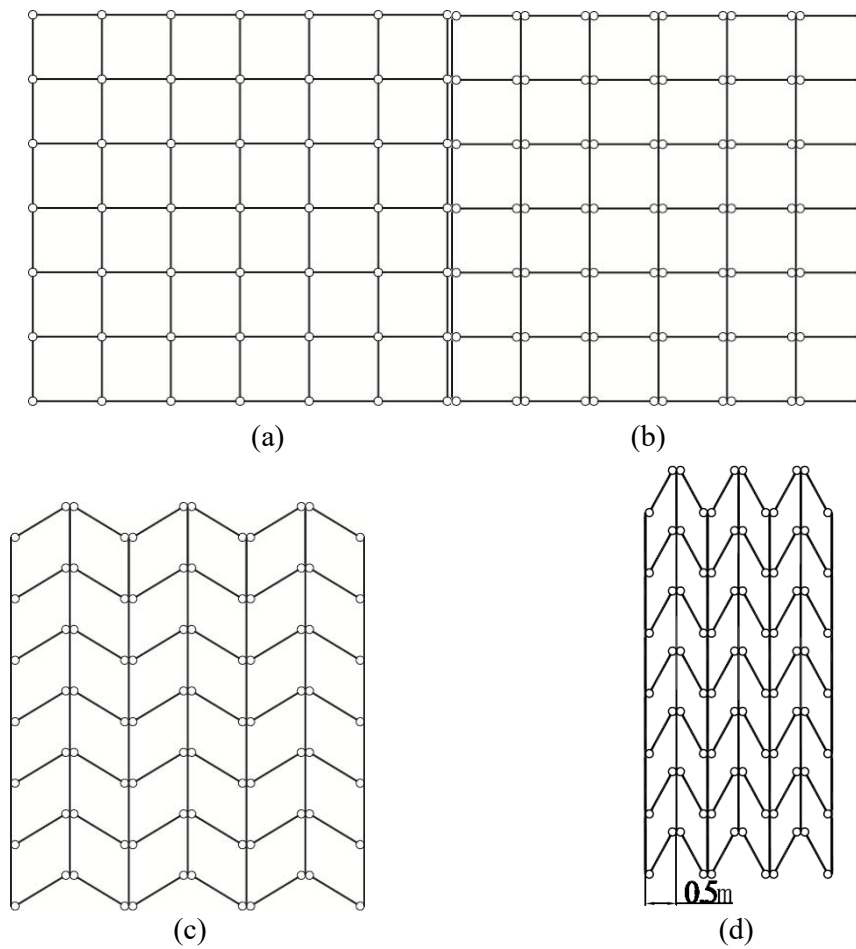
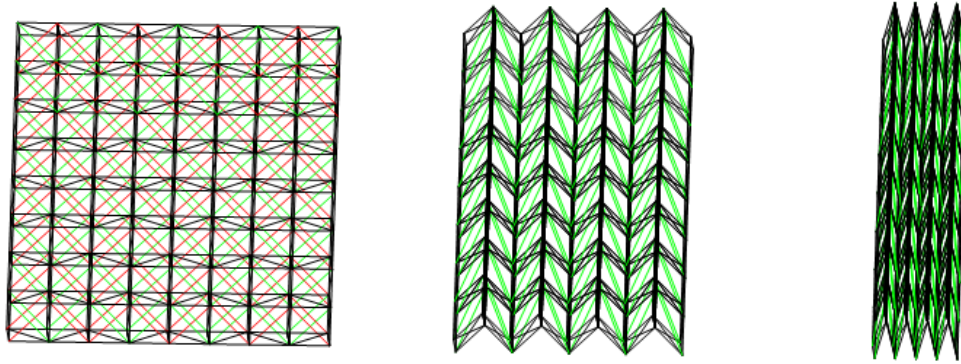


Figure 4. Foldable Truss Structures



(a) Fully open configuration (b) Semi-open configuration (c) Fully closed configuration

Figure 5. 3-D View of the Foldable Truss Structure
(Active Cables not given in Figure 5(b) and 5(c) to Avoid Confusion)

Figure 4(a) presents the plan view of a foldable truss structure formed by the arrangement of spatial foldable units in the horizontal and vertical directions. It can be shown that this truss has high degrees of freedom of this foldable. Therefore, in order to reduce the degree-of-freedom and the complexity of joints, the elements in a row are revised as a non-movable truss shown in Figure 4(b). The foldable truss roof can be then moved in the ways as shown in Figure 4(c) and (d). It should be noted that the distance between two adjacent planar trusses of the structure shown in Figure 4(d) is 0.5m. This is because the two trusses cannot be totally overlapped due to the actual dimensions of bars and joints. Three-dimensional views of the foldable truss structure during the folding are shown in Figure 5, where active cables are in red and passive cables in green.

3. MECHANICAL BEHAVIOR

The mechanical behavior of the foldable truss structure in the fully deployable configuration is studied using ABAQUS, a commercial finite element software package. Main members of the structure are steel bars of yield stress 345 MPa and Young's modulus 2.1×10^5 MPa, which are modeled by beam element B31 with a pipe section of 90mm×4mm (outer diameter × wall thickness). The cables, which are designed to carry tension only, are modeled by truss element T3D2 with a cable radius of 6 mm, yield stress and Young's modulus 1.95×10^5 MPa. The initial stress of cables is 100 MPa. The span, length and height of the grid structure is 24 m in X direction, 24 m in Y direction, 3m in Z direction respectively with a 3 m spacing between two adjacent planar trusses. The boundary condition is given in Figure 6, where supports are arranged every 6 m to provide the vertical and horizontal constraints. Additional horizontal constraints in the X direction are added to the corner nodes of the structure. Obviously, the open or folding of the structure occurs when the horizontal constraints in the X direction of corner nodes are released.

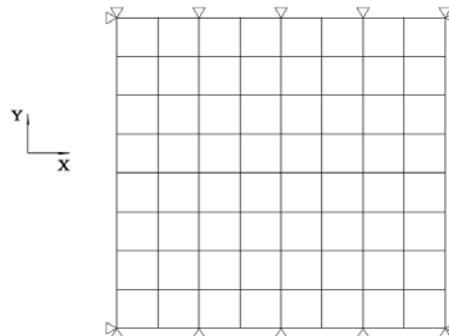


Figure 6. The Support Conditions in the Fully Deployable Configuration

The self-weight of all bars and cables are calculated by the software. The dead load consists of a self-weight of 0.5 kN/m^2 for the roof and the live load is applied to the top surface of the structure in the vertical direction with a magnitude of 0.5 kN/m^2 .

The ultimate capacity of some reticulated grid structures can be overestimated if only geometrical non-linearity is considered. It is significantly influenced by the material non-linearity. Therefore, as a new type of foldable reticulated grid structure model, both the material non-linearity and geometrically non-linearity are taken into account in the ultimate capacity analysis of foldable truss structures. The Newton-Raphson method is used to obtain the total load-displacement equilibrium path.

Due to large axial compressive stresses in bars of the grid structure, the load capacity may be greatly affected by the member buckling. Therefore, two models are considered in this paper. One is analyzed without considering the non-linearity due to member buckling while the other one is a non-linear model by meshing a bar into six beam elements. Load-displacement curves of the two models are shown in Figure 7, where the load factor F is defined as

$$F = \frac{\text{Imposed load}}{1.2 \times \text{dead load} + 1.4 \times \text{live load}} \quad (2)$$

The load is plotted against the displacement of a node chosen in the area of maximum deformation.

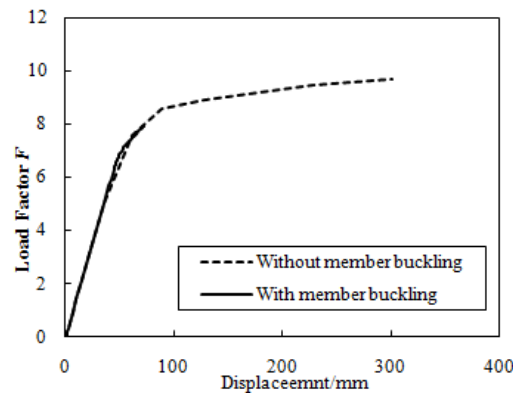


Figure 7. Load factor vs. Displacement for Different Models

The results show that the ultimate capacity of the foldable truss structures without considering the non-linearity due to member buckling is larger than that of the model considering member buckling (where the failure load factor is about 22.4% higher and the maximal displacement is about 314.8% higher). It can be seen that the initial segment of the load-displacement curve is nearly straight due to the slight material and geometrical non-linearity. Moreover, curves for the two different models are almost coinciding. With further application of load, the member suddenly buckles, leading to the ductility of the model, which is considering member buckling, is poor. Therefore, it can be concluded that the result is inaccurate without considering member buckling.

4. EFFECTS OF IMPERFECTIONS ON THE STRUCTURAL BEHAVIOR

The inaccuracy from construction and installation of a structure may have a significant influence on the structural behavior [35]. Thus it is of great importance to study the effect of imperfections on the ultimate capacity. Several methods are available for analyzing the geometrical imperfections, such as the random imperfection mode method, the consistent imperfection mode method, etc. In the latter method, the imperfection distribution is assumed to be consistent with the first buckling mode of the structure. Many researchers have extended the idea of this method to consider the imperfection distribution that is consistent with other deflected shapes of the structure, such as the eigenvalue buckling modes and nonlinear buckling shapes.

It is obvious from the calculation that the first 30 eigenmodes of the foldable truss structure are local buckling. Therefore, imperfections introduced to the structure based on eigenvalue buckling modes almost have no effects on the structural ultimate capacity. Then the non-linear buckling mode, which is shown in Figure 8, is used as the initial imperfection. It can also be found that for prestressed spatial structures, imperfections imposed according to buckling modes may increase the structural failure load if the imperfection is added in the improper direction [36]. Therefore, imperfections are imposed in both positive and negative directions in this paper and parametric analysis on the size of imperfections is carried out.

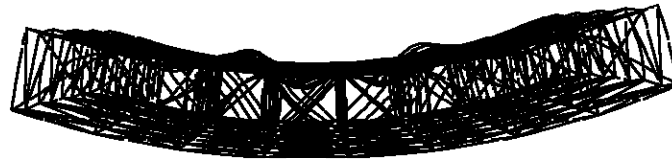
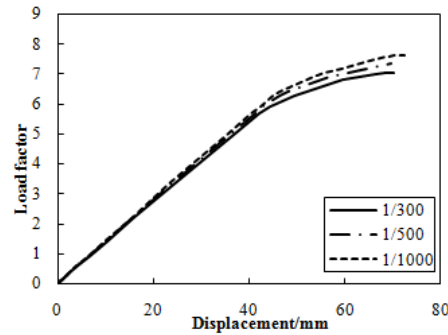
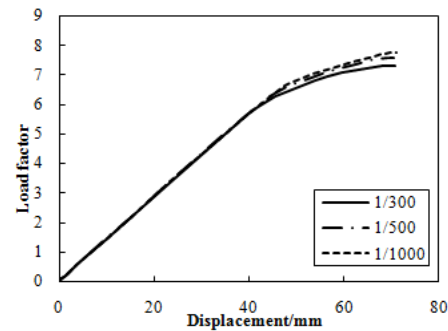


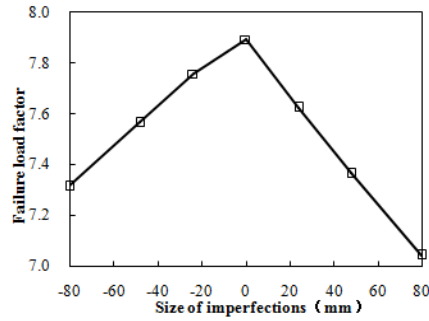
Figure 8. Non-linear Buckling Mode



(a) Load-displacement curves with positive imperfections



(b) Load-displacement curves with negative imperfections



(c) Failure load factors with different sizes of imperfections

Figure 9. Effects of Imperfections on Structural Behavior

The load-displacement curves are given in Figures. 9(a) and 9(b) while Figure 9(c) shows the comparison of the failure load factor with different size of imperfections. It can be seen that the structural stiffness and failure loads reduce slightly with the increase of imperfection and the effect of positive imperfections is more significant than that of negative imperfections.

5. MOVEMENT PROCESS ANALYSIS

It can be seen from Figure 5 that the deployment of the foldable truss structure is implemented by the relative motion between adjacent planar trusses. The release of constraints in the X direction of nodes at one side end will transfer the structure into a mechanism. Then the system moves after the application of the displacement in the Y direction on the interval planar trusses. Considering dimensions of members and joints, the two adjacent planar trusses cannot totally overlap. The maximal displacement in the Y direction of the interval planar truss is 2.9 m while the distance between two adjacent trusses is 0.77 m in fully open configuration.

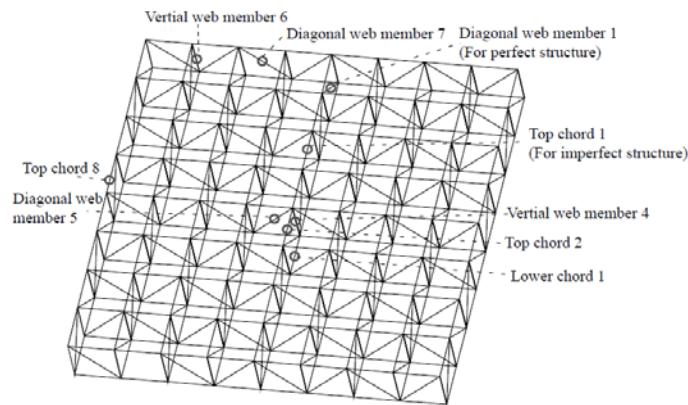


Figure 10. Typical Element Number

In order to investigate the stress distribution of the foldable truss roof during the movement, 8 typical steel bars are chosen as shown in Figure 10. The stresses of these bar elements are given in Figure 11. The Mises stress contours at different time during the motion is also shown in Figure 12. It can be seen from these figures that the structure is in fully close configuration when there is no displacement in the Y direction over the interval planar trusses. The maximal member stresses at this time is lower than 40 MPa. During the movement, the member stress of some bars increases while the remaining decreases, but all of them vary slightly. At the end of the deployment, the

maximal element stress is 31.86 MPa. Overall the element stresses in the movement of foldable truss structures have changed little.

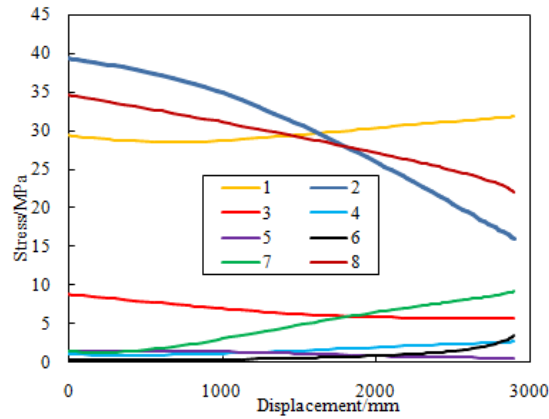


Figure 11. Element Stresses during the Motion

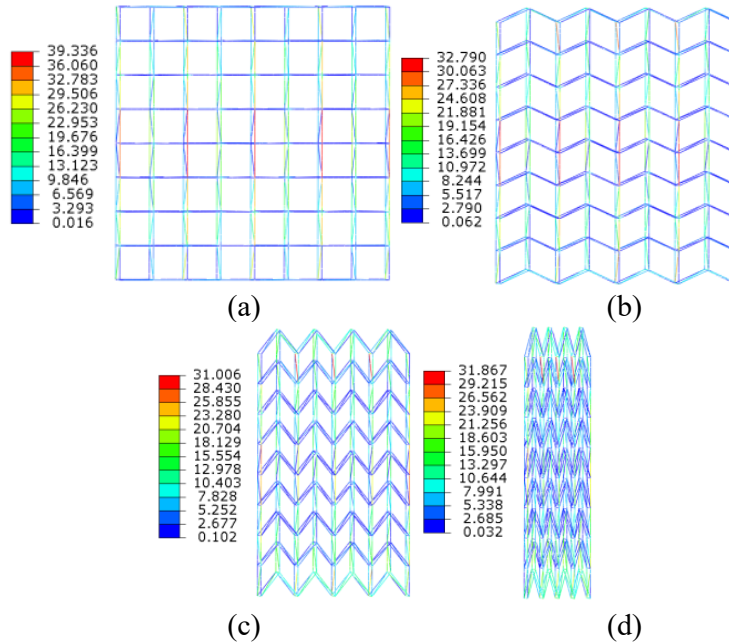
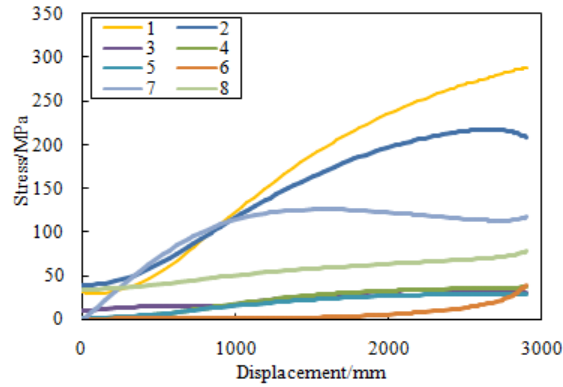


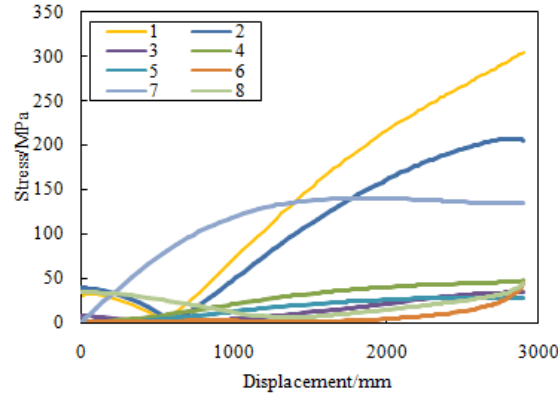
Figure 12. Mises Stress Contour at Different Time (MPa)

6. EFFECTS OF IMPERFECTIONS ON THE MOVING PROCESS

The influence of imperfections on structural behaviour during the motion is investigated in this section. The nonlinear buckling mode [37-41] is chosen as the imperfection distribution for the consistent imperfection mode method. Both positive imperfection and negative imperfection are applied. The stress displacement curves are shown in Figure 13. Note the maximal size of imperfection is assumed to be $L/300$, where L is the span of the structure.



(a) Structures with positive imperfections



(b) Structures with negative imperfections

Figure 13. Element Stresses of Imperfect Structures during the Motion

For structures with positive initial imperfections in motion, it is obvious from Figure 13(a) that element stresses in most members have a significant rise and the maximal stress is 288 MPa at the end of the deployment. In the meantime, the overall stress trend of structures with negative imperfections, given in Figure 13(b), is consistent with that of positive imperfections. The maximal member stress after the deployment is 305 MPa, close to the yield stress of steel member. The member with the maximal stress is located in the region with the largest initial imperfection.

In order to better understand the structural behavior during the motion, Figure 14 presents the Mises stress contour of the structure with positive imperfections at different time. It can be seen that imperfections have a significant influence on the movement of foldable truss structures. Therefore, it is essential to study the effect of sizes of initial imperfections on the movement of the structure. As shown in Figure 15, the effect of different maximal value of initial imperfections with $L/300$, $L/500$ and $L/1000$ on the maximal element stress of the foldable truss structure during the deployment are considered. Obviously, larger initial imperfections will lead to higher maximal member stress. Negative imperfections, however, have a more sensitive effect on the maximal member stress.

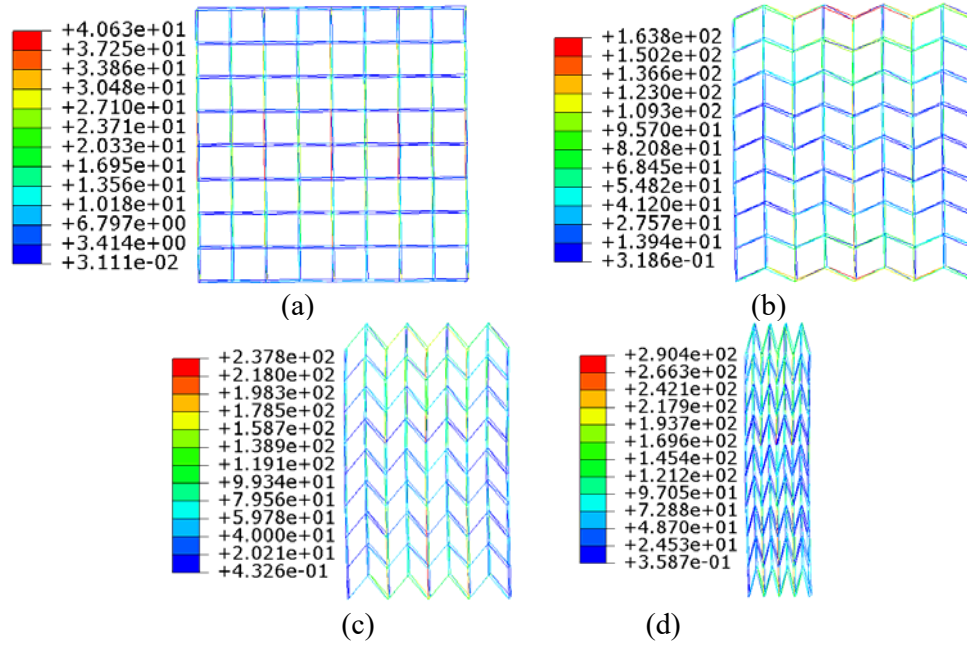


Figure 14. Mises Stress Contour of Positive Imperfect Structures at Different Time (MPa)

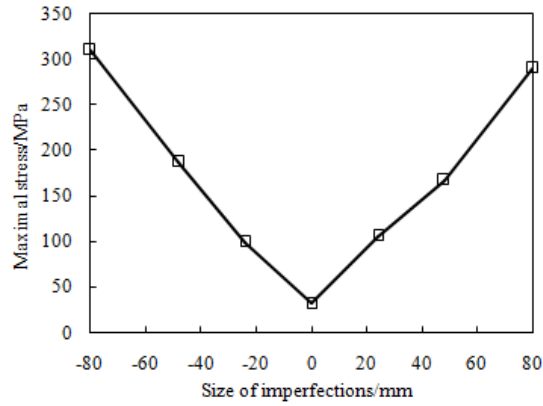


Figure 15. Effects of the Size of Imperfections on Moving Process

7. CONCLUSIONS

In this paper, based on the investigation of the planar four-bar linkage, a type of foldable truss structures are proposed as a retractable roof. Then the mechanical behaviors of the roof system in the fully close configuration and the moving process are studied. From analyses in this paper, conclusions can be drawn as:

(1) The member buckling has a great effect on the ultimate capacity of foldable truss structures. The failure load of the structure with consideration of member buckling is smaller than that regardless of member buckling. Furthermore, the ductility of the structure considering member buckling is poor because of the sudden buckling of bars.

(2) With the increase of imperfections, the structural stiffness and the failure load of the system decrease slightly. Therefore, the effect of imperfections on the ultimate capacity of the foldable structure at the fully closed state is limited.

(3) The variation of member stresses of ideal structures during the folding of the system is small. However, when initial imperfections are introduced, the maximal member stress during the motion increases almost close to the yield stress.

ACKNOWLEDGEMENTS

The work presented in this article was supported by the National Natural Science Foundation of China (Grant No. 51822805 and No. 51578133), the Natural Science Foundation of Jiangsu Province (Grant No. BK20170083), the Six top talent peak projects of Jiangsu Province (Grant No. JZ-001), the Opening Project of Key Laboratory of Electronic Equipment Structure Design of Ministry of Education at Xidian University, a Project Funded by the Priority Academic Program Development of Jiangsu Higher Education Institutions, and the Excellent Young Teachers Program of Southeast University. Authors also thank the anonymous reviewers for their valuable comments and thoughtful suggestions which improved the quality of the presented work.

REFERENCES

- [1] Gantes, C.J., "Deployable Structures: Analysis and Design", WIT Press, Southampton, UK, 2001.
- [2] Piñero, E.P., "Project for a Mobile Theatre", Architectural Design, 1961, Vol. 12, pp. 570.
- [3] Escrig, F., "Expandable Space Frame Structures", Proceedings of the 3rd International Conference on Space Structures, London, UK, 1984.
- [4] Escrig, F., "Expandable Space Structures", International Journal of Space Structures, 1985, Vol. 1, No. 2, pp. 79- 91.
- [5] Escrig, F. and Valcarcel, J.P., "Curved Expandable Space Grids", Proceedings of the International Conference on the Design and Construction of Non-Conventional Structures, 1987, pp. 157-168.
- [6] Escrig, F., Valcarcel, J.P. and Sanchez, J., "Deployable Cover on a Swimming Pool in Seville", Journal of the IASS, 1996, Vol. 37, No. 120, pp. 39-70.
- [7] Zeigler, T.R., "Collapsible Self-supporting Structures and Panels and Hubtherefore", United States Patent 4290244, 1981.
- [8] Gantes, C., Logcher, R.D., Connor, J.J. and Rosenfeld, Y., "Deployability Conditions for Curved and Flat, Polygonal and Trapezoidal Deployable Structures", International Journal of Space Structures, 1993, Vol, 8, pp. 97-106.
- [9] Gantes, C.J., "A Creative Aspect of a Destructive Phenomenon: Using Snap Trough Buckling as a Form of Prestressing", IASS/IABSE International Symposium on Conceptual Design of Structures, I, 1996, pp. 222-229.
- [10] Gantes, C.J. and Konitopoulou, E., "Geometric Design of Arbitrarily Curved Bistable Deployable Arches with Discrete Joint Size", International Journal of Solids and Structures, 2004, Vol, 41, pp. 5517-5540.
- [11] Shan, W., "Computer Analysis of Foldable Structures", Computer and Structures, 1992, Vol. 42, No. 6, pp. 903-912.
- [12] Kaveh, A. and Davaranl, A. "Analysis of Pantograph Foldable Structures", Computers and Structures, 1996, Vol. 59, No. 1, pp. 131-140.
- [13] Langbecker, T., "Kinematic Analysis of Deployable Scissor Structures", International Journal of Space Structures, 1999, Vol. 14, No. 1, pp. 1-16.
- [14] Nagaraj, B.P., Pandiyan, R. and Ghosal, A., "A Constraint Jacobian based Approach for Static Analysis of Pantograph Masts", Computers and Structures, 2010, Vol. 88, pp. 95-104.

- [15] Zhao, J.S., Chu, F.L. and Feng, Z.J., "Themechanism Theory and Application of Deployable Structures based on SLE", Mechanism and Machine Theory, 2009, Vol. 44, No. 2, pp. 324-335.
- [16] Van Mele, T., "Scissor-Hinged Retractable Membrane Roof", Ph.D. Dissertation, Vrije Universiteit Brussel, 2008.
- [17] Hoberman, C., "Reversibly Expandable Doubly-curved Truss Structures", US Patent 4942700, 1990.
- [18] Hoberman, C., "Radial Expansion/Retraction Truss Structures", US Patent 5024031, 1991.
- [19] You, Z., and Pellegrino, S. "Foldable bar Structures", International Journal of Solids and Structures, 1997, Vol. 34, pp. 1825-1847.
- [20] Kassabian, P.E., You, Z. and Pellegrino, S., "Retractable Roof Structures", Proceedings of the Institution of Civil Engineers, Structures and Buildings, 1999, Vol. 134, pp. 45-56.
- [21] Buhl, T., Jensen, F.V. and Pellegrino, S., "Shape Optimization of Cover Plates for Retractable Roof Structures", Computers and Structures, 2004, Vol. 82, pp. 1227-1236.
- [22] Jensen, F.V., "Concepts for Retractable Roof Structures", University of Cambridge, UK, 2004.
- [23] Wei, G., Ding, X. and Dai, J.S., "Mobility and Geometric Analysis of the Hoberman Switch-pitch Ball and its Variant", Journal of Mechanisms and Robotics, 2010, Vol. 2, No. 3, pp. 031010.
- [24] Cai, J.G., Xu, Y.X. and Feng, J., "Kinematic Analysis of Hoberman's Linkages with the Screw Theory", Mechanism and Machine Theory, 2013, Vol. 63, pp. 28-34.
- [25] Wohlhart, K., "Double-chainmechanisms", Kluwer Academic Publishers, Southampton, UK, 2000.
- [26] You, Z., "A New Approach to Design of Retractable Roofs", Kluwer Academic Publishers, Southampton, UK, 2000.
- [27] Cai, J.G., Deng, X.W. and Feng, J., "Mobility Analysis of Planar Radially Foldable Bar Structures", Proceedings of the Institution of Mechanical Engineers Part G: Journal of Aerospace Engineering, 2015, Vol. 229, No. 4, pp. 694-702.
- [28] Kowaka, T., "Structural Idea of Retractable Loop-dome", Journal of the IASS, 2003, Vol. 41, No. 133, pp. 111-116.
- [29] Cai, J.G., Deng, X.W., Zhao, Y.Z. and Feng, J., "Effects of Thermal Loading on the Deployment of Four-bar Linkages for Retractable Roof Structures, Mechanika, 2017, Vol. 23, No. 2, pp. 253-258
- [30] Cai, J.G., Feng, J. and Jiang, C., "Development and Analysis of a Long-span Retractable Roof Structure". Journal of Constructional Steel Research, 2014, Vol. 92, pp. 175-182.
- [31] Ishii, K., "Structural Design of Retractable Roof Structures", WIT Press, Southampton, UK, 2000.
- [32] Chen, W.J., Fu, G.Y., Gong, J.H., He Y.L. and Dong S.L., "A New Design Conception for Large Span Deployable Flat Grid Structures", International Journal of Space Structures, 2002, Vol. 17, No. 4, pp. 293-299.
- [33] Teall, M.J., "Deployable Roof Structures", University of Cambridge, UK, 1996.
- [34] Nagaraj, B. P., Pandiyan, R. and Ghosal, A., "A Constraint Jacobian based Approach for Static Analysis of Pantograph Masts", Computers and Structures, 2010, Vol. 88, pp. 95-104.
- [35] Du, Z.L., Liu, Y.P. and Chan, S.L., "A Second-order Flexibility-based Beam-column Element with Member Imperfection", Journal of Engineering Structures, 2017, Vol. 143, pp. 410-426
- [36] Cai, J.G., Xu, Y.X., Feng, J. and Zhang, J., "Nonlinear Stability of a Single-layer Hybrid Grid Shell", Journal of Civil Engineering and Management, 2012, Vol. 18, No. 5, pp. 752-760.

- [37] Cai, J.G., Zhang, Q., Jiang, Y.B., Xu, Y.X., Feng, J. and Deng, X.W., “Nonlinear Stability Analysis of a Radially Retractable Hybrid Grid Shell in the Closed Position”, *Steel and Composite Structures*, 2017, Vol. 24, No. 3, pp. 287-296.
- [38] Fan, F., Wang, D.Z., Zhi, X.D. and Shen, S.Z., “Failure Modes of Reticulated Domes subjected to Impact and the Judgment”, *Thin-Walled Structures*, 2010, Vol. 48, pp.143–149.
- [39] Zhi, X.D., Fan, F. and Shen, S.Z., “Elasto-plastic Instability of Single-layer Reticulated Shells under Dynamic Actions”, *Thin-Walled Structures*, 2010, Vol. 48, pp. 837-845.
- [40] Cai, J.G., Zhou, Y., Xu, Y.X. and Feng, J., “Non-linear Stability Analysis of a Hybrid Barrel Vault Roof”, *Steel and Composite Structures*, 2013, Vol. 14, No. 6, pp. 571-586.
- [41] Cai, J.G., Liu, Y.Q., Feng, J., Ma, R.J. and Tu, Y.M., “Nonlinear Stability Analysis of a Radially Retractable Suspen-dome”, *Advanced Steel Construction*, 2017, Vol. 13, No. 2, pp. 117-131.

FATIGUE LIFE ASSESSMENT OF INCLINED WELDED JOINTS IN STEEL BRIDGES SUBJECTED TO COMBINED NORMAL AND SHEAR STRESSES

Z.Y. Jie^{1,*}, Y.D. Li², X. Wei² and P. Zhuge¹

¹ Faculty of Architectural, Civil Engineering and Environment, Ningbo University, Ningbo 315211, China

² School of Civil Engineering, Southwest Jiaotong University, Chengdu 610031, China

*(Corresponding author: Email: jiezhiyu_8@163.com)

Received: 22 December 2016; Revised: 12 July 2017; Accepted: 12 December 2017

ABSTRACT: The paper presents fatigue life assessment of inclined welded joints with a new geometric configuration in steel bridges. Fatigue tests on full penetration load-carrying fillet cruciform welded joints with inclination angles of 0°, 15°, 30°, and 45° subjected to uniaxial cyclic loading are performed. Hot spot normal and shear stress ranges are obtained by a linear extrapolation, and a sensitivity analysis is carried out to determine the appropriate mesh size. The fatigue life results predicted by the equivalent stress range method, DNV(Det Norske Veritas), Eurocode 3, and IIW(the International Institute of Welding) are compared with test results. The results show that the fatigue cracks in all of the specimens initiate at the weld toe but propagate in different directions. There are two cracking types: (a) cracking along the weld ($\theta=0^\circ, 15^\circ$); (b) cracking perpendicular to the direction of the applied load ($\theta=30^\circ, 45^\circ$). The fatigue life increases with an increase in the inclined angle due to a decrease in the normal stress range perpendicular to the weld. The fatigue life tends to be overpredicted by Eurocode 3 at the large inclination angle. The FAT90 used by DNV is more conservative than the FAT100 recommended by Eurocode 3 and IIW, so that the fatigue life is underestimated. It is concluded that the equivalent stress range method and IIW are in good agreement with the fatigue test results. The equivalent stress range method is more suitable to assess the fatigue life of inclined welded joints subjected to combined normal and shear stresses due to the ease of implementation and low computational cost. The fatigue design curve of FAT100 is recommended for the equivalent stress range method.

Keywords: Welded joint, steel bridge, inclined angle, fatigue life assessment, hot spot stress

DOI: 10.18057/IJASC.2018.14.6

1. INTRODUCTION

Steel bridges have been widely used in long-span bridges due to their light weight, high strength, short installation time and relatively low monetary costs. There are a large number of welded joints (butt joints, T joints, cruciform joints, etc.) in steel bridges. The weld toes and roots can create high stress concentrations due to the geometric discontinuity. Consequently, fatigue cracks are more likely to appear in weld toes and roots rather than in the base metal subjected to repeated loadings [1]. During crack propagation, when a crack size reaches a critical value, welded joints suddenly fracture due to a reduction in the cross-sectional area and consequently the inability to resist further loading. Therefore, specific design guidelines are needed to avoid fatigue failures of welded joints in steel bridges during service life [2].

Three approaches are commonly employed for fatigue assessment of welded joints. The nominal stress approach is usually used for simple welded joints and loadings where nominal stresses can clearly be determined. Most fatigue design specifications use nominal stresses to assess the fatigue life of welded details according to different nominal stress design curves. This method cannot be applied in complex welded joints and loadings, but the hot spot stress approach can be used for this situation [3]. The hot spot stress approach was initially developed for fatigue assessment of offshore tubular joints [4]. Now, this approach is applied to welded plate structures and included in fatigue design specifications, such as Eurocode 3 [5], IIW(the International Institute of Welding)

[6], and DNV(Det Norske Veritas) [7]. There are five methods for determining the hot spot stress in the literature, including surface extrapolation, one point stress method, through thickness method, the Dong method, and 1 mm method [6, 8-10]. Many studies have been conducted to improve the accuracy of the hot spot stress estimation in three aspects: mesh density [11], element type [12], and computational method [13]. The local stress at the weld root cannot be described in detail by nominal and hot spot stresses [14]. The notch stress approach [15-17] used the maximum elastic notch stress at the weld toe or root for fatigue analysis. However, this approach requires more modelling and analysis work for the numerical simulation of complex welded structures.

There are many welded details in a steel bridge subjected to combined tension and shear stresses, such as welded rib-diaphragm connections in steel orthotropic decks [18] and welds that join corrugated plates to flange plates [19]. In these welded details, the crack initiation sites of the weld toe are in multiaxial stress states. The multiaxial fatigue damage mechanism is different from that of the uniaxial fatigue counterpart. Many methods are proposed for multiaxial fatigue assessment of welded structures. These approaches are applied in nominal stress, hot spot stress, and local stress concepts. These methods include principal stress or Von Mises stress methods, the interaction equation method in Eurocode 3 and IIW, and the modified Wöhler curve method [20]. The fatigue life based on conventional fatigue design methods has been under- or overestimated when combined normal and shear stresses were applied in phase simultaneously, so an equivalent stress range method has been proposed in [21]. The interaction equations from Eurocode 3, IIW, and DNV for calculating effective stress ranges based on the normal and shear stress ranges perpendicular and parallel to the weld respectively have been used to assess fatigue strength [22]. Bäckström [23] used the interaction equations from SFS 2378 [24], Eurocode 3, and IIW to evaluate the fatigue life. It is found in [23] that the fatigue life estimated using IIW is more closely in accordance with the experimental result. Kainuma et al. [25] clarified that the effect of the inclined angle on fatigue strength was small for welded specimens. Jen et al. [26] studied the effect of oblique loading on fatigue strength of butt-welded structures and found that the normal stress parallel to the loading direction played a significant role in the fatigue strength design and critical crack locations, which were identical to those experiencing the maximum Von Mises stress. Susmel [27] proposed the modified Wöhler curve method for estimating fatigue strength of inclined welded connections. The fatigue life assessment process based on the modified Wöhler curve method is complex and difficult to use in practice. The accuracy of fatigue life prediction results is extremely dependent on the use of reference fatigue curves in the specification, and the choice of fatigue design curves for complex welded joints remains a challenging and unsolved issue [28]. The main aim of this study is to determine a convenient method and an appropriate fatigue design curve for fatigue life estimation of inclined welded joints.

According to the statement above, full penetration load-carrying fillet cruciform welded joints largely used in steel bridges are taken as research objects, and 0° , 15° , 30° , and 45° weld inclined angles are constructed to simulate different complex stress states. To date, fatigue life assessment of these new welded joints has not been investigated. Consequently, it is necessary to carry out an in-depth study. Fatigue tests on cruciform welded joints with full penetration load-carrying welds inclined to the direction of the uniaxial cyclic loading are performed. Due to this complex geometry, it is difficult to estimate the nominal stress of a cross section. Welded joints are directly modelled by normal and shear stresses perpendicular and parallel to the weld from a multiaxial fatigue point of view, respectively. Thus, the hot spot stress approach is applied to obtain hot spot the normal stress range and shear stress range by a linear extrapolation method based on a numerical analysis. A sensitivity analysis is carried out for determining the appropriate mesh size. Fatigue life assessment is conducted by the equivalent stress range method, DNV, Eurocode 3, and IIW. Finally, the fatigue design curves and appropriate fatigue life evaluation methods for inclined welded joints in steel bridges subjected combined normal and shear stresses are determined.

2. FATIGUE TEST

The crack initiation locations of the welded joints with inclined welds are in multiaxial stress states subjected to uniaxial cyclic loading. The nominal stress range can be decomposed into the normal stress range $\Delta\sigma_x$ and the shear stress range $\Delta\tau_{xy}$ perpendicular and parallel to the weld from a multiaxial fatigue point of view, respectively (Figure 1) [27]. They can be expressed as

$$\Delta\sigma_x = \Delta\sigma_{\text{nom}} \cdot \cos^2 \theta \quad (1)$$

$$\Delta\tau_{xy} = \Delta\sigma_{\text{nom}} \cdot \sin \theta \cdot \cos \theta \quad (2)$$

where $\Delta\sigma_{\text{nom}}$ is the nominal stress range, and θ is the angle between the weld and the direction perpendicular to the applied load.

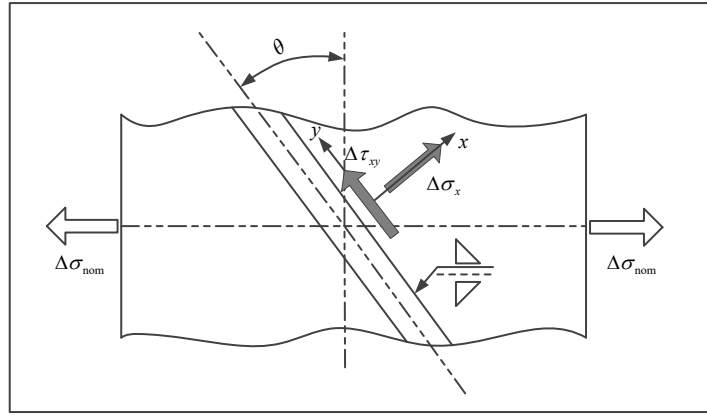


Figure 1. Inclined Fillet Weld subjected to Uniaxial Fatigue Loading

2.1 Specimens and Loading

The cruciform welded joints with different inclined angles were machined by Q345qC steel [29]. The chemical composition of Q345qC steel consisted of C(0.17%), Si(0.27%), Mn(1.43%), P, S, V, Cr, Mo, and Ni. The yield and tensile strength were 360 MPa and 575 MPa, respectively, and the elongation was 28%.

Fatigue tests were performed on a servo-hydraulic machine under a sine wave axial cyclic load. According to the maximum force of the machine and the specimen size, a uniform axial tensile stress range of 160 MPa was applied at one end of the plate. The maximum and minimum fatigue loads were $P_{\text{max}}=142.2$ kN and $P_{\text{min}}=14.2$ kN, respectively. The testing frequency was between 5 and 10 Hz depending on the load level and rigidity, and the load ratio R ($R=P_{\text{min}}/P_{\text{max}}$) was 0.1. Three identical specimens were tested under the same stress range due to the scatter in the fatigue test results. The dimensional parameters of the cruciform welded joints were listed in Table 1. The geometric configurations of the cruciform welded joints and fatigue specimen loading were illustrated in Figures 2-3.

Table 1. Dimensional Parameters of the Cruciform Welded Joints

Specimen Number	Inclined angle	Stress range(MPa)	Length b (mm)
D1S2	0°	160	92.0
D2S2	15°	160	85.3
D3S2	30°	160	77.6
D4S2	45°	160	67.0

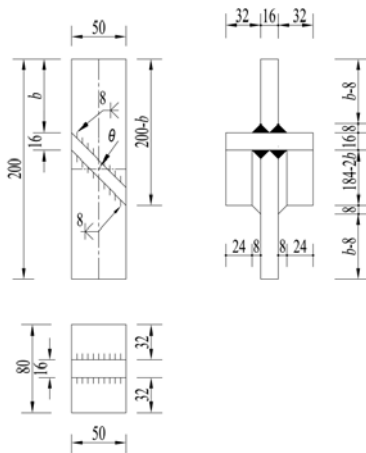


Figure 2. Geometric Configurations of the Cruciform Welded joints



Figure 3. Fatigue Specimen Loading

2.2 Test Results

The number of cycles was recorded once a macroscopic crack was found, and the crack propagation was observed by a magnifier. The fatigue life was determined when the first through-thickness crack was founded. The fatigue life test results of the cruciform welded joints with different inclination angles were listed in Table 2.

Table 2. Fatigue Life Test Results of the Cruciform Welded Joints with different Inclination Angles

Specimen Number	Inclined angle	Stress range(MPa)	Fatigue life(cycles)
D1S2	0°	160	4.11×10^5
D2S2	15°	160	5.16×10^5
D3S2	30°	160	6.27×10^5
D4S2	45°	160	9.77×10^5

The fatigue cracks in all of the specimens were initiated at the weld toe, where the stress concentration was higher than others, but propagated in different directions. There were two cracking types: (a) cracking along the weld; (b) cracking perpendicular to the direction of applied load (Figure 4). The cracks propagated along the weld when the weld inclined angle was 0° or 15°. However, the cracks propagated along the perpendicular direction of the applied load for 30° and 45° inclined angles. The main reason for this phenomenon was that with an increase in the inclined

angle, the weld length and the shear stress parallel to the weld and rigidity increased, but the normal stress perpendicular to the weld decreased. The crack propagation was perpendicular to the direction of the maximum principal stress [30]. The direction of the maximum principal stress was perpendicular to the weld when the inclined angle was small. However, the direction of the maximum principal stress was parallel to the direction of the applied load when the inclined angle was relatively large.



Figure 4. Fatigue Crack Propagation

The fatigue fracture morphology of the specimens can be divided into two regions: (1) the smooth region of fatigue crack initiation and propagation; (2) the rough region of brittle fracture (Figure 5). The fatigue crack was initiated from the bottom left corner under cyclic loading and then gradually propagated. The crack surface became smooth due to repeated friction, and a quarter elliptic crack growth trajectory was formed. When the strength of material cannot resist external loads due to a reduction in the effective cross section, the specimens suddenly ruptured.

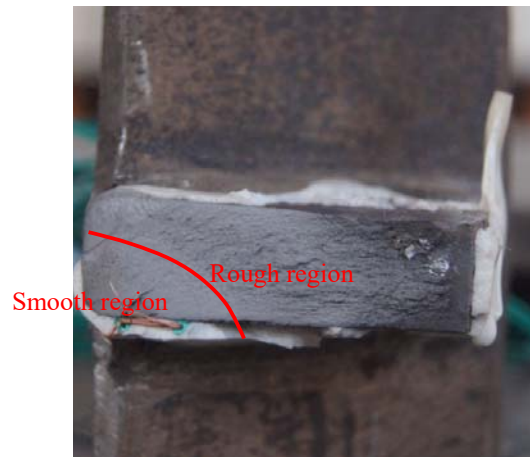


Figure 5. Fatigue Fracture Morphology

3. FINITE ELEMENT MODELLING

3.1 The Hot Spot Stress Approach

The term ‘hot spot’ refers to the critical point in a structure where fatigue cracking can be expected to occur due to a discontinuity or a notch [31]. The hot spot is usually located at the weld toe in

welded structures. The hot spot stress σ_{hs} is the value of the stress at the hot spot but excludes the local nonlinear stress peak produced by the weld shape or the notch. This value can be obtained by a linear elasticity formulas or a finite element method. The hot spot stress is composed of the membrane stress σ_m and the bending stress σ_b (Figure 6).

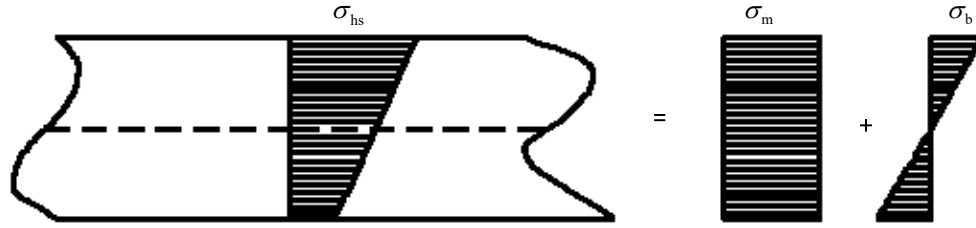


Figure 6. The Composition of the Hot Spot Stress

Two types of hot spots are defined according to their location on the plate and their orientation to the weld toe, as defined in Figure 7 according to IIW. Different methods are used to evaluate the hot spot stress for each type of weld toe. It can be seen that the fatigue failures of weld toes belong to the Type “a” hot spot according to test results. Due to its relative ease of use, a surface extrapolation method is widely used in fatigue assessment and can be divided into linear and quadratic extrapolations. It is found that there is no significant difference between linear and quadratic extrapolations in evaluating the hot spot stress [12]. The element type and mesh size of the finite element model also affect the results. A 3D solid model including the weld is recommended for simulating complex welded structures according to IIW. When a fine mesh with an element length not more than $0.4t$ at the Type “a” hot spot is used, the linear extrapolation equation using nodal stresses at two reference points $0.4t$ and $1.0t$ from the weld toe is provided below, where t is the main plate thickness (Figure 8(a)).

$$\sigma_{hs} = 1.67\sigma_{0.4t} - 0.67\sigma_{1.0t} \quad (3)$$

However, DNV recommends that the extrapolation reference points should be located at distances of $0.5t$ and $1.5t$ from the weld toe (Figure 8(b)). Similarly, the hot spot stress can be expressed as

$$\sigma_{hs} = 1.5\sigma_{0.5t} - 0.5\sigma_{1.5t} \quad (4)$$

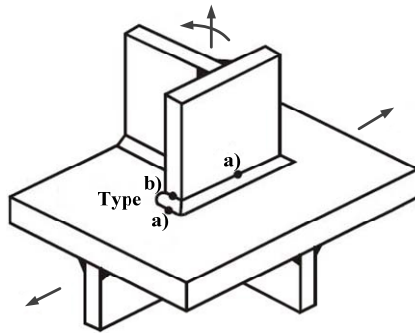


Figure 7. Types of Hot Spots

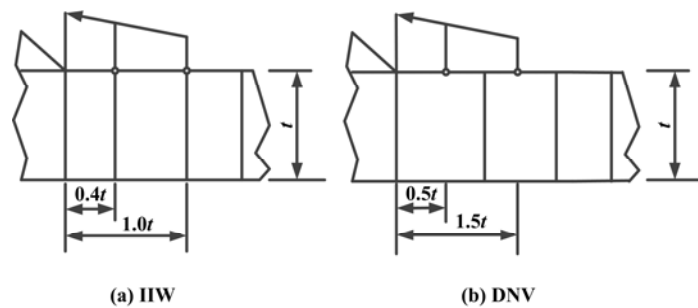


Figure 8. The Linear Extrapolation of Hot Spot Stress

3.2 Calculation of the Hot Spot Stress

According to the discussion above, the linear extrapolation is used to calculate the hot spot stress by a finite element analysis. Finite element models for cruciform welded joints with 0° , 15° , 30° , and 45° inclined angles are created using the commercial finite element software ANSYS [32]. The 8-node solid element (SOLID45) is selected to simulate these models, and the weld shape is

simplified as an isosceles right triangle. A uniform axial tensile stress of 160 MPa is applied at one end of the plate, and a fixed constraint is applied at the other end of the plate. According to the symmetry, only one-half finite element model is considered, and the symmetric constraints are applied to the nodes of the symmetric surface (Figure 9). Young's modulus E and Poisson's ratio ν are 2.1×10^5 MPa and 0.3, respectively. However, the mesh size has an important effect on the hot spot stress. Therefore, the appropriate mesh size should be determined using a sensitivity analysis. Three different mesh sizes are provided below by the recommendations of IIW. The element numbers at a distance $1.5t$ from weld toe are 5, 15, and 30. The element numbers along the weld are 10, 20, and 40. The number of elements along the thickness is 4. These mesh sizes are represented by MS1(5×10), MS2(15×20), and MS3 (30×40). Hot spot stress ranges based on the linear extrapolation method at different inclined angles and mesh sizes are shown in Table 3.

Table 3. Hot Spot Stress Ranges under Different Inclined Angles and Mesh Sizes(MPa)

Inclined angle	Mesh size	Normal stress range	Shear stress range	Hot spot normal stress range		Hot spot shear stress range	
				IIW	DNV	IIW	DNV
0°	MS1	160.00	-	188.33	169.14	-	-
	MS2			165.89	160.99		
	MS3			165.96	161.06		
15°	MS1	149.28	40.00	178.16	159.32	46.86	43.11
	MS2			156.54	151.13	44.62	43.25
	MS3			156.44	151.16	44.77	43.38
30°	MS1	120.00	69.28	145.69	130.71	79.85	75.27
	MS2			130.99	123.72	76.59	73.76
	MS3			130.17	123.42	76.48	73.68
45°	MS1	80.00	80.00	107.19	94.92	98.29	90.01
	MS2			95.45	89.38	91.43	87.46
	MS3			95.28	89.41	91.22	87.50

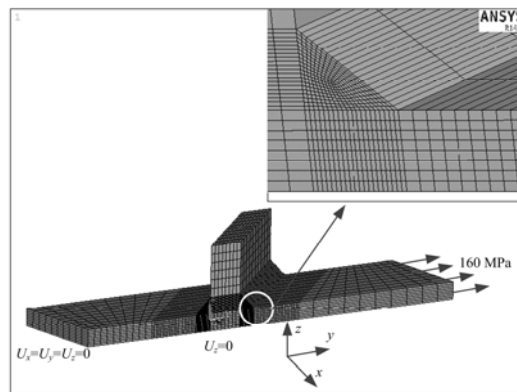


Figure 9. One-half Finite Element Model

It can be seen from Table 3 that with an increase in the inclined angle, the hot spot normal stress range decreases, while the hot spot shear stress range increases. Additionally, the hot spot stress range increases with an increase in the mesh size. The hot spot stress range calculated by the linear extrapolation rule of DNV is slightly lower than that of IIW. The difference in the hot spot stress ranges for various mesh sizes caused by DNV is small but relatively large by IIW. The maximum relative errors are 6.2% and 13.9% for DNV and IIW, respectively. The main reason is that the distance from the weld toe is farther, and hot spot stress is smaller. When the minimum mesh size is less than $0.1t$, the effect of the mesh size on the hot spot stress range is very small. Finally, MS2 is recommended to calculate the hot spot stress range considering the accuracy and computational efficiency.

4. FATIGUE LIFE ASSESSMENT

Kim and Yamada [33] recommended the equivalent stress range $\Delta\sigma_{\text{eqv}}$ to evaluate the fatigue life of inclined fillet welded joints by the following equation

$$\Delta\sigma_{\text{eqv}} = \Delta\sigma_{\text{nom}} \cdot \cos\theta = \sqrt{\Delta\sigma_x^2 + \Delta\tau_{xy}^2} \quad (5)$$

According to DNV, the effective stress range $\Delta\sigma_{\text{eff}}$ considering the normal stress range $\Delta\sigma_x$ and the shear stress range $\Delta\tau_{xy}$ can be expressed in the following form

$$\Delta\sigma_{\text{eff}} = \sqrt{\Delta\sigma_x^2 + \beta\Delta\tau_{xy}^2} \quad (6)$$

The S - N category C2 may be used for the continuous shear stress in a full penetration weld [34]. The effective hot spot stress range combined with the hot spot S - N curve D is derived as

$$\Delta\sigma_{\text{eff}} = \max \begin{cases} \sqrt{\Delta\sigma_x^2 + 0.81\Delta\tau_{xy}^2} \\ \alpha\Delta\sigma_1 \\ \alpha|\Delta\sigma_2| \end{cases} \quad (7)$$

where $\alpha=0.90$ if the detail is classified as C2 with stress parallel to the weld at the hot spot, $\alpha=0.80$ if the detail is classified as C1 with stress parallel to the weld at the hot spot, $\alpha=0.72$ if the detail is classified as C with stress parallel to the weld at the hot spot, and $\Delta\sigma_1$ and $\Delta\sigma_2$ are principal stress ranges. Principal stress ranges can be calculated as

$$\begin{aligned} \Delta\sigma_1 &= \frac{\Delta\sigma_x}{2} + \frac{1}{2}\sqrt{\Delta\sigma_x^2 + 4\Delta\tau_{xy}^2} \\ \Delta\sigma_2 &= \frac{\Delta\sigma_x}{2} - \frac{1}{2}\sqrt{\Delta\sigma_x^2 + 4\Delta\tau_{xy}^2} \end{aligned} \quad (8)$$

According to Eurocode 3, in the case of the combined normal and shear stress ranges, the fatigue analysis should be verified by the following equation

$$\left(\frac{\gamma_{\text{Ff}}\Delta\sigma_{\text{E},2}}{\Delta\sigma_{\text{C}}/\gamma_{\text{Mf}}} \right)^3 + \left(\frac{\gamma_{\text{Ff}}\Delta\tau_{\text{E},2}}{\Delta\tau_{\text{C}}/\gamma_{\text{Mf}}} \right)^5 \leq 1.0 \quad (9)$$

where γ_{Ff} is the partial factor for equivalent constant amplitude stress ranges $\Delta\sigma_{E,2}$ and $\Delta\tau_{E,2}$ ($\gamma_{Ff}=1$), and γ_{Mf} is the partial factor for fatigue strength $\Delta\sigma_C$ and $\Delta\tau_C$ related to 2 million cycles ($\gamma_{Mf}=1$). Eq. 9 can be rewritten according to [22]

$$D_\sigma + D_\tau \leq 1 \quad (10)$$

where D_σ and D_τ represent fatigue damage caused by the normal and shear stress ranges, respectively. They can be expressed as

$$D_\sigma = \left(\frac{\Delta\sigma_{E,2}}{\Delta\sigma_C} \right)^3 \quad (11)$$

$$D_\tau = \left(\frac{\Delta\tau_{E,2}}{\Delta\tau_C} \right)^5 \quad (12)$$

The fatigue life N_f can be expressed as

$$\frac{N_f}{N_\sigma} + \frac{N_f}{N_\tau} = 1 \Rightarrow N_f = \frac{N_\sigma N_\tau}{N_\sigma + N_\tau} \quad \text{and } N_f < 10^7 \text{ (cycles)} \quad (13)$$

where N_σ and N_τ are the fatigue lives subjected to the normal and shear stress ranges, respectively, and N_f is the fatigue life subjected to the combined normal and shear stress ranges. According to Eurocode 3, the fatigue lives N_σ and N_τ can be respectively expressed as

$$\Delta\sigma_{E,2}^3 N_\sigma = 2 \times 10^6 \Delta\sigma_C^3 \Rightarrow N_\sigma = 2 \times 10^6 \frac{\Delta\sigma_C^3}{\Delta\sigma_{E,2}^3} \quad (14)$$

$$\Delta\tau_{E,2}^5 N_\tau = 2 \times 10^6 \Delta\tau_C^5 \Rightarrow N_\tau = 2 \times 10^6 \frac{\Delta\tau_C^5}{\Delta\tau_{E,2}^5} \quad (15)$$

Therefore, Eq. 13 can be rewritten as

$$N_f = \frac{2 \times 10^6 \cdot \left(\frac{\Delta\sigma_C}{\Delta\sigma_{E,2}} \right)^3 \cdot \left(\frac{\Delta\tau_C}{\Delta\tau_{E,2}} \right)^5}{\left(\frac{\Delta\sigma_C}{\Delta\sigma_{E,2}} \right)^3 + \left(\frac{\Delta\tau_C}{\Delta\tau_{E,2}} \right)^5} \quad \text{and } N_f < 10^7 \text{ (cycles)} \quad (16)$$

For the evaluation of the biaxial stress states with the combined normal and shear stress ranges under constant amplitude proportional loading according to IIW, the following relationship should be met based on the Gough-Pollard criterion [35]

$$\left(\frac{\Delta\sigma_{S,d}}{\Delta\sigma_{R,d}}\right)^2 + \left(\frac{\Delta\tau_{S,d}}{\Delta\tau_{R,d}}\right)^2 \leq 1.0 \quad (17)$$

where $\Delta\sigma_{R,d}$ and $\Delta\tau_{R,d}$ are the design resistances of the normal and shear stress ranges at 2 million cycles, respectively, and $\Delta\sigma_{S,d}$ and $\Delta\tau_{S,d}$ are the design values of the normal and shear stress ranges, respectively. Eq. 17 can be rewritten based on Eqs. 11 and 12

$$D_\sigma^{2/3} + D_\tau^{2/5} \leq 1 \quad (18)$$

The fatigue life N_f can be expressed as

$$\left(\frac{N_f}{N_\sigma}\right)^{2/3} + \left(\frac{N_f}{N_\tau}\right)^{2/5} = 1 \quad \text{and } N_f < 10^7 \text{ (cycle)} \quad (19)$$

where

$$\Delta\sigma_{S,d}^3 N_\sigma = 2 \times 10^6 \Delta\sigma_{R,d}^3 \Rightarrow N_\sigma = 2 \times 10^6 \frac{\Delta\sigma_{R,d}^3}{\Delta\sigma_{S,d}^3} \quad (20)$$

$$\Delta\tau_{S,d}^5 N_\tau = 2 \times 10^6 \Delta\tau_{R,d}^5 \Rightarrow N_\tau = 2 \times 10^6 \frac{\Delta\tau_{R,d}^5}{\Delta\tau_{S,d}^5} \quad (21)$$

Given an initial value, the fatigue life can be obtained by iterative numerical methods using Eq. 19.

According to hot spot stress results, the parameters used to calculate the fatigue life are listed in Table 4. Based on welded details in fatigue design specifications, the fatigue design curves of FAT100 (a stress range of 100 MPa at 2 million cycles with a survival probability $P_s=97.7\%$) and FAT120 for the hot spot normal stress range and shear stress range should be taken according to Eurocode 3 and IIW, respectively. The fatigue design curves of FAT100 and FAT90 are used by the equivalent stress range method and DNV, respectively. The fatigue life prediction results of full penetration load-carrying fillet cruciform welded joints at various inclined angles by using the equivalent stress range method, DNV, Eurocode 3, and IIW are summarized in Table 5. A comparison of the fatigue life prediction and experimental results and the relationship between fatigue life and inclined angle are shown in Figures 10 and 11.

Table 4. Calculated Parameters (MPa)

θ	$\Delta\sigma_{\text{eqv}}$	$\Delta\sigma_{\text{eff}}$	$\Delta\sigma_{\text{E},2} = \Delta\sigma_{\text{S},d}$	$\Delta\tau_{\text{E},2} = \Delta\tau_{\text{S},d}$
0°	165.89	160.99	165.89	-
15°	161.58	155.33	156.54	44.62
30°	146.56	140.00	130.99	76.59
45°	127.24	124.57	95.45	91.43

Table 5. Fatigue Life Prediction Results (cycles)

θ	Equivalent stress range method	DNV	Eurocode 3	IIW
0°	4.38×10^5	3.49×10^5	4.38×10^5	4.38×10^5
15°	4.74×10^5	3.89×10^5	5.20×10^5	4.62×10^5
30°	6.35×10^5	5.31×10^5	8.50×10^5	5.80×10^5
45°	9.71×10^5	7.54×10^5	1.78×10^6	9.75×10^5

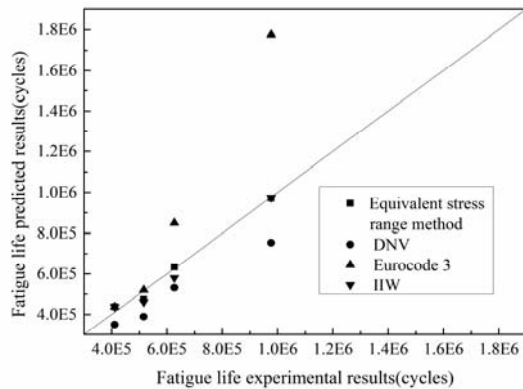


Figure 10. A Comparison of the Fatigue Life Prediction and Experimental Results

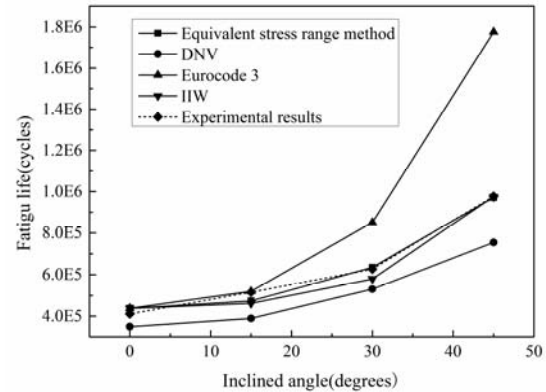


Figure 11. The Relationship Between Fatigue Life and Inclined Angle

It can be seen from Table 5 and Figures 10-11 that the fatigue life increases with an increase in the inclined angle due to a decrease in the normal stress range perpendicular to the weld. Fatigue life test results of welded joints with $\theta=15^\circ$, 30° , and 45° are 1.26, 1.52, and 2.38 times larger than that at $\theta=0^\circ$, respectively. Because the fatigue resistance value of the hot spot stress curve is conservative according to DNV, the fatigue life prediction results are less than the other three methods and approximately 0.8 times that of fatigue life test results. When the inclined angle θ is less than or equal to 15° , the fatigue life values predicted by the equivalent stress range method, Eurocode 3, and IIW have no significant difference and are close to experimental results. The fatigue life results predicted by Eurocode 3 are 35.5% and 81.8% larger than those of the experimental results at $\theta=30^\circ$ and 45° , respectively. The equivalent stress range method and IIW are in good agreement with the fatigue test data and the maximum relative error is only -10.5%. However, it is easier and more convenient to calculate the fatigue life using the equivalent stress

range method compared with IIW. Therefore, the equivalent stress range method is recommended to assess the fatigue life of inclined welded joints subjected to combined tension and shear stresses. The fatigue design curve of FAT100 is a better choice than FAT90.

5. CONCLUSIONS

Fatigue life assessment of inclined welded joints in steel bridges subjected to a combination of normal and shear stresses using the equivalent stress range method, DNV, Eurocode 3, and IIW are investigated in this study. Fatigue tests on cruciform welded joints with full penetration load-carrying welds inclined to the direction of the uniaxial cyclic loading are carried out. Hot spot normal and shear stress ranges are obtained with a linear extrapolation, and a sensitivity analysis is conducted to determine the appropriate mesh size. Based on the numerical analysis and fatigue test results, the following conclusions can be drawn.

(1) Fatigue failure in all of the specimens is initiated at the weld toe but propagates in different directions. There are two cracking types: (a) cracking along the weld; (b) cracking perpendicular to the direction of the applied load. When the inclined angle is 0° or 15° , the cracks propagate along the weld. However, when the inclined angle is 30° or 45° , the cracks propagate along the perpendicular direction of the applied load.

(2) With an increase in the inclined angle, the hot spot normal stress range decreases, while the hot spot shear stress range increases. The hot spot stress range increases with an increase in the mesh size. The mesh size used in IIW is more sensitive than that used in DNV due to the difference in linear extrapolation rules. When the minimum mesh size is less than $0.1t$, the effect of the mesh size on the hot spot stress range is fairly small. Fatigue evaluation techniques for complex welded joints in steel bridges should be based on accurate stress calculations determined by a mesh sensitivity analysis.

(3) The fatigue life increases with an increase in the inclined angle due to a decrease in the normal stress range perpendicular to the weld. The fatigue life test results of welded joints with $\theta=15^\circ$, 30° , and 45° are 1.26, 1.52, and 2.38 times larger than that at $\theta=0^\circ$, respectively. The design recommendations by Eurocode 3 tend to overpredict the fatigue life at large inclination angles. The FAT90 used by DNV is more conservative than the FAT100 recommended by Eurocode 3 and IIW, so that the fatigue life is underestimated. The equivalent stress range method and IIW are found to be in good agreement with the fatigue test data. However, the equivalent stress range method is recommended to assess the fatigue life of inclined welded joints subjected to a combination of normal and shear stresses due to the ease of implementation and low computational cost. The fatigue design curve of FAT100 in Eurocode 3 and IIW is appropriate for the equivalent stress range method.

ACKNOWLEDGEMENTS

This research is supported by National Natural Science Foundation of China (Grant Nos. 51708305, 51378430, and 51378431), Zhejiang Provincial Natural Science Foundation of China (Grant Nos. LQ17E080005, LY15E080012, and LY17E080007), and K. C. Wong Magna Fund in Ningbo University.

REFERENCES

- [1] Fricke, W., "Fatigue Analysis of Welded Joints: State of Development", *Marine Structures*, 2003, Vol. 16, No. 3, pp. 185-200.
- [2] Maddox, S.J., "Review of Fatigue Assessment Procedures for Welded Aluminium Structures", *International Journal of Fatigue*, 2003, Vol. 25, No. 12, pp. 1359-1378.
- [3] Park, W. and Miki, C., "Fatigue Assessment of Large-size Welded Joints based on the Effective Notch Stress Approach", *International Journal of Fatigue*, 2008, Vol. 30, No. 9, pp. 1556-1568.
- [4] Van Wingerde, A.M., Packer, J.A. and Wardenier, J., "Criteria for the Fatigue Assessment of Hollow Structural Section Connections", *Journal of Constructional Steel Research*, 1995, Vol. 35, No. 1, pp. 71-115.
- [5] EN 1993-1-9, "Eurocode 3: Design of Steel Structures Part 1-9: Fatigue", European Committee for Standardization, 2005.
- [6] Hobbacher, A., "Recommendations for Fatigue Design of Welded Joints and Components", the International Institute of Welding, 2007.
- [7] Det Norske, Veritas, "Fatigue Design of Offshore Steel Structures", Det Norske Veritas, 2010.
- [8] Dong, P., "A Structural Stress Definition and Numerical Implementation for Fatigue Analysis of Welded Joints", *International Journal of Fatigue*, 2001, Vol. 23, No. 10, pp. 865-876.
- [9] Fricke, W., "Recommended Hot-spot Analysis Procedure for Structural Details of Ships and FPSOs based on Round-robin FE Analyses", *International Journal of Offshore and Polar Engineering*, 2002, Vol. 12, No. 1, pp. 40-47.
- [10] Xiao, Z.G. and Yamada, K., "A Method of Determining Geometric Stress for Fatigue Strength Evaluation of Steel Welded Joints", *International Journal of Fatigue*, 2004, Vol. 26, No. 12, pp. 1277-1293.
- [11] Doerk, O., Fricke, W. and Weissenborn, C., "Comparison of Different Calculation Methods for Structural Stresses at Welded Joints", *International Journal of Fatigue*, 2003, Vol. 25, No. 5, pp. 359-369.
- [12] Lee, J., Seo, J. and Kim, M., et al., "Comparison of Hot Spot Stress Evaluation Methods for Welded Structures", *International Journal of Naval Architecture and Ocean Engineering*, 2010, Vol. 2, No. 4, pp. 200-210.
- [13] Liu, R., Liu, Y.Q. and Ji, B.H., et al., "Hot Spot Stress Analysis on Rib-deck Welded Joint in Orthotropic Steel Decks", *Journal of Constructional Steel Research*, 2014, Vol. 97, pp. 1-9.
- [14] Oh, D.J., Lee, J.M. and Kim, M.H., "Fatigue Strength Assessment of Invar Alloy Weld Joints using the Notch Stress approach", *Engineering Failure Analysis*, 2014, Vol. 42, pp. 87-99.
- [15] Barsoum, Z., Khurshid, M. and Barsoum, I., "Fatigue Strength Evaluation of Friction Stir Welded Aluminium Joints using the Nominal and Notch Stress Concepts", *Materials & Design*, 2012, Vol. 41, pp. 231-238.
- [16] Radaj, D., Sonsino, C.M. and Fricke, W., "Recent Developments in Local Concepts of Fatigue Assessment of Welded Joints", *International Journal of Fatigue*, 2009, Vol. 31, No. 1, pp. 2-11.
- [17] Sonsino, C.M., Fricke, W. and De Bruyne, F., et al., "Notch Stress Concepts for the Fatigue Assessment of Welded Joints-Background and Applications", *International Journal of Fatigue*, 2012, Vol. 34, No. 1, pp. 2-16.
- [18] Connor, R.J. and Fisher, J.W., "Consistent Approach to Calculating Stresses for Fatigue Design of Welded Rib-to-web Connections in Steel Orthotropic Bridge Decks", *Journal of Bridge Engineering*, 2006, Vol. 11, No. 5, pp. 517-525.

- [19] Wang, Z.Y. and Wang, Q.Y., "Fatigue Assessment of Welds Joining Corrugated Steel Webs to Flange Plates", *Engineering Structures*, 2014, Vol. 73, pp. 1-12.
- [20] Susmel, L., Sonsino, C.M. and Tovo, R., "Accuracy of the Modified Wöhler Curve Method Applied along with the $r_{\text{re}}=1$ mm concept in Estimating Lifetime of Welded Joints subjected to Multiaxial Fatigue Loading", *International Journal of Fatigue*, 2011, Vol. 33, No. 8, pp. 1075-1091.
- [21] Kim, I.T. and Yamada, K., "Fatigue Life Evaluation of Welded Joints under Combined Normal and Shear Stress Cycles", *International Journal of Fatigue*, 2005, Vol. 27, No. 6, pp. 695-701.
- [22] Lotsberg, I., "Assessment of Design Criteria for Fatigue Cracking from Weld Toes subjected to Proportional Loading", *Ships and Offshore Structures*, 2009, Vol. 4, No. 2, pp. 175-187.
- [23] Bäckström, M., "Multiaxial Fatigue Life Assessment of Welds based on Nominal and Hot Spot Stresses", Lappeenranta: Lappeenranta University of Technology, 2003.
- [24] SFS 2378, "Load Capacity of Welded Joints in Fatigue Loaded Steel Structures", Federation of the Finnish Metal and Engineering Industries, 1992.
- [25] Kainuma, S., Katsuki, H. and Iwai, I., et al., "Evaluation of Fatigue Strength of Friction Stir Butt-welded Aluminum Alloy Joints inclined to Applied Cyclic Stress", *International Journal of Fatigue*, 2008, Vol. 30, No. 5, pp. 870-876.
- [26] Jen, Y., Chang, L. and Fang, C., "Assessing the Fatigue Life of Butt-welded Joints under Oblique Loading by using Local Approaches", *International Journal of Fatigue*, 2008, Vol. 30, No. 4, pp. 603-613.
- [27] Susmel, L., "Nominal Stresses and Modified Wöhler Curve Method to Perform the Fatigue Assessment of Uniaxially Loaded Inclined Welds", *Proceedings of the Institution of Mechanical Engineers, Part C: Journal of Mechanical Engineering Science*, 2014, pp.1-10.
- [28] Khurshid, M., Barsoum, Z. and Barsoum, I., et al., "The Multiaxial Weld Root Fatigue of Butt Welded Joints subjected to Uniaxial Loading", *Fatigue & Fracture of Engineering Materials & Structures*, 2016, pp. 1-18.
- [29] GB/T 714, "Structural Steel for Bridge", Standardization Administration of the People's Republic of China, 2015.
- [30] Fatemi, A. and Socie, D.F., "A Critical Plane Approach to Multiaxial Fatigue Damage Including out-of-Phase Loading" *Fatigue & Fracture of Engineering Materials & Structures*, 1988, Vol. 11, No. 3, pp. 149-165.
- [31] Bäckström, M. and Marquis, G., "A Review of Multiaxial Fatigue of Weldments: Experimental Results, Design Code and Critical Plane Approaches", *Fatigue & Fracture of Engineering Materials & Structures*, 2001, Vol. 24, No. 5, pp. 279-291.
- [32] ANSYS Inc., "ANSYS Mechanical User's Guide", ANSYS Inc., 2012.
- [33] Kim, I.T. and Yamada, K., "Fatigue Behaviour of Fillet Welded Joints Inclined to a Uniaxial Load", *The International Institute of Welding*, 2004.
- [34] Lotsberg, I., "Fatigue Design Criteria as Function of the Principal Stress Direction Relative to the Weld Toe", *Proceedings of the ASME 27th International Conference on Offshore Mechanics and Arctic Engineering*, Estoril, Portugal, 2008.
- [35] Gough, H.J. and Pollard, H.V., "The Strength of Metals under Combined Alternating Stresses", *Proceedings of the Institution of Mechanical Engineers*, 1935, Vol. 131, No. 1, pp. 3-103.

PARTIAL INTERACTION SHEAR FLOW FORCES IN SIMPLY SUPPORTED COMPOSITE STEEL-CONCRETE BEAMS

Y. Zou, X.H. Zhou, J. Di and F.J. Qin*

Key Laboratory of New Technology for Construction of Cities in Mountain Area; School of Civil Engineering, Chongqing University, Chongqing, China, 400030

**(Corresponding author: Email: qinfengjiang@cqu.edu.cn)*

Received: 30 November 2016; Revised: 19 November 2017; Accepted: 19 November 2017

ABSTRACT: Most existing codes simply limit the shear stress range of stud shear connectors in composite steel-concrete beams to prevent the fatigue failure of studs, and the shear stress range is determined on the basis of a full interaction assumption, which ignores the effects of slip between steel and concrete. However, this hypothesis would overestimate the shear stress range, thereby resulting in the misestimate of the fatigue behaviours of studs. This study herein proposes a method to determine the interface shear flow under either a moving concentrated load or uniform load on the basis of the partial interaction assumption, which considers the effects of slip. Moreover, the interface shear flow, including the shear range and shear peak, under general loading can be predicted using the superposition of moving the concentrated load and uniform load. Furthermore, this method is simplified according to a practically possible range of parameters and is further validated by the finite element method (FEM) model in the case of composite beams with uniformly and non-uniformly distributed shear studs. Finally, a case study is performed using the proposed method and the existing methods to predict the shear stresses and the fatigue life of studs. The results show that the proposed method can provide more accurate and reliable predictions.

Keywords: Composite beams, stud shear connector, fatigue, partial interaction, shear flow

DOI: 10.18057/IJASC.2018.14.7

1. INTRODUCTION

Since the composite structures, particularly for composite bridges, are subjected to fatigue loading, the fatigue behaviours of steel beams and shear connectors in composite structures have attracted increasing attention among researchers and designers in the past decade [1]. Moreover, stud shear connectors are one of the most common connectors used in composite structures due to their advantages of excellent mechanical properties and construction convenience. However, most of the available literature indicates that fatigue loading could decrease the static strength, increase the plastic slip or even cause the fatigue failure of studs. As a consequence, it is of great significance to investigate the fatigue behaviours of studs in composite structures.

Most studies concerning stud fatigue focus on the relation between the shear stress range and the fatigue life of studs. Based on the experimental data, Johnson [2] proposed a simplified equation to predict the fatigue life of studs using the regression method. Although this equation considers the shear stress range as the only parameter, it has been adopted in Euro code 4 (EC4) [3,4] because of its reliability and simplicity. In 1990, Oehlers [5] investigated the reduction of the static strength of the shear studs due to high-cycle preloading, and this adverse effect is not considered in the existing codes. Moreover, based on the push-out experiments of 71 specimens according to the standard EC4, Hanswille observed the significant plastic slip and shear capacity reduction after high-cycle preloading, and he also argued that the peak load could influence the fatigue behaviours of studs besides the loading range [6,7]. Therefore, it is necessary to consider the effects of the peak load on the fatigue behaviour of shear studs, especially in the case of a large peak load. In addition, two full-scale tests of composite beams were conducted and the results verified that fatigue loading

reduced the interface stiffness and shear capacity of composite beams due to the fatigue behaviours of shear studs [8].

Although the fatigue behaviours of shear studs play a critical role in the performance of composite structures such as composite bridges, the current codes [3,4,9] simply limit the shear stress range based on the full interaction assumption and ignore the effects of the peak load on the fatigue behaviours of shear studs. However, because the partial interaction will significantly affect the interface shear flow force [10-24] and the fatigue behaviours are sensitive to shear force, the fatigue assessment of shear studs would be inaccurate according to the current codes or standards.

Nowadays, various formulations have been developed to determine the stress state of shear studs since it is quite crucial to assess their fatigue behaviours. Seracino [11,12] developed an approach to determine the partial interaction distribution of the interface shear flow of composite beams subjected to a moving concentrated load. Nevertheless, this approach does not take into account the uniform load case, nor analyses the applicability of the approach for composite beams with non-uniformly distributed shear studs. Moreover, it could provide inaccurate results in case of a weak composite action.

According to the linear elastic partial interaction theory, this paper aims to develop a method to determine the distribution of the interface shear flow of the composite beams subjected to the moving concentrated load and/or uniform load. In addition, in the linear elastic analysis, the interface shear flow, including the shear force range and the peak shear, under general loading conditions can be predicted by superposing both the moving concentrated load and the uniform load. Thus, combined with a suitable fatigue formula of studs, the proposed method can be used to more accurately predict the fatigue state of studs under general loading conditions. Furthermore, the proposed method is validated in comparison with the FEM model for cases of composite beams with uniformly and non-uniformly distributed shear studs. Finally, a case study aiming to determine the shear stresses by means of the proposed method and other available methods is given.

2. LINEAR ELASTIC PARTIAL INTERACTION THEORY

The method developed herein is based on the linear elastic partial interaction theory originally developed by Newmark et al. [10]. The slip s at the design point x measured from the mid-span is given by the following equation [13]:

$$s = K_1 \sinh(\alpha x) + K_2 \cosh(\alpha x) + \beta V^* \quad (1)$$

where V^* is the total vertical shear at cross-section x ; K_1 and K_2 are the integration constants; the parameters α and β govern the behaviour of the composite beam, and they are functions of material and geometric properties of the cross section and the stiffness of the shear connection as follows:

$$\alpha = \sqrt{\frac{k}{pE_s} \left(\frac{n}{A_c} + \frac{1}{A_s} + \frac{nd_c^2}{nI_s + I_c} \right)} \quad (2)$$

and

$$\beta = \frac{d_c p}{k[d_c^2 + (I_s + \frac{I_c}{n})(\frac{n}{A_c} + \frac{1}{A_s})]} \quad (3)$$

where k is the secant stiffness [25]; p is the shear connector spacing; d_c is the distance between the centroids of the steel and concrete components; E is the modulus of elasticity; I is the second moment of area; A is the area of cross-section; the subscripts s and c represent the steel and concrete, respectively; n is the modular ratio of E_s/E_c .

The load-slip relationship is

$$q_{pi} = \frac{ks}{p} \quad (4)$$

where q_{pi} is the shear flow fore based on the partial interaction theory, and the subscript pi represents the partial interaction.

3. DISTRIBUTION OF THE PARTIAL INTERACTION SHEAR FLOW FORCES

In general, the loading range is dominated by the fluctuations of the live load, while the peak load is the combination of the live load and the dead load. In practice, a uniform load and a moving concentrated load, as shown in Figure 1, can be adopted to represent most of the traffic loadings.

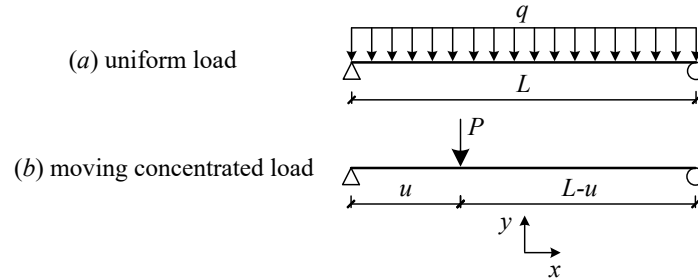


Figure 1. Load Cases

L is the length of the beam; u is the distance from the loading point to the left support of the beam; q is the magnitude of the uniform load; P is the magnitude of the moving concentrated load. The mid-span is assumed as the origin of the coordinates.

3.1 DISTRIBUTION UNDER THE UNIFORM LOAD

Under the uniform load, the total vertical shear $V^* = -qx$. Substituting it into Eq. 1 gives the distribution of slip:

$$s = K_1 \sinh(\alpha x) + K_2 \cosh(\alpha x) - \beta qx \quad (5)$$

The integration constants K_1 and K_2 can be determined using the following two boundary conditions:

$$\frac{ds}{dx} = 0 \quad x = -L/2 \quad (6)$$

$$\frac{ds}{dx} = 0 \quad x = L / 2 \quad (7)$$

where ds/dx =slip strain, that is the difference between the axial strain in the steel and the concrete at the interface. Due to the zero longitudinal strain in the steel and the concrete at two supports, the slip strain is equal to zero. Solving the simultaneous equations, the integration constants can be obtained as follows:

$$K_1 = \frac{\beta q L}{\alpha L \cosh(\alpha L / 2)} \quad (8)$$

$$K_2 = 0 \quad (9)$$

Substituting Eq. 4 into 5, we obtain the distribution of the interface shear flow:

$$\begin{aligned} q_{pi} &= \frac{\beta k q L}{2 p} \left[\frac{2 \sinh(\alpha x)}{\alpha L \cosh(\alpha L / 2)} - \frac{2x}{L} \right] \\ &= q_0 \left[\frac{2 \sinh(\alpha x)}{\alpha L \cosh(\alpha L / 2)} - \frac{2x}{L} \right] \end{aligned} \quad (10)$$

Where

$$q_0 = \beta k q L / 2 p \quad (11)$$

The q_0 is the full interaction interface shear flow force under uniform load at the left support.

As shown in Eq. 10, αL is a parameter considering the material and geometric properties of the beam and the stiffness of the shear connections, and can represent the effects of a partial interaction on the distribution of the interface shear flow. In fact, previous studies [14-16] on composite beams state that the parameter αL governs the partial interaction behaviour of the composite beams with the interlayer slip. When $\alpha L=0$, there is no interaction between steel and concrete; with the increase of αL , the interaction between steel and concrete increases; When $\alpha L=\infty$, the composite beam satisfies the hypothesis of full interaction. Additionally, the practical value of αL is normally greater than 5 [26] in common cases; therefore, the parameter αL is adopted to investigate the effects of a partial interaction on the shear flow distribution.

In this part, the proposed method is verified as compared with the FEM model for a simply supported composite beam with a 30m span. The details regarding the composite structures including the material and geometric properties are shown in Figure 2(a) and the numerical simulation of the composite beam is conducted using a commercial FEM software (ABAQUS) [27]. As shown in Figure 2(b), the shear connection is modelled by shear springs with a spacing of 150 mm and the concrete slab and steel beam are modelled by solid and shell elements [24]. The transverse and longitudinal relative displacements between the slab and steel beam are constrained by coupling nodes. The change of parameter αL is achieved by the change in stiffness of the shear springs.

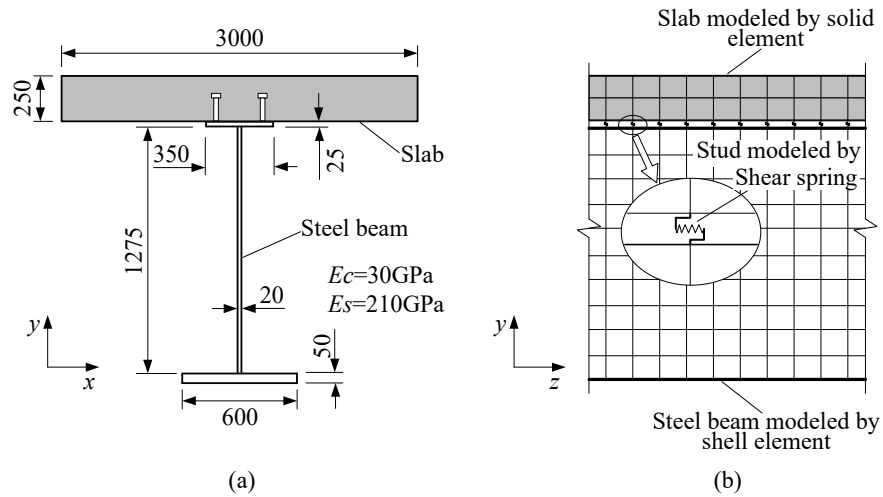
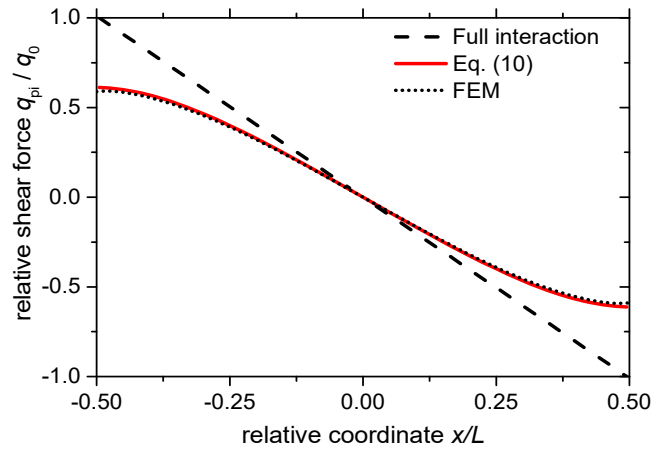
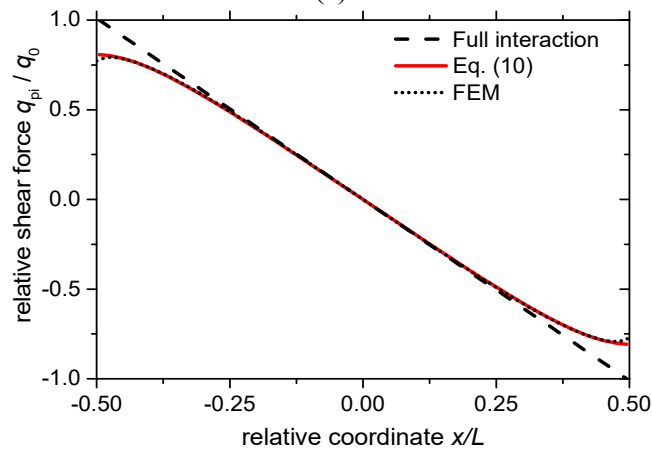


Figure 2. (a) Cross-section of General Simply Supported Composite Beam ;
(b) Modelling of Shear Connectors, Slab and Steel Beam



(a)



(b)

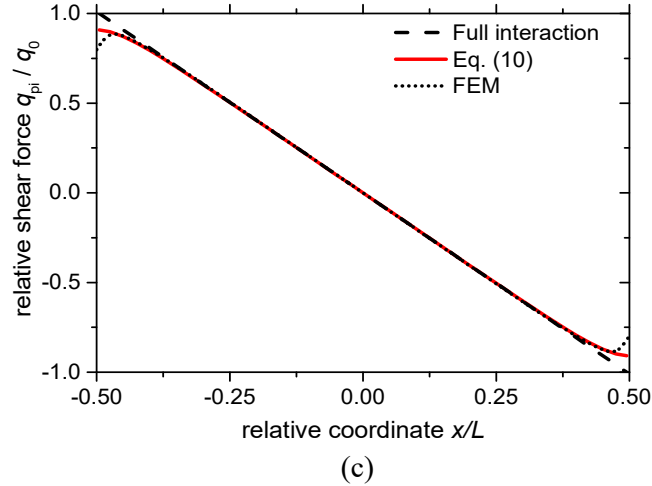


Figure 3. Distribution of q_{pi}/q_0 under Uniform Load: (a) $\alpha L = 5$; (b) $\alpha L = 10$; (c) $\alpha L = 20$

As shown in Figure 3, with the decrease of αL , the difference between the result of the proposed method and the full interaction method increases. When αL is equal to 5, which implies a relatively weak composite action, the maximum discrepancy reaches about 40%, and thus leads to the use of the full-interaction theory being quite unreliable. In cases of larger values of αL , the discrepancies between the results by the proposed method and those by the full-interaction method are also quite obvious. As expected, there is excellent agreement between the proposed method and the numerical simulation.

3.2 DISTRIBUTION UNDER A MOVING CONCENTRATED LOAD

Seracino [11,12] proposed a method to determine the reduction in the full interaction shear flow due to a partial interaction. The reduction is defined by the following reduction factor

$$RF_R = \frac{q_{pi}}{q_{fi}} \quad (12)$$

where q_{pi} is the partial interaction interface shear flow force and q_{fi} is the full interaction interface shear flow force. The simplified distribution of RF_R , shown in Fig.4, is determined by $(RF_R)_{sup}$, $(RF_R)_{const}$, and l_{const} . The simplified expression of RF_R at supports is

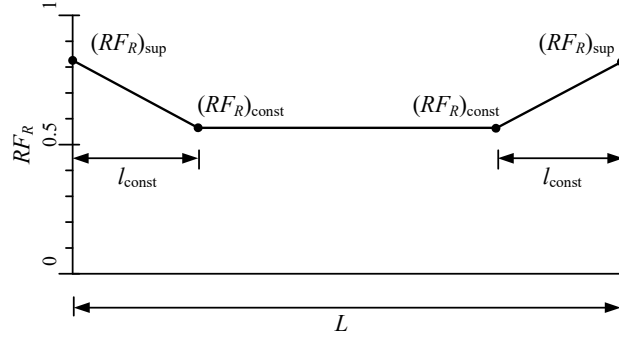
$$(RF_R)_{sup} = 1 + \frac{1}{\alpha L} \ln\left(\frac{1}{\alpha L}\right) - \frac{2}{(\alpha L)^2 + 1} \quad (13)$$

The displacement l_{const} that defines the location where RF_R first becomes constant when measured from the supports is

$$l_{const} = \frac{-1}{\alpha} \ln\left(\frac{1}{\alpha L}\right) \quad (14)$$

Finally, the constant magnitude of RF_R in the vicinity of the mid-span is

$$(RF_R)_{const} = 1 + \frac{1}{\alpha L} \left\{ \ln\left[\frac{2}{(\alpha L)^2 + 1}\right] - 1 \right\} \quad (15)$$

Figure 4. Simplified Shear Flow Range Reduction Factors RF_R [11,12]

The disadvantage of the method proposed by Seracino is its computational complexity, while the values in the vicinity of the supports require a linear interpolation. In addition, this method is compared with the method proposed herein in the context of accuracy in the following part.

In this part, the method proposed herein is presented in detail. For the composite structures subjected to a moving concentrated load P , the shear force distribution is that, on the left side of the load point, $V^*=P(L-u)/L$; on the right side of the load point, $V^*=-Pu/L$. By combining with Eq. 1, we can obtain the slip distribution as follows:

$$s_L = K_1 \sinh(\alpha x) + K_2 \cosh(\alpha x) + \beta P \frac{L-u}{L} \quad (-L/2 \leq x < u-L/2) \quad (16)$$

$$s_R = K_3 \sinh(\alpha x) + K_4 \cosh(\alpha x) - \beta P \frac{u}{L} \quad (u-L/2 \leq x \leq L/2) \quad (17)$$

where the subscripts L and R represent the left and right shear spans. For the purpose of analysis convenience in the following part, Eqs. 16 and 17 in the exponential form are adopted as follows:

$$s_L = C_1 e^{\alpha x} + C_2 e^{-\alpha x} + \beta P \frac{L-u}{L} \quad (-L/2 \leq x < u-L/2) \quad (18)$$

$$s_R = C_3 e^{\alpha x} + C_4 e^{-\alpha x} - \beta P \frac{u}{L} \quad (u-L/2 \leq x \leq L/2) \quad (19)$$

The following four boundary conditions are used to determine the integration constants:

$$\frac{ds_L}{dx} = 0 \quad x = -L/2 \quad (20)$$

$$\frac{ds_R}{dx} = 0 \quad x = L/2 \quad (21)$$

$$s_L = s_R \quad x = u-L/2 \quad (22)$$

$$\frac{ds_L}{dx} = \frac{ds_R}{dx} \quad x = u-L/2 \quad (23)$$

Eqs. 20 and 21 represent the boundary conditions at ends, same as the aforementioned Eqs. 6 and 7. Additionally, Eqs. 22 and 23 are obtained according to the continuity conditions of deformation. Solving the simultaneous equations gives the integration constants:

$$C_1 = \frac{-\beta P}{2} \frac{e^{\alpha L} (e^{\alpha(3L/2-u)} - e^{\alpha(u-L/2)})}{e^{2\alpha L-1}} \quad (24)$$

$$C_2 = \frac{-\beta P}{2} \frac{(e^{\alpha(3L/2-u)} - e^{\alpha(u-L/2)})}{e^{2\alpha L-1}} \quad (25)$$

$$C_3 = \frac{\beta P}{2} \frac{(e^{\alpha(L/2+u)} - e^{\alpha(L/2-u)})}{e^{2\alpha L-1}} \quad (26)$$

$$C_4 = \frac{\beta P}{2} \frac{e^{\alpha L} (e^{\alpha(L/2+u)} - e^{\alpha(u-L/2)})}{e^{2\alpha L-1}} \quad (27)$$

Substituting Eqs. 24 and 25 into Eq. 18 and 4 gives the distribution of interface shear flow force on the left shear span:

$$\begin{aligned} q_{pi} &= \frac{\beta k P}{p} \left[\frac{L-u}{L} - \frac{e^{2\alpha u} - e^{2\alpha L}}{1 - e^{2\alpha L}} \left(\frac{e^{\alpha(L+x)} + e^{-\alpha x}}{2e^{\alpha(L/2+u)}} \right) \right] \\ &= q_0 \left[\frac{L-u}{L} - f(u) \left(\frac{e^{\alpha(L+x)} + e^{-\alpha x}}{2e^{\alpha(L/2+u)}} \right) \right] \end{aligned} \quad (28)$$

where

$$q_0 = \beta k P / p \quad (29)$$

$$f(u) = \frac{e^{2\alpha u} - e^{2\alpha L}}{1 - e^{2\alpha L}} \quad (30)$$

The q_0 is the maximum full interaction interface shear flow force under a moving concentrated load at the left support. As the envelope curve of the interface shear flow is antisymmetric, it is straightforward to determine the minimum of the interface shear flow using the antisymmetric function in Eq. 28. As q_{pi} is the function of u and x , the load position corresponding to the maximum partial interaction positive shear flow at design point x satisfies the following equation:

$$\frac{dq_{pi}(x,u)}{du} = 0 \quad (31)$$

However, due to the complexity of Eq. 30, it is quite cumbersome to assess an explicit solution of u_{max} . As the distribution of $f(u)$ illustrated in Figure 5 is close to unity when the value of αL is greater than 5, it is reasonable to assume that $f(u)=1$.

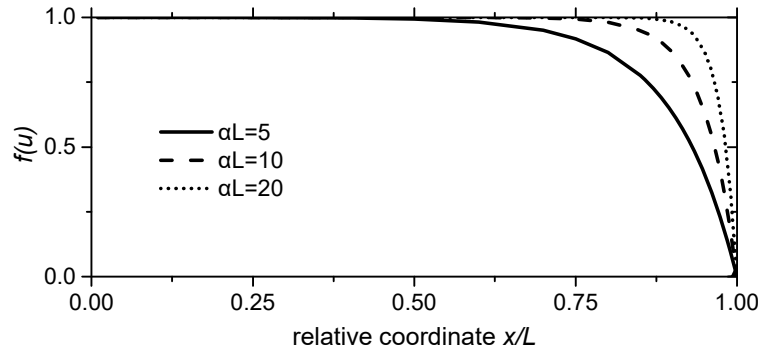


Figure 5. Distribution of $f(u)$

Substituting $f(u)=1$ into Eq. 31, and simplifying, gives

$$u_{\max} = \frac{1}{\alpha} \ln[\alpha L \cosh(\alpha L / 2 + \alpha x)] \quad (32)$$

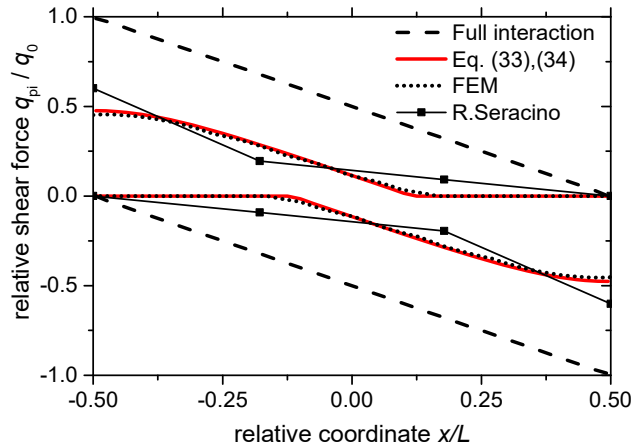
Substituting Eq. 32 into Eq. 28, and simplifying, gives

$$q_{\text{pi,max}} = q_0 \left\{ 1 - \frac{\ln[\alpha L \cosh(\alpha L / 2 + \alpha x)] + 1}{\alpha L} \right\} \quad (33)$$

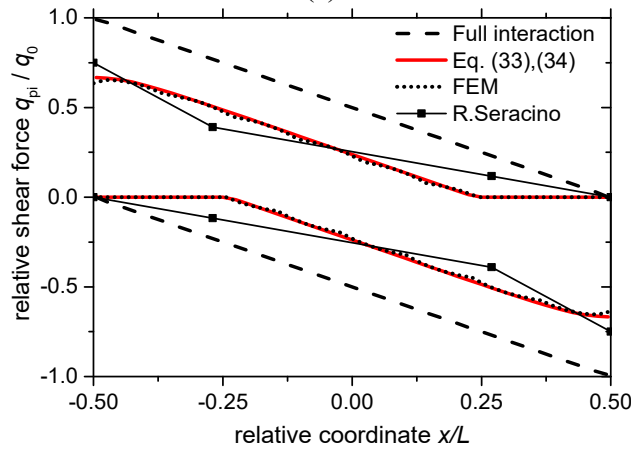
Since the maximum interface shear flow is required, let $q_{\text{pi,max}}$ equal to zero when $q_{\text{pi,max}}$ is less than 0. Since the envelope curve of the interface shear flow is antisymmetric, the minimum of the interface shear flow is given

$$q_{\text{pi,min}} = -q_0 \left\{ 1 - \frac{\ln[\alpha L \cosh(\alpha L / 2 - \alpha x)] - 1}{\alpha L} \right\} \quad (34)$$

Let $q_{\text{pi,min}}$ equal to zero when $q_{\text{pi,min}}$ is greater than 0. The maximum or minimum shear flow under a moving concentrated load at each design point can be determined using Eqs. 33 and 34, as the red line indicates in Figure 6.



(a)



(b)

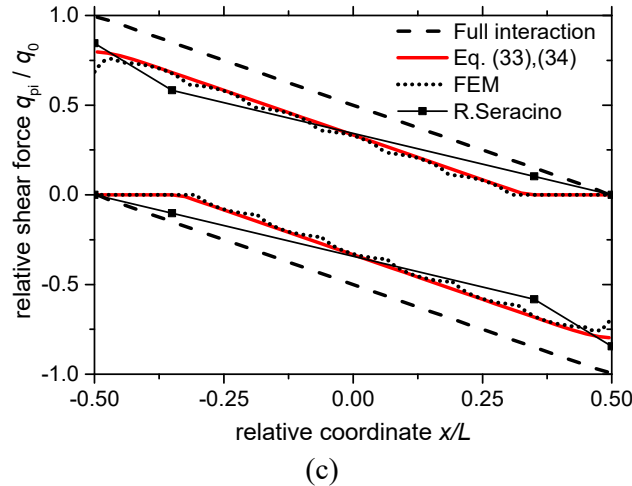


Figure 6. Envelope Curve of the Interface Shear Flow under a Moving Concentrated Load:
(a) $\alpha L = 5$; (b) $\alpha L = 10$; (c) $\alpha L = 20$

As illustrated in Figure 6, under a moving concentrated load, the reduction of shear flow due to partial interaction reached about 50% when αL is equal to 5, and this reduction is more remarkable than that in the uniform loading condition. The proposed method is once again in very good agreement with the numerical simulation and is more accurate than the method proposed by Seracino R [11,12].

4. ANALYSIS OF APPLICABILITY

The theoretical derivation of the partial interaction theory is based on the assumption that the distribution of shear studs is uniform. However, the distribution of shear studs is usually non-uniform because of the non-uniform distribution of the interface shear force. It is necessary to validate the proposed approach for the composite beams with non-uniformly distributed shear studs by the FEM model.

Figure 7 shows three cases of composite beams with non-uniformly distributed shear studs, where L is the length of the beam, p is the shear connector spacing, the reference connector spacing p_0 is 300mm. The material and geometric properties of the composite beam are shown in Figure 2(a) and the stiffness of each row of studs is 1.063×10^4 kN/m. In cases 1 and 3, the distribution density of studs on both sides of the beam is about twice that at the mid-span, but the absolute distribution density in case 3 is much larger than that in case 1. In case 2, distribution density of studs on both sides of the beam is about four times that at the mid-span. As the change of the distribution of studs is reflected in the change of parameter αL , the value of αL is also shown in Figure 7. The red solid lines in Figs. 8 and 9 show the distribution of the shear flow determined by the respective values of α .

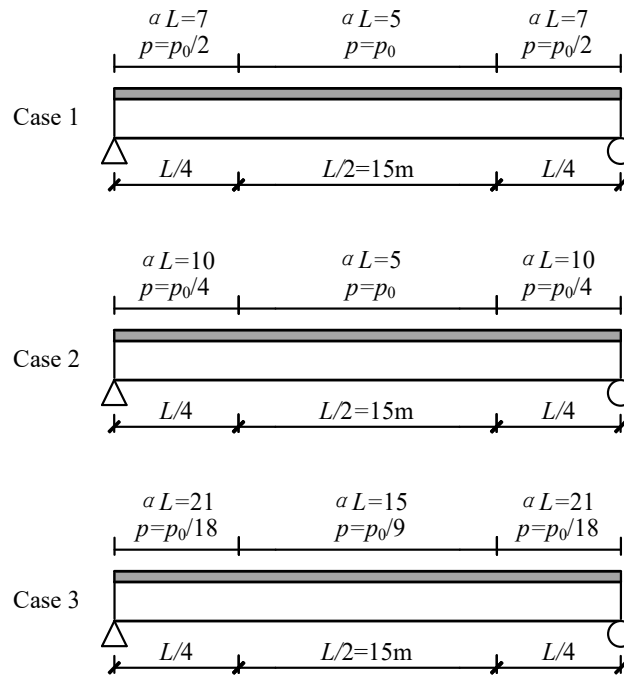
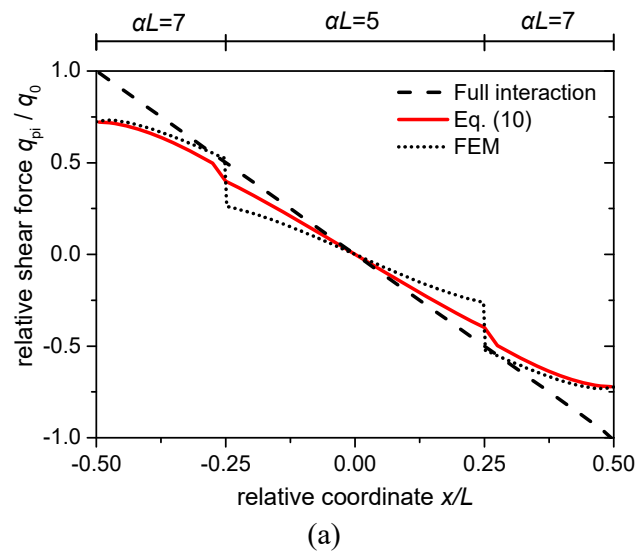


Figure 7. Three Cases of Composite Beams with Non-uniformly Distributed Shear Studs



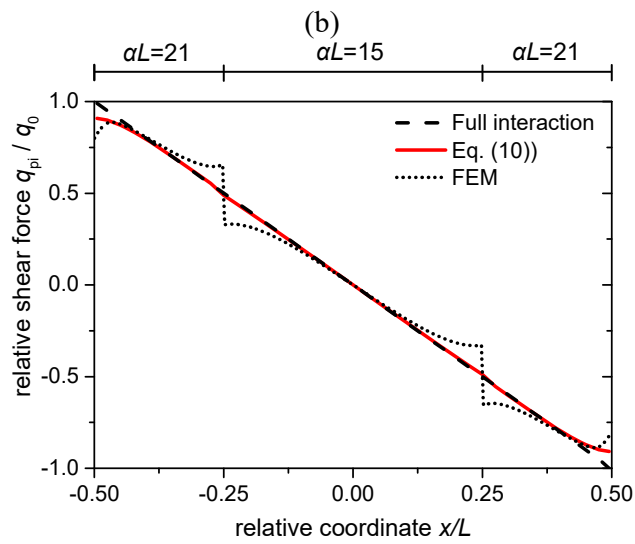
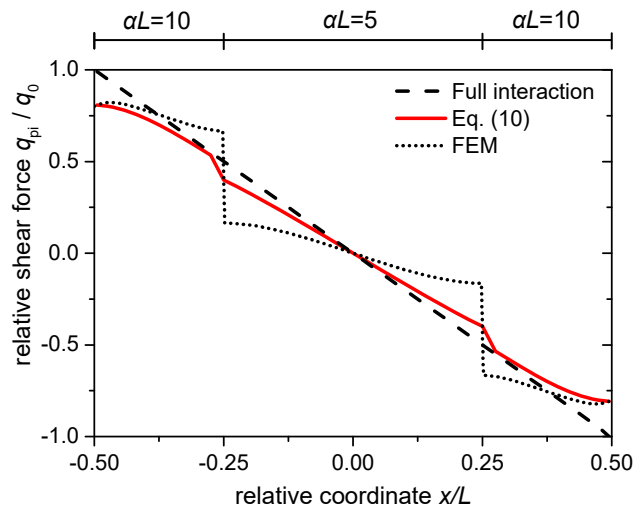
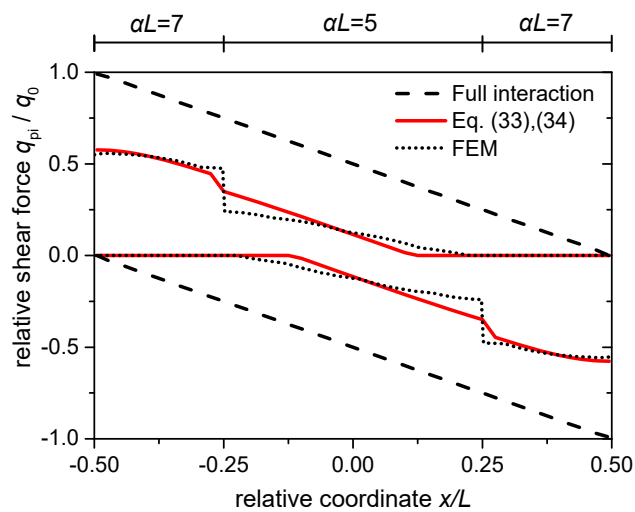


Figure 8. Distribution of q_{pi}/q_0 under Uniform Load: (a) Case 1; (b) Case 2; (c) Case 3



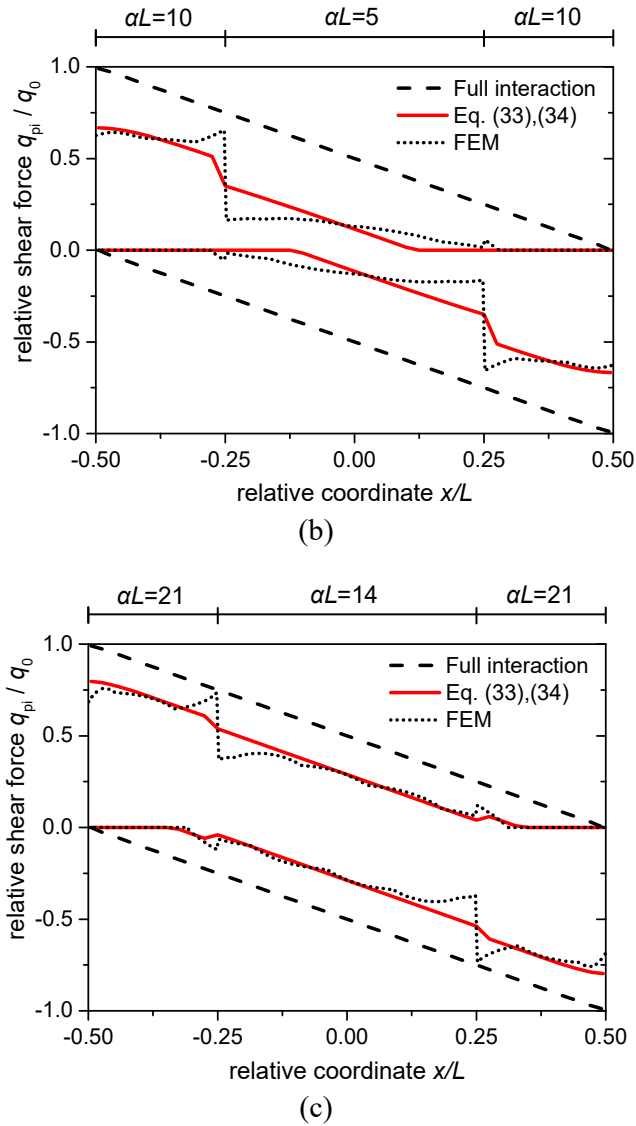


Figure 9. Distribution of q_{pi}/q_0 under a Moving Concentrated Load:
(a) Case 1; (b) Case 2; (c) Case 3

When the distribution density of studs on both sides is about four times that at mid-span, as illustrated in Figure 8(b) and 9(b), there are differences between the proposed method and the numerical simulation, especially for the uniform load case. However, the significantly different distribution density of studs is quite rare in practice.

When the distribution density of studs on both sides is about twice that at the mid-span, as illustrated in Figure 8(a) and (c) and Figure 9(a) and (c), with the increase in αL , the discrepancies between the proposed method and the numerical simulation also increase. However, limited differences are observed in the local area where α varies, and the proposed method is in good agreement with the numerical simulation on the other locations, especially at the support where the shear force is at a maximum value. This shows that the distribution of shear flows on each part is mainly determined by the respective value of α , and the proposed method is also applicable for composite beams with non-uniformly distributed shear studs.

5. CASE STUDY

The following example demonstrates the use of the proposed method in determining the partial interaction force on studs at support and compares the results with those obtained from the full interaction method and from the method developed by Seracino R [11,12]. Combined with the fatigue life predicting equation provided by Euro code 4 [3,4] and Hanswille [7], the fatigue life of studs is predicted to illustrate the accuracy and applicability of different methods. The prediction of the reduction of static strength and accumulation of plastic slip due to fatigue loading is not analysed in this paper, but the predicting process is similar to that of fatigue life.

The Euro code 4 [3,3] specifies that the fatigue life of studs can be calculated as:

$$\lg N + 8 \lg \Delta \tau = 21.935 \quad (35)$$

where the $\Delta \tau$ is the shear stress range of studs, N is the fatigue life of studs.

Hanswille G [7] suggests that the fatigue life of studs should be calculated as:

$$\lg N = \frac{P_{u,0} - P_{\max}}{0.1267 P_{u,0} - 0.1344 P_{\text{mean}}} \quad (36)$$

where $P_{u,0}$ is the static strength of studs, P_{\max} is the peak of fatigue loading, P_{mean} is the mean value of the fatigue loading, and N is the fatigue life of the studs.

Suppose that a 30m long simply supported composite beam is subjected to a uniform load of 20kN/m as dead load and a moving concentrated load of 320kN as live load. The material and geometric properties of the composite beam are shown in Figure 2. a. A uniform distribution of connectors was used consisting of two rows of 19 mm diameter studs with a spacing of 150 mm, giving a static strength of 118.3 kN per stud and connector stiffness of 2.736×10^4 kN/ m per stud. In this example, the αL is equal to 11.34 according to Eq. 2. The fatigue shear stress range is given by Eq. 33, because the live load in this example is a moving concentrated load. The shear stress caused by the dead load is given by Eq. 10, because the dead load in this example is a uniform load. The shear stress peak is the sum of the shear stress range and the shear stress caused by dead load. Detailed calculation results are given in Table 1.

Table 1. Comparisons of Shear Stress and Fatigue Life Predicted by Different Methods

Calculating method of stud force	Shear stress range/MPa	Shear stress peak/MPa	Fatigue life/ 10^6	
			Euro code 4	Hanswille G
Full interaction	58.6	113.4	62.2	20.5
Seracino R	45.1	—	503.8	—
Proposed method	40.8	86.0	1117.2	33.2

After consideration of the partial interaction effect, as illustrated in Table 1, the calculated shear stress decreased and the predicted fatigue life of studs significantly increased. Compared with the shear stress range predicted by the full interaction theory, the result of the method developed by Seracino R is reduced by about 23%, and the result of the proposed method is reduced by about 30%. Combined with the fatigue life predicting equation provided by Euro code 4, fatigue life predicted by the method developed by Seracino R is about 8 times that of the full interaction theory, and the proposed method predicts about 18 times the fatigue life expectancy of the full interaction

theory. Compared to the method developed by Seracino R, the proposed method can make full use of the beneficial effect of partial interaction. Combined with the fatigue life predicting equation provided by Hanswille G, fatigue life predicted by proposed method is about 62% higher than that of the full interaction theory. The method developed by Seracino R cannot be applied to the equation provided by Hanswille G, because the method does not consider the influence of dead load.

6. CONCLUSIONS

A method has been developed to determine the distribution of partial interaction interface shear flows of composite beams subjected to a moving concentrated load and uniform load. This method is validated by the finite element model (FEM) of the composite beam with uniformly and non-uniformly distributed shear studs. Also, an example of predicting shear stresses and the fatigue life of studs in composite beams with different methods is given. The main conclusions from the study are as follows:

- (1) Under the uniform load, the reduction of shear flow due to partial interaction can reach about 40% when the composite action is relatively weak. The proposed method is in excellent agreement with the numerical simulation.
- (2) Under a moving concentrated load, the reduction of shear flow due to partial interaction reach about 50% when the composite action is relatively weak. Since the proposed method is reasonably simplified according to a practically possible range of αL , it is in better agreement with the numerical simulation than the existing methods. When used with an appropriate fatigue model, this method can be used to more accurately assess the fatigue behaviour of studs.
- (3) When the proposed method is applied to composite beams with uniformly or non-uniformly distributed shear studs, the discrepancies between the proposed method and numerical simulation are obvious only in the local area where the change of stiffness is drastic. On the other positions, especially at supports where the shear force is maximum, the proposed method is in good agreement with the numerical simulation.
- (4) The interface shear flows, including shear range and peak shear, can be predicted using the superposition of the moving concentrated load and uniform load, and therefore the method can be applied to more general loading conditions. When used with an appropriate fatigue model, this method can provide an accurate and reliable assessment of the fatigue behaviours of shear studs.

ACKNOWLEDGMENT

The authors express their sincere gratitude for the financial support provided by the National Key R&D Program of China (2016YFC0701202), Science and technology R&D Project of China Communications Construction Co (2014-ZJKJ-PTJC03), the Traffic Science and Technology Projects of the Ministry of Transport (2013318798320), and the National Natural Science Foundation of China (51608069).

REFERENCES

- [1] Wang, Y.H., Nie, J.G. and Li, J.J., "Study on Fatigue Property of Steel-concrete Composite Beams and Studs", *Journal of Constructional Steel Research*, 2014, Vol. 94, No. 94, pp. 1-10.
- [2] Johnson, R.P., "Shear Connection for Composite Bridges and Eurocode 4: Part 2", *Proceedings of Composite Construction-Conventional and Innovative, International Conference, Innsbruck, Austria*, 1997, pp. 573-578.
- [3] EN 1994-1-1, "Eurocode 4: Design of Composite Steel and Concrete Structures. Part 1-1: General Rules and Rules for Buildings", European Committee for Standardization, 2004.
- [4] EN 1994-2, "Eurocode 4: Design of Composite Steel and Concrete Structures. Part 2: General Rules and Rules for Bridges", European Committee for Standardization, 2004.
- [5] Oehlers, D.J., "Deterioration in Strength of Stud Connectors in Composite Bridge Beams", *Journal of Structural Engineering*, 1990, Vol. 116, No. 12, pp. 3417-31.
- [6] Hanswille, G., Porsch, M. and Ustundag, C., "Resistance of Headed Studs Subjected to Fatigue Loading, Part I: Experimental Study", *Journal of Constructional Steel Research*, 2007, Vol. 63, No. 4, pp. 475-484.
- [7] Hanswille, G., Porsch, M. and Ustundag, C., "Resistance of Headed Studs Subjected to Fatigue Loading, Part II: Analytical Study", *Journal of Constructional Steel Research*, 2007, Vol. 63, No. 4, pp. 485-493.
- [8] Hanswille, G. and Porsch, M., "Lifetime Oriented Design Concepts of Steel-Concrete Composite Structures Subjected to Fatigue Loading", *Proceedings of Composite Construction in Steel and Concrete VI, ASCE*, 2011, pp. 14-25.
- [9] AASHTO LRFD, "Bridge Design Specifications", 3rd Ed. American Association of State Highway and Transportation Officials, 2004.
- [10] Newmark, N.M., "Test and Analysis of Composite Beams with Incomplete Interaction", *Proc. Society for Experimental Stress Analysis, New York*, 1951, Vol. 9, No. 1, pp. 75-92.
- [11] Seracino, R., Oehlers, D.J. and Yeo, M.F., "Partial-interaction Fatigue Assessment of Stud Shear Connectors in Composite Bridge Beams", *Structural Engineering and Mechanics*, 2002, Vol. 13, No. 4, pp. 455-464.
- [12] Seracino, R., Lee, C.T. and Tan, Z., "Partial Interaction Shear Flow Forces in Continuous Composite Steel-concrete Beams", *Journal of Structural Engineering, ASCE*, 2006, Vol. 132, No. 2, pp. 227-236.
- [13] Johnson, R.P., "Composite Structures of Steel and Concrete, Vol. 1: Beams, columns, frames and applications in buildings", 3rd Ed. Oxford: Blackwell Scientific, 2004.
- [14] Girhammar, U.A. and Gopu, V.K.A., "Composite Beam-Columns with Interlayer Slip—Exact Analysis", *Journal of Structural Engineering, ASCE*, 1993, Vol. 119, No. 4, pp. 1265-1282.
- [15] Girhammar, U.A. and Pan, D. H., "Exact Static Analysis of Partially Composite Beams and Beam-columns", *International Journal of Mechanical Sciences*, 2007, Vol. 49, No. 2, pp. 239-255.
- [16] Girhammar, U.A., "A Simplified Analysis Method for Composite Beams with Interlayer Slip", *International Journal of Mechanical Sciences*, 2009, Vol. 51, No. 7, pp. 515-530.
- [17] Ranzi, G., Bradford, M.A. and Uy, B., "A General Method of Analysis of Composite Beams with Partial Interaction", *Steel & Composite Structures*, 2003, Vol. 3, No. 3, pp. 169-184.
- [18] Zanuy, C., "Analytical Equations for Interfacial Stresses of Composite Beams due to Shrinkage", *International Journal of Steel Structures*, 2015, Vol. 15, No. 4, pp. 999-1010.
- [19] Hwang, J.W. and Kwak, H.G., "Improved FE Model to Simulate Interfacial Bond-slip Behavior in Composite Beams under Cyclic Loadings", *Computers & Structures*, 2013, Vol. 125, No. 1, pp. 164-176.

- [20] Gara, F., Ranzi, G. and Leoni, G., “Partial Interaction Analysis with Shear-lag Effects of Composite Bridges: A Finite Element Implementation for Design Applications”, *Advanced Steel Construction*, 2011, Vol. 7, No. 1, pp. 1-16.
- [21] Mirza, O. and Uy, B., “Effects of Strain Regimes on the Behaviour of Headed Stud Shear Connectors for Composite Steel-concrete Beams”, *Advanced Steel Construction*, 2010, Vol. 6, No. 1, pp. 635-661.
- [22] Lin, W.W. and Yoda, T., “Experimental and Numerical Study on Mechanical Behavior of Composite Girders under Hogging Moment”, *Advanced Steel Construction*, 2013, Vol. 9, No. 4, pp. 309-333.
- [23] Aleksandar, P., Besevic. M.T. and Vojnic-Purcar, M., “A Numerical Method for Free Vibration of Axially Loaded Composite Timoshenko Beam”, *Advanced Steel Construction*, 2016, Vol. 12, No. 1, pp. 55-65.
- [24] Queiroz, F.D., Vellasco, P. and Nethercot, D.A., “Finite Element Modelling of Composite Beams with Full and Partial Shear Connection”, *Journal of Constructional Steel Research*, 2007, Vol. 63, No. 4, pp. 505-521.
- [25] Wang, Y.C., “Deflection of Steel-concrete Composite Beams with Partial Shear Interaction”, *Journal of Structural Engineering, ASCE*, 1998, Vol. 124, No. 10, pp. 1159–65.
- [26] Nie, J., Shen, J. and Yu, Z., “A Reduced Rigidity Method for Calculating Deformation of Composite Steel-concrete Beams”, *China Civil Engineering Journal*, 1995, Vol. 28, No. 6, pp. 11-17. (in Chinese)
- [27] ABAQUS Documentation, Version 6.10, Dassault System, USA, 2010.

SEISMIC BEHAVIOR OF BOLTED CONNECTIONS WITH SLOT BOLT HOLES AT AMBIENT AND ELEVATED TEMPERATURE

Z.X. Hou¹, C. Gong², Y. Zhang^{1,5}, Y.Z. Sun¹, J. Jiang^{1,3,*} and G.Q. Li^{1,4}

¹ College of Civil Engineering, Tongji University, Shanghai 200092, China

² Central Research Institute of Building and Construction Co., Ltd, Beijing 100088, China

³ Engineering Laboratory, National Institute of Standards and Technology, MD 20899-8611, USA

⁴ State Key Laboratory for Disaster Reduction in Civil Engineering, Tongji University, Shanghai 200092, China

⁵ Department of Building Engineering, Logistics University of PAPF, Tianjin 300309, China

*(Corresponding author: Email: jiangjian_0131@163.com)

Received: 6 March 2017; Revised: 30 October 2017; Accepted: 25 November 2017

ABSTRACT: This paper experimentally studies the seismic behavior of high strength bolted connections with slot bolt holes at ambient and elevated temperatures. A total of 6 specimens varying in bolt diameters, pretensions, temperatures are designed and tested. The results show that the connections with slot holes at both ambient and elevated temperatures have good energy dissipation capacity. It is found that connections with M30 bolts have better energy dissipation capacity and load-bearing capacity than those with M20 bolts, due to the larger friction force and sliding distance in M30 bolts since they have a larger pretention and wider slot hole. The sliding forces of the connections decrease with the increase of the number of loops. The sliding force decrease by about 50% after 60 loops at elevated temperatures, compared with 35% at ambient temperature. While the ultimate bearing capacity of the connections does not decrease much. The friction coefficient and area of hysteresis curves decrease in a similar trend by about 40% after the first 30 loops. After 60 loops, they are reduced to 40% and 50% of their initial values for the connections with M20 bolts and M30 bolts, respectively. The experimental results indicate the potential application of the connections with slot bolt holes for a dual-function component in a structure to simultaneously provide stiffness and energy dissipation capacity.

Keywords: Experiment, bolted connection, slot hole, seismic behavior, elevated temperature, sliding force, energy dissipation capacity

DOI: 10.18057/IJASC.2018.14.8

1. INTRODUCTION

Historically, most major structural failures of steel structures in earthquake have been due to some form of connection failure [1]. A large amount of brittle failures of connections were observed in the Northridge earthquake in 1994 [2] which was due to their limited plastic deformation capacity. In the Kobe earthquake in 1995, a total of 988 steel constructions were damaged most of which were due to the brittle failure of beam-column joints. In addition, connections account for more than half the cost of structural steelwork, and their design and detailing are therefore of primary importance for the safety and economy of structures.

It is found to be difficult to generate sufficient ductility of welded connections even if the welding quality is ensured by removing beam column welding lining board [3-5]. As an alternative, connections with high strength bolts are a preferred method of connecting members on the site [6]. The standard circular bolt holes would become elliptical holes under cyclic loads, leading to a reduction in their energy consumption capacity [7]. To address the issues for connections with standard holes such as demand of high installation accuracy, limited energy dissipation capacity, decreased load-bearing capacity when deforming to an elliptical shape, slot bolt holes have been applied. Astaneh-Asl [8] proposed to allow high-strength bolting joints to slip under strong earthquake. The friction between the interfaces and the extrusion of hole wall consumed the

earthquake energy to avoid the brittle failure or collapse of structures. Grigorian [9] designed the long elliptical slot bolt holes. The slot was parallel to the force direction of members. When the tensile force in a connection was more than the static friction force between the friction surfaces, the connection would slide to consume energy. This kind of connections could also be used for a single support or beam-column connections in steel frames [10-12] to improve the ductility of the joints and avoid brittle failure at the joints. Peng *et al.* [13] explored the relationship between the opening area of the high strength bolt connection and the pretension loss, the friction coefficient, respectively, and gave the suggested value of the hole shape coefficient. ANSI/AISC360-10 [14] and European standard (EC3) [15] also provide the hole shape coefficient according to different hole shape. The length of the short axis of slot holes equals to the diameter of the corresponding standard hole, while the long axis is 1.7 times as long as the short axis. They also provide corresponding provisions in the case of different bolt hole spacing and margins. Compared to standard-hole connections, the installation of slot-hole connections is more convenient and cost-effective since it requires less machining precision [16].

While steel structures are not inherently fire resistant because much of the strength of steel will be lost when its temperature reaches 600°C or above during a fire. In addition, the large thermal conductivity of steel leads to a quick temperature rise in unprotected steel members of 600°C in 15min [17]. As an essential component of steel structures, the behavior of connections under fire conditions plays a key role in the global stability of structures against collapse. Yang *et al.* [18] and Yu [19] investigated the anti-sliding capacity of high strength bolts at elevated temperatures. They found that the anti-sliding capacity of the connection increased as the temperature increased for temperatures below 400°C.

The seismic or fire behaviour of steel connections have been investigated extensively but separately. The coupled effect of seismic and fire loads on the performance of steel connections is not well studied and understood. Recently, many efforts have been made for investigating the behaviour of structures subjected to post-earthquake fire [20-24]. The earthquake-induced damage in the structural members are considered in the following structural analysis of structures exposed to fire. However, there is few research on steel beam-to-column connections with slot bolt holes subjected to extreme hazards.

In contrast to the extensive studies on the behavior of structures under post-earthquake fire, there is a lack of research on the post-fire seismic behavior of structures. This is a realistic event for the successive earthquakes or secondary earthquakes, considering that the previous earthquake may cause the ignition of fire. This paper experimentally studied the seismic behavior of high strength bolted connections with slot holes at ambient and elevated temperatures. A total of six specimens with M20 and M30 bolts were designed and tested. The results of force-displacement curves and energy dissipation capacity were output and compared.

2. TEST LAYOUT

2.1 Design of Specimens

For traditional bolted connections between steel beams and columns, the bottom flange of the beam is bolted connected to the corbel which is welded to the flange of the column, as shown in Figure 1. To avoid the local buckling of the corbel and beam web, the key part of the bolted connection was selected to be tested in this study. A total of 6 specimens with sandblasting surfaces were designed, as listed in Table 1 and Figure 2. They were tested at ambient temperature (20°C) and elevated temperature (130°C) temperatures, respectively. The low temperature of the heated specimens was

to consider the fire protection of steel beam-to-column connections as well as the thermal shielding effect at the connections (where many components in a relatively small space). The tested specimens were divided into two groups (S1 and S2) by varying the diameter of bolts and pretension forces. The diameters of M20 and M30 bolts are 20mm and 30mm, respectively. The grade 10.9 high strength bolts were used with a tensile strength of 1000MPa and yield to tensile strength ratio of 0.9. The Young's modulus of the bolts was 200GPa. The measured elongation of bolts was 15%. The slot bolt holes were used for the corbel plate and their dimensions are shown in Figure 3. The holes were parallel to the axis of the beam. The maximum slip of the M20 and M30 bolt holes were 8.5mm and 12.5mm, respectively. Figure 4 shows a specimen in the test. In order to prevent the local buckling of the specimen under compression, stiffening ribs were added on the corbel plate and part of the web of the beam was kept.

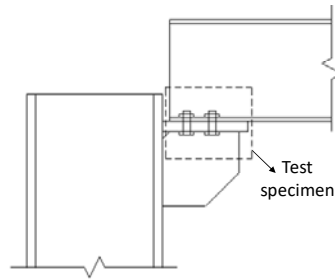
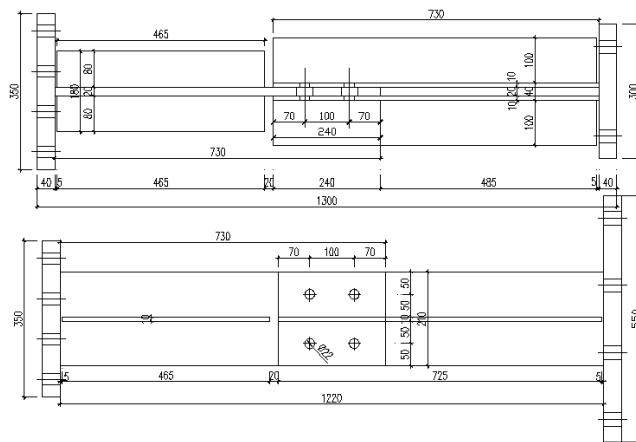


Figure 1. Schematic of Steel Beam-column Connection

Table 1. List of the Tested Specimens

Test No.	Type of Bolts	Temperature of specimens (°C)	Type of holes	Pretension (kN)
S1-1	M20	20 or 130	slot	143
S1-2	M20	20 or 130	slot	140
S1-3	M20	20 or 130	slot	152
S2-1	M30	20 or 130	slot	337
S2-2	M30	20 or 130	slot	316
S2-3	M30	20 or 130	slot	354



(a) S1 (M20 bolts)

where T_c is the ultimate torque, in N·m; k is the average value of the torque coefficient of the bolt connecting pair which is determined by experiments; P_c is the pretension in the high strength bolt, in kN, which can be determined by Table 3.2.5 of the design code JGJ82-2011. The design pretensions of M20 and M30 bolts were calculated as 155kN and 355kN, respectively, according to the grade (10.9) and diameter of the bolts; d is the diameter of the bolt screw, in mm.

It is required that the applied pretension of bolts in practice should fall in the range of $0.95 \sim 1.05 P_c$. During the twist, the bolt pretension was measured by the strain gauge, as shown in Figure 5. High temperature strain gauges were used and arranged in the two grooves made on the symmetrical positions of the shank below the nut. The data wires of the strain gauges passed through the holes predrilled in the nut. The measured pretensions of bolts satisfied the requirement of maximum error of $5\% P_c$.

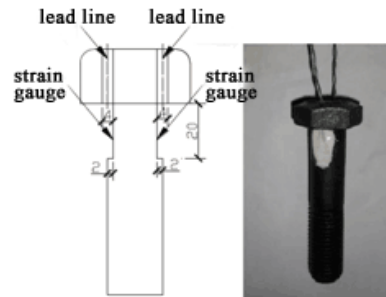


Figure 5. Arrangement of Strain Gauges on the Bolt

2.3 Measurement

An electric furnace was used to heat the specimens up to 200°C , as shown in Figure 6. The furnace has a heating capacity of $20^\circ\text{C} \sim 1200^\circ\text{C}$ and a maximum heating rate of 15kW. It consisted of two heating panels and concrete insulation panels at the two ends. The temperature inside the furnace was monitored by 2 K-type thermocouples and the average temperature of these two measurements was calculated and used as the gas temperature in the furnace. Four K type thermocouples were arranged at the upper part, the middle part and the lower part of the specimens, respectively, to monitor its temperature, as shown in Figure 7. The deformation of the connections was measured by two symmetrically placed extensometers (Figure 8).

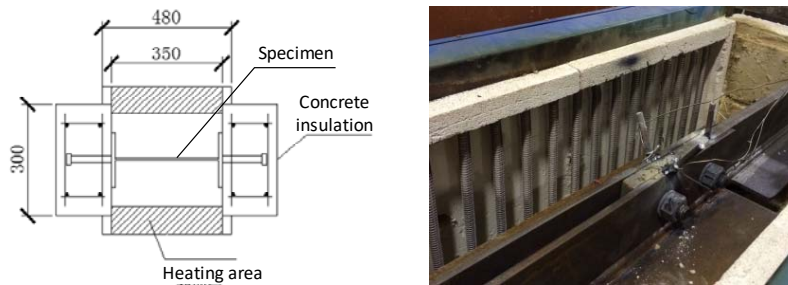


Figure 6. Specimens in the Electronic Furnace (All Units are mm)

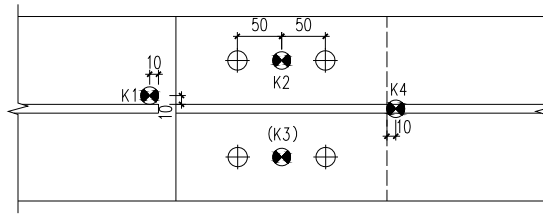


Figure 7. Arrangement of the Thermocouples

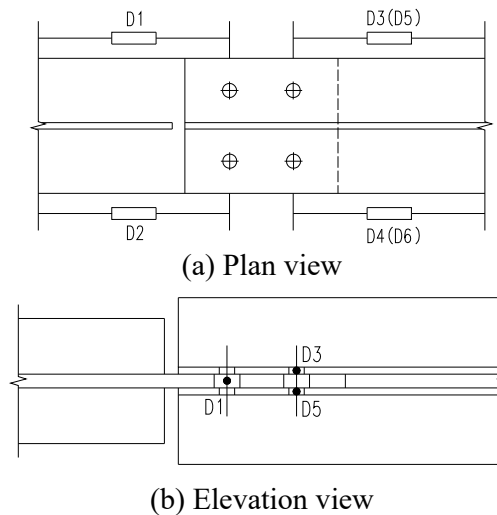


Figure 8. Layout of Displacement Measurements

2.4 Loading

The specimens were firstly heated in the furnace (Figure 6) with a heating rate of 4~5°C/min until reaching the target temperature of 130°C. When the target temperature was reached, it remained for at least 30min to guarantee the temperature of the component was constant and stable.

Loads were imposed based on Chinese codes GB50205-2001 and JGJ 101-96, as shown in Figure 9. At the beginning of the tests, force control was adopted until the load increased up to 10% of the slip load. The loading was held for 1 min, after which it was applied smoothly in a speed of 3~5kN/s until the occurrence of sliding of the connection. The displacement control was then adopted in an interval of 1mm until the bolt was in contact with the hole. For each displacement level, three cyclic loadings were conducted. Once the bolt shank contacted against the hole wall, a cyclic loading of 60 loops was conducted to study the low cycle fatigue performance and energy dissipation capacity of the bolted connections with slot bolt holes.



Figure 9. Loading of the Specimens

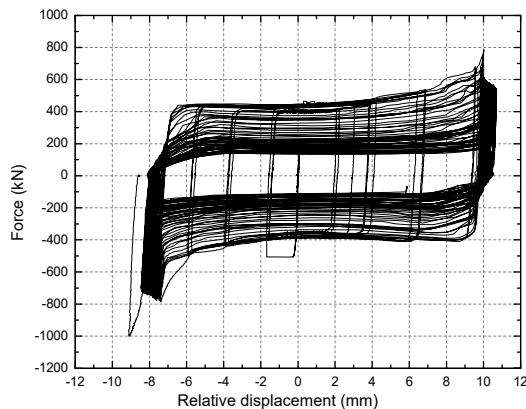
3. TEST RESULTS

In the initial stage of loading, the specimens were in elastic stage. The relative displacement of the connections increased with the increase of the load, and the connections did not make a sound. When the load reached the sliding load, there was a loud noise, and the members experienced a first slide. A further loading on the connections led to gradual sliding accompanied by successive noises. For the latter cyclic loading stage, the connections in the first half of the loading process, issued a continuous ringing sound. The sound gradually declined until the loading was completed.

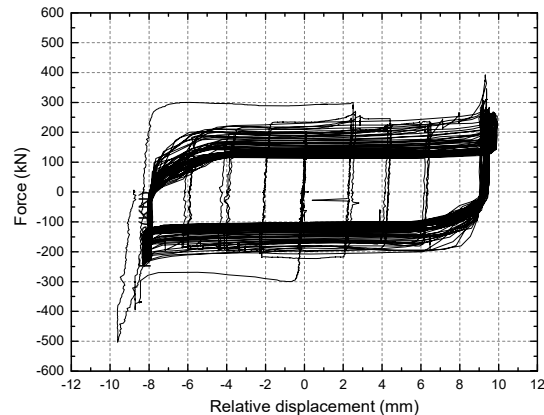
3.1 Load vs Relative Displacement Curves of Specimens

A comparison of force-displacement curves of the specimens S1 and S2 at 20°C and 130°C is shown in Figures 10 and 11, respectively. In general, the hysteresis loops of experiments at 130°C were similar to them at normal temperature. The seismic behaviour specimens at different temperatures shows the following common features as:

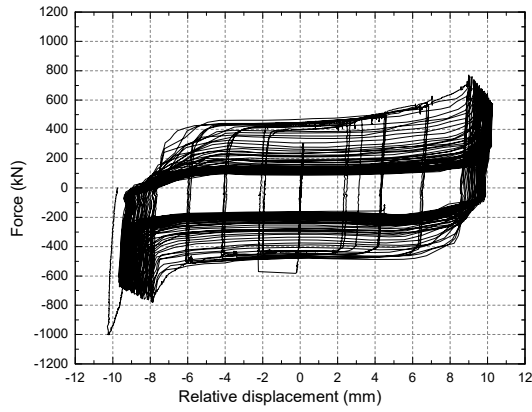
- (1) The force-displacement curves were linear before the occurrence of bolt sliding in each loop. After the sliding, the stiffness of the connections degenerated rapidly, leading to a large increment of displacement as the force kept stable. The hysteresis curves were stretched as the loops of loading increased, and the area of the hysteresis loops increased greatly.
- (2) As the number of loops increased, the sliding force decreased and the hysteresis curves had a slight tendency of pinching. This tendency occurred for both M20 and M30 bolts.
- (3) The ultimate load-bearing capacity of the connections did not decrease much with the increasing loops of hysteresis loops.
- (4) The hysteresis curves were symmetrical, and the middle part of the sliding section were rectangular and full. This indicated the significant energy dissipation capacity of bolted connections with slot bolt holes.
- (5) Compared with the hysteresis loops of M20 bolts, those of M30 bolts were more full and the pinch phenomena were less obvious. This is due to the larger pretension and wider slot hole for M30 bolts compared to M20 bolts, leading to larger friction forces and sliding distances. This indicated that the slot holes of M30 bolts had a better seismic performance.



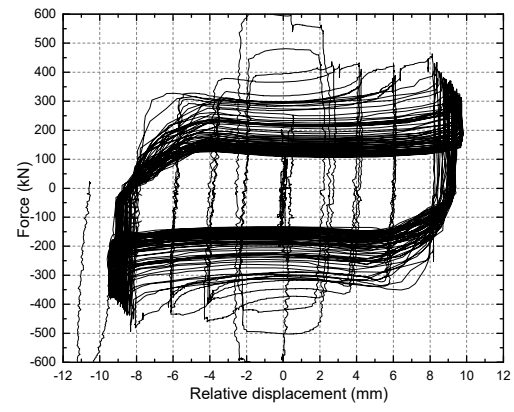
(a) S1-1 (20°C)



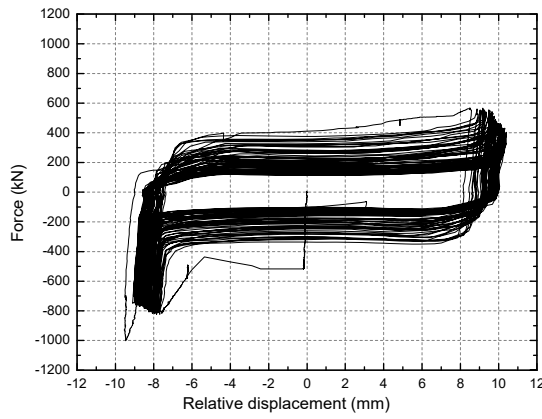
(b) S1-1 (130°C)



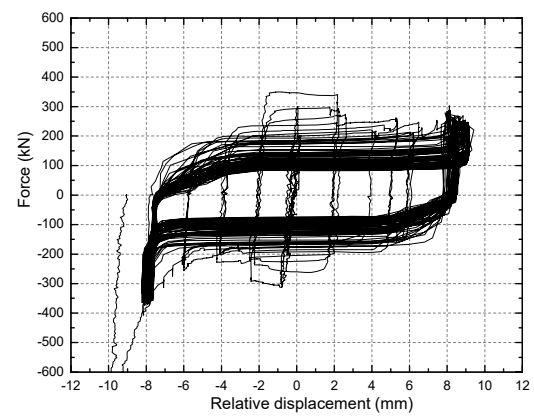
(c) S1-2 (20°C)



(d) S1-2 (130°C)

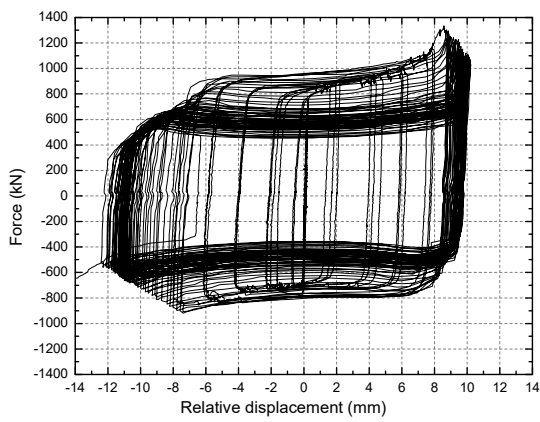


(e) S1-3 (20°C)

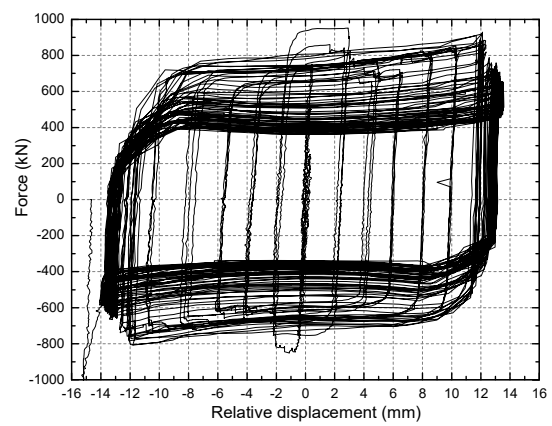


(f) S1-3 (130°C)

Figure 10. Comparison of Force-slip Displacement Curves of Specimens S1 with M20 bolts at Different Temperatures



(a) S2-1 (20°C)



(b) S2-1 (130°C)

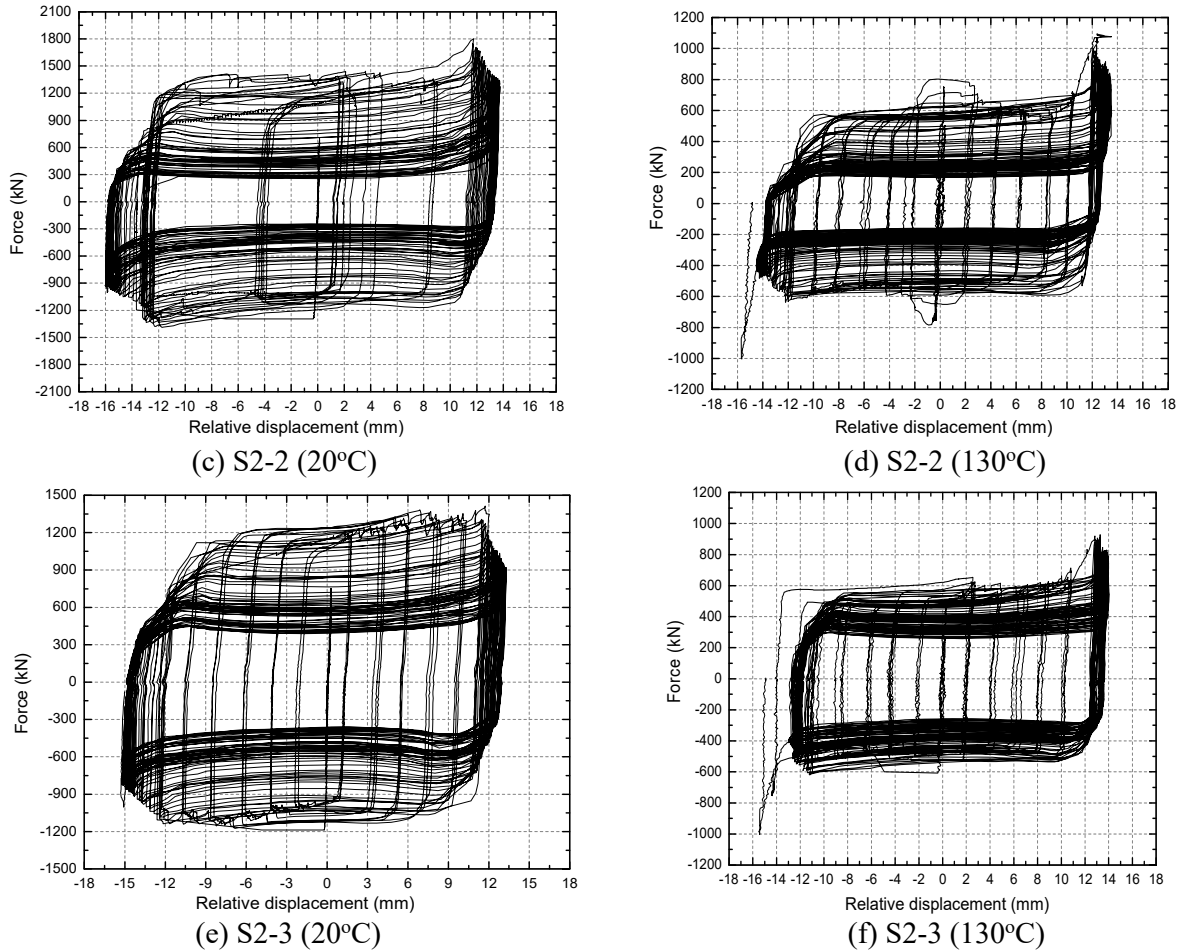


Figure 11. Comparison of Force-slip Displacement Curves of Specimens S2 with M30 Bolts at Different Temperatures

There was no obvious deformation of bolts at ambient and elevated temperatures. The deformation of holes for the specimens S1 (M20 bolts) and S2 (M30 bolts) after test was shown in Figures 12 and 13, respectively. It was found that the holes for M20 bolts deformed due to the contact between the bolt and hole. This deformation effect was less significant in the holes for M30 bolts. Both specimens showed obvious sliding distances which is helpful for dissipating seismic energy.

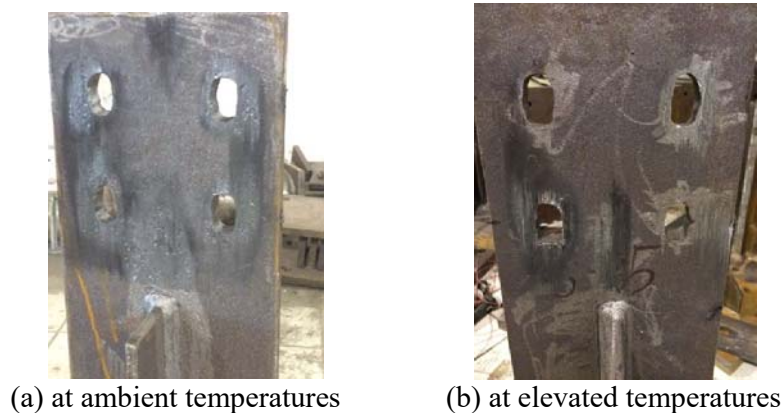


Figure 12. Deformation of Holes for M20 Bolts after Test



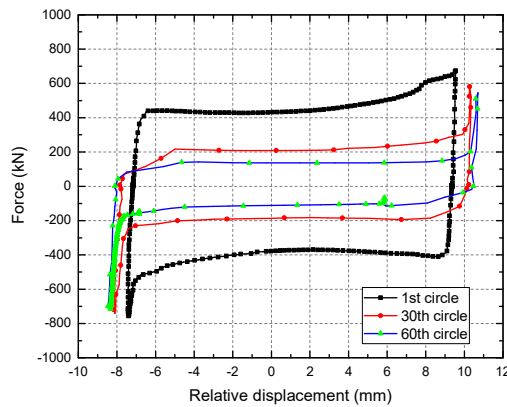
(a) at ambient temperatures



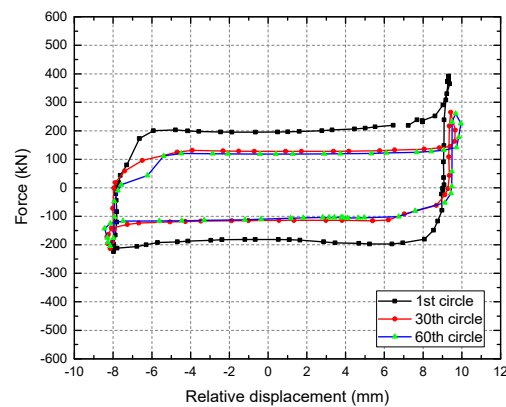
(b) at elevated temperatures

Figure 13. Deformation of Holes for M30 Bolts after Test

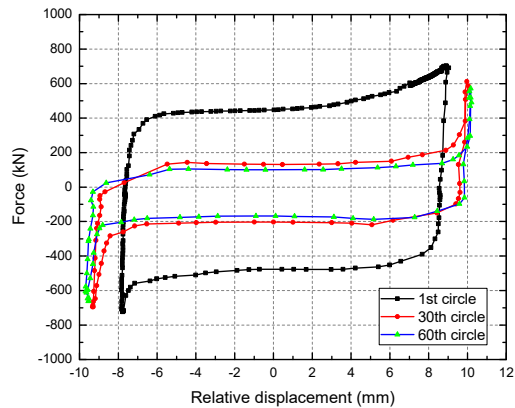
To quantitatively investigate the variation of hysteresis loops against number of loops, the hysteresis curves for the 1st, 30th and 60th loops were compared, as shown in Figures 14 and 15. There are some common features that the sliding load decreased more in the first 30 loops compared with the latter 30 loops. The decrease of sliding load may be due to that the friction surface tended to be smooth and the coefficient of friction decreased. After the first 30 loops of sliding, the smoothness of the friction surface became stable and thus there was no significant reduction in the sliding force for the latter 30 loops. This explanation was consistent with the continuous sound in first 30 loops and less sound in the latter 30 loops. During the experiments, the screw constantly impacted the hole wall causing the hole wall deformation which was more obvious in the first 30 loops. The effect of temperature lies in the rate of decay of friction. It was found in Figures 14 and 15 that the drop of sliding force at elevated temperatures was much smaller than that at ambient temperature. This means the elevated temperature increases the stability of the friction coefficient.



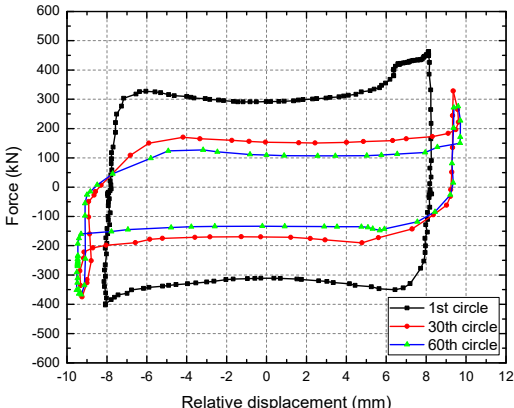
(a) S1-1 (20°C)



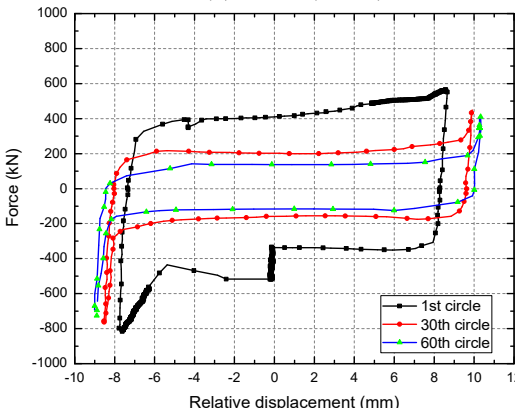
(b) S1-1 (130°C)



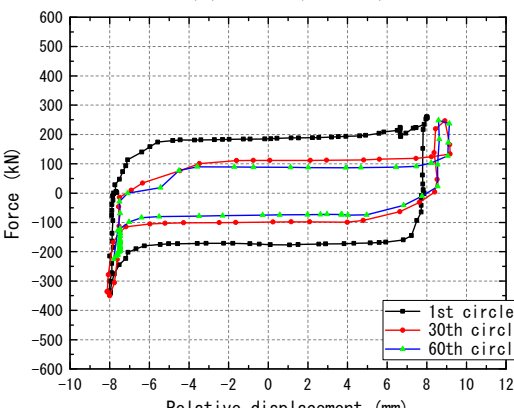
(c) S1-2 (20°C)



(d) S1-2 (130°C)

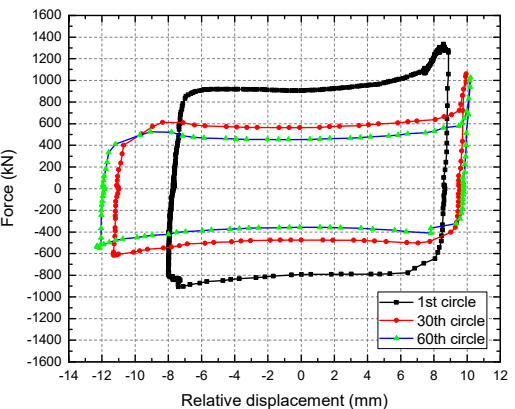


(e) S1-3 (20°C)

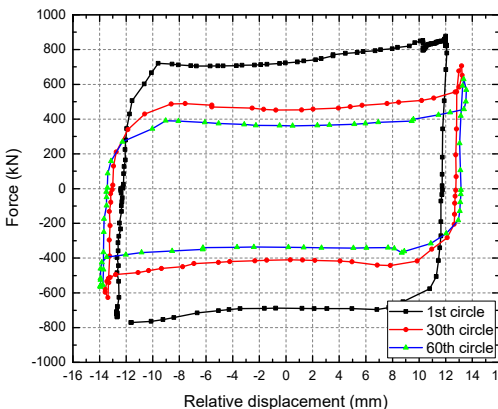


(f) S1-3 (130°C)

Figure 14. Comparison of Three Hysteresis Loops of Specimens S1 with M20 Bolts at Different Temperatures



(a) S2-1 (20°C)



(b) S2-1 (130°C)

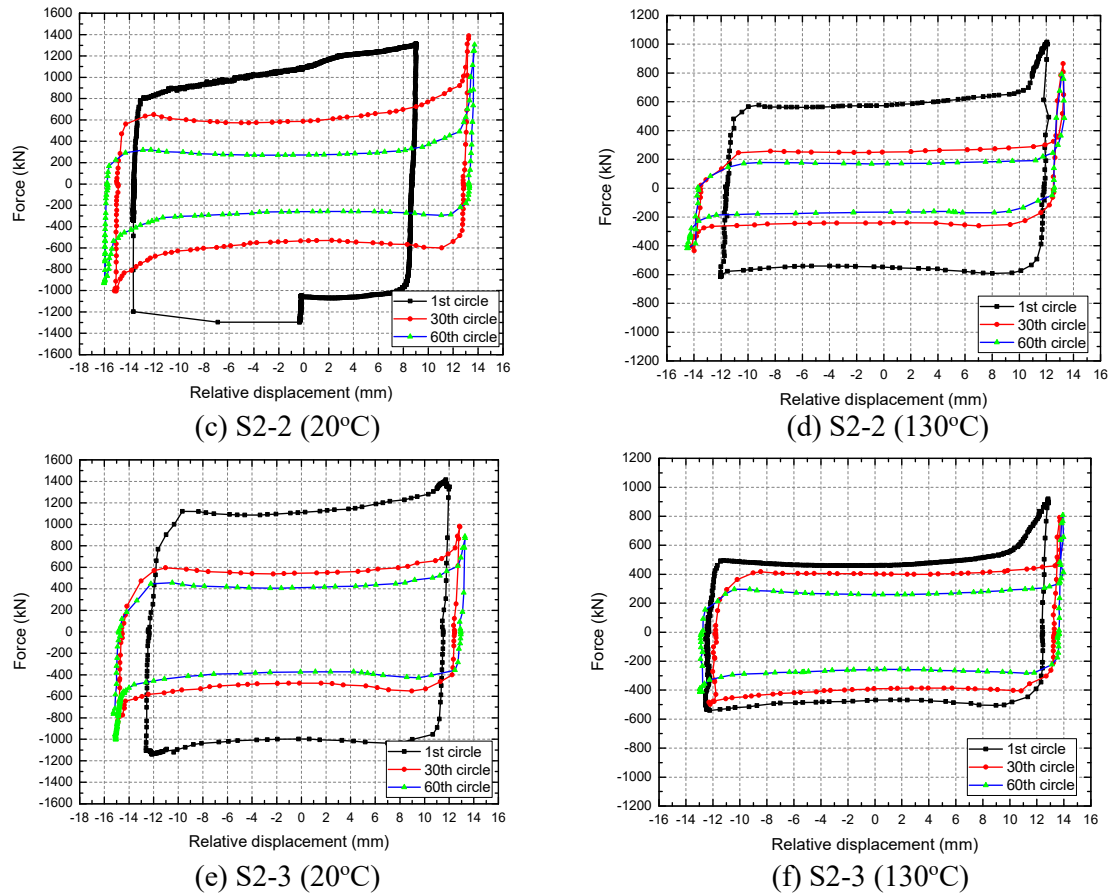


Figure 15. Comparison of Three Hysteresis Loops of Specimens S2 with M30 bolts at Different Temperatures

Tables 2 and 3 list the sliding forces of specimens at ambient and elevated temperature, respectively. The average results of the three specimens for S1 and S2 were calculated, respectively. Table 2 showed that, after the first 30 loops, the sliding force decreased by more than 50% for both M20 and M30 bolts, while it decreased by more than 65% after 60 loops. The reduction of sliding forces for the M20 bolts was greater than that for the M30 bolts. This indicates that the M30 bolts have a better load-bearing capacity under cyclic loads. For the connections at elevated temperature (Table 3), the reduction of sliding forces was smaller than that at ambient temperature. This may be due to the fact that the pretension in the bolts increased as the temperature increased.

Table 2. Sliding Force of the Specimens against Number of Loops at Ambient Temperatures (20°C)

Specimen	Bolt	Design Value (kN)	Measured value (kN)				
			Fs1	Fs30	$(Fs1-Fs30)/Fs1$	Fs60	$(Fs1-Fs60)/Fs1$
S1	M20	372	418	198	53%	120	71%
S2	M30	852	1074	567	47%	377	65%

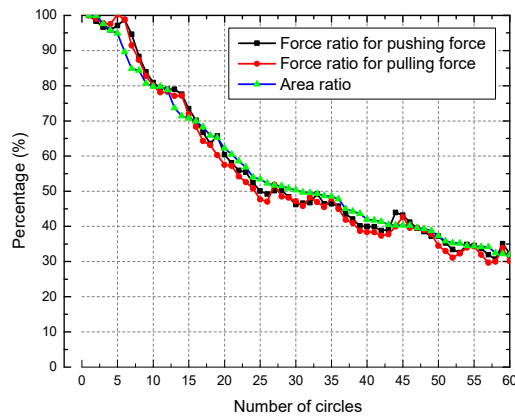
Table 3. Sliding Forces of the Specimens against Number of Loops at Elevated Temperatures (130°C)

Specimen	Bolt	Design Value (kN)	Measured value (kN)				
			Fs1	Fs30	(Fs1-Fs30)/Fs1	Fs60	(Fs1-Fs60)/Fs1
S1	M20	372	225	132	41%	106	53%
S2	M30	852	586	368	37%	264	55%

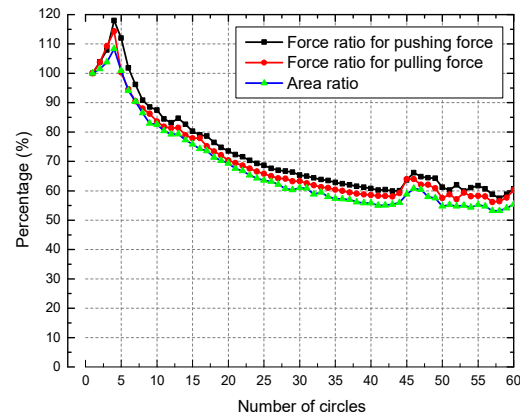
3.2 Fatigue Property

To clearly reflect the energy dissipation capacity and friction coefficients of the tested connections, the relationship between them and the number of cyclic loading loops were expressed in Figures 16 and 17. The "force ratio" represents the ratio of the external force to the sliding force when the displacement became zero. Similarly, the "area ratio" represents the ratio of the hysteresis loop area enclosed by each loop to that of the first loop. The force ratios for the pushing and pulling loading process were presented. As shown in Figures 16 and 17, the hysteretic curve area and surface friction coefficient decreased with the increase of loading loops in a similar trend. The similar trend may be due to the fact that the energy consumption of high strength bolt connections with slot holes mainly depended on the friction of the surfaces.

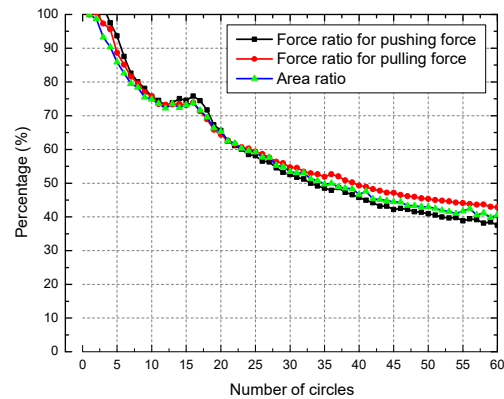
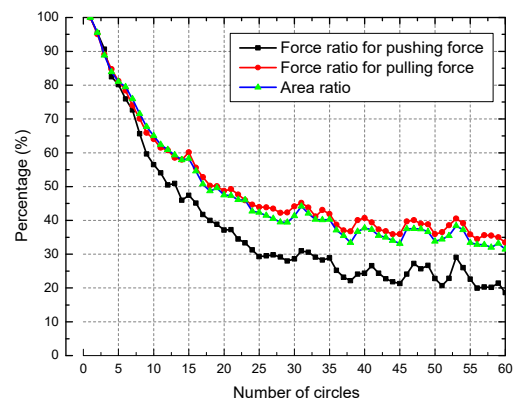
The friction coefficient and the area of the hysteresis curve decreased by about 40% after the first 30 loops. After 60 loops, the reduction ratio of M20 bolt connections and M30 bolts connections dropped to 40% and 50% of the initial values, respectively. Therefore, the connection with M30 bolts had a better energy dissipation capacity and fatigue performance.



(a) S1-1 (20°C)



(b) S1-1 (130°C)



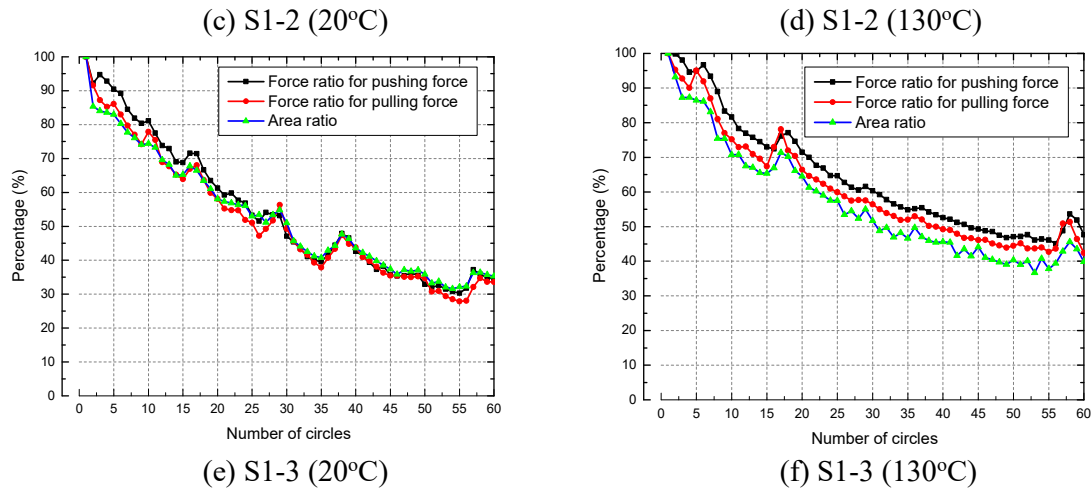
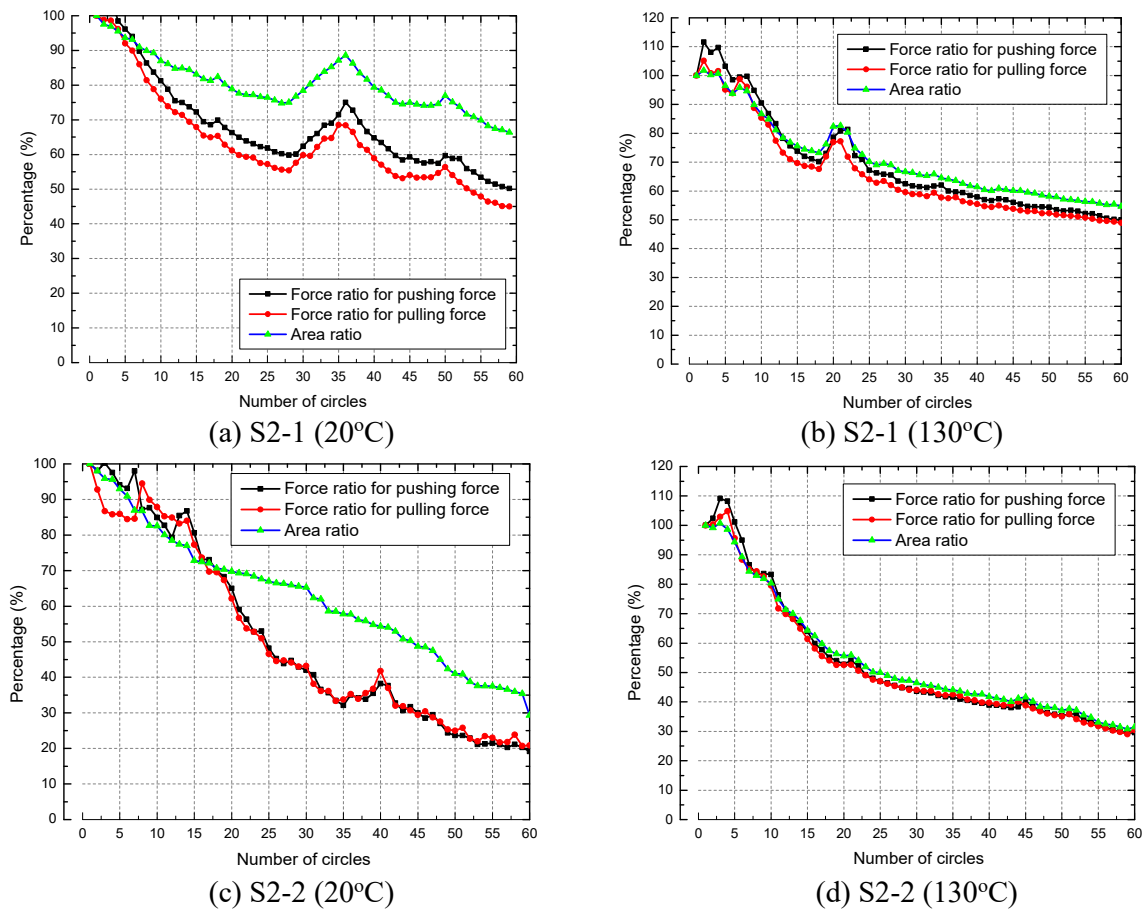


Figure 16. Relation between the Energy Dissipation Capacity and Friction Coefficients of the Tested Connections S1 and the Number of Loading Loops



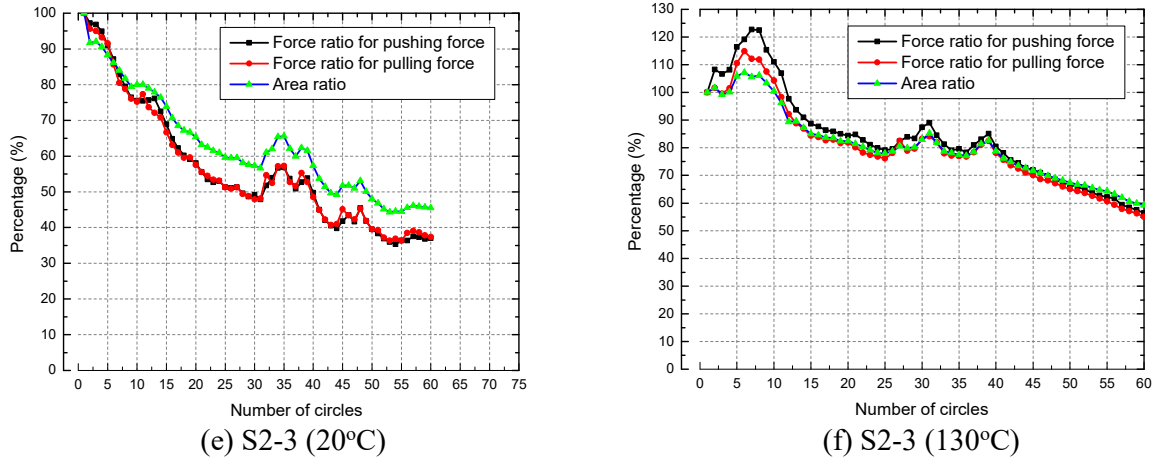


Figure 17. Relation between the Energy Dissipation Capacity and Friction Coefficients of the Tested Connections S2 and the Number of Loading Loops

Compared with the experiments results at ambient temperature, the energy consumption of high strength bolt connections at 130°C increased by about 10% of its initial value, which was consistent with the conclusion that the friction coefficient increased as the temperature increased, which determined the capacity of dissipating earthquake energy.

4. CONCLUSIONS

This paper experimentally studied the seismic behavior of high strength bolted connections with slot holes at ambient and elevated temperatures. The following conclusions can be drawn:

- (1) High strength bolt connections with slot holes had full hysteretic loops and thus good energy dissipation capacity at both ambient and elevated temperatures.
- (2) It was found that connections with M30 bolts had better energy dissipation capacity and load-bearing capacity than those with M20 bolts. This is because that the M30 bolts had a larger pretension and wider slot hole compared to M20 bolts, which lead to larger friction forces and sliding distances.
- (3) The sliding forces of the connections decreased with the increase of the number of loops, and the hysteresis curves had a slight tendency of pinching. The sliding force reduced by about 50% after 60 loops at elevated temperature, compared with 35% at ambient temperature.
- (4) The ultimate bearing capacity of the connections did not decrease much with the increase of the number of loading loops.
- (5) The friction coefficient and the area of the hysteresis curve decreased by 40% after the first 30 loops. After 60 loops, the reduction ratio of connections with M20 bolts and M30 bolts dropped to 40% and 50% of their initial values, respectively.

The experimental results showed that the bolted connections with slot holes had good energy dissipation capacity at both ambient and elevated temperatures. They can be used as a friction damper by dissipating energy through the friction of plate surfaces. This type of connections can also provide both bearing capacity and stiffness before sliding. This means the connection with slot holes can be used as a dual-function component in a structure to provide stiffness and energy

dissipation at the same time. However, the large decrease of bearing capacity along with sliding should be avoided by improving the property of friction surfaces. The use of paint on the contact surface may be an effective method to enhance the sliding resistance which needs further investigations.

ACKNOWLEDGEMENT

The work presented in this paper was supported by the National Natural Science Foundation of China with Grants 51408418, 51120185001 and 51508412. This work was also supported by the Ministry of Science and Technology of China with Grant SLDRCE14-A-05, and Natural Science Foundation of Tianjin 16JCQNJC07000.

REFERENCES

- [1] Shi, G., Wang, M., Wang, Y.Q. and Wang, F., "Cyclic Behavior of 460MPa High Strength Structural Steel and Welded Connection under Earthquake Loading", *Advances in Structural Engineering*, 2013, Vol. 16, No. 3, pp. 451-462.
- [2] Mille, D.K., "Lessons Learned from the Northridge Earthquake", *Engineering Structures*, 1998, Vol. 20, No. 4, pp. 249-260.
- [3] Engelhardt, M.D. and Sabol, T.A., "Test of Steel Moment Resist Connections in Response to Earthquake", Program Report to the AISC Advisory Subcommittee on Special Moment Resisting Frame Research, Oct.1994.
- [4] Jayachandran, S., Marimuthu, V., Prabha, P., Seetharaman, S. and Pandian, N., "Investigations on the Behaviour of Semi-rigid Endplate Connections", *Advanced Steel Construction*, 2009, Vol. 5, No. 4, pp. 432-451.
- [5] Qin, Y., Chen, Z. and Wang, X., "Seismic Behavior of Through-diaphragm Connections between CFRT Columns and Steel Beams-experimental Study", *Advanced Steel Construction*, 2014, Vol. 10, No. 3, pp. 351-371.
- [6] Henriques J., Jaspert J.P. and Simões da Silva L., "Ductility Requirements for the Design of Bolted Lap Shear Connections in Bearing", *Advanced Steel Construction*, 2014, Vol. 10, No. 1, pp. 33-52.
- [7] Bernuzzi, C., Calado, L. and Castiglioni, C.A., "Behaviour of Steel Beam-to-column Joints under Cyclic Reversal Loading: An Experimental Study", *Proceedings of 5th Int. Coll. on Stability and Ductility of Steel Structures, SDSS, Nagoya*, 1997, Vol. 1, pp. 335-342.
- [8] ASTANEH-Asl, A., "Seismic Design of Steel Column-tree Moment-resisting Frames", *Steel Tips*, Structural Steel Educational Council, Moraga, CA, 1997.
- [9] Grigorian, C.E., Yang, T.S. and Popov, E.P., "Slotted Bolted Connections for Energy Dissipators", College of Engineering University of California at Berkeley, 1992.
- [10] Zhao, X.M. and Ha, K.H., "Friction Connection for Seismic Control of Moment Resisting Steel Frame", *Proceedings of 11th World Conference on Earthquake Engineering*, 1996, pp. 1963.
- [11] Way, D. and Loh, E., "Friction-Damped Moment Frame", *Proceedings of 11th World Conference on Earthquake Engineering*, 1996, pp. 19.
- [12] John, J.W. and Charles, G.C., "Performance of Hierarchical Friction Dissipating Joints in Moment Resisting Steel Frame", *Proceedings of 11th World Conference on Earthquake Engineering*, 2000, pp. 718.
- [13] Peng, T.H., Hou, Z.X., Wen, S.L. and Gao, J.Z., "Experiment on Effect of Hole Size and Hole Shape on Bearing Capacity of High Strength Bolt Friction Type Connection", *Steel Construction*, 2007, Vol. 8, No. 22, pp.30-34.

- [14] ANSI/AISC360-10. Specification for Structural Steel Buildings, American Institute of Steel Construction, 2010.
- [15] Eurocode 3: Design of Steel Structures: Part 1. General Requirements, European Committee for Standardization, 1992.
- [16] Ronald, N.A., "The Effect of Over Size and Slotted Holes on the Behavior of a Bolted Joint", PhD Thesis, Lehigh University, 1967.
- [17] Li, G.Q. and Wang, P.J., "Advanced Analysis and Design for Fire Safety of Steel Structures", Zhejiang: Zhejiang University Press, 2013, pp. 43-48.
- [18] Yang, K.C., Hsu, R.J. and Chen, Y.J., "Shear Strength of High-strength Bolts at Elevated Temperature", Construction and Building Materials, 2011, Vol. 25, pp. 3656-3660.
- [19] Yu, L., "Behavior of Bolted Connections during and after a Fire", PhD Thesis, The University of Texas at Austin, 2006.
- [20] Braxtan, N.L. and Pessiki, S.P., "Postearthquake Fire Performance of Sprayed Fire-Resistive Material on Steel Moment Frames", Journal of Structural Engineering, 2011, Vol. 137, No. 9, pp. 946-953.
- [21] Corte, G.D., Landolfo, R. and Mazzolani, F.M., "Post-earthquake Fire Resistance of Moment Resisting Steel Frames", Fire Safety Journal, 2003, Vol. 38, No. 7, pp. 593-612.
- [22] Pucinotti, R., Bursi, O.S. and Franssen, J.M., "Seismic-induced Fire Resistance of Composite Welded Beam-to-column Joints with Concrete-filled Tubes", Fire Safety Journal, 2011, Vol. 46, No. 6, pp. 335-347.
- [23] Kamath, P., Sharma, U.K. and Kumar, V., "Full-scale Fire Test on an Earthquake-damaged Reinforced Concrete Frame", Fire Safety Journal, 2015, Vol. 73, pp. 1-19.
- [24] Wen, B., Wu, B. and Niu, D., "Post-earthquake Fire Performance of Reinforced Concrete Columns", Structure and Infrastructure Engineering, 2015, Vol. 12, No. 9, pp. 1-21.

SAFETY ASSESSMENT OF EUROCODE 3 STABILITY DESIGN RULES FOR THE LATERAL-TORSIONAL BUCKLING OF PRISMATIC BEAMS

Luís Simões da Silva¹, Trayana Tankova^{1,*}, Liliana Marques¹, Carlos Rebelo¹ and Andreas Taras²

¹ *ISISE, Department of Civil Engineering, University of Coimbra, Coimbra, Portugal*

² *Institute of Structural Engineering, Bundeswehr University Munich, Germany*

**(Corresponding author: Email: ttankova@uc.pt)*

Received: 17 June 2017; Revised: 26 December 2017; Accepted: 27 December 2017

ABSTRACT: This paper presents the safety assessment of the European rules for the lateral-torsional buckling of beams using hot-rolled I and H cross-sections based on a large number of advanced numerical simulations covering the relevant parameters.

The methods for LTB in Eurocode 3 are briefly presented and assessed. Despite the large scatter of results, the conservative nature of the “General Case” design rule was confirmed. The “Special Case” systematically led to significantly lower safety levels. A new Ayrton-Perry-based method was also assessed and it was shown to provide good accuracy.

The magnitude of the partial factor γ_{M1}^* is addressed, whereby a good homogeneity of results is observed across the different buckling curves, with maximum variations of 0.05, except for the “Special Case”, which systematically presents higher factors for most of the subsets. The “General Case” presents the lowest partial factors, but is clearly over conservative, leading in many cases up to 40% lower resistance.

The γ_{M1}^* values are compared for the “General Case” and the new Ayrton-Perry method with the results obtained for the flexural buckling resistance of columns. It is concluded that the partial factors for LTB are generally lower than those for flexural buckling.

Keywords: Beam, lateral-torsional buckling, safety assessment, design rules, steel, Eurocode 3, stability

DOI: 10.18057/IJASC.2018.14.9

1. INTRODUCTION

The design verification of beams susceptible to lateral-torsional instability in Eurocode 3 [1] is based on the buckling curve approach. The code proposes two methods for the lateral-torsional buckling verification – the “General” and the “Special” cases. The safety and accuracy of these methods was addressed in the past, e.g. by Snijder and Hoenderkamp [4] and Rebelo et al [5], where discrepancies between numerical simulations and the code predictions were identified. Recently, a new design method based on a mechanically sound analytical derivation was proposed by Taras [3] that strictly implements an Ayrton-Perry approach akin to the derivation of the flexural buckling resistance of columns [6].

There are various parameters which influence the stability behaviour of beams: material properties, geometrical dimensions, imperfections. Some of these parameters are constantly monitored as part of the quality control production procedures, while others are occasionally measured, such as residual stresses and initial imperfections, making it more difficult to choose representative values to be used in numerical simulations. Moreover, the development of new structural steels with largely improved mechanical and geometrical properties and improved quality control procedures further supports the need for a reassessment of the safety levels of the European design rules for lateral-torsional buckling.

Hence, based on the findings of the RFCS SAFEBRIC TILE project [9] and similarly to a previous paper on columns [10], this paper addresses a systematic assessment of the safety levels of the lateral-torsional buckling of I-shaped hot-rolled steel beams according to Eurocode 3 [1]. Firstly, the adopted assumptions for the assessment are summarized. A parametric study for the evaluation of lateral-torsional buckling design rules for prismatic beams in EUROCODE 3 [1] is subsequently carried out. It covers several slenderness groups, yield stress, cross-section shapes, and bending moment distributions such that a thorough evaluation of the analyzed design rules is achieved, using advanced nonlinear numerical simulations. Finally, a discussion on the value of the partial factor γ_{M1} to be adopted based on the obtained results is presented.

2. DESIGN APPROACHES FOR THE LATERAL-TORSIONAL BUCKLING OF PRISMATIC HOT-ROLLED BEAMS

According to Eurocode 3 [1], the design resistance of beams prone to lateral-torsional buckling can be estimated using clauses 6.3.2.2 and 6.3.2.3, the so-called General Case and Special Case, respectively. Both of them make use of the buckling curve approach, thus assuming that the columns and beams have similar behaviour regarding their buckling resistance.

The General Case (see Table 1) uses the column buckling curves; however, the split between the various cases is done only according to the section depth-to-width (h/b) ratios, since beams with lower h/b have higher torsional rigidity and thus higher lateral-torsional buckling resistance. The method has been criticised for being overly conservative for variable bending moment distributions and for the large scatter of results [3], [5].

As an alternative for H and I sections, the Special Case (see Table 1) considers the beneficial effect of the torsional resistance of the member and accounts for the favourable effect of varying bending moment distributions along the beam length by modifying the reduction factor χ_{LT} with a factor f (see Table 3). The Special Case also makes use of a longer plateau length by recommending $\bar{\lambda}_{LT,0} = 0.4$. However, its estimation of the design resistance is often found to be unconservative when compared to numerical simulations. [3], [5]. As a result, in [5] a modification of the General case was proposed, referred to as General Case/ f , whereby the reduction factor χ_{LT} calculated using the General Case's curves is modified by the factor f provided for the Special Case.

Recent research by Taras [3] has resulted in a new Ayrton-Perry design rule (see Table 1), which is based on a mechanically consistent analytical derivation and imperfection factors (Table 2) calibrated based on an extensive numerical parametric study. The method was also statistically assessed using available experimental test results and Monte Carlo simulations. It is henceforth referred to as New EC3 method or nEC3.

All methods rely on a reference case (simply-supported beam with fork conditions at the supports and uniform bending moment). The application to different loading types or boundary conditions is addressed by calculating the appropriate elastic critical moment and a specific coefficient to correct the second-order critical location. It is noted that for cases with restrained warping conditions at the supports this approach leads to slightly unsafe sided results, when compared to the correct derivation of the design resistance.

The design procedures are summarized in Table 1, whereas the imperfection factors and additional factors are summarized in Table 2 and Table 3 respectively.

Table 1. Lateral-torsional Buckling Resistance of Beams

<i>Method</i>	EC 3 GC (clause 6.3.2.2)	EC 3 GC/f (GC mod. with f factor [5])	EC 3, SC (clause 6.3.2.3)	New EC3 method
$M_{y,Rk}$	$W_{pl,y} \cdot f_y$ – class 1 or 2 cross sections $W_{el,y} \cdot f_y$ – class 3 cross sections $W_{eff,y} \cdot f_y$ – class 4 cross sections			
M_{cr}	Elastic critical moment (LBA)			
$\bar{\lambda}_{LT}$	$\bar{\lambda}_{LT} = \sqrt{M_{y,Rk} / M_{cr}}$			
α_{LT}	See Table 2			
η_{LT}	$\alpha_{LT} (\bar{\lambda}_{LT} - 0.2)$	$\alpha_{LT} (\bar{\lambda}_{LT} - \bar{\lambda}_{LT,0})$ $\bar{\lambda}_{LT,0} = 0.4$ (recommended)		$\alpha_{LT} (\bar{\lambda}_z - 0.2)$

Table 1. (continued) Lateral-torsional buckling resistance of beams.

<i>Method</i>	EC 3 GC (clause 6.3.2.2)	EC 3 GC/f (GC mod. with f factor [5])	EC 3, SC (clause 6.3.2.3)	New EC3 method
η_{LT}	$\alpha_{LT} (\bar{\lambda}_{LT} - 0.2)$	$\alpha_{LT} (\bar{\lambda}_{LT} - \bar{\lambda}_{LT,0})$ $\bar{\lambda}_{LT,0} = 0.4$ (recommended)		$\alpha_{LT} (\bar{\lambda}_z - 0.2)$
Φ_{LT}	$0.5 \times (1 + \eta_{LT} + \bar{\lambda}_{LT}^2)$	$0.5 \times (1 + \eta_{LT} + \beta \bar{\lambda}_{LT}^2)$ $\beta = 0.75$ (recommended)		$0.5 \times \left(1 + f_M \left(\eta_{LT} \frac{\bar{\lambda}_{LT}^2}{\bar{\lambda}_z^2} + \bar{\lambda}_{LT}^2 \right) \right)$ (Table 3 for f_M)
χ_{LT}	$\frac{1}{\phi_{LT} + \sqrt{\phi_{LT}^2 - \bar{\lambda}_{LT}^2}} \leq 1$	$\frac{1}{\phi_{LT} + \sqrt{\phi_{LT}^2 - \beta \bar{\lambda}_{LT}^2}}$ $\leq \begin{cases} 1 \\ \frac{1}{\bar{\lambda}_{LT}^2} \end{cases}$		$\frac{f_M}{\phi_{LT} + \sqrt{\phi_{LT}^2 - f_M \bar{\lambda}_{LT}^2}} \leq 1$
$(\chi_{LT,mod})$	-	$\frac{\chi_{LT}}{f} \leq 1$ (Table 3 for f)	$\frac{\chi_{LT}}{f} \leq 1$	-
Verification	$M_{y,Ed} \leq M_{b,Rd} = \chi_{LT(mod)} \times M_{y,Rk} / \gamma_{M1}$			

f_M , k_c and f are additional factors respectively for nEC3 and SC, see Table 3.

Additionally, whenever $\bar{\lambda}_{LT} \leq \bar{\lambda}_{LT,0}$ and $\frac{M_{y,Ed}}{M_{cr}} \leq \bar{\lambda}_{LT,0}^2$, lateral torsional buckling does not need to be verified and only cross-sectional checks apply ($\chi_{LT} = 1$).

In order to provide a more thorough overview, the 2010 AISC [11] design rules for the lateral-torsional buckling resistance of doubly symmetric I-shaped members and channels bent about their major axis are also briefly presented in Table 4.

The AISC lateral-torsional buckling verification considers three slenderness regions that depend on the length L_b between points that are either braced against lateral displacement of the compression flange or braced against twist of the cross section. All symbols are explained in the notation.

Table 2. Imperfection Factors and Generalized Imperfection Limits for Lateral-torsional Buckling

Fabrication	Limits		Source and Imperfection factor			
	[3]		EUROCODE 3	EUROCODE 3 GC; GC/f	EUROCODE 3 SC	New EC3 method
Rolled	$h/b > 1,2$	$t \leq 40\text{mm}$	$h/b > 2.0$ $h/b \leq 2.0$	0.34 0.21	0.49 0.34	$0.12 \sqrt{\frac{W_{y,el}}{W_{z,el}}} \leq 0.34$
		$40\text{mm} < t \leq 100\text{mm}$	$h/b > 2.0$ $h/b \leq 2.0$	0.34 0.21	0.49 0.34	$0.16 \sqrt{\frac{W_{y,el}}{W_{z,el}}} \leq 0.49^*$
	$h/b \leq 1,2$	$t \leq 100\text{mm}$	$h/b \leq 2.0$	0.21	0.34	$0.16 \sqrt{\frac{W_{y,el}}{W_{z,el}}} \leq 0.49$
*originally identical with $h/b \geq 1.2$ and $t \leq 40\text{mm}$						

Table 3. Additional Auxiliary Factors for GC/f; SC; nEC3






Method	GC/f; SC		nEC3
Loading/ Factor	k_c	f	f_M
	$\frac{1}{1.33 - 0.33\psi} = 1$	$1 - 0.5(1 - k_c) \times [1 - 2(\bar{\lambda}_{LT} - 0.8)^2] = 1$	$1.25 - 0.1\psi - 0.15\psi^2 = 1$
	$\frac{1}{1.33 - 0.33\psi} = 0.75$	Function of the slenderness	$1.25 - 0.1\psi - 0.15\psi^2 = 1.25$
	0.94		1.05
	$\frac{1}{1.33 - 0.33\psi} = 0.60$		$1.25 - 0.1\psi - 0.15\psi^2 = 1.2$
	0.86		1.11

Table 4. Lateral-torsional Buckling Resistance of Beams according to AISC

	$L_b \leq L_p$	$L_p < L_b \leq L_r$	$L_b > L_r$
M_n	$F_y Z_x = M_p$	$C_b \left[M_p - (M_p - 0.7 F_y S_x) \left(\frac{L_b - L_p}{L_r - L_p} \right) \right] \leq M_p$	$F_{cr} S_x \leq M_p$
$L_p = 1.76 r_y \sqrt{\frac{E}{F_y}}$ $L_r = 1.95 r_{ts} \frac{E}{0.7 F_y} \sqrt{\frac{Jc}{S_x h_0} + \sqrt{\left(\frac{Jc}{S_x h_0} \right)^2 + 6.76 \left(\frac{0.7 F_y}{E} \right)^2}}$			

It is noted that both the Special Case and the AISC rule [11] present an extended plateau region of the buckling curve that leads to unsafe results, as reported in [5], [12] and [13] that suggest that a shorter plateau length should be adopted.

3. SAFETY ASSESSMENT METHODOLOGY

3.1 Scope and Assumptions

In order to give a complete overview of the stability design of beams according to Eurocode 3 [1], the study covers the design rules summarized in Table 1. For each method, a wide range of I-shaped cross-sections is analyzed covering different h/b ratios and flange thicknesses across various slenderness ranges. In addition, as the bending moment distribution has a considerable influence on the lateral-torsional buckling resistance, five different bending moment distributions are included in the parametric study, detailed in section 0.

The lateral-torsional resistance of the beams is obtained using advanced numerical finite element simulations. The adopted numerical model is summarized in section 0.

In the safety assessment of the design rules carried out in section 0, the following assumptions are considered:

- The variability of the input variables in the design model is not considered for the calibration of V_8 ; the value is obtained from nominal properties since the “experimental” results are considered with nominal properties;
- The coefficient of variation of the basic variables, V_{rt} , considers only the variability of cross section dimensions, yield stress and modulus of elasticity; for these parameters, more information is known and documented with recent data. The adopted distributions are discussed in section 0.

3.2 Basis of Design

The basis for the statistical assessment of the steel members was presented and discussed in [8]. The procedure proposed in Annex D of EN 1990 [2] is summarized in Figure 1:

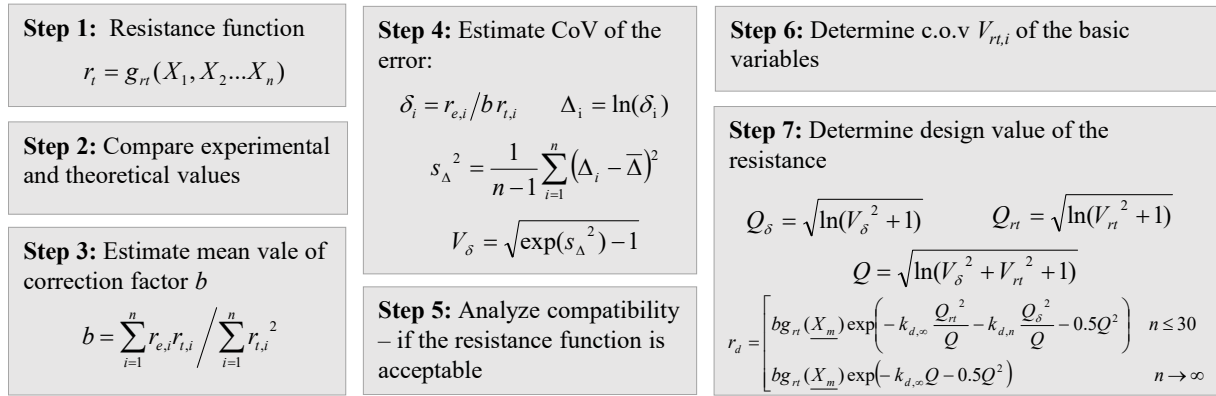


Figure 1. Flow Chart – Annex D

In Step 6 of the procedure given in Figure 1, V_{rt} is determined as follows:

$$V_{rt}^2 = \frac{1}{g_{rt}(X_m)^2} \sum_{j=1}^k \left(\frac{\partial g_{rt}(X_j)}{\partial X_j} \sigma_j \right)^2 \quad (1)$$

The partial derivatives are computed numerically using expression (2) and very small values of “ ΔX_i ” for each test specimen separately, leading to a scatter of $\gamma_{M,i}^*$ for each specimen.

$$\frac{\partial r_i}{\partial X_i} \approx \frac{r_i(X_1, \dots, X_i + \Delta X_i, \dots, X_j) - r_i(X_1, \dots, X_i, \dots, X_j)}{\Delta X_i} \quad (2)$$

3.3 Adopted Distributions

In order to apply the assessment procedure, pre-information regarding the statistical distributions of all basic input parameters which are used in the design calculation is necessary in step 6 of the procedure summarized in Figure 1.

In this evaluation, the variability of the material and geometrical properties are considered. The presence of imperfections is accounted using representative values of those parameters.

The recommended distributions from the European project SAFEBRICKTILE [9] were used in this paper that reflect current European steel production. The statistical parameters summarized in Table 5 were considered as the reference for the variability of the yield stress. The statistical properties in Table 5 refer to the thickness range $t_f < 16$ mm. For higher flange thicknesses, the corresponding mean value should be obtained by multiplying the nominal value according to EN 10025 [14] with the ratio $f_{ym}/f_{y,nom}$ and the coefficient of variation should be kept constant. These distributions were considered for the computation of the γ_{Mi}^* value of each beam, according to its cross-section flange thickness according to the nominal yield stress from EN 10025 [14].

Table 5. Adopted Reference Yield Stress Distributions

Steel grade	$f_{y,nom}$	$f_{ym}/f_{y,nom}$	c.o.v.
S235	235	1.25	5.5%
S355	355	1.2	5%
S460	460	1.15	4.5%

The statistical distributions of the geometrical properties were also considered according to the recommendations of the SAFEBRITILE project Table 6:

Table 6. Adopted Geometrical Distributions

Dimension	b	h	t_w	t_f
mean/nom	1	1	1	0.975
c.o.v	0.9%	0.9%	2.5%	2.5%

The adopted distribution for the modulus of elasticity was based on the recommendations given in DNV[15], and is summarized in Table 7:

Table 7. Statistical Distributions for Modulus of Elasticity DNV [15]

Mean, E_m	σ_E
1.0 E_{nom}	0.05 E_m

Concerning the assumptions for the imperfections (material and geometrical), there is not sufficient recent information on initial bow imperfections and residual stresses to allow for the proposal of statistical distributions for these variables. Hence, as for the columns [10], representative values are selected, following the recommendations of EN [2] and [16]. The geometrical imperfections are assumed as an initial imperfection according to the first global buckling mode with an amplitude $e_0=L/1000$. The residual stresses are considered according to Figure 3.2, following ECCS [17]. The value of f_y^* indicated in Figure 3.2 is considered equal to 235 MPa.

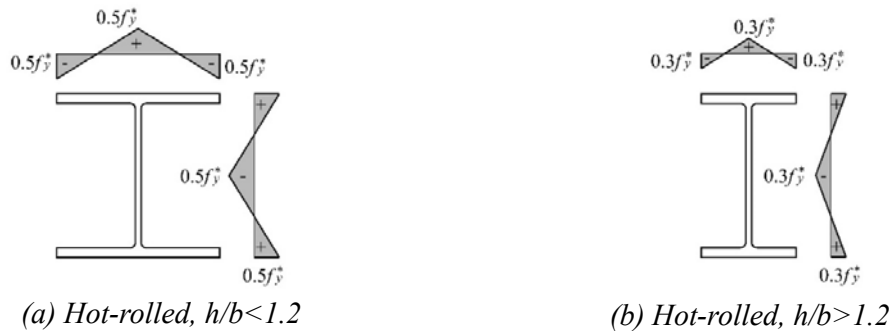


Figure 2. Residual Stresses (“+” Tension and “-” Compression)

It is noted that Taras [3] performed a sensitivity study for the magnitude of the out-of-plane geometrical imperfection, with e_0 varying between $L/500$, $L/1000$ and $L/2000$. According to his results, the maximum differences found between $L/1000$ and the two extremes was about 8% in the medium slenderness range. Furthermore, a similar study on the magnitude of the residual stresses revealed more than 15% difference with respect to the consideration of no residual stresses.

Subramanian and White [18], have recently raised some questions concerning the appropriate imperfections to adopt for numerical simulations of the lateral-torsional buckling resistance. Firstly, they have shown that there is no good correlation between experimental tests and numerical simulations when the usual reference values of the imperfections are adopted in the numerical models. Following an “inverse strategy” [18], they back calculated the residual stresses pattern and geometrical imperfection that leads to good agreement with the experimental results reviewed in their paper. Interestingly, they obtained about half the values of the present European recommendations for both imperfections. Furthermore, they have identified that the ECCS recommendations for both geometrical imperfection and residual stresses adopted above are clearly conservative in comparison to the ones adopted in the United States (both in the AISC and the AASHTO recommendations).

These results show that the adopted representative values for the material and the geometrical imperfections should lead to safe-sided estimates of the lateral-torsional buckling resistance.

3.4 Numerical Modelling

In Step 3 of the procedure given in Figure 1, it is required to estimate the relation between the theoretical and experimental estimates of the member resistance. It is considered that advanced finite element simulations can reproduce with sufficient accuracy the real behaviour and therefore those were carried out to obtain “experimental” results. The simulations were performed using finite element software product Abaqus 6.12 [19], using the guidelines established by Marques et al [20] for the modelling of tapered beams subject to LTB with shell elements.

Each beam is modelled with four-node linear shell elements (S4). The analyses were performed using geometrical and material nonlinearities with imperfections, also known as GMNIA. This type of analysis allows capturing the second order effects which are essential for stability problems.

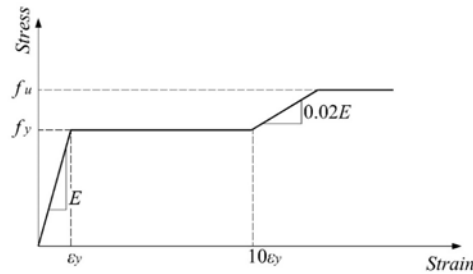


Figure 3. Constitutive Law

Material nonlinearity is incorporated in the model by using elastic-plastic constitutive law with strain-hardening, according to Figure 3, following the recommendations from ECCS [21]. Geometrical imperfections and residual stresses were modelled as described in section 3.3, i.e the initial sweep is assumed according to the first global buckling mode from a linear buckling analysis and the residual stresses are adopted using the ECCS patterns for hot-rolled sections.

The load was applied using a load stepping routine, in which the increment size is chosen in order to meet the accuracy and convergence criteria. The equilibrium equations are solved for each increment using the Newton-Raphson iteration technique.

The adopted mesh comprises 16 sub-divisions in the web and flanges transversely and 100 to 900 divisions along the members' axis depending on the length of the member. Due to the diversity of the cross-sections and the slenderness involved, a maximum relation between the dimensions of the finite elements of about 1/4 was adopted.

The boundary conditions are implemented as end fork conditions in the shell model. The following restraints are imposed: vertical (δy) and transverse (δz) displacements and rotation about xx axis (ϕx) are prevented at nodes 1 and 2. In addition, the longitudinal displacement (δx) is prevented at node 1. The flanges and the web at cross-sections A and B (Figure 4) are modelled to remain straight however allowing for warping, i.e., the flanges can move independently from the web.

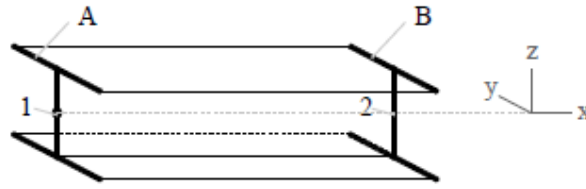


Figure 4. Boundary Conditions

4. SAFETY ASSESSMENT

The results from the safety assessment are summarized in this section. Firstly, the scope of the parametric study is defined, followed by the presentation of the methodology to discuss the results and a general overview of the results for all methods. Then, the results for the General Case are presented as reference results for the subsequent comparisons between all the methods. These comparisons are carried out considering only the yield stress f_y as a random variable. Finally, the influence of the number of random variables is discussed.

4.1 Parametric Study: Definition

Table 8 summarizes the hot-rolled sections selected for the assessment, organized according to the h/b ranges considered by the methods presented in section 2.

The parametric study consists of 3523 numerical calculation runs. It includes several levels of slenderness and different steel grades (the ones currently included in EUROCODE 3 [1]). The parameters are summarized in Table 9. Due to the diversity of the cross-sections and in order to avoid unrealistic lengths, only beams with ratios $L/h < 40$, where L is the beam length and h is the cross-section depth, were considered in the parametric study.

4.2 Parametric Study: Methodology

In the following sections, the results for lateral-torsional buckling of beams are detailed. The main topics that are discussed are:

- Comparison of the various design methodologies for the determination of the lateral-torsional buckling resistance of hot-rolled I-beams with fork conditions;
- Influence of the bending moment distribution;
- Assessment of the imperfection factors for the New EC3 method;
- Influence of the number of random variables

Throughout the following paragraphs, charts and tables, the following methodology is adopted:

- The General Case is presented as the reference method for comparative purposes;
- The partial factors for the different subsets are computed considering the *Annex D* procedure summarized in section 3.2;
- A lower tail approximation is applied to all subsets;
- Whenever a subset according to slenderness is analyzed, the following division is adopted:
 - *Low* slenderness – normalized slenderness $\bar{\lambda} \in [0.2; 0.8]$;
 - *Medium* slenderness – normalized slenderness $\bar{\lambda} \in (0.8; 1.2]$;
 - *High* slenderness – normalized slenderness $\bar{\lambda} \in (1.2; 2.1]$;

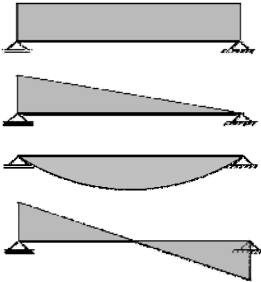
- For the first three topics listed above, only the variability of the yield stress is considered, as a relative assessment is sufficient to establish the influence of each parameter;
- In order to establish the influence of additional random variables, the following variables are considered: yield stress, geometrical dimensions of the cross-section and modulus of elasticity.

All detailed results are given in Annex A.

Table 8. Sections of the Parametric Study for Beams

Fabrication	Limits			Sections		
	[2] and EC1993-1-1 columns	t_f	EC1993-1-1 Beams	h/b	t_f [mm]	Profiles
Rolled	$h/b > 1.2$	$t_f \leq 40\text{mm}$	$h/b > 2.0$	2.22	13.5	IPE400
				2.50	16	IPE500
				2.73	19	IPE600
			$h/b \leq 2.0$	1.82	5.7	IPE100
				2.00	8.5	IPE200
				2.00	9.8	IPE240
				2.00	10.7	IPE300
		$40\text{mm} < t_f \leq 100\text{mm}$	$h/b > 2.0$	2.30	68.1	HL920x725
				2.56	70	HL1000x748
				2.31	73.9	HL920x787
				3.36	64	HE1000x584
				3.08	65	W920x310x576
				2.05	69.1	W610x325x551
			$h/b \leq 2.0$	1.41	40	HE400M
				1.71	40	HE500M
				1.30	19	HE400A
				1.33	24	HE400B
	$h/b \leq 1.2$	$t_f \leq 100\text{mm}$	-	2.0	30	HE600B
				2.52	41.9	HL1000x443
				2.52	46	HL1000x483
				2.27	51.1	HL920x537
				1.00	19	HE300B
				1.00	15	HE200B
				1.00	10	HE100B
				1.13	20	HE100M
				1.10	21	HE300M
				0.95	8	HE120A
				1.09	67.6	HD400x551
				1.10	72.3	HD400x592
				1.12	77.1	HD400x634

Table 9. Parametric Study for Beams: Additional Parameters

Fabrication	$\bar{\lambda}_{LT}$	Material standard for f_y	Material imperfections	Load
Rolled	0.2; 0.4; 0.6; 0.8; 1.0; 1.1; 1.2; 1.3; 1.4; 1.5; 1.6; 1.7; 1.8; 2.0; 2.1	EN 10025: S235 S355 S460	$h/b \leq 1.2$: $f_{y,235}$ $h/b > 1.2$: $f_{y,235}$	

4.3 Overview of Results

Before applying the Annex D procedure for statistical evaluation, it is useful to examine the design model accuracy. In Figure 5 and Figure 6 scatterplots for all the methods are given. In the abscissa, the estimation of the advanced numerical simulations is plotted, while the ordinates correspond to one of the design methods.

In order to give a quantitative measure of the model variations, the statistical parameters for the ratio experimental over theoretical values (r_e/r_t) are given in Table 10, where ratios higher than unity indicate a safe-sided estimation, and on the contrary, ratios lower than 1.0 indicate unsafe results. The General Case and GC/f show a high variability of the results, with coefficients of variation of 8.8% and 7.7% respectively. The ratios r_e/r_t vary from about 10% unsafe to about 40% safe.

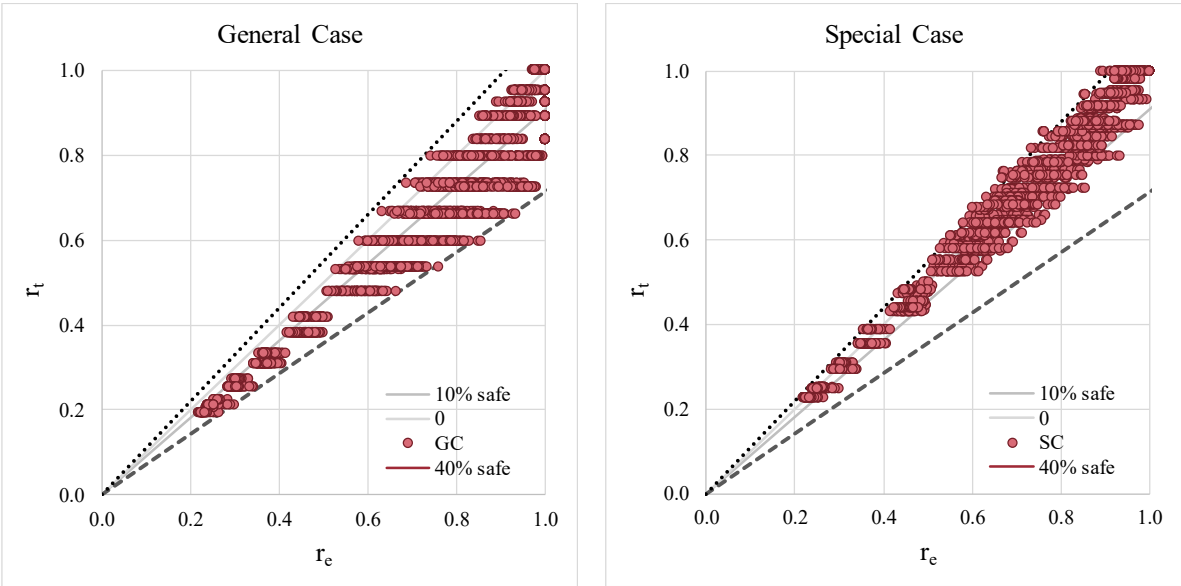


Figure 5. Scatterplots General and Special Case

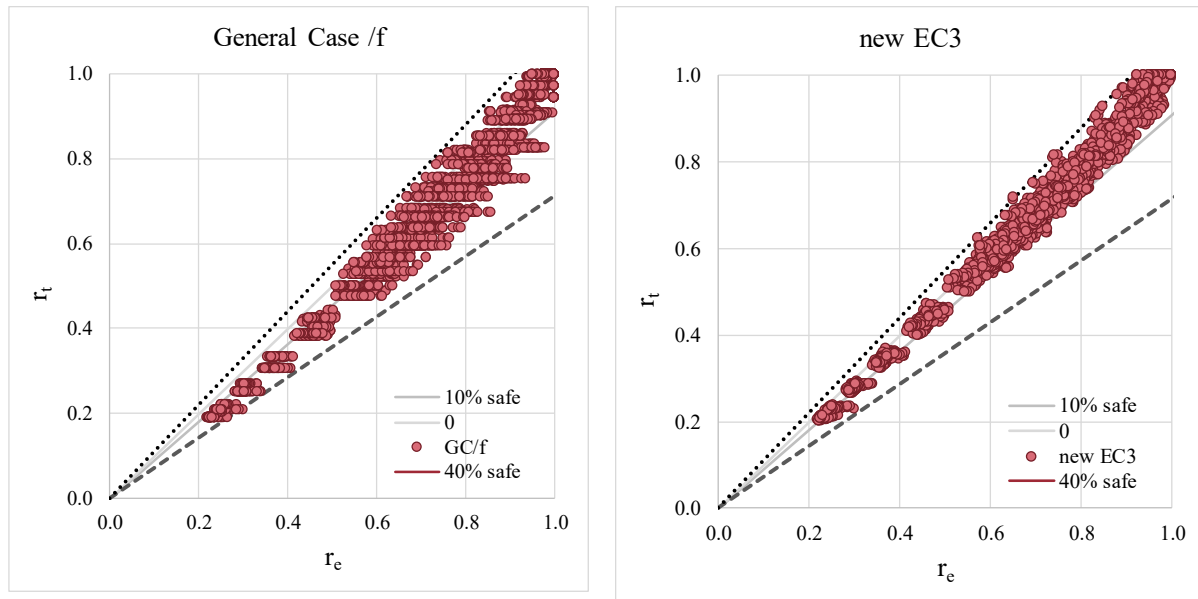


Figure 6. Scatterplots General Case/f and Taras

The other two methods, Special Case and New EC3 have lower coefficients of variation (4.9% and 4.5%, respectively) but the level of overestimation of the resistance by the Special Case is significantly higher than for the New EC3 method.

Finally, Figure 4.3 illustrates the same results for the AISC [11] code specifications, highlighting a large number of unsafe results ($> 55\%$) and a high scatter (9.7%).

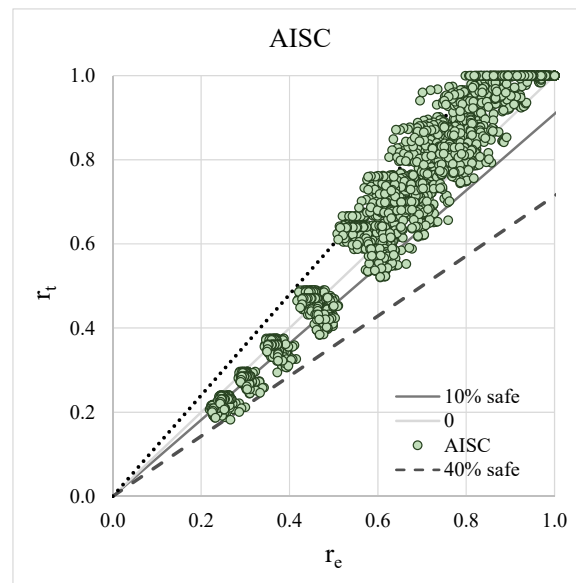


Figure 7. Scatterplots AISC

Table 10. Statistical Parameters

	nEC3	GC	SC	GC/f	AISC
mean	1.03	1.13	1.01	1.08	0.97
std	0.05	0.10	0.05	0.08	0.09
cov	4.5%	8.8%	4.9%	7.7%	9.7%
min	0.91	0.93	0.88	0.93	0.73
max	1.30	1.44	1.21	1.43	1.46
<0.97	144	20	625	73	1641
<1	719	214	1230	431	1966

These results confirm earlier studies on the lateral torsional buckling of beams [3], [5], [22], whereby a high scatter of the LTB resistances across the slenderness was also observed, from unsafe to very safe for the three first methods.

4.4 Results and Discussion: General Case

In this section reference cases considering the General Case are presented. In Figure 8 the γ_M^* results are divided according to slenderness and steel grade. It is observed that there is not a significant difference between the considered steel grades. The higher results in the low slenderness range occur for all steel grades, reflecting the more decisive role that f_y plays for this slenderness range.

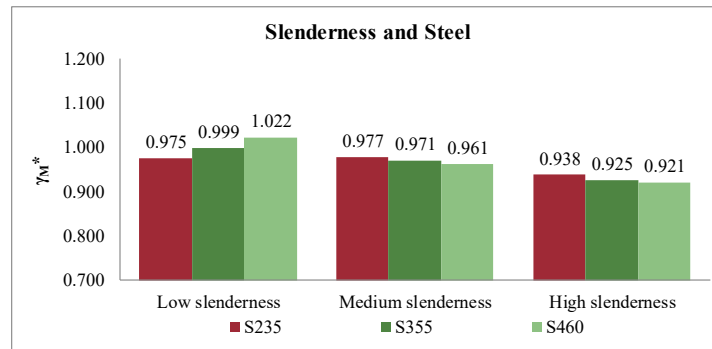
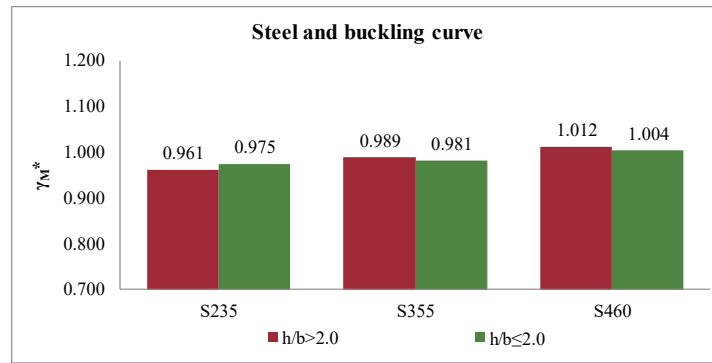
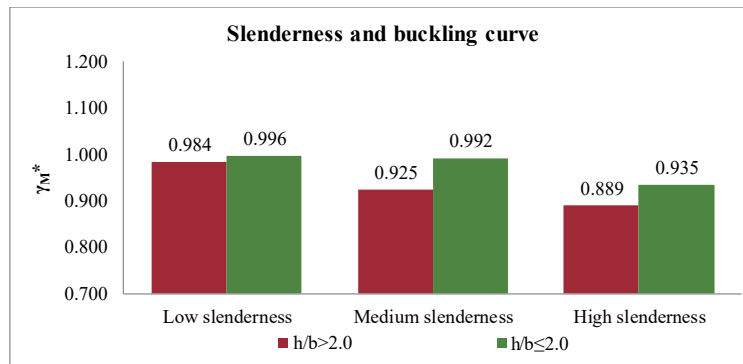
Figure 8. γ_M^* organized by Slenderness and Steel

Figure 9 and Figure 10 organize the results by buckling curve sub-division. The first compares different steel grades, while the latter compares different slenderness ranges. Figure 9 shows that considering subsets organized by steel grade there is a trend of the γ_M^* values to increase with the steel grade. This contrasts with the results of Figure 8, highlighting the importance of the consideration of subsets and the sensitivity of results to the choice of subsets [16]. Figure 10 shows that the safety level of the two buckling curves is not homogeneous.

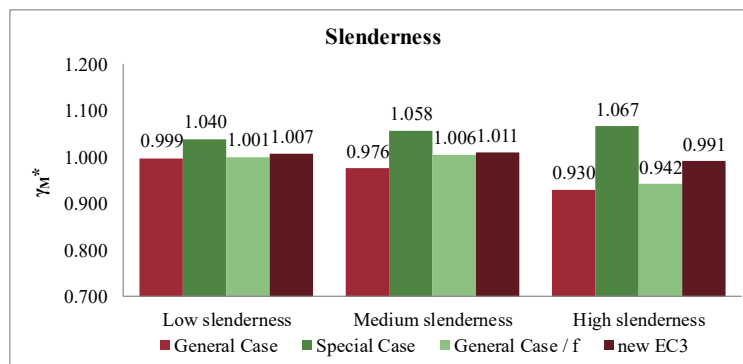
Figure 9. γ_M^* organized by Buckling Curve and Steel Grade for General CaseFigure 10. γ_M^* organized by Buckling Curve and Slenderness for General Case

4.5 Comparison of the design methods

4.5.1 General results

This section compares the 4 methods. In particular, the influence of the buckling curves and the shape of the bending moment are examined in detail.

Figure 11 compares the General Case, the Special Case, General Case/ f and the New EC3 method, according to the slenderness range based on all results available. The Special Case exhibits lower safety, confirming the results of Table 4.3. New EC3 method shows consistent safety across the various slenderness ranges, while the General Case yields significantly higher safety for the medium and high slenderness ranges.

Figure 11. γ_M^* organized by Slenderness

4.5.2 Influence of the buckling curve

In order to verify the consistency according to the buckling curves, the respective subsets are considered. Figure 12 and Figure 13 compare the several methodologies organized by their respective buckling curve and slenderness divisions (General Case, Special Case and General Case/f are split for $h/b \leq 2$, while for the New EC3 method the buckling curves are divided for $h/b > 1.2$, in order to match the definition of buckling curves for the columns). This subdivision of the buckling curves presents the advantage of matching the subdivision of column buckling curves. The imperfection factors are adopted as given in Table 2.

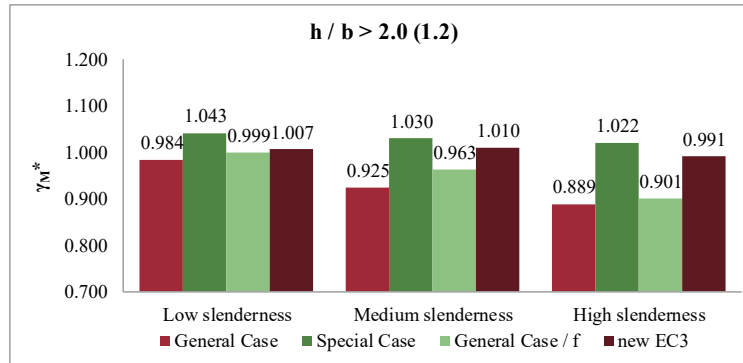


Figure 12. γ_M^* organized by Buckling Curve and Slenderness

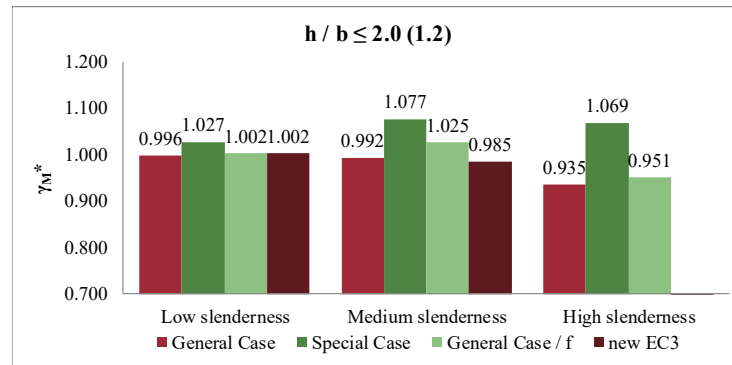


Figure 13. γ_M^* organized by Buckling Curve and Slenderness

It is seen that for all methods except the New EC3 method, the results for $h/b \leq 2.0 (1.2)$ are higher in the medium and high slenderness ranges.

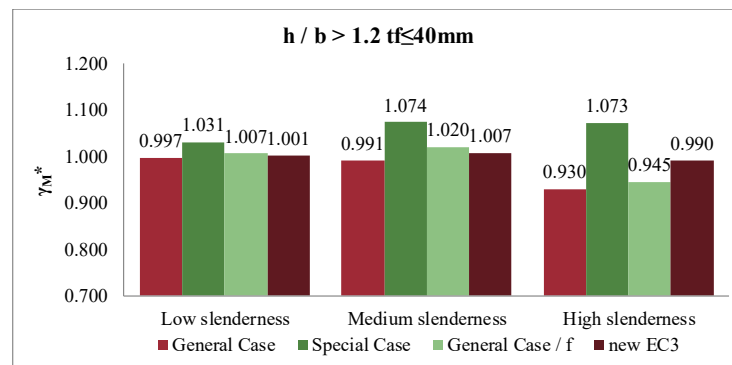


Figure 14. γ_M^* organized by Buckling Curve Division for Hot-rolled Columns and Slenderness

Unlike the buckling curve divisions for columns, the imperfection factors for beams are independent of the flange thickness. In order to verify the influence of the flange thickness, further subsets according to the divisions for buckling curves for the columns are considered. Figure 14, Figure 15 and Figure 16 summarize the results according to slenderness for each interval of the column buckling curves. The results for General Case, Special Case and General Case / f given in Figure 14 and Figure 15 are not very different than the ones in Figure 13, the Special Case showing results with higher safety factors with significant differences in the medium and high slenderness. Finally, for $h/b \leq 1.2$ (Figure 16) all methods show similar results except the General Case in the intermediate slenderness range that is significantly more conservative. It is noted that, in this case, there are no cases in the high slenderness range because they would correspond to unrealistic long beams.

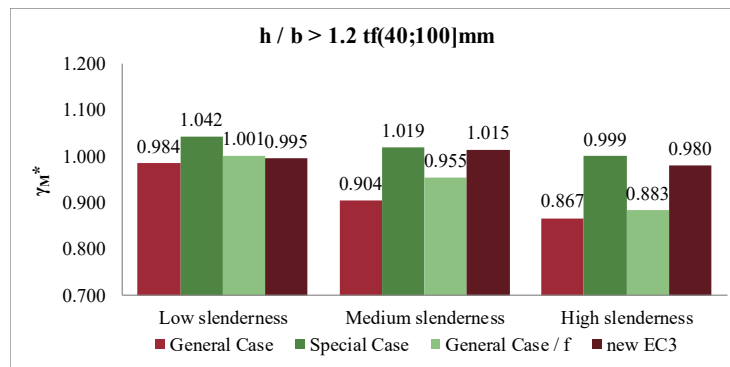


Figure 15. γ_M^* organized by Buckling Curve Division for Hot-rolled Columns and Slenderness

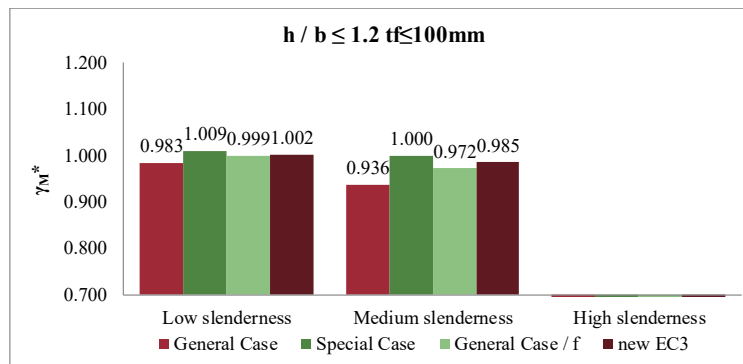


Figure 16. γ_M^* organized by Buckling Curve Division for Hot-rolled Columns and Slenderness

4.5.3 Influence of the shape of the bending moment

The bending moment distribution is an important parameter, which influences the lateral-torsional buckling behaviour of beams. Hence, in this section divisions according to load case and slenderness are presented for the various methods (Figure 17 to Figure 21).

Firstly, it is clearly seen that the General Case is unable to capture the beneficial effect of non-uniform bending moment distributions and thus severely underestimates the LTB resistance, (Figure 17 to Figure 21). As discussed in [5], the GC/ f provides a good estimation of the resistance, despite the f factor being based on calibration to numerical results without any mechanical meaning [3]. The New EC3 method provides relatively uniform partial factors for all load cases and across the various slenderness ranges. The Special Case exhibits considerably higher results mainly in the high slenderness range for all load cases.

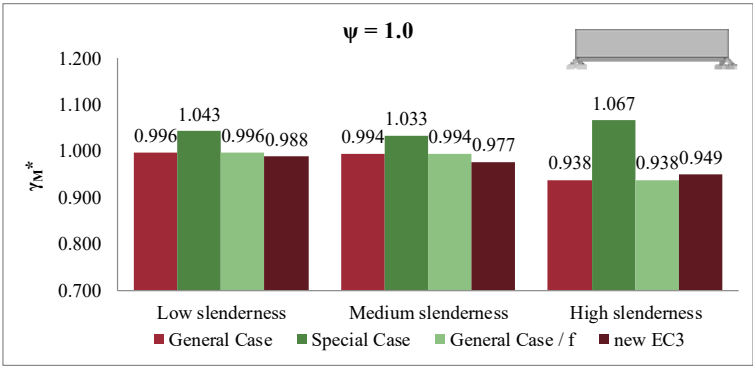


Figure 17. γ_M^* organized by Bending Moment Distribution – Constant Bending Moment

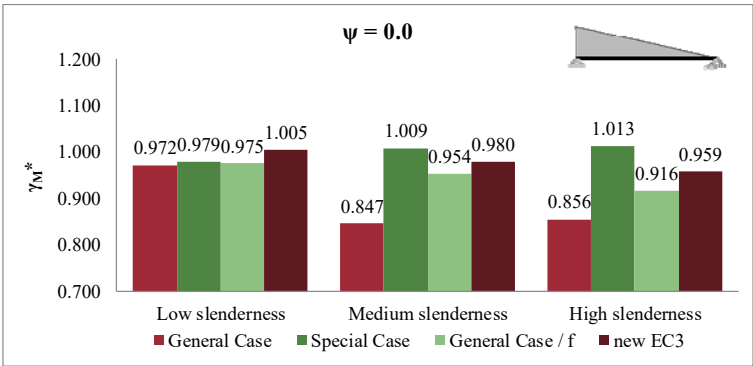


Figure 18. γ_M^* organized by Bending Moment Distribution – Triangular Bending Moment

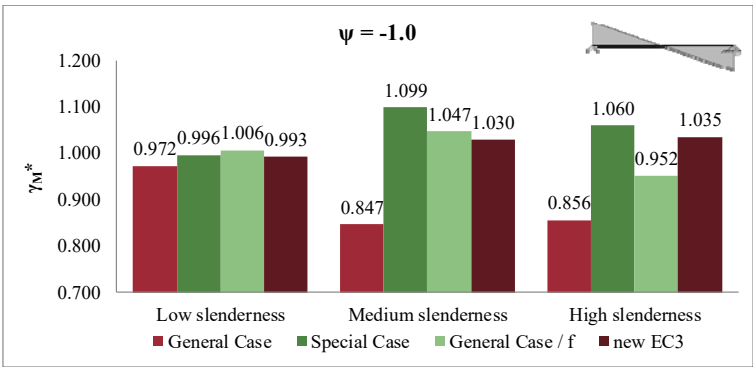


Figure 19. γ_M^* organized by Bending Moment Distribution – bi-triangular Bending Moment

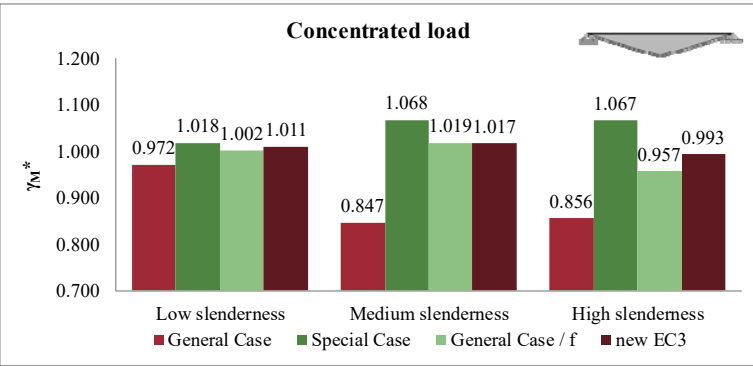
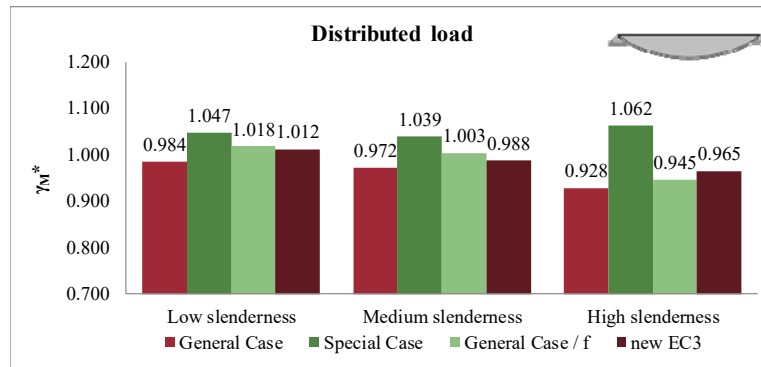


Figure 20. γ_M^* organized by Bending Moment Distribution – Concentrated Load

Figure 21. γ_M^* organized by Bending Moment Distribution – Distributed Load

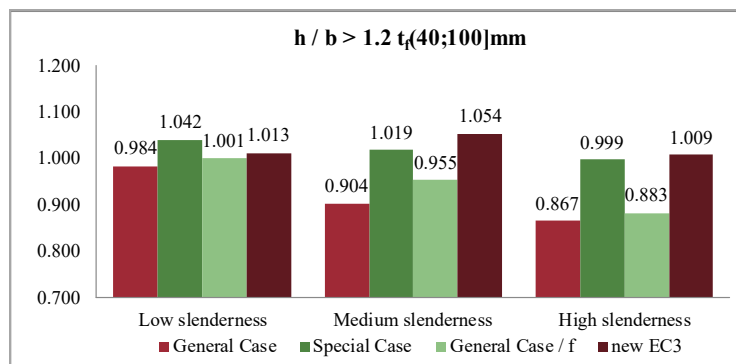
4.6 Buckling Curves for the New EC3 Method

Originally, the buckling curves for the *New EC3 method* were proposed as shown in Table 11 that differs from Table 2 for the range $h/b > 1.2$, $40\text{mm} < t \leq 100\text{mm}$.

Table 11. Original Imperfection Factors for the New EC3 Method

Fabrication	Limits		Source and Method			
	[3]		EUROCODE 3	EUROCODE 3 GC; GC/f	EUROCODE 3 SC	nEC3
Rolled	$h/b > 1.2$	$t \leq 40\text{mm}$	$h/b > 2.0$ $h/b \leq 2.0$	0.34 0.21	0.49 0.34	$0.12 \sqrt{\frac{W_{y,el}}{W_{z,el}}} \leq 0.34$
		$40\text{mm} < t \leq 100\text{mm}$	$h/b > 2.0$ $h/b \leq 2.0$	0.34 0.21	0.49 0.34	$0.12 \sqrt{\frac{W_{y,el}}{W_{z,el}}} \leq 0.34$
	$h/b \leq 1.2$	$t \leq 100\text{mm}$	$h/b > 2.0$ $h/b \leq 2.0$	0.34 0.21	0.49 0.34	$0.16 \sqrt{\frac{W_{y,el}}{W_{z,el}}} \leq 0.49$

Figure 21 compares the values of γ_M^* for the thickness range 40 mm to 100 mm for all methods using the original imperfections from Table 11 for the New EC3 method. It shows that the New EC3 method presents worse results than the SC for this thickness range. This reflects the fact that the method was calibrated for sections with flange thicknesses lower than 40 mm [3].

Figure 22. γ_M^* organized by Buckling Curve Division for Hot-rolled Columns and Slenderness (Old Imperfection Factors)

Hence, recalibration of the imperfections for the thickness range 40 mm to 100 mm led to the imperfection factor of Table 2. The corresponding comparison is illustrated in Figure 22, showing a clear improvement by adopting the same buckling curve as for cross-sections with $h/b > 1.2$.

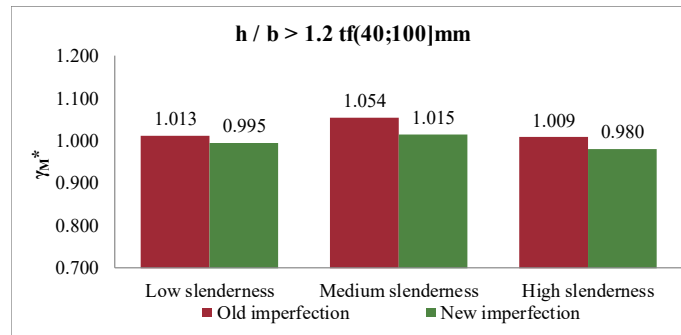


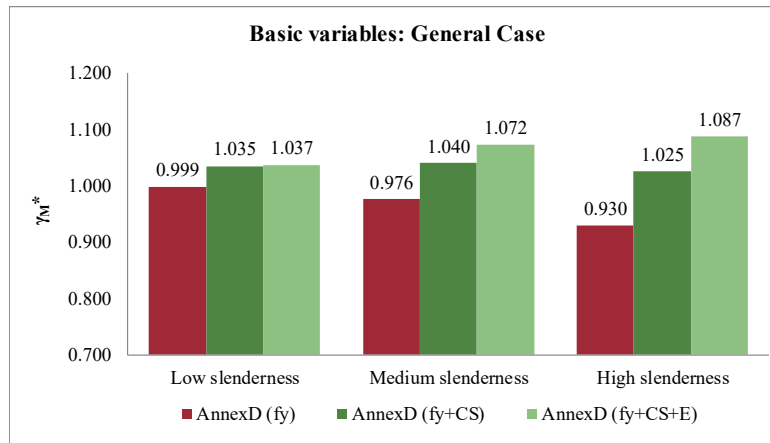
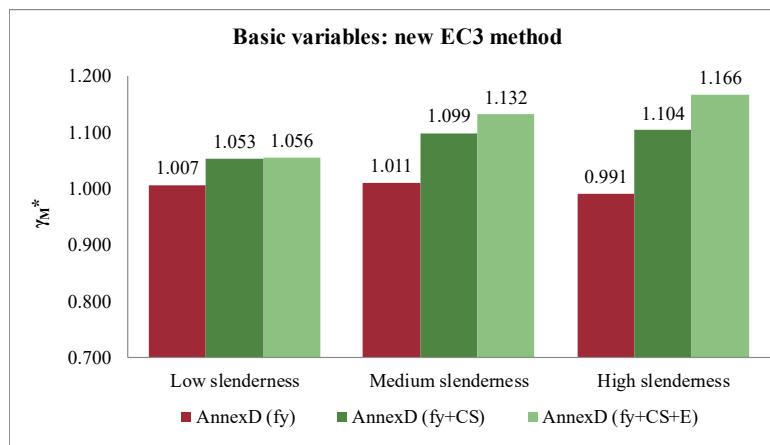
Figure 23. γ_M^* Evaluated Using Old and Recommended Imperfection Factors for New EC3 Method

4.7 Influence of the Number of Random Variables

In all previous comparisons, only the yield stress f_y was considered as a random variable. In reality, in the case of lateral-torsional buckling of beams, other basic variables also affect the behavior of a beam, such as the cross-section dimensions and the Young's modulus. It is noted that geometrical and material imperfections such as initial curvature and residual stresses are not considered as basic random variables as they are included implicitly in the design model [8]. Hence, in this section, the following basic variables are considered as random variables: yield stress – f_y ; geometrical dimensions – b , h , t_w , t_f ; and Young's modulus – E . Their statistical parameters were defined in section 0. In order to highlight their influence, the following cases are considered:

- **Annex D (fy)** – considers the yield stress as the only basic variable, the other parameters are assumed as deterministic quantities with no variability;
- **Annex D (fy+CS)** – considers the yield stress and the geometrical dimensions of the cross-section as random variables;
- **Annex D (fy+CS+E)** – considers the yield stress, the geometrical dimensions of the cross-section and the modulus of elasticity as random variables;

The General Case is presented as the reference case for this assessment. Figure 24 compares the results for the 3 cases defined above, according to slenderness range. Similarly, to the observations in [10], the increased number of random variables leads to higher partial factors. This effect becomes more noticeable with increasing slenderness due to the increased influence of the geometrical properties and the modulus of elasticity. Similar results are obtained for the other methods (see Table A.1). Figure 25 illustrates the corresponding results for the New EC3 method.

Figure 24. γ_M^* by Slenderness and Using Different Number of Random Variables: GCFigure 25. γ_M^* by Slenderness and Using Different Number of Random Variables: New EC3

5. ASSESSMENT OF THE VALUE OF THE PARTIAL FACTOR

Table 12 summarizes the results for γ_M^* for the three different sets of random variables that were considered and the four design methods, using a lower tail approximation due to the systematic deviation from a normal distribution. The conclusion from the previous section is confirmed for all methods - depending on the random variables included in the analysis (just f_y ; f_y and cross-section geometry; or f_y , cross-section geometry and modulus of elasticity E) the partial factor increases its magnitude.

Firstly, except for the Special Case, a good homogeneity of results is observed across the different buckling curves, with maximum variations of 0.05. However, it is interesting to notice that making the assessment only considering sub-sets according to slenderness for all cases (see also Table A.1) leads to significantly higher values of γ_M^* , highlighting the importance of considering different buckling curves.

Secondly, the Special Case systematically presents higher partial factors (0.05 higher on average) for most of the subsets. The General Case presents the lowest partial factors. However, recalling Table 10, it is clearly over conservative, leading in many cases of practical relevance to values of design resistance up to 40% lower than those obtained from advanced numerical simulations.

Table 12. Values of γ_{M1}^* Obtained Using Different Combinations of Basic Variables for All Methods

Limits		Annex D (fy)				Annex D (fy+CS)				Annex D (fy+CS+E)			
		GC	nEC3	GC/f	SC	GC	nEC3	GC/f	SC	GC	nEC3	GC/f	SC
$h/b > 1.2$	$t_f \leq 40\text{mm}$	0.987	1.003	1.004	1.056	1.030	1.058	1.056	1.128	1.039	1.069	1.072	1.160
	$40\text{mm} < t_f \leq 100\text{mm}$	0.983	0.978	0.978	1.032	1.017	1.027	1.018	1.082	1.020	1.034	1.023	1.094
	$t_f > 100\text{mm}$	-	-	-	-	-	-	-	-	-	-	-	-
$h/b \leq 1.2$	$t_f \leq 100\text{mm}$	0.983	1.006	0.999	1.010	1.018	1.051	1.038	1.050	1.018	1.054	1.039	1.052

Table 13. Partial Factors for Beams and Columns (fy+CS+E)

Limits		Axis	Flexural Buckling		Lateral-torsional buckling		
			S235 S355	S460	EC3	GC	nEC3
$h/b > 1.2$	$t_f \leq 40\text{mm}$	y-y	1.079	1.120	$h/b > 2.0$	1.039	1.069
		z-z	1.098	1.118	$h/b \leq 2.0$		
	$40\text{mm} < t_f \leq 100\text{mm}$	y-y	1.011	1.063	$h/b > 2.0$	1.020	1.034
		z-z	1.021	1.048	$h/b \leq 2.0$		
	$t_f > 100\text{mm}$	y-y	1.018	1.067	-	-	-
		z-z	1.043	1.070			
$h/b \leq 1.2$	$t_f \leq 100\text{mm}$	y-y	1.046	1.094	$h/b \leq 2.0$	1.018	1.054
		z-z	1.115	1.109			
	$t_f > 100\text{mm}$	y-y	-	-	-	-	-
		z-z	-	-			

The results from Table 13 support the recent decision by CEN TC250/SC3 to adopt the new Ayrton-Perry-based method [3] as the reference methodology for double symmetric I-and H cross-sections, while retaining the General Case for the cases that are currently not covered by the New EC3 method (mono-symmetric sections and other cross-sectional shapes).

Table 13 compares the γ_M^* values for the General Case and the New EC3 method with the results obtained for the flexural buckling resistance of columns considering f_y , cross-section geometry and E as random variables, using the same statistical characterization of the random variables.

It is observed that the partial factors obtained for LTB of beams are generally lower than those obtained for flexural buckling of columns.

Finally, comparing the Eurocode methods with the AISC methodology, the latter would lead to significantly higher values of the partial factor γ_M^* (See Table 10).

6. CONCLUSIONS

In this paper, the safety assessment of EUROCODE 3 [1] rules for lateral-torsional buckling of prismatic beams with hot-rolled I-shaped cross sections was performed and the partial factor was evaluated considering several subsets, including slenderness range, level of yield stress, EUROCODE 3 [1] buckling curves; flange thickness. The assessment also covered the new EC3 method [3].

Firstly, similar conclusions as stated in [10] for columns are also valid for beams concerning the influence of the adopted minimum yield stress using EN 10025 or Table 3.1 of Eurocode 3 [1].

The results highlight a strong sensitivity of γ_{M1}^* to the subsets that are considered in the calculation. This trend is also confirmed by comparing these results with the corresponding results from [5] and [22]. This difference led to the consideration of a lower tail approximation that significantly improved the homogeneity of results. Globally, the partial factor γ_{M1}^* for the New EC3 method is 1.05, with a c.o.v. of 1.7%.

Regarding the design methods, the conservative nature of the General Case was confirmed, the Special Case systematically led to higher values of γ_{M1}^* for the majority of subsets and the accuracy of the New EC3 method was confirmed. Regarding this method, an adjustment of the imperfection factors is proposed for cross-sections with $h/b > 1.2$ and flange thickness higher than 40 mm, because this geometric range was not considered in the original derivation of the imperfection factors.

It was shown that the AISC design rules lead to higher resistance predictions, with large scatter. The underlying safety associated with those rules reflects the lower reliability index that is accepted by the American code ($\beta = 2.6$ (approximate value for members) instead of 3.8 as in EN 1993-1-1). Finally, the magnitude of the partial factors was found to be similar or lower than the one obtained for columns and therefore, provided the proposed statistical distributions are respected, it is recommended to keep $\gamma_{M1} = 1.0$ for beams.

ACKNOWLEDGEMENTS

The research leading to these results has received funding from:

- the European Community's Research Fund for Coal and Steel (RFCS) under grant agreement SAFEBRICKTILE RFS-PR-12103 – SEP no. 601596;
- the Portuguese Foundation for Science and Technology (FCT) under grant agreement SFRH/BD/99702/2014
- partly financed by FEDER funds through the Competitiveness Operational Programme - COMPETE and by national funds through FCT – Foundation for Science and Technology within the scope of the project POCI-01-0145-FEDER-007633”

NOTATIONS

Latin upper-case letters

C_b	Lateral-torsional buckling modification factor
C_w	Warping constant
E	Modulus of elasticity (210GPa in EN1993 and 200GPa for AISC)
F_y	Specified minimum yield stress
GMNIA	Geometrically and materially non-linear imperfection analysis
J	Torsional constant
L_b	Length between points that are either braced against lateral displacement of the compression flange or braced against twist of the cross section
L_p	Limiting length
L_r	Limiting length
$M_{y,Rk}$	characteristic resistant bending moment
$M_{y,Ed}$	design value of the bending moment
M_{cr}	elastic buckling critical moment
$M_{b,Rd}$	design lateral-torsional buckling resistance of the member in bending
M_n	Nominal flexural strength
M_p	Plastic bending moment
S_x	Elastic section modulus about the x-axis
V_X	Coefficient of variation
V_δ	Estimator for the coefficient of variation of the error term
\underline{X}_m	Array of mean values of basic variables
$W_{pl,y}$	plastic bending modulus
$W_{el,y}$	elastic bending modulus
$W_{eff,y}$	effective bending modulus
Z_x	Plastic section modulus about the x-axis

Latin lower-case letters

b	Correction factor
c	Coefficient (=1.0 for I sections)
f	additional factor for bending moment distribution (Special Case)
h_0	Distance between flange centroids
$g_{rt}(\underline{X})$	Resistance function used as a design model
$k_{d,n}$	Design fractile factor
N	Number of experiments or numerical results
r_d	Design value of the resistance
r_e	Experimental resistance value
r_n	Nominal value of the resistance
r_t	Theoretical resistance determined with $g_{rt}(\underline{X})$
r_{ts}	Effective radius of gyration
r_y	Radius of gyration about y-axis (AISC)
S	Estimated value for the standard deviation σ
s_A	Estimated value for the standard deviation σ_A

Greek upper-case letters

Δ	Logarithm of the error term δ
$\overline{\Delta}$	Estimated value for $E(\Delta)$

Greek lower-case letters

α_{LT}	imperfection factor for lateral-torsional buckling
B	an additional factor for SC
Δ	Error term
δ_i	Observed error term for test specimen i
η_{LT}	generalized imperfection for lateral-torsional buckling
σ	Standard deviation
σ_{Δ}^2	Variance of the term Δ
Φ	additional factors for bending moment distribution
χ_{LT}	reduction factor for lateral-torsional buckling

REFERENCES

- [1] Eurocode – EN 1993-1-1, Eurocode 3: Design of Steel Structures - Part 1-1: General Rules and Rules for Buildings CEN, Brussels, 2005.
- [2] Eurocode – EN 1990, Eurocode – Basis of Structural Design, CEN, Brussels, 2002.
- [3] Taras, A., “Contribution to the Development of Consistent Stability Design Rules for Steel Members”, PhD Thesis, Technical University of Graz, Graz, Austria, 2010.
- [4] Snijder, H.H. and Hoenderkamp, J.C.D., “Buckling Curves for Lateral Torsional Buckling of Unrestrained Beams”, Rene Maquoi 65th birthday anniversary, 2007, Liège Belgium.
- [5] Rebelo, C., Lopes, N., Simões da Silva, L., Nethercot D. and Vila Real, P.M.M., “Statistical Evaluation of the Lateral-Torsional Buckling Resistance of Steel I-beams, Part 1: Variability of the Eurocode 3 resistance model”, Journal of Constructional Steel Research., Elsevier, 2009, Vol. 65, pp. 818-831.
- [6] Maquoi, R., Rondal, J., “Mise en Équation des Nouvelles Courbes Européennes de Flambement”, Construction Métallique, 1978, No.1, pp. 17-30.
- [7] CEN/TC250, Eurocode 3: Design of Steel Structures - Part 1-1: General Rules and Rules for Buildings, CEN/TC 250/SC 3 N 2440 - prEN 1993-1-1 - 2nd draft, 2017.
- [8] Tankova, T., Simões da Silva, L., Marques, L., Rebelo, C. and Taras, A., “Towards a Standardized Procedure for the Safety Assessment of Stability Design Rules”, Journal of Constructional Steel Research, Elsevier, 2014, Vol. 103, pp. 290-302.
- [9] Simões da Silva, L., Marques, L., Tankova, T., Rebelo, C., Kuhlmann, U., Kleiner, A., Spiegler, J., Snijder, H.H., Dekker, R., Dehan, V., Haremza, C., Taras, A., Cajot, L.G., Vassart, O. and Popa, N., “Safebrictile: Standardization of Safety Assessment Procedures across Brittle to Ductile Failure Modes”, 2017, RFSR-CT-2013-00023, Final Report.
- [10] Simões da Silva, L., Tankova, T., Marques, L. and Rebelo, C., “Safety Assessment of EC3 Stability Design Rules for Flexural Buckling of Columns”, Advanced Steel Construction – an International Journal, 2016, Vol. 12, No. 3, pp. 328-358.
- [11] ANSI/ASCI 360-10, AISC, American Institute of Steel Construction, Specification for Structural Steel Buildings, Chicago, Illinois, USA, 2010.
- [12] Kim, Y.D., “Behavior and Design of Metal Building Frames Using General Prismatic and Web-Tapered Steel I-Section Members”, Doctoral Dissertation, School of Civil and Environmental Engineering, Georgia Institute of Technology, Atlanta, GA, 2010.

- [13] Subramanian, L.P., Jeong, W.Y., Yellepeddi, R. and White, D.W., “Assessment of I-Section Member LTB Resistances Considering Experimental Tests and Practical Inelastic Buckling Solutions”, Structural Engineering, Mechanics and Materials Report No.110, School of Civil and Environmental Engineering, Georgia Institute of Technology, Atlanta, GA, 2016.
- [14] CEN, European Committee for Standardization, EN 10025: 2004 – Hot Rolled Products of Structural Steels, 2004.
- [15] DNV, Guideline for Offshore Structural Reliability Analysis – Chapter 7, DNV Report No. 95-2018, Det Norske Veritas, Hovik, Norway, 1995.
- [16] Taras, A., Dehan, V., Simões da Silva, L., Marques L. and Tankova, T., “Guideline for the Safety Assessment of Design Rules for Steel Structures in Line with EN 1990”, Deliverable D1.1, SAFEBRIC TILE RFSR-CT-2013-00023, 2017.
- [17] ECCS, Ultimate Limit State Calculation of Sway Frames with Rigid Joints, Publication No.33 Brussels, 1984.
- [18] Subramanian, L.P. and White, D.W., “Resolving the Disconnect between Lateral Torsional Buckling Experimental Tests and Tests Simulations, and Design Strength Equations”, Journal of Constructional Steel Research, Elsevier, 2017, Vol. 128, pp. 321-334.
- [19] Abaqus, v.6.12, Dassault Systems/Simulia, Providence, RI, USA, 2012.
- [20] Marques, L., Simões da Silva, L., Greiner, R., Rebelo, C. and Taras, A., “Development of a Consistent Design Procedure for Lateral-torsional Buckling of Tapered Beams”, In: Journal of Constructional Steel Research, 2013, Vol. 89, pp. 213–235
- [21] ECCS, “European Recommendations for Steel Construction”, Brussels, 1978.
- [22] Simões da Silva, L., Rebelo C., Nethercot D. Marques, L., Simões, R. and Vila Real, P.M.M, “Statistical Evaluation of the Lateral-Torsional Buckling Resistance of Steel I-beams, Part 2: Variability of steel properties”, Journal of Constructional Steel Research, Elsevier, 2009, Vol. 65, No. 4, pp. 832-849.

BEHAVIOR OF PLASTIC GREENHOUSES UNDER SYMMETRIC LOADING BEFORE AND AFTER STRENGTHENING WITH TENSION TIES

S.H. Lee¹, K.J. Shin^{2,*} and H.D. Lee³

¹ Assistant Professor, School of Convergence & Fusion System Engineering,
Kyungpook National University, 2559, Gyeongsang-daero, Sangju-si, Gyeongsangbuk-do, 37224, Republic of Korea

² Professor, School of Architectural Engineering,

³ Associate Research Engineer, School of Architectural Engineering,
Kyungpook National University, 80 Daehak-ro, Buk-gu, Daegu 41566, Republic of Korea

*(Corresponding author: E-mail: shin@knu.ac.kr)

Received: 1 October 2017; Revised: 21 November 2017; Accepted: 13 December 2017

ABSTRACT: In recent years, climate anomalies have led to major snowfall and heat waves causing immeasurable loss of life and property. Particularly, sudden snowfall led to the collapse of several plastic greenhouse in South Korea within the last five years. This study proposes a strengthening method that uses tension ties to prevent the collapse of plastic greenhouses. Five full-scale frames were prepared to investigate the strengthening effect of the ties. A frame included a controlled specimen without tension ties, and the other frames were strengthened frames. The variables in this study were divided into two categories: (a) tension tie materials consisting of a fiber rope and a steel wire and (b) pretension forces of 100 N and 200 N. The testing results revealed that the normal frame failed in flexure, and that the failure of the strengthened frames occurred through out-of-plane buckling. The load capacities of the strengthened frames exceeded those of the reference frames without tension ties by 30% to 65%.

Keywords: Plastic greenhouse, strengthening, tension tie, heavy snowfall, plastic hinge, flexure, collapse

DOI: 10.18057/IJASC.2018.14.10

1. INTRODUCTION

Over the past five years, the number of plastic greenhouses that have collapsed in South Korea has increased (see Figure 1) because of sudden heavy snowfall and the insufficient resistance of greenhouse frames. In 2010, the total monetary amount of plastic greenhouse damage due to heavy snow reached approximately \$19.9 million, and the heavy snowfall of 2011 caused \$20.4 million in greenhouse damages according to an announcement by the National Disaster Information Center (NDIC) [1]. Additionally, in December 28, 2012, up to 100 mm of snow fell in the Pusan and Gyeongsangnam-do regions. This resulted in damages of \$9.5 million due to the partial and total damage of plastic greenhouses. Typically, Pusan and Gyeongsangnam-do areas were characterized by an absence of snowfall, and thus the snowfall in 2012 significantly damaged the plastic greenhouses in these areas. In December 2010, the Ministry for Food, Agriculture, Forestry and Fisheries (MFAFF), and the Rural Development Administration (RDA) initiated a plan against these types of natural disasters [2]. The government actively encouraged the standardization of existing pipes for plastic greenhouses according to technical specifications of 2016. The limitations of steel pipe material included the following: 1) SPVHS or SPVHS-AZ with yield and tensile strength exceeding 295 MPa and 400 MPa, respectively, should be always used for the structural pipes of plastic greenhouse; 2) The elongation of the pipe should exceed 20%; and 3) A zinc galvanizing pipe with a thickness exceeding 6 μm should be used to prevent corrosion at the weld zones. Furthermore, from 2017, the government will not pay compensation for damages to plastic greenhouses that do not use SPVHS or SPVHS-AZ.

A greenhouse is shaped like an arch, but the actual behavior of a green house is closely associated with the frame. The greenhouse is created by bending a long single pipe into a curved arch element (or beam) and a vertical element (or column). The curved arch element and the vertical element are geometrically continuous without any connection element, as shown in Figure 2. The greenhouse is very weak, slender, and exhibits a limited ability to resist the forces because the bending moment is larger than the axial force due to external loads. In order to improve these weaknesses, several researches (Lee *et al.* [3]; Lee *et al.* [4]; Kim *et al.* [6]) proposed certain strengthening methods (such as horizontal bracing, X-type bracing, pillar supports, and high-performance sections) and carried out analyses to demonstrate the strengthening effect by using commercial software programs. In this study, a strengthening method using tension ties was temporarily set at the joint of the arch and the column when the snowfall was expected. The tie changed the frame behavior to tie-arch action in the greenhouse and increased the load capacity while tie installed. This study focused on the effect of the proposed strengthening method through experimental and analytical investigations of plastic greenhouses consisting of $\phi 25.4 \times 1.5$ mm SPVHS pipes. It may be noted that the SPVHS represented a zinc galvanized steel pipe used for vinyl housing structures in South Korea. The equivalent concentrated loading tests at four points were carried out in accordance with the roof slope factor for cold roofs based on ASCE/SEI 7-10 [7] or KBC 2009 [8]. Additionally, the results from a theoretical approach to flexural and plastic analyses, and a buckling analysis using a commercial software Midas Gen [9], were compared to the test results.



Figure 1. Collapse of a Plastic Greenhouse due to Heavy Snow

2. EXPERIMENTAL PROGRAM

2.1 Test Specimens and Variables

There are 18 kinds of plastic greenhouses with a single span against disasters in MIFAFF and RDA [2]. With respect to these greenhouses, the greenhouse frames with dimensions as illustrated in Figure 2 were designed for the loading test in this study. The distance L_1 between columns at the base was 6500 mm; the distance L_2 between the tops of the columns was 6100 mm; the vertical height H_1 was 1700 mm (it may be noted that the actual height of the column used in the analysis was approximately 1500 mm, because the bottom of the column was inserted into a support); the arch rise H_2 was 1200 mm; and the frame space s was 880 mm. Seven crossbars were installed as braces between two frames, and four crossbars were set in loading positions. A pipe of $\phi 25.4 \times 1.5$ mm was bent around a forming mold at room temperature. The arch part of the frame, particularly the top of the column, yielded in this bending process. The tension ties (such as a $\phi 4$ mm steel wire

or a fiber rope with dimensions of $37 \text{ mm} \times 2 \text{ mm}$) were connected at the tops of the columns, and pretension forces of 100 N or 200 N were determined to be within the ranges of human limits. Table 1 shows the test variables consisting of types of tension ties and pretension forces. The specimen names were defined according to the variables. Specifically, “FR” denoted frame; “6” represented a distance of 6500 mm between the bases; “25” symbolized $\phi 25.4 \times 1.5\text{t}$; “TR” and “TW” represented a tension rope tie and tension wire tie, respectively; and “100” and “200” corresponded to pretension forces.

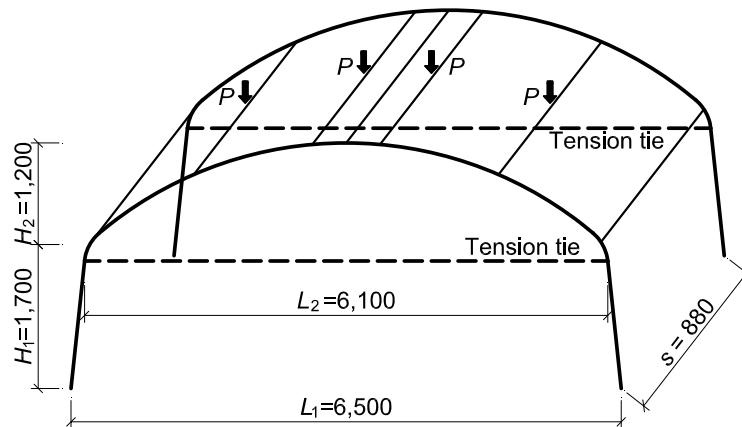
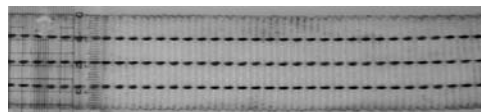


Figure 2. Dimensions of the Test Frame (unit: mm)

Table 1. Type and Pretension of Ties

Specimen	Tie	Pretension (N)
FR6-25	—	—
FR6-25-TR-100	Fiber rope*	100
FR6-25-TR-200	Fiber rope	200
FR6-25-TW-100	Steel wire*	100
FR6-25-TW-200	Steel wire	200



*Fiber rope



*Steel wire

2.2 Material Properties

The sectional and material properties of the pipe utilized in the study are summarized in Tables 2 and 3. The material properties of the pipe were obtained through stub-column testing, and the measured strengths exceeded the nominal strength. A length of the stub-column test specimen was three times the outer-diameter of pipe. The test was carried out on a universal test machine with a maximum capacity of 1000 kN. Based on the tensile tests for tension ties as shown in Table 1, the average ultimate load and stiffness corresponded to 5.49 kN and 7.5 N/mm for the fiber rope; and 10.15 kN and 50 N/mm for the steel wire, respectively.

Table 2. Type and Pretension of Ties

A (mm ²)	I (mm ⁴)	S (mm ³)	Z (mm ³)
112.6	8073.3	635.7	857.9

Note: A is the cross-sectional area; I is the moment of inertia; S is the section modulus; Z is the plastic section modulus.

Table 3. Material Properties of a $\phi 25.4 \times 1.5$ t Pipe

Section (mm)	Nominal strength		Stub-column test		
	F_y (MPa)	F_u (MPa)	F_y (MPa)	F_u (MPa)	F_y/F_u (%)
$\phi 25.4 \times 1.5$ t	≥ 295	≥ 400	430	525	82

Note: F_y is the yield strength; F_u is the ultimate strength.

2.3 Sloped Roof Snow Loads based on ASCE/SEI 7-10

Snow loads acting on a sloping surface were assumed to act on the horizontal projection of the surface. The sloped roof snow load p_s could be obtained by multiplying the flat roof snow load p_f by the roof slope factor C_s as following Eq. 1.

$$p_s = C_s p_f \quad (1)$$

where C_s was assumed for cold roofs. Additionally, because the plastic (or vinyl) as covering materials for the greenhouse had unobstructed slippery surfaces that allowed the snow to slide off the eaves, C_s was denoted by the dashed line as shown in Figure 7-2c of Chapter 7 in ASCE/SEI 7-10 [7] given by the following conditions: i) for slopes between 0° and 15° , C_s corresponded to 1.0; ii) for slopes above 70° , C_s was considered free of snow loads; and iii) for slopes between 15° and 70° , C_s was calculated by linear interpolation. By assuming the plastic greenhouse was an unheated and open-air structure, the thermal factor C_t was determined as 1.2. Given that the snow load p_s was proportional to C_s , the equivalent four loading points according to C_s are depicted in Figure 3. In the figure, L_a is 1450 mm; L_b is 1400 mm; and L_c is 800 mm.

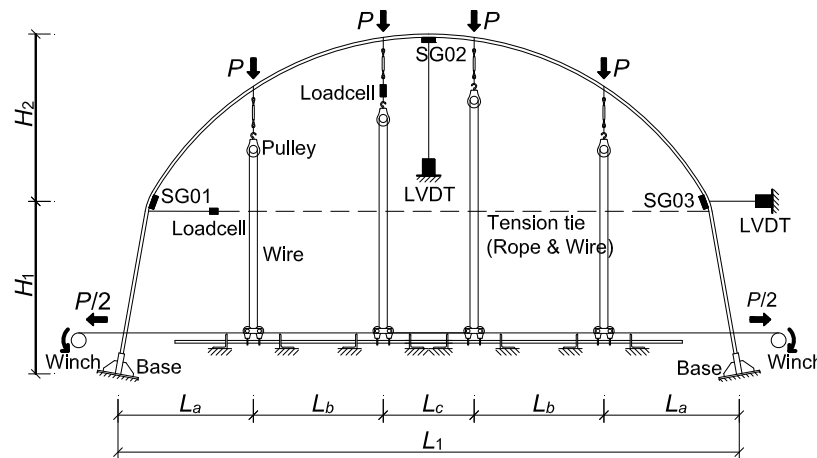


Figure 3. Positions of the Loading Points

2.4 Loading Method for Large Deformation

It was difficult to load the structure using a general actuator or a universal testing machine in the case where an arch rise was high and the loading points were few, as shown in Figure 3. The arched jigs used to load the structure at a few points did not apply the load to the frame uniformly and did not continue loading when the arch frame collapsed and formed a large deformed shape. Hence, for the arch type frame, a loading apparatus that could uniformly act on the frame regardless of its indented shape and appropriately load the structure at a few points according to the number of pulleys was developed, as shown in Figure 3 [10].

Figure 4 shows the detailed view of the pulleys. Two pulleys at the bottom were merged into a fixed pulley to avoid splitting, and the fixed pulley could be easily moved from side-to-side by utilizing shackles to transfer vertical loads even when large lateral deformation occurred. Two winches as shown in Figure 5 were placed outside both ends of the frame and the loading was initiated by manually winding up these winches using a steel wire and a few pulleys, as illustrated in Figure 4.

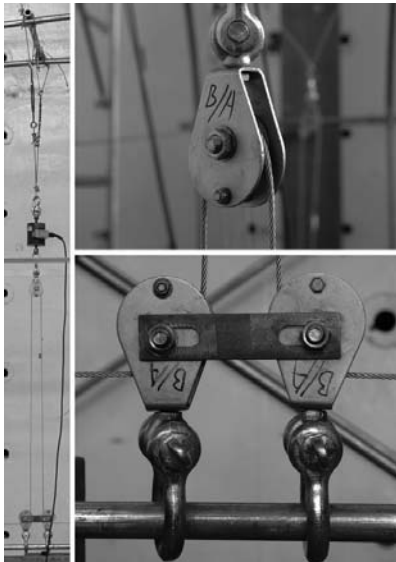


Figure 4. The Experimental Set-up Depicting a Movable Pulley at the Top and a Fixed Pulley at the Bottom

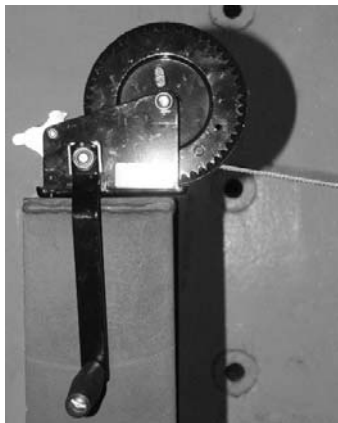


Figure 5. Winch used for Loading

Figure 6 shows the devices used in the study for pretensioning the tension ties. A ratchet, shown in Figure 6a, is a mechanical device that allows continuous linear or rotary motion in only one direction while preventing motion in the opposite direction. A turnbuckle in Figure 6b is a device used for adjusting the tension or length of the wire. The pretension force and added tension by external loading were monitored through a load cell inserted between the tension ties (ropes or wires).

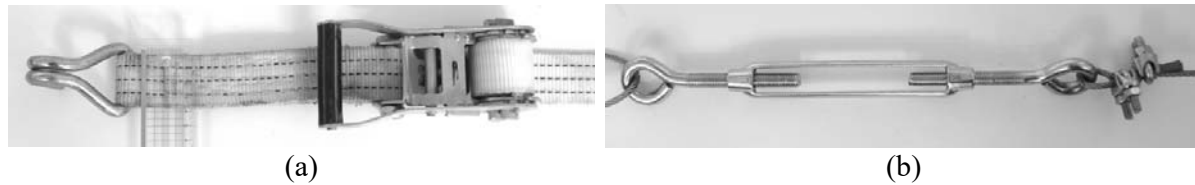


Figure 6. Device for Pretension: (a) Ratchet for the fiber rope; (b) Turn-buckle for the steel wire.

The greenhouse bases in the field were generally driven into the ground. In order to simulate this field condition, a fixed support consisting of a base plate with a cylinder, which was more rigid than the main pipe and enhanced with stiffeners, as shown in Figure 7, was used. The rigid cylinder was 200 mm deep.

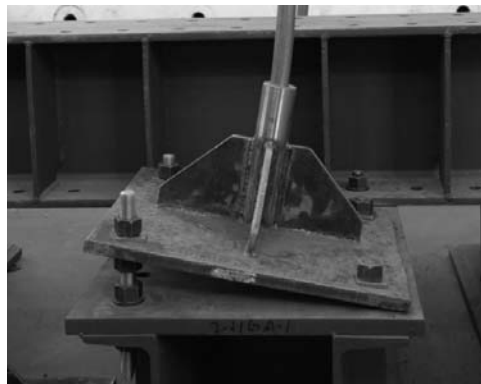


Figure 7. Fixed Support of Foundation

2.5 Test Results

Figure 8 illustrates the vertical load versus deflection at mid-span for all the specimens. The vertical load was half the value measured by the load cell because it corresponded to two frames. An unstrengthened frame failed in flexure at a deflection of 329 mm, corresponding to a peak load of 228 N. The uplift caused by the pretension was as follows: 12.2 mm for TR-100; 17.0 mm for TR-200; 10.8 mm for TW-100; and 23.3 mm for TW-200. The results of the FR6-25-TR-200 specimen indicated an error because the steel wire for the main vertical loading had been fixed when the pretension was applied. The main vertical loading after pretension was initiated at the uplift point. In the case of the strengthened frames with the fiber ropes, the load capacity increased by 35% and 41% but the deflection decreased by 59% and 54%. The testing results revealed that the stiffness of the steel wire was 6.7 times that of the fiber rope, and thus the peak load substantially increased (by 58% and 65%) while indicating a 90% reduction in the deflection. All the strengthened frames failed in out-of-plane buckling. Additionally, the strains monitored by attached three strain gauges declined with the reduction of vertical and horizontal displacements. The test results are summarized in Table 4.

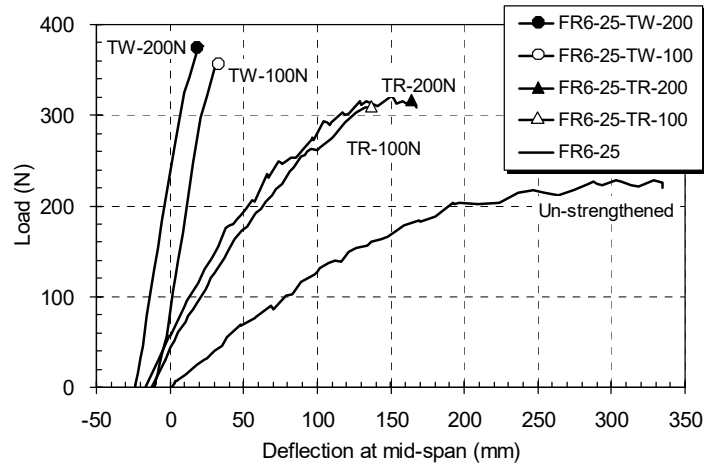


Figure 8. Load versus Deflection at Mid-span of all the Specimens

Table 4. Summary of the Test Results

Specimen	Uplift (mm)	Peak load (N)	Deflection (mm)	SG01 ($\mu\epsilon$)	SG02 ($\mu\epsilon$)	SG03 ($\mu\epsilon$)
		Increase	Decrease	Decrease	Decrease	Decrease
FR6-25	—	228	329	-3038	4191	-3317
FR6-25-TR-100	-12.2	309 (35%)	136 (-59%)	-1413 (-53%)	2298 (-45%)	-1250 (-62%)
FR6-25-TR-200	-17.0	321 (41%)	150 (-54%)	-1383 (-54%)	2396 (-43%)	-1252 (-62%)
FR6-25-TW-100	-10.8	361 (58%)	32 (-90%)	-143 (-95%)	441 (-89%)	409 (-112%)
FR6-25-TW-200	-23.3	377 (65%)	23 (-93%)	-71 (-98%)	399 (-90%)	658 (-120%)

The failure of the unstrengthened frame occurred through in-plane flexural failure mode. The plastic hinges formed at the tops of the columns and both supports. Conversely, the strengthened frames failed in out-of-plane buckling (see Figure 9).

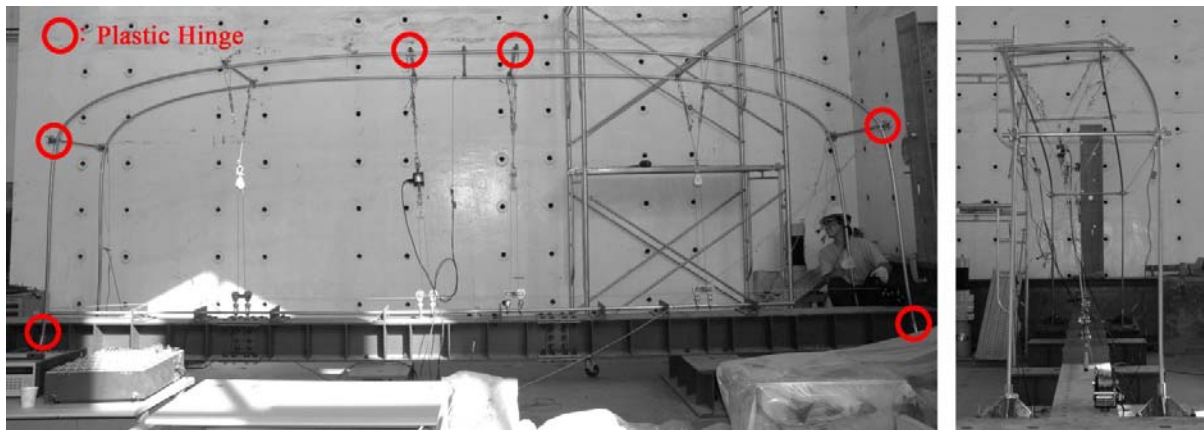


Figure 9. Failure Mode (left: unstrengthened frame; right: strengthened frame with tension ties)

In next section, a flexural analysis and a plastic analysis were conducted to evaluate the elastic behavior and the collapse load, respectively for an unstrengthened frame. A buckling analysis using a commercial program was also performed for the strengthened frame.

3. ANALYSIS METHOD

The applied load-vertical deflection relationship for greenhouses with or without tension ties was determined by using a bilinear relationship through analytical approaches (e.g. flexural, plastic, and buckling analysis). The first stage involved a linear elastic state using flexural analysis. The second stage included the establishment of the peak load by a plastic analysis using the failure mechanism for the unstrengthened frame or the buckling load results obtained by Midas Gen software for the strengthened frame.

3.1 Flexural Analysis

The plastic greenhouse was arranged in a symmetric form. Responses including member forces and deformations of the entire structure under any loading could be obtained from the responses of one of the portions of the structure separated by the axis of symmetry [11]. The plastic greenhouse could be considered as symmetric with respect to an OE axis as illustrated in Figure 10. Point A was considered as fixed by the foundation shown in Figure 7, and point E on the symmetric axis was assumed to have horizontal displacement and moment that were fixed. A horizontal spring with a stiffness of k_B at point B was used to model the tension tie (but k_B was zero in the unstrengthened frame), and an imaginary vertical spring at point E was used to calculate the vertical deflection (it may be noted that k_E was zero in all the frames). Hence, the unstrengthened frame had two redundants (M_E and H_E), and the strengthened frame had three redundants (H_E , M_E , and F_B).

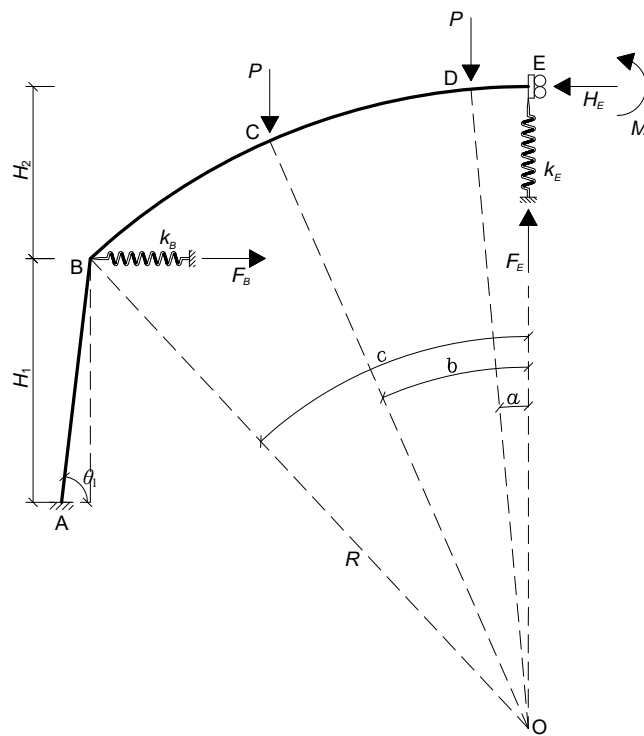


Figure 10. Analysis Model for Flexural Analysis (note that a, b and c are in radians)

The unknown values of H_E , M_E , $\delta_{E,v}$, and $\delta_{B,h}$ that denoted a horizontal reaction force, a moment reaction, a vertical deflection at point E, and a horizontal displacement at point B, respectively, were calculated through a linearly elastic analysis using Castigliano's theorem. First, the bending moment distributions are determined as follows:

(i) for the region corresponding to $0 \leq \theta \leq a$ (θ is varied from point E to B)

$$M_\theta = M_E + H_E R[1 - \cos \theta] + F_E R \sin \theta \quad (2a)$$

(ii) for the region corresponding to $a \leq \theta \leq b$ (θ is varied from point D to C)

$$M_\theta = M_E + H_E R[1 - \cos(\theta + a)] + F_E R \sin(\theta + a) - PR[\sin(\theta + a) - \sin a] \quad (2b)$$

(iii) for the region corresponding to $a \leq \theta \leq c$ (θ is varied from point C to B)

$$M_\theta = M_E + H_E R[1 - \cos(\theta + b)] + F_E R \sin(\theta + b) - PR[2 \sin(\theta + b) - (\sin a + \sin b)] \quad (2c)$$

(iv) for the region corresponding to $0 \leq s \leq H_1$ (s is varied from point B to A)

$$M_s = M_E + H_E [R(1 - \cos c) + s] + F_E [R \sin c + s \tan(\pi/2 - \theta_1)] - P[R(2 \sin c - \sin a - \sin b) + 2s \tan(\pi/2 - \theta_1)] - F_B s \quad (2d)$$

where M_θ is the bending moment at arbitrary θ ; M_E and H_E are the moment reaction and the horizontal reaction force at point E, respectively; R is the radius of the arch; F_E is the imaginary force due to a vertical spring at point E; F_B is the force applied to the spring (e.g., tension tie) at point B; P is the external load; a is the angle between point E and D; b is the angle between point E and C; c is the angle between point E and B; θ_1 is the angle of the column with respect to the ground; and s is the arbitrary vertical distance from point B to A.

Second, the deformations of the main points were determined by Castigliano's theorem. The rotation θ_E , the horizontal displacement $\delta_{E,h}$ and the vertical deflection $\delta_{E,v}$ of point E are given as following Eqs. 3-5.

$$\begin{aligned} \theta_E &= \frac{1}{EI} \left(\int_0^s \frac{M_\theta \partial M_\theta}{\partial M_E} ds + \int_0^{H_1} \frac{M_s \partial M_s}{\partial M_E} ds \right) \\ &= \frac{1}{EI} \left(\int_0^c \frac{M_\theta \partial M_\theta}{\partial M_E} R d\theta + \int_0^{H_1} \frac{M_s \partial M_s}{\partial M_E} ds \right) \end{aligned} \quad (3)$$

$$\begin{aligned} \delta_{E,h} &= \frac{1}{EI} \left(\int_0^s \frac{M_\theta \partial M_\theta}{\partial H_E} ds + \int_0^{H_1} \frac{M_s \partial M_s}{\partial H_E} ds \right) \\ &= \frac{1}{EI} \left(\int_0^c \frac{M_\theta \partial M_\theta}{\partial H_E} R d\theta + \int_0^{H_1} \frac{M_s \partial M_s}{\partial H_E} ds \right) \end{aligned} \quad (4)$$

$$\begin{aligned}\delta_{E,v} &= \frac{1}{EI} \left(\int_0^s \frac{M_\theta \partial M_\theta}{\partial F_E} ds + \int_0^{H_1} \frac{M_s \partial M_s}{\partial F_E} ds \right) \\ &= \frac{1}{EI} \left(\int_0^c \frac{M_\theta \partial M_\theta}{\partial F_E} R d\theta + \int_0^{H_1} \frac{M_s \partial M_s}{\partial F_E} ds \right)\end{aligned}\quad (5)$$

where E is the modulus of elasticity of the pipe; I is the moment of inertia of the pipe, and θ_E and $\delta_{E,h}$ are zero because rotation and horizontal displacement are fixed at point E.

The F_B term was considered only in the column because there was no F_B term in the arch region ($0 \leq \theta \leq c$). As a result, the horizontal displacement $\delta_{B,h}$ at point B could be calculated by the following Eq. 6.

$$\delta_{B,h} = \frac{1}{EI} \int_0^{H_1} \frac{M_s \partial M_s}{\partial F_B} ds \quad (6)$$

Substituting Eq. 2 into Eqs. 3-6, the equations for the unknown values could be expressed in matrix form as shown below:

$$\frac{1}{EI} \begin{bmatrix} k_{11} & k_{12} & k_{13} & k_{14} \\ k_{21} & k_{22} & k_{23} & k_{24} \\ k_{31} & k_{32} & k_{33} & k_{34} \\ k_{41} & k_{42} & k_{43} & k_{44} \end{bmatrix} \begin{bmatrix} M_E \\ H_E \\ F_E \\ F_B \end{bmatrix} - \frac{P}{EI} \begin{bmatrix} p_1 \\ p_2 \\ p_3 \\ p_4 \end{bmatrix} = \begin{bmatrix} 0 \\ 0 \\ \delta_{E,v} \\ \delta_{B,h} \end{bmatrix} \quad (7)$$

The spring forces F_B and F_E could be defined by using Hooke's law (i.e., $F_B = -k_B \delta_{B,h}$ and $F_E = -k_E \delta_{E,v}$). The negative sign indicates that the spring reaction force and the deformation force are in opposite directions. After replacing F_E and F_B and rearranging, the matrix form could be rewritten as shown Eqs 8a or 8b.

$$\begin{bmatrix} k_{11} & k_{12} & k_{13}(-k_E) & k_{14}(-k_B) \\ k_{21} & k_{22} & k_{23}(-k_E) & k_{24}(-k_B) \\ k_{31} & k_{32} & k_{33}(-k_E) - EI & k_{34}(-k_B) \\ k_{41} & k_{42} & k_{43}(-k_E) & k_{44}(-k_B) - EI \end{bmatrix} \begin{bmatrix} M_E \\ H_E \\ \delta_{E,v} \\ \delta_{B,h} \end{bmatrix} = P \begin{bmatrix} p_1 \\ p_2 \\ p_3 \\ p_4 \end{bmatrix} \quad (8a)$$

$$[\bar{K}][\bar{U}] = [\bar{P}] \quad (8b)$$

where the components (k_{ii} and p_i) of the matrix are summarized in the Appendix. In order to obtain the unknown matrix $[\bar{U}]$ of the unstrengthened frame, " $k_B = 0$ " was inserted into the matrix. In the frames with the tension ties, values of twice the stiffness measured by the tensile test were applied since the analysis model shown in Figure 10 corresponded to half of the entire structure. Hence, k_B was 15 N/mm for the fiber rope and 100 N/mm for the steel wire. The externally applied load P (that was a collapse load) for the greenhouse frame was obtained through a plastic or buckling analysis as described in the next section.

The initial deformations and redundants resulting from pretensioning could be obtained by changing the right side of Eq. 8 and substituting $k_B = k_E = 0$. The right side components could be replaced with equations representing the pretensioning force P_{pre} as following Eq. 9.

$$P_{pre} \begin{bmatrix} \frac{1}{2} H_1^2 \\ \frac{1}{2} R H_1^2 (1 - \cos c) + \frac{1}{3} H_1^3 \\ \frac{1}{2} R H_1^2 \sin c + \frac{1}{3} H_1^3 \tan(\pi/2 - \theta_1) \\ -\frac{1}{3} H_1^3 \end{bmatrix} \quad (9)$$

Figure 11 shows the three relative bending moment distributions resulting from the external load when there was no pretension tie or when there was rope or wire as a tie irrespective of the pretension force. The bending moment in a frame without a tie was much larger than that in a frame with a rope or wire. The decreased bending moment distribution demonstrated the effect of using a pretension tie. A frame without a tie had large bending moments at points A, B, D and E. In an unstrengthened frame, the bending moment was approximately zero at loading point C on the arch and was 700 mm away from the top of the column. When the rope or wire was used as a strengthening material, the moment distribution between points B and C was visibly changed. In other words, a bending moment at point B (top of column) in an unstrengthened frame was large, but following the strengthening, the moments were larger at points between points B and C or loading point D.

Assuming that the stiffness of the tie was infinite, the result was not significantly different from that of a frame with wire tie ($k_B = 100$ N/mm). However, the moment sign in the lower part of the column was reversed when compared with $k_B = 100$ N/mm. If ties with stiffnesses of 5, 15, 100, and ∞ N/mm were used as strengthening materials, the maximum moments decreased by 63%, 35%, 22%, and 18%, respectively. Thus, any fiber material at hand could help prevent flexural failure in plastic greenhouses caused by heavy snowfall.

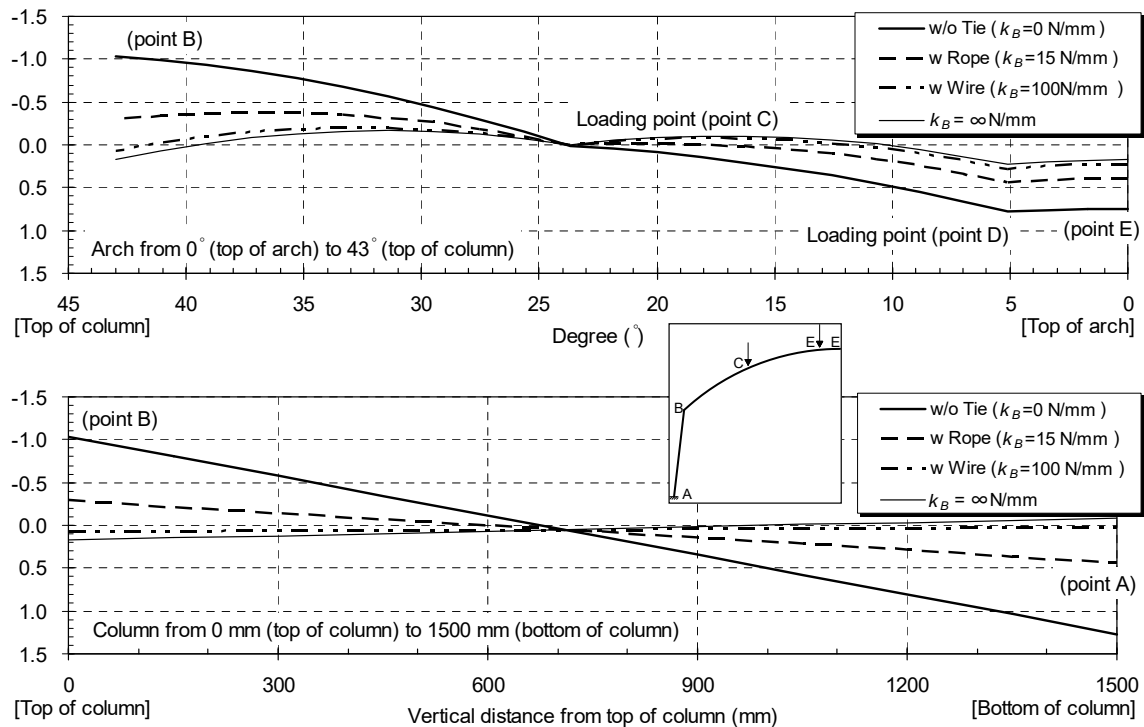


Figure 11. Bending Moment Diagram by the External Load

3.2 Plastic Analysis of Unstrengthened Model

The plastic analysis using a virtual work method reported by Lee *et al.* [12] is introduced in this section. The unstrengthened frame failed in flexure while forming plastic hinges at three points, namely at the top of the column, the support, and the loading point D corresponding to points A, B, and D, respectively. The collapse mode is shown in Figure 9. If the plastic moment capacity of the straight pipe prior to bending was assumed as M_p , a moment capacity at the base (point A) indicated a positive M_p when subjected to an external load P . The plastic moment capacities at points B, C, D, and E could be assumed as βM_p , γM_p , ηM_p , and λM_p , respectively, because these sections were deformed due to plastic bending (see Figure 12a). However, the magnitudes of γ , η , and λ factors were defined as “1” since the deformation was small and that of β was assumed as 0.8 because of the excessive deformation. A dashed line indicated an undeflected shape before loading, and a solid line denoted a deflected shape after loading. Points denoted by ‘•’ show the assumed plastic hinge locations. Figure 12b is an analytical model presented for simplicity.

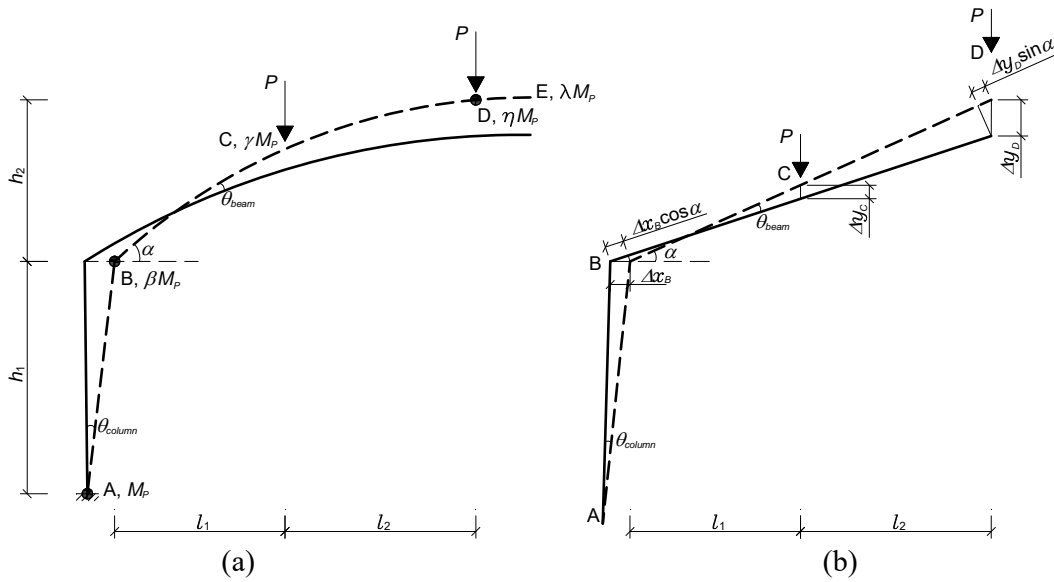


Figure 12. Determinate Arch Frame subjected to Applied Loads and Plastic Hinges: (a) Deformed shape of plastic greenhouse; (b) Deformed shape for simplicity.

In Figure 12b, a horizontal displacement at point B (Δx_B) and a vertical deflection at point D (Δy_D) could be expressed by the following Eqs. 10 and 11.

$$\Delta x_B = h_1 \theta_{column} \quad (10)$$

$$\Delta y_D = \sqrt{(l_1 + l_2)^2 + h_2^2} \theta_{beam} \cos \alpha \quad (11)$$

Assuming that beam length was not changed before and after the external loading, Δx_B and Δy_D shared the following relationship of Eq. 12.

$$\Delta y_D \sin \alpha = \Delta x_B \cos \alpha \quad (12)$$

From Eqs. 10-12, θ_{column} and θ_{beam} could be rearranged as the following Eq. 13.

$$\theta_{column} = \frac{\sqrt{(l_1 + l_2)^2 + h_2^2} \sin \alpha}{h_1} \theta_{beam} \quad (13)$$

The internal work (W_i) at the plastic hinges and the external work (W_e) by the external loading were calculated by using the following Eqs. 14 and 15.

$$\begin{aligned} W_i &= M_p \theta_{column} + \beta M_p (\theta_{column} + \theta_{beam}) + M_p \theta_{beam} \\ &= (1 + \beta) M_p (\theta_{column} + \theta_{beam}) \\ &= (1 + \beta) M_p \left[\frac{\sqrt{(l_1 + l_2)^2 + h_2^2} \sin \alpha}{h_1} + 1 \right] \theta_{beam} \end{aligned} \quad (14)$$

$$\begin{aligned} W_e &= (\Delta y_C + \Delta y_D) P \\ &= \left(\frac{2l_1 + l_2}{l_1 + l_2} \right) \Delta y_D P \\ &= \left(\frac{2l_1 + l_2}{l_1 + l_2} \right) \sqrt{(l_1 + l_2)^2 + h_2^2} \theta_{beam} \cos \alpha P \end{aligned} \quad (15)$$

Finally, the collapse load P_p was expressed as following Eq. 16.

$$P_p = (1 + \beta) M_p \left[\frac{\sqrt{(l_1 + l_2)^2 + h_2^2} \sin \alpha}{h_1} + 1 \right] \left/ \left(\frac{2l_1 + l_2}{l_1 + l_2} \right) \sqrt{(l_1 + l_2)^2 + h_2^2} \cos \alpha \right. \quad (16)$$

where h_1 and h_2 denoted the height of column and the vertical height between points B and D, respectively; θ_{column} is the plastic rotation at column bottom; l_1 is the horizontal distance between points B and C; l_2 is the horizontal distance between points C and D; θ_{beam} is the plastic rotation of the beam element; α is the angle between beam and column elements; and Δy_C and Δy_D are the vertical deflections at point C and D, respectively. From the plastic analysis above, the collapse load in an unstrengthened frame was conservatively computed as approximately 304 N.

3.3 Buckling Analysis of Strengthened Model

For the buckling analysis, the analytical model was generated with a commercial software, Midas Gen. In this section, a linear (eigenvalue) buckling analysis was performed to obtain the critical load factors and buckling mode shapes. The equilibrium equation shown in Eq. 17 was formulated as an eigenvalue equation where K is the elastic stiffness of the greenhouse; λ is the eigenvalue or buckling load factor; K_G is the additional geometric stiffness due to the stresses caused by the initial loading; and U is the displacement of the greenhouse as indicated by the following Eq. 17.

$$[K + \lambda K_G][U] = 0 \quad (17)$$

The strengthened frame failed in out-of-plane buckling in the first buckling mode shape at buckling loads of 361 N and 427 N as shown in Figure 13.

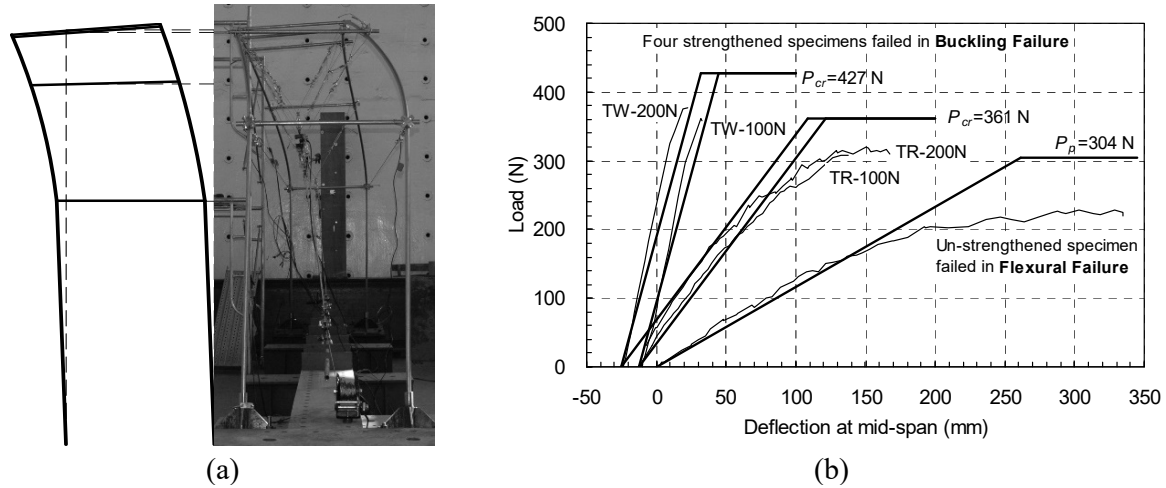


Figure 13. Results of the Test and Analyses:

(a) Buckling mode in the strengthened specimen; (b) Load-deflection curves of all the specimens

4. SUMMARY AND CONCLUSION

In this study, a strengthening method using tension ties (i.e., fiber rope and steel wire) was proposed to prevent plastic greenhouse collapse due to heavy snow in South Korea. The equivalent concentrated loading test at four points and analytical approaches were carried out. The test results indicated that the tension tie could increase the load capacity by 35%–65%. The strengthened arch frames failed due to out-of-plane buckling during the test, which indicated a high probability of increasing the load capacity if out-of-plane buckling was prevented. Specifically, because the plastic greenhouse frame was restricted by the cover material (or vinyl) and rope (for preventing the flapping of the cover material) in the field, the collapse resulting from heavy snowfall was due to flexural failure rather than buckling (see Figure 1). Furthermore, in unstrengthened plastic greenhouse frames, the flexural elastic and plastic analyses could predict the responses including elastic stiffness and collapse load.

ACKNOWLEDGEMENT

This research was supported by Fire Fighting Safety & 119 Rescue Technology Research and Development Program funded by the Ministry of Public Safety and Security (MPSS-fire safety-2015-72) and Basic Science Research Program through the National Research Foundation of Korea (NRF) funded by the Ministry of Science, ICT & Future Planning (No. NRF-2015R1C1A1A01054899).

APPENDIX

$$k_{11} = Rc + H_1 \quad (\text{A.1a})$$

$$k_{12} = R^2(c - \sin c) + RH_1(1 - \cos c) + \frac{1}{2}H_1^2 \quad (\text{A.1b})$$

$$k_{13} = R^2(1 - \cos c) + RH_1 \sin c + \frac{1}{2} H_1^2 \tan(\pi/2 - \theta_1) \quad (\text{A.1c})$$

$$k_{14} = -\frac{1}{2} H_1^2 \quad (\text{A.1d})$$

$$k_{21} = k_{12} \quad (\text{A.2a})$$

$$k_{22} = R^3 \left(\frac{3}{2} c - 2 \sin c + \frac{\sin 2c}{4} \right) + R^2 H_1 (1 - \cos c)^2 + RH_1^2 (1 - \cos c) + \frac{1}{3} H_1^3 \quad (\text{A.2b})$$

$$k_{23} = R^3 \left(\frac{3}{4} - \cos c + \frac{\cos 2c}{4} \right) + R^2 H_1 (1 - \cos c) \sin c \\ + \frac{1}{2} RH_1^2 [(1 - \cos c) \tan(\pi/2 - \theta_1) + \sin c] + \frac{1}{3} H_1^3 \tan(\pi/2 - \theta_1) \quad (\text{A.2c})$$

$$k_{24} = -\frac{1}{2} RH_1^2 (1 - \cos c) - \frac{1}{3} H_1^3 \quad (\text{A.2d})$$

$$k_{31} = k_{13} \quad (\text{A.3a})$$

$$k_{32} = k_{23} \quad (\text{A.3b})$$

$$k_{33} = R^3 \left(\frac{c}{2} - \frac{\sin 2c}{4} \right) + R^2 H_1 \sin^2 c + RH_1^2 \sin c \tan(\pi/2 - \theta_1) + \frac{1}{3} H_1^3 \tan^2(\pi/2 - \theta_1) \quad (\text{A.3c})$$

$$k_{34} = -\frac{1}{2} RH_1^2 \sin c - \frac{1}{3} H_1^3 \tan(\pi/2 - \theta_1) \quad (\text{A.3d})$$

$$k_{41} = k_{14} \quad (\text{A.4a})$$

$$k_{42} = k_{24} \quad (\text{A.4b})$$

$$k_{43} = k_{34} \quad (\text{A.4c})$$

$$k_{44} = \frac{1}{3} H_1^3 \quad (\text{A.4d})$$

$$p_1 = R^2 [(\cos a - \cos b) + (a - b) \sin a + 2(\cos b - \cos c) + (b - c)(\sin a + \sin b)] \\ + RH_1 (2 \sin c - \sin a - \sin b) + H_1^2 \tan(\pi/2 - \theta_1) \quad (\text{A.5a})$$

$$p_2 = R^3 \left[(\cos a - \cos b) + (a - b) \sin a - \frac{\cos 2a - \cos 2b}{4} - \sin a (\sin a - \sin b) + 2(\cos b - \cos c) \right. \\ \left. + (b - c)(\sin a + \sin b) - \frac{\cos 2b - \cos 2c}{2} - (\sin a + \sin b)(\sin b - \sin c) \right] \\ + R^2 H_1 (1 - \cos c)(2 \sin c - \sin a - \sin b) \\ + RH_1^2 \left[(1 - \cos c) \tan(\pi/2 - \theta_1) + \frac{1}{2} (2 \sin c - \sin a - \sin b) \right] \\ + \frac{2}{3} H_1^3 \tan(\pi/2 - \theta_1) \quad (\text{A.5b})$$

$$\begin{aligned}
p_3 = R^3 & \left[\frac{1}{2}(b-a) + \frac{\sin 2a - \sin 2b}{4} - \sin a(\cos a - \cos b) + (c-b) \right] \\
& + \frac{\sin 2b - \sin 2c}{2} - (\sin a + \sin b)(\cos b - \cos c) \\
& + R^2 H_1 (2 \sin c - \sin a - \sin b) \sin c \\
& + R H_1^2 \tan(\pi/2 - \theta_1) \left[\sin c + \frac{1}{2}(2 \sin c - \sin a - \sin b) \right] \\
& + \frac{2}{3} H_1^3 \tan^2(\pi/2 - \theta_1)
\end{aligned} \tag{A.5c}$$

$$p_4 = - \left[\frac{1}{2} R H_1^2 (2 \sin c - \sin a - \sin b) + \frac{2}{3} H_1^3 \tan^2(\pi/2 - \theta_1) \right] \tag{A.5d}$$

REFERENCES

- [1] National Disaster Information Center (NDIC), <http://www.safekorea.go.kr> (in Korea).
- [2] Ministry for Food, Agriculture, Forestry and Fisheries (MFAFF) and Rural Development Administration (RDA), "Standard Plan and Specification of Horticulture Facilities against Disaster", 2010, <http://www.rda.go.kr> (in Korea).
- [3] Lee, T.-H., Lee, D.-G. and Ahn, S.-K., "The Repair and Strengthening of Vinyl-house Providing Against Heavy Snow", Proceedings of Architectural Institute of Korea, Seoul, South Korea, 2001, Vol. 21, No. 1, pp. 119-122.
- [4] Lee, S.-G., Lee, J.-W. and Lee, H.-W., "Development of Reinforcement Strategy of One-span Vinyl House for Reduction of Damage by Heavy Snow", Journal of Bio-Environment Control, 2005, Vol. 14, No. 2, pp. 131-137.
- [5] Kim, B.-K., Lee, S.-H. and Shin, K.-J., "Reinforcing Method of Plastic-house Frame for Heavy Snow using Pretension Tie", Proceeding of 7th International Symposium on Architectural Interchanges in Asia (ISAIA 2008), Beijing, China, 2008, pp. 876-879.
- [6] Shin, D.-H., Lim, B.-H., Ju, G.-S. and Chae, S.-H., "Experimental Study on Strengthening Effect of Plastic Greenhouse using Tension-tie", Proceeding of 9th Pacific Structural Steel Conference (PSSC 2010), Beijing, China, 2010, pp. 1573-1580.
- [7] ASCE/SEI 7-10, Minimum Design Loads for Buildings and Other Structures, American Society of Civil Engineering (ASCE), 2010.
- [8] KBC 2009, Korean Building Code and Commentary, Architectural Institute of Korea (AIK), 2009.
- [9] MIDAS IT, MIDAS/GEN 2016 User's Manual, MIDAS Information Technology Co., Ltd.,
- [10] Kim, H.-J., Shin, K.-J., Kim, W.-J. and Huh, P.-S., "A Loading Apparatus for Frame of Arch Type (Patent No.1010434940000)", Korean Intellectual Property Office (KIPO), 2011.
- [11] Kassimali, A., "Structural Analysis. 3rd ed", Nelson, 2005.
- [12] Lee, S.-G., Shin, K.-J. and Lee, S.-H., "Plastic Analysis of Structure". Kimoondang, 2012 (in Korea).

INTERACTION CURVES FOR CONCRETE-FILLED L-SHAPED MULTI-CELLED STEEL TUBE SECTIONS UNDER COMBINED BIAXIAL BENDING AND AXIAL FORCE

G.S. Tong* and X.G. Li

*College of Civil Engineering and Architecture,
Zhejiang University, Hangzhou, Zhejiang Province, China
(Corresponding author: E-mail: tonggs@zju.edu.cn)

Received: 19 April 2018; Revised: 23 July 2018; Accepted: 25 July 2018

ABSTRACT: Ultimate yield surfaces of concrete-filled L-shaped multi-celled steel tube column (L-CFT) under biaxial bending and axial force are studied in this paper. The characteristics of the axial force-bending moment interaction curves under uniaxial bending is first revealed, while the rotational symmetry of the overall interaction curve is verified mathematically. Based on the relative positions of the elastic centroid axis and the plastic neutral axis under pure bending, six cases are identified whose interaction curves show slightly different features. The interaction curves between axial force and bending moments are grouped into two categories. Finally, the interaction surfaces of L-CFT under biaxial bending and axial force are analyzed. The characteristics of these curves are discussed and verified mathematically, and further the approximate formulas for design purpose are provided. Based on the comparative study of a large number of examples, the proposed formulas show good accuracy and are on the conservative side.

Keywords: Concrete-filled steel tube, multi-celled, strength, biaxial bending, interactive relation

DOI: 10.18057/IJASC.2018.14.11

1 INTRODUCTION

L-shaped, T-shaped and cruciform columns can be designed to be invisible at four corners of a room, making better use of living space, and therefore are welcomed by architects who need to meet the captious requirement of apartment buyers in their design work. In the case of reinforced concrete frames, the Ministry of Housing and Urban-Rural Development of China issued a technical specification (JGJ149-2006 [1]) to codify the application of such members and this specification was renewed in 2017. Such types of columns in reinforced concrete under biaxial bending had been experimentally and numerically investigated (Hsu [2-3]). The Structural analysis of frames built of such columns requires a slightly modified stiffness matrix where the product of inertia of the column cross section must be included (Sun [4]). Steel-reinforced concrete (SRC) columns of such special types have also been studied (Zhao [5]). Concrete-filled steel tube columns (CFT) are now the most frequently used members in high-rise buildings. It has high bearing capacity, excellent seismic and good fire-resistant behavior, is easy to construct and therefore relatively cost-effective. In the case of residential buildings, concrete-filled multi-celled L-shaped and T-shaped steel tube columns have been attracting the attention of structural engineers and researchers due to the same demand on living spaces.

As regards to the 3D ($P-M_x-M_y$) cross section strength, Chen and Atsuta [6] developed systematic approaches to find the section strength of steel under axial force and biaxial bending. For CFT members, Hajjar and Gourley [7] provided a perfect description on modeling of stress-strain relations of both steel and concrete and developed polynomial expressions to represent the three-dimensional surface for the section strength of rectangular CFTs, the proposed equations

may be applied in the pushover analysis. The China Association for Engineering Construction Standardization issued in 2004 a specification (CECS159-2004 [8]) on the design of CFT members, in deriving the design equations, the stress distribution in steel and concrete is based on full plasticity assumption. The effect of confinement of steel tube to concrete is assumed to produce only an increase in ductility of the concrete and no increase in strength. The stress in concrete is shown in Figure 1a, the interaction curves are shown in Figure 1b, and can be expressed by

$$\frac{P}{P_p} \leq \alpha_c : \frac{M_x}{M_{px0}} = 1 \quad (1a)$$

$$\frac{P}{P_p} \geq \alpha_c : \frac{P}{P_p} + (1 - \alpha_c) \frac{M_x}{M_{px0}} = 1 \quad (1b)$$

where

P -- axial force;

P_p -- axial plastic capacity of the CFT section, $P_p = A_s f_y + A_c f_{ck}$;

M_x -- bending moment;

M_{px0} -- plastic bending moment of the CFT section in case of no axial force;

f_y -- yield strength of steel;

f_{ck} -- characteristic strength of concrete;

A_s -- area of steel tube;

A_c -- area of concrete;

$$\alpha_c = \frac{A_c f_{ck}}{P_p}$$

Both the theoretical results based on full plasticity assumption and the curves of Eq. 1 are shown in Figure 1b. Eq. 1 is safe and simple, so it was included in the most widely applied software SATWE as a new type of cross section immediately after the issuing of CECS159-2004.

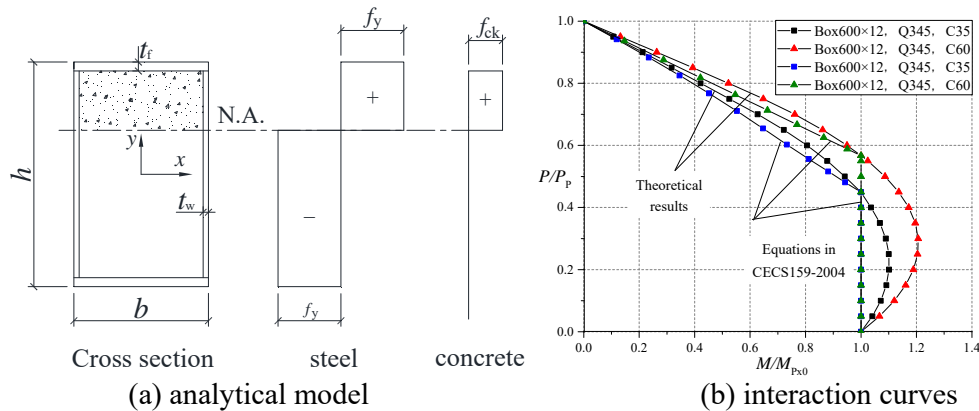


Figure 1. Comparison of Theoretical Results with CECS159-2004

Although a general method for computing the 3D strength surface is available, and the software XTRACT (Chadwell and Imbsen [9]) is free and has found application in the research work, there exists true need by the designers for simple design equations of L-shaped/T-shaped CFT sections. The present paper will address this need.

In recent years, several groups of researchers (Shen *et al.* [10]; Zuo *et al.* [11]; Zhang *et al.* [12]; Wang and Lv [13]) investigated the static and seismic behavior of L-shaped/T-shaped concrete-filled tube columns, including the local stability of the L-shaped/T-shaped tube, and the strengthening effect of penetrating binding bolts. Zuo *et al.* [11] computed the 3D strength of L-shaped CFT with equal legs and one thickness of the tube wall. Lei *et al.* [14] investigated T-shaped tubes with their total width identical to total depth. Both proposed complicated interaction equations for the combined action of axial force and biaxial bending and applicable only for the investigated shape of the cross section.

In this paper, the L-shaped CFT members are slightly different from the above studies in that the cross-section is composed of 3 rectangular and/or square tubes. A multi-celled tube column has the merit that the concrete in each cell is confined by its own tube so that the improvement in ductility may be estimated by currently available researches on square or rectangular CFTs. Also, the limit on the width-to-thickness ratio of the steel plate elements, specified for CFT members in CECS 159-2004, is directly applicable.

The maximum yield strength of concrete-filled L-shaped multi-celled tube column (abbreviated L-CFT hereafter) under axial force and uniaxial or biaxial bending is studied in this paper. L-shaped and T-shaped CFT cross sections comprise of 3(L) and 4(T) rectangular/square tubes, so it is assumed that the effect of confinement of steel tube to concrete is assumed to produce only an increase in ductility of the concrete and no increase in strength (Hajjar and Gourley [7]), so uniform stress blocks are assumed both for the steel and the concrete as in the equations of CECS159-2004.

2 ULTIMATE STRENGTH UNDER UNIAXIAL ECCENTRIC LOAD

2.1 Elastic Properties of L-shaped Section

The sections of concrete-filled L-shaped multi-celled steel tube column investigated in this paper are shown in Figure 2, the section is composed of a flange box and a web box, the size of the flange box is $h_1 \times b_1$, the size of the web box is $h_2 \times b_2$, and they are actually composed of two different kinds of steel plates with thickness of t_1 and t_2 . Each plate of the section is assigned a name as shown in Figure 2. The total width of L-shaped section is $b = h_1 + b_2$, the total height is $h = b_1 + h_2$, the steel tube is filled with concrete.

The origin of the coordinate system is first located at the left-bottom corner of the section shown in Figure 2. Both steel and concrete are elastic, the elastic modulus of them are E_s and E_c respectively. The elastic centroid of the section is located at Point C(x_{sc}, y_{sc}). The following assumptions are adopted: 1) The L-shaped CFT section obeys the Bernoulli's assumption; 2) In the full plastic hinge state, the steel reaches the compressive yield strength f_y , the compression concrete reaches its standard value of compressive yield strength f_{ck} , the tensile strength of concrete is ignored.

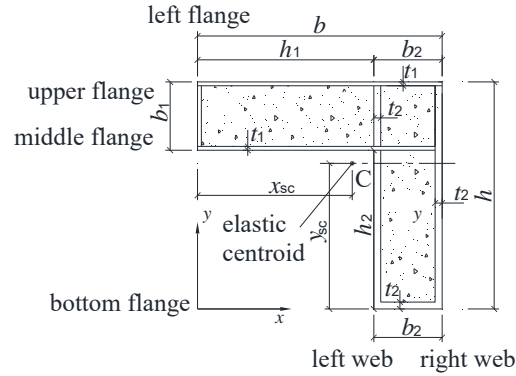


Figure 2. L-shaped Steel Tube Column Section

According to the parameters illustrated in Figure 2, the area of steel and concrete respectively in flange box and web box can be given by (c-concrete, s-steel, f-flange, w-web)

$$A_{cf} = (b_1 - 2t_1)(b - t_1 - 2t_2) \quad (2a)$$

$$A_{sf} = 2bt_1 + (b_1 - 2t_1)(t_1 + 2t_2) \quad (2b)$$

$$A_{cw} = (h_2 - t_2)(b_2 - 2t_2) \quad (2c)$$

$$A_{sw} = 2h_2t_2 + (b_2 - 2t_2)t_2 \quad (2d)$$

Denoting $\alpha_E = E_s / E_c$, the transformed area of the section is

$$A_{tot} = A_{sf} + A_{sw} + \frac{A_{cf} + A_{cw}}{\alpha_E} \quad (3)$$

The coordinate of the elastic centroid (x_{sc}, y_{sc}) is

$$x_{sc} = \frac{1}{A_{tot}} \left\{ \left[2ht_2 + (b_2 - 2t_2)(t_2 + 2t_1) + \frac{A_{cw} + (b_1 - 2t_1)(b_2 - 2t_2)}{\alpha_E} \right] \left(b - \frac{1}{2}b_2 \right) + (h_1^2 - t_1^2) \left[t_1 + \frac{b_1 - 2t_1}{2\alpha_E} \right] + \frac{1}{2}b_1t_1^2 \right\} \quad (4a)$$

$$y_{sc} = \frac{1}{A_{tot}} \left\{ \left(A_{sf} + \frac{A_{cf}}{\alpha_E} \right) \left(h - \frac{1}{2}b_1 \right) + (h_2 + t_2) \left[(h_2 - t_2)t_2 + \frac{A_{cw}}{2\alpha_E} \right] + \frac{1}{2}b_2t_2^2 \right\} \quad (4b)$$

After the elastic centroid has been found, the origin of the coordinate system will be moved to the centroid. All properties and bending moments will be calculated about the centroid coordinate system.

The moment of inertia about the x - and y -axis are

$$I_x = I_{x,\text{bot}} - A_{\text{tot}} y_{\text{sc}}^2 \quad (5a)$$

$$I_{x,\text{bot}} = \left(\frac{A_{\text{cf}}}{\alpha_E} + A_{\text{sf}} \right) \left(h - \frac{1}{2} b_1 \right)^2 + \frac{1}{12} b_1 (t_1^3 + 2t_2^3) + (b - t_1 - 2t_2) \left[t_1 (b_1 - t_1)^2 + \frac{(b_1 - 2t_1)^3}{12\alpha_E} \right] \\ + \frac{1}{3} \left(2t_2 + \frac{b_2 - 2t_2}{\alpha_E} \right) h_2^3 + \frac{1}{3} \left(1 - \frac{1}{\alpha_E} \right) (b_2 - 2t_2) t_2^3 \quad (5b)$$

$$I_y = I_{y,\text{bot}} - A_{\text{tot}} x_{\text{sc}}^2 \quad (5c)$$

$$I_{y,\text{bot}} = \left[\frac{(b_2 - 2t_2)(h - 2t_1 - t_2)}{\alpha_E} + 2ht_2 + (2t_1 + t_2)(b_2 - 2t_2) \right] \left(b - \frac{1}{2} b_2 \right)^2 + \frac{1}{3} \left(1 - \frac{1}{\alpha_E} \right) (b_1 - 2t_1) t_1^3 \\ + \frac{1}{12} b_2 (2t_1^3 + t_2^3) + (h - 2t_1 - t_2) \left[t_2 (b_2 - t_2)^2 + \frac{(b_2 - 2t_2)^3}{12\alpha_E} \right] + \frac{1}{3} \left(2t_1 + \frac{b_1 - 2t_1}{\alpha_E} \right) h_1^3 \quad (5d)$$

$$I_{xy} = I_{xy,\text{bot}} - A_{\text{tot}} x_{\text{sc}} y_{\text{sc}} \quad (5e)$$

$$I_{xy,\text{bot}} = \frac{1}{2} b^2 t_1 (h + h_2) + (b_1 - 2t_1) \left(h - \frac{1}{2} b_1 \right) \left(\frac{1}{2} t_1^2 + h_1 t_2 + b t_2 \right) + \frac{1}{2} t_2 h_2^2 (b + h_1) \\ + \frac{1}{2} t_2^2 (b_2 - 2t_2) \left(b - \frac{1}{2} b_2 \right) + \frac{1}{\alpha_E} \left\{ \left(h - \frac{1}{2} b_1 \right) (b_1 - 2t_1) \left[\frac{1}{2} (h_1^2 - t_1^2) + (b_2 - 2t_2) \left(b - \frac{1}{2} b_2 \right) \right] \right. \\ \left. + \frac{1}{2} (h_2 - t_2) (b_2 - 2t_2) \left(b - \frac{1}{2} b_2 \right) (h_2 + t_2) \right\} \quad (5f)$$

where $I_{x,\text{bot}}$ is the moment of inertia around $y=0$, $I_{y,\text{bot}}$ is the moment of inertia around $x=0$, $I_{xy,\text{bot}}$ is the moment of inertia around the origin of the coordinate system.

When both steel and concrete of the section yield, the center of the axial compressive strength is located at $(x_{\text{cc}}, y_{\text{cc}})$ (measured from the left-bottom corner):

$$x_{\text{cc}} = \frac{1}{P_p} \left\{ \left[2ht_2 f_y + (b_2 - 2t_2)(2t_1 + t_2) f_y + (b_2 - 2t_2)(h - 2t_1 - t_2) f_{\text{ck}} \right] \left(b - \frac{1}{2} b_2 \right) \right. \\ \left. + t_1 h_1^2 f_y + \frac{1}{2} (b_1 - 2t_1) (h_1^2 - t_1^2) f_{\text{ck}} + \frac{1}{2} (b_1 - 2t_1) t_1^2 f_y \right\} \quad (6a)$$

$$y_{\text{cc}} = \frac{1}{P_p} \left\{ \left(A_{\text{sf}} f_y + A_{\text{cf}} f_{\text{ck}} \right) \left(h - \frac{b_1}{2} \right) + t_2 h_2^2 f_y + \frac{1}{2} (b_2 - 2t_2) (h_2^2 - t_2^2) f_{\text{ck}} + \frac{1}{2} (b_2 - 2t_2) t_2^2 f_y \right\} \quad (6b)$$

The center of the axial tensile strength is located at (x_{tc}, y_{tc}) (measured from the left-bottom corner):

$$x_{tc} = \frac{1}{A_{sf} + A_{sw}} \left\{ [2ht_2 + (b_2 - 2t_2)(2t_1 + t_2)] \left(b - \frac{1}{2}b_2\right) + t_1h_1^2 + \frac{1}{2}(b_1 - 2t_1)t_1^2 \right\} \quad (7a)$$

$$y_{tc} = \frac{1}{A_{sf} + A_{sw}} \left[A_{sf} \left(h - \frac{1}{2}b_1 \right) + t_2h_2^2 + \frac{1}{2}(b_2 - 2t_2)t_2^2 \right] \quad (7b)$$

Introduce the following notations for axial forces and bending moments

$$P_s = (A_{sf} + A_{sw})f_y \quad (8a)$$

$$P_c = (A_{cf} + A_{cw})f_{ck} \quad (8b)$$

$$P_p = P_s + P_c \quad (8c)$$

$$\alpha_{ck} = P_c / P_p \quad (9)$$

$$M_{x,rc} = P_p(y_{cc} - y_{sc}) \quad (10a)$$

$$M_{x,rt} = P_s(y_{sc} - y_{tc}) \quad (10b)$$

$$M_{y,rc} = P_p(x_{cc} - x_{sc}) \quad (10c)$$

$$M_{y,rt} = P_s(x_{sc} - x_{tc}) \quad (10d)$$

where

P_s -- axial plastic capacity of the steel part of the L-CFT section;

P_c -- compressive capacity of the concrete part of the L-CFT section;

$M_{x,rc}$ -- the bending moment around the centroid axis x when the full L-CFT section yields in compression;

$M_{x,rt}$ -- the bending moment around the centroid axis x when the full L-CFT section yields in tension;

$M_{y,rc}$ -- the bending moment around the centroid axis y when the full L-CFT section yields in compression;

$M_{y,rt}$ -- the bending moment around the centroid axis y when the full L-CFT section yields in tension;

f_y -- yield strength of steel, $f_y = 235\text{N/mm}^2$ and $f_y = 345\text{N/mm}^2$ respectively in this paper;

f_{ck} -- standard value of compressive yield strength of concrete, C30-C60 (cubic strength) are adopted in this paper.

2.2 $P - M_x - M_{y,x}$ Curve of L-CFT Sections for the Plastic Neutral Axis Parallelled to x -axis

Uniaxial bending means that the plastic neutral axis is parallel to the centroid axis. Uniaxial bending around the x axis of the section will be studied first.

2.2.1 Characteristics of $P - M_x$ interaction curves

When a plastic hinge forms under the action of axial force and bending moment, the plastic neutral axis may be located in the upper flange, in the flange concrete, in the middle flange, in the web concrete or in the bottom flange. The axial force and the bending moment of the L-CFT section for these 5 cases can be written down respectively, they are not presented in this paper for brevity.

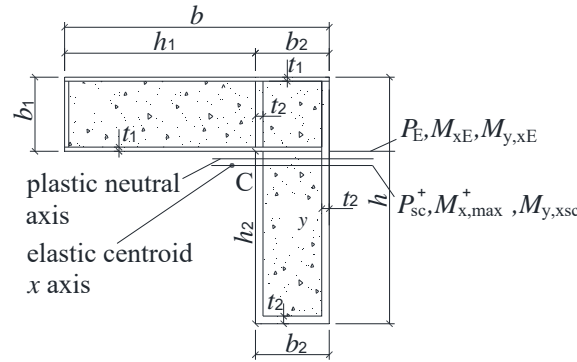


Figure 3. Interactive Relation of L-shaped Section when Plastic Neutral Axis is Parallel to the x axis

Let $M_{y,x}$ be the bending moment around the y axis when the plastic neutral axis is parallel to the x axis. Assume P (the axial force) is positive when it is compression, M_x is positive when it produces compressive stress in the upper flange, $M_{y,x}$ is positive when it produces compressive stress in the right web. As the plastic neutral axis is located in different locations, the axial forces and bending moments are given different notations, they are defined in Figure 3 and Table 1.

Table 1. Notations of Forces when Plastic Neutral Axis is Parallel to the x Axis

Forces	Position of plastic neutral axis
$P_t, M_{x,rt}, M_{y,rt}$	Full tension
$P_E, M_{xE}, M_{y,xE}$	Bottom surface of the middle flange
$P_p, M_{x,rc}, M_{y,rc}$	Full compression
$P_{sc}^+, M_{x,max}^+, M_{y,xsc}$	Elastic centroid x axis

After graphical presentations of the $P - M_x$ and $P - M_{y,x}$ curves for many different combinations of dimensional parameters and material strengths, a typical $P - M_x$ curve is identified and shown in Figure 4.

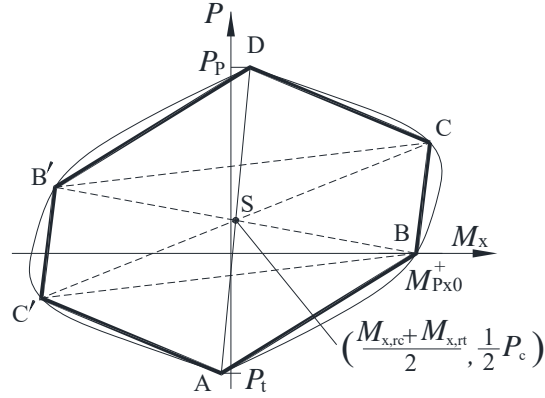


Figure 4. Geometric Symmetry Point of the $P-M_x$ Curves

There are 4 points on the curve:

Point A ($M_{x,rt}, -P_s$): full tension

Point B ($M_{Px0}^+, 0$): pure bending when the flange box in compression

Point C (M_C, P_C): $P_C = \max(P_E, P_{sc}^+, P_c)$, M_C is the corresponding bending moment

Point D ($M_{x,rc}, P_p$): full compression

We note that Point D is rotationally symmetric with Point A about Point S $\left(\frac{1}{2}(M_{x,rt} + M_{x,rc}), \frac{1}{2}P_c \right)$.

M_{Px0}^+ is the plastic bending moment when the section is under pure bending around the x axis.

P_{sc}^+ is the axial force when the plastic neutral axis coincides with the elastic centroid axis x . It can be verified that at this location the plastic bending moment is maximum for any variation of the cross sections and any strength combinations of steel and concrete, and will be denoted by $M_{x,max}^+$.

The maximum negative moment is $(M_{x,max}^-, P_{sc}^-)$ when the flange box is in tension and the plastic neutral axis coincides with the elastic centroid axis.

The centroid axis x divides the steel into two parts, A_{s+} and A_{s-} , and it divides the concrete into two parts, A_{c+} and A_{c-} . Referring to Figure 5, when the plastic neutral axis coincides with the elastic centroid axis, we have the follow relations.

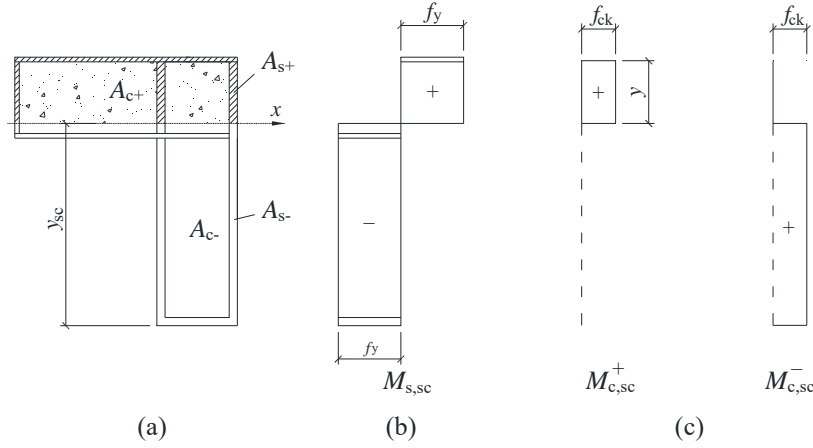


Figure 5. Plastic Moments when Plastic Neutral Axis Coincides with the Centroid Axis

The axial force and the bending moment when the flange box is in compression:

$$P_{sc}^+ = (A_{s+} - A_{s-})f_y + A_{c+}f_{ck} \quad (11a)$$

$$M_{x,max}^+ = f_y \left(\int_{A_{s+}} y dA - \int_{A_{s-}} y dA \right) + f_{ck} \int_{A_{c+}} y dA = M_{s,sc} + M_{c,sc}^+ \quad (11b)$$

The axial force and the bending moment when the flange box is in tension:

$$P_{sc}^- = -(A_{s+} - A_{s-})f_y + A_{c-}f_{ck} \quad (11c)$$

$$M_{x,max}^- = -f_y \left(\int_{A_{s+}} y dA - \int_{A_{s-}} y dA \right) + f_{ck} \int_{A_{c-}} y dA = -M_{s,sc} + M_{c,sc}^- \quad (11d)$$

where $M_{s,sc}$ is the plastic moment of steel (Figure 5b);

$M_{c,sc}^+$ is the plastic moment of concrete above the centroid axis (Figure 5c);

$M_{c,sc}^-$ is the plastic moment of concrete below the centroid axis (Figure 5c);

These moments are provided by stresses in steel and concrete shown in Figure 5.

$$M_{s,sc} = f_y \left(\int_{A_{s+}} y dA - \int_{A_{s-}} y dA \right) = M_{s,sc}^+ + M_{s,sc}^- \quad (12a)$$

$$M_{c,sc}^+ = f_{ck} \int_{A_{c+}} y dA \quad (12b)$$

$$M_{s,sc}^+ = f_y \int_{A_{s+}} y dA \quad (12c)$$

$$M_{s,sc}^- = -f_y \int_{A_{s-}} y dA \quad (12d)$$

$$P_{sc}^+ = (A_{s+} - A_{s-})f_y + A_{c+}f_{ck} \quad (12e)$$

Because $P_{sc}^+ + P_{sc}^- = A_c f_{ck} = P_c$, so one has

$$P_{sc}^+ - 0.5P_c = 0.5P_c - P_{sc}^- \quad (13a)$$

Summation of two maximum bending moments

$$M_{x,max}^+ + M_{x,max}^- = f_{ck} \int_{A_{c+}} ydA + f_{ck} \int_{A_{c-}} ydA = M_{c,sc}^+ + M_{c,sc}^- = S_{x,c} f_{ck} \quad (13b)$$

where $S_{x,c} = \int_{A_c} ydA$.

When the cross section is in full tension and in compression, the bending moments are

$$M_{x,rt} = -f_y \int_{A_{s+}} ydA - f_y \int_{A_{s-}} ydA = -M_{s,sc}^+ + M_{s,sc}^- = -S_{x,s} f_y \quad (14a)$$

$$M_{x,rc} = S_{x,s} f_y + S_{x,c} f_{ck} = -M_{x,rt} + M_{c,sc}^+ + M_{c,sc}^- \quad (14b)$$

where $S_{x,s} = \int_{A_s} ydA$

Thus

$$M_{x,rt} + M_{x,rc} = M_{c,sc}^+ + M_{c,sc}^- = M_{x,max}^+ + M_{x,max}^- \quad (14c)$$

So Point $(M_{x,max}^-, P_{sc}^-)$ is rotationally symmetric with the maximum positive moment $(M_{x,max}^+, P_{sc}^+)$ about Point $S\left(\frac{1}{2}(M_{x,rt} + M_{x,rc}), \frac{1}{2}P_c\right)$.

For any location of the plastic neutral axis (Figure 6), $A'_{s+}, A'_{s-}, A'_{c+}, A'_{c-}$ are the steel and concrete areas above and below the neutral axis. The axial force and bending moment when the upper flange is in compression are

$$P^+ = (A'_{s+} - A'_{s-})f_y + A'_{c+}f_{ck} \quad (15a)$$

$$M_x^+ = f_y \left(\int_{A'_{s+}} ydA - \int_{A'_{s-}} ydA \right) + f_{ck} \int_{A'_{c+}} ydA \quad (15b)$$

the axial force and the bending moment when the web concrete is in compression are

$$P^- = -(A'_{s+} - A'_{s-})f_y + A'_{c-}f_{ck} \quad (15c)$$

$$M_x^- = -f_y \left(\int_{A'_{s+}} ydA - \int_{A'_{s-}} ydA \right) + f_{ck} \int_{A'_{c-}} ydA \quad (15d)$$

and

$$P^+ + P^- = P_c$$

$$M_x^+ + M_x^- = f_{ck} \int_{A'_{c+}} y dA + f_{ck} \int_{A'_{c-}} y dA = S_{x,c} f_{ck}$$

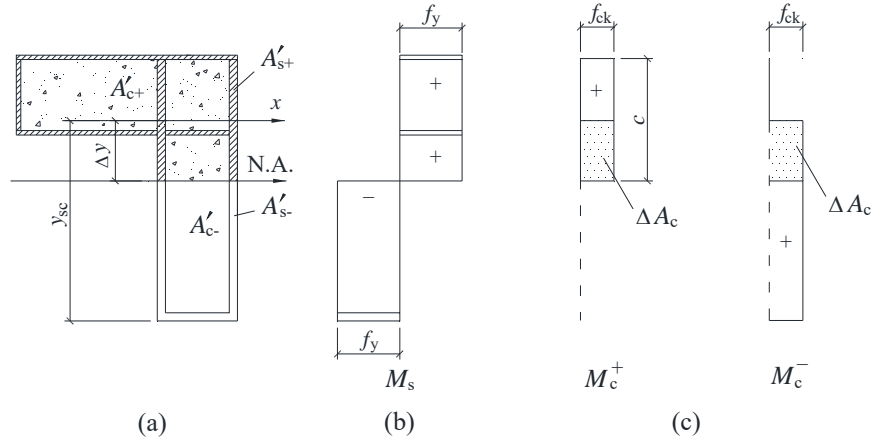


Figure 6. Plastic Moments for Different Location of the Plastic Neutral Axis

so we have

$$P^+ - 0.5P_c = 0.5P_c - P^- \quad (16a)$$

$$M_c^+ + M_c^- = M_{c,sc}^+ + M_{c,sc}^- = M_{x,rt} + M_{x,rc} = M_{x,max}^+ + M_{x,max}^- \quad (16b)$$

So we have verified that the left of the $P - M_x$ curves in Figure 4 is rotationally symmetric with the right of the $P - M_x$ curves about Point S $\left(\frac{1}{2}(M_{x,rt} + M_{x,rc}), \frac{1}{2}P_c \right)$.

The pure bending plastic moment is M_{px0}^- when the flange concrete is in tension. The rotationally symmetric Point of $(M_{px0}^-, 0)$ on the right of Figure 4 is (M_c, P_c) , and

$$M_c = -M_{px0}^- + (M_{x,rt} + M_{x,rc}) \quad (17)$$

Extensive examples show that $M_{c,sc}^+ + M_{c,sc}^-$ are small quantities, and

$$\frac{M_{x,max}^+}{M_{x,max}^-} = 1 \pm 0.02 \quad (18)$$

2.2.2 Determination of Point C and Point E

Except Point A $(M_{x,rt}, -P_s)$, Point B $(M_{px0}^+, 0)$ and Point D $(M_{x,rc}, P_p)$, the following 3 points will be

used to define Point C on the $P-M_x$ curves:

$$(M_{xE}, P_E), (M_{x,\max}^+, P_{sc}^+) \text{ and } (M_c, P_c)$$

Many $P-M_x$ interaction curves are obtained, several typical curves are shown in Figure 7, they are plotted with m_x as the abscissa against p as the ordinate, where

$$m_x = \frac{M_x}{M_{Px0}^+} \quad (19a)$$

$$p = \frac{P}{P_p} \quad (19b)$$

Six cases are identified and are listed in Table 2 according to the relative positions of the elastic centroid axis x and the plastic neutral axis under pure bending around the x axis. The relative values of axial forces for these 6 cases are also given in Table 2.

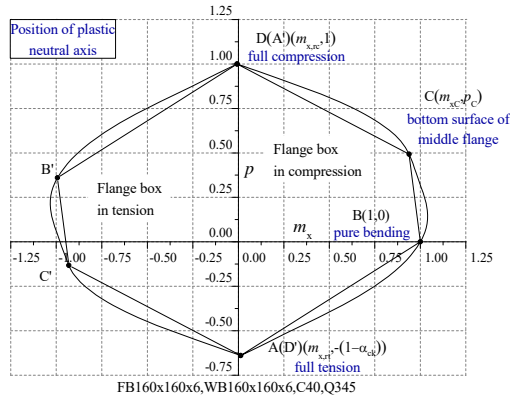
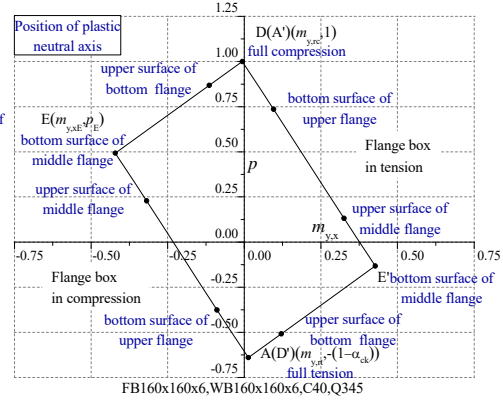
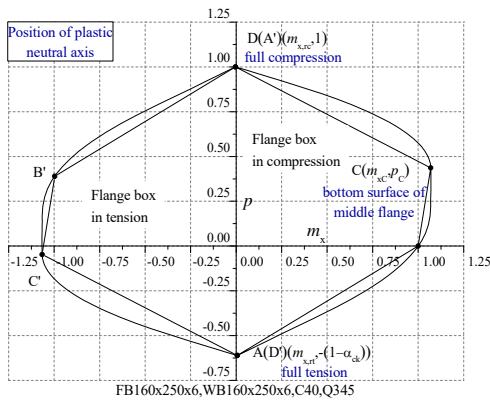
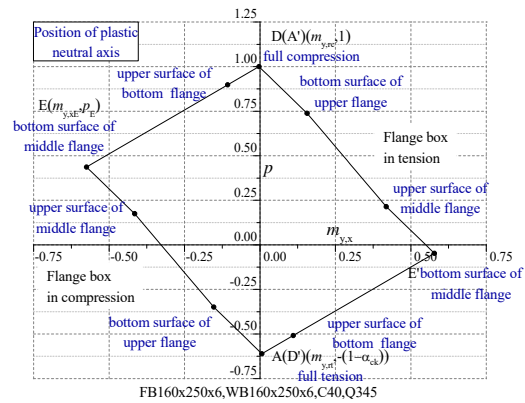
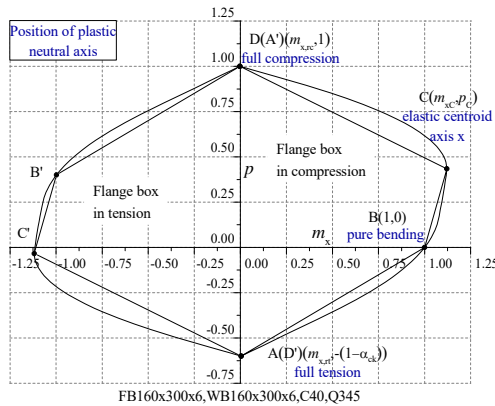
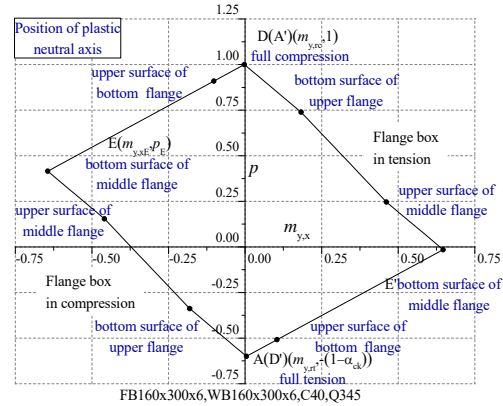
Table 2. Classification of Section Type

Case No	Position of plastic neutral axis under pure bending	Position of elastic centroid axis x	Maximum of P_E, P_c, P_{sc}^+ (Point C)	Figure
Case1a	Flange concrete	Flange concrete	P_E	Figure 7a
Case1b		Middle flange	P_E	Figure 7b
Case1c		Web concrete	P_{sc}^+	Figure 7c
Case2a	Middle flange	Middle flange	P_E	Figure 7d
Case2b		Web concrete	P_c	Figure 7e
Case3	Web concrete	Web concrete	P_c	Figure 7f

In Figure 7, the axial force at Point C is

$$P_C = \max(P_E, P_{sc}^+, P_c) \quad (20a)$$

M_{xC} are the bending moments corresponding to P_C (i.e. if $P_C = \max(P_E, P_{sc}^+, P_c) = P_E$, then $M_{xC} = M_{xE}$; if $P_C = \max(P_E, P_{sc}^+, P_c) = P_c$, then $M_{xC} = M_c = -M_{Px0}^-$). The axial forces at Point C of these 6 cases are listed in Table 2.

(a1) $p - m_x$ curve of Case1a(a2) $p - m_{y,x}$ curve of Case1a(b1) $p - m_x$ curve of Case1b(b2) $p - m_{y,x}$ curve of Case1b(c1) $p - m_x$ curve of Case1c(c2) $p - m_{y,x}$ curve of Case1c

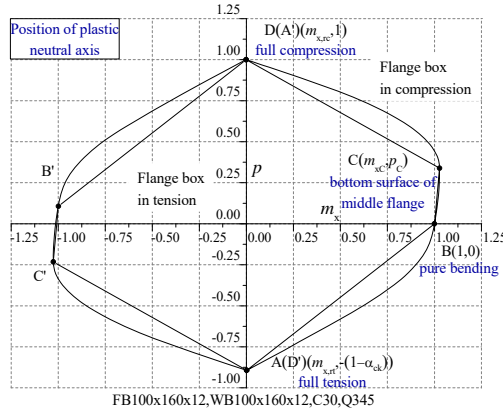
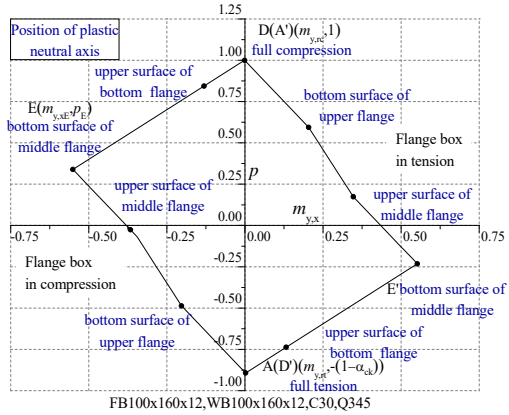
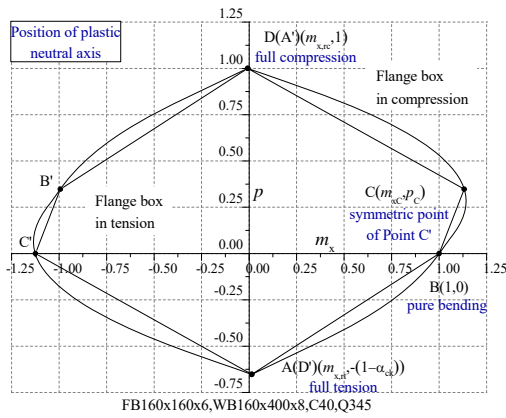
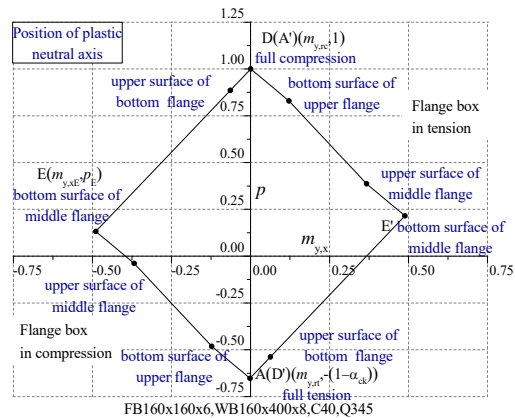
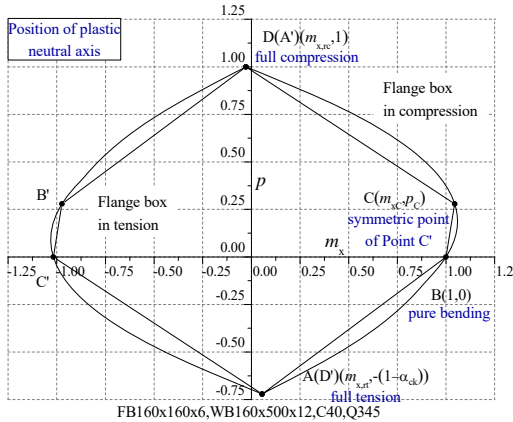
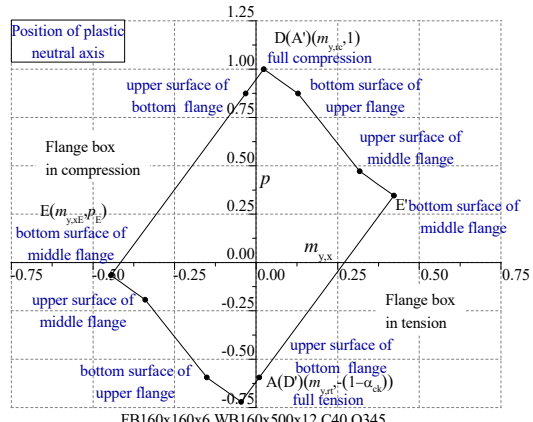
(d1) $p - m_x$ curve of Case2a(d2) $p - m_{y,x}$ curve of Case2a(e1) $p - m_x$ curve of Case2b(e2) $p - m_{y,x}$ curve of Case2b(f1) $p - m_x$ curve of Case3(f2) $p - m_{y,x}$ curve of Case3

Figure 7. Interaction Curves of L-shaped Section when Plastic Neutral Axis is Parallel to the x -axis
(Notation: FB $h_1 \times b_1 \times t_1$, WB $h_2 \times b_2 \times t_2$, FB=flange box, WB=web box)

According to the characteristics mentioned above, for these six cases, we can use piecewise linear model ABCD to express the $p - m_x$ curve when the section is under uniaxial compression and bending around x -axis as

$$\text{Line A-B: } -\frac{1-m_{x,rt}}{1-\alpha_{ck}}p + m_x = 1 \quad (21a)$$

$$\text{Line B-C: } \frac{1-m_{xC}}{p_C}p + m_x = 1 \quad (21b)$$

$$\text{Line C-D: } p + \frac{1-p_C}{m_{xC}-m_{x,rc}}(m_x - m_{x,rc}) = 1 \quad (21c)$$

where

$$m_{x,rt} = \frac{M_{x,rt}}{M_{Px0}^+}, \quad m_{x,rc} = \frac{M_{x,rc}}{M_{Px0}^+}, \quad p_C = \frac{P_C}{P_P}, \quad m_{xC} = \frac{M_{xC}}{M_{Px0}^+} \quad (22)$$

The interaction curves of the axial force P and the accompanying bending moment $M_{y,x}$ are also shown in Figure 7, they are plotted with $m_{y,x}$ as the abscissa against p as the ordinate, where

$$m_{y,x} = \frac{M_{y,x}}{M_{Py0}^+} \quad (23)$$

where M_{Py0}^+ is the plastic bending moment when the section is under pure bending around the y-axis and the web box is in compression, it is calculated by a similar method as M_{Px0}^+ .

There are three key points for each curve shown in Figure 7(a2, b2, c2, d2, e2, f2), the bending moment $M_{y,x}$ and the axial force P at each point can be represented by

$$A(M_{y,rt}, -P_s), E(M_{y,xE}, P_E), D(M_{y,rc}, P_P)$$

where Point E is related to the plastic neutral axis at the bottom surface of the middle flange (see in Table 1).

After that, we can use piecewise linear model AED to express the $p - m_{y,x}$ curves in Figure 7 as

$$\text{Line A-E: } \alpha_{ck} - p - \frac{\alpha_{ck} - 1 - p_E}{m_{y,xE} - m_{y,rt}}(m_{y,x} - m_{y,rt}) = 1 \quad (24a)$$

$$\text{Line E-D: } p + \frac{1 - p_E}{m_{y,xE} - m_{y,rc}}(m_{y,x} - m_{y,rc}) = 1 \quad (24b)$$

In Figure 7(a2, b2, c2, d2, e2, f2), the bending moment $M_{y,x}$ and the axial force P at Points A'-D' are also rotationally symmetrical with Points A-D about the point $\left(\frac{1}{2}(M_{y,rt} + M_{y,rc}), \frac{1}{2}P_c\right)$.

After the right of the $P-M_x$ and $P-M_{y,x}$ curves have been formulated, the left of these curves can be found using the rotational symmetry. Similarly, the $P-M_y-M_{x,y}$ curve can be found when the plastic neutral axis is parallel to the y-axis.

2.2.3 Simplified equations for practical application

Designers truly need simple design equations for L-shaped and T-shaped CFTs, so we simplify Eq. 21 and Eq. 24 for practical application.

Based on the results of a large number of examples, when the section is in full tension, we take the coordinate of Point A as $(0, -P_s)$ approximately. When the section is in full compression, we take the coordinate of Point D as $(0, P_p)$.

So Eq. 21 can be simplified as

$$\text{Line A-B: } -\frac{P}{P_s} + \frac{M_x}{M_{px0}^+} = 1 \quad (25a)$$

$$\text{Line B-C: } \left(1 - \frac{M_{xc}}{M_{px0}^+}\right) \frac{P}{P_c} + \frac{M_x}{M_{px0}^+} = 1 \quad (25b)$$

$$\text{Line C-D: } \frac{P}{P_p} + \left(1 - \frac{P_c}{P_p}\right) \frac{M_x}{M_{xc}} = 1 \quad (25c)$$

Eq. 24 can be simplified as

$$\text{Line A-E: } -\frac{P}{P_s} + \left(1 + \frac{P_E}{P_s}\right) \frac{M_{y,x}}{M_{y,xE}} = 1 \quad (26a)$$

$$\text{Line E-D: } \frac{P}{P_p} + \left(1 - \frac{P_E}{P_p}\right) \frac{M_{y,x}}{M_{y,xE}} = 1 \quad (26b)$$

Obviously, Eq. 25 and Eq. 26 are simple enough and can be used by designers conveniently.

3. $P-M_x-M_y$ RELATIONS OF L-CFT SECTIONS

An ultimate yield surface of the L-CFT section under biaxial bending and axial force is shown in Figure 8, the curves are plotted with m_x as the abscissa and m_y as the ordinate for a given axial force ratio p .

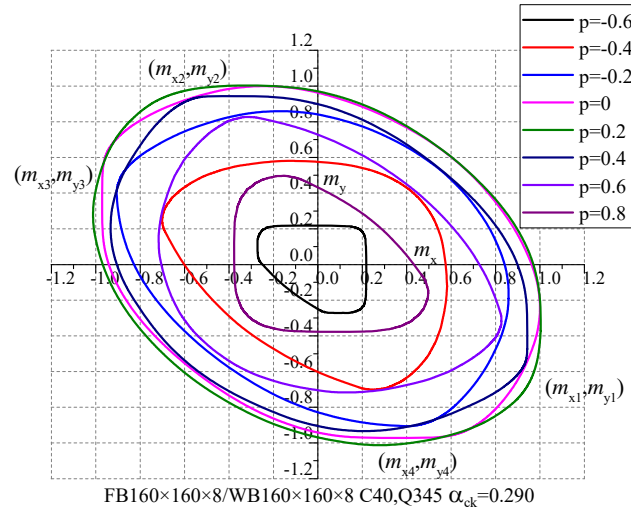


Figure 8. $m_x - m_y$ Curves of L-shaped Section under Biaxial Bending and Axial Force

There are 4 key points on each $m_x - m_y$ curve for a prescribed value of p , the coordinates of these 4 key points are given as (m_{xi}, m_{yi}) , $i = 1, 2, 3, 4$:

Point (m_{x1}, m_{y1}) is the right-most point of each curve,

Point (m_{x2}, m_{y2}) is the highest point of each curve,

Point (m_{x3}, m_{y3}) is the left-most point of each curve,

Point (m_{x4}, m_{y4}) is the negative highest point of each curve.

It has been found that they are points when the plastic neutral axis is parallel to the x axis or the y axis, so they can be calculated by equations presented in Section 2.

Figure 9(a) shows a plastic neutral axis passing through a rectangular section, the upper part is in compression. If it is a concrete section, the axial force and bending moment are

$$P = 2b(d - e)f_{ck} \quad (27a)$$

$$M_x = bf_{ck} \left[d^2 - (e + b \tan \theta)^2 \right] + 2b^2 f_{ck} \left(e \tan \theta - \frac{2}{3} b \tan^2 \theta \right) \quad (27b)$$

$$M_y = \frac{2}{3} b^3 f_{ck} \tan \theta \quad (27c)$$

when the parameter e is unchanged, and the neutral axis crosses two vertical boundaries, then the axial force is constant.

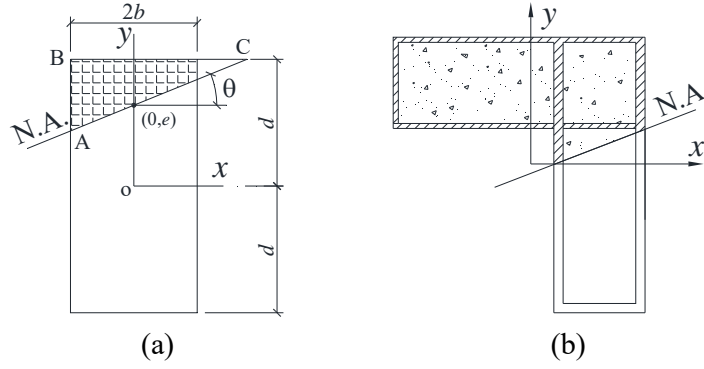


Figure 9. The Influence of Plastic Neutral Axis on the Axial Force and Bending Moment

Differentiate M_x with respect to θ , and let the derivative be zero:

$$\frac{dM_x}{d\theta} = \left[-2b^2(e + b \tan \theta) f_{ck} + 2b^2 f_{ck} \left(e - \frac{4}{3} b \tan \theta \right) \right] \frac{1}{\cos^2 \theta} = 0$$

from which, we obtain $\theta = 0$.

The second derivative is

$$\frac{d^2 M_x}{d\theta^2} = \left(-2b^3 f_{ck} - \frac{8}{3} b^3 f_{ck} \right) \frac{1}{\cos^2 \theta} + \left[-2b^2(e + b \tan \theta) f_{ck} + 2b^2 \left(e - \frac{4}{3} b \tan \theta \right) f_{ck} \right] \frac{2 \sin \theta}{\cos^3 \theta}$$

and its value at $\theta = 0$ is

$$\left. \frac{d^2 M_x}{d\theta^2} \right|_{\theta=0} = -2b^3 f_{ck} - \frac{8}{3} b^3 f_{ck} < 0$$

That is, when the plastic neutral axis is parallel to the x axis, M_x is a maximum. If the rectangle is in steel, this conclusion is also valid, and M_x is either a maximum or a minimum (negative maximum).

Figure 9(b) shows the L-shaped CFT section with a sloped neutral axis and the coordinate system. From the above derivation it can be deduced that for the L-shaped CFT section, when the plastic neutral axis is parallel to the x or y axis, the bending moment is either a maximum or a minimum under a prescribed axial force, because the L-CFT section can be seen a combination of several rectangular steel and concrete subsections.

Points (m_{xi}, m_{yi}) divide the $m_x - m_y$ curves into four segments, they can be fitted by

On the upper right side $m_{x2} \leq m_x \leq m_{x1}, m_{y1} \leq m_y \leq m_{y2}$:

$$\left(\frac{m_x - m_{x2}}{m_{x1} - m_{x2}} \right)^{2-p} + \left(\frac{m_y - m_{y1}}{m_{y2} - m_{y1}} \right)^{2-p} = 1 \quad (28a)$$

On the upper left side $m_{x3} \leq m_x \leq m_{x2}, m_{y3} \leq m_y \leq m_{y2}$:

$$\left(\frac{m_{x2} - m_x}{m_{x2} - m_{x3}} \right)^{1.6 + \frac{1}{2}p} + \left(\frac{m_y - m_{y3}}{m_{y2} - m_{y3}} \right)^{1.6 + \frac{1}{2}p} = 1 \quad (28b)$$

On the lower right side $m_{x4} \leq m_x \leq m_{x1}, m_{y4} \leq m_y \leq m_{y1}$:

$$\left(\frac{m_x - m_{x4}}{m_{x1} - m_{x4}} \right)^{2-p} + \left(\frac{m_{y1} - m_y}{m_{y1} - m_{y4}} \right)^{2-p} = 1 \quad (28c)$$

On the lower left side $m_{x3} \leq m_x \leq m_{x4}, m_{y4} \leq m_y \leq m_{y3}$:

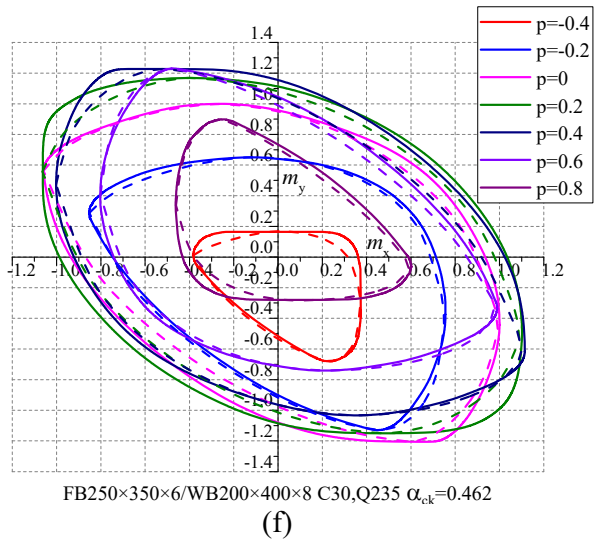
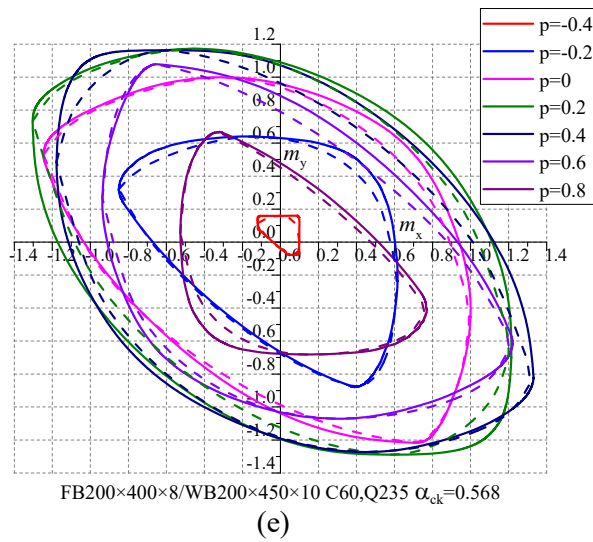
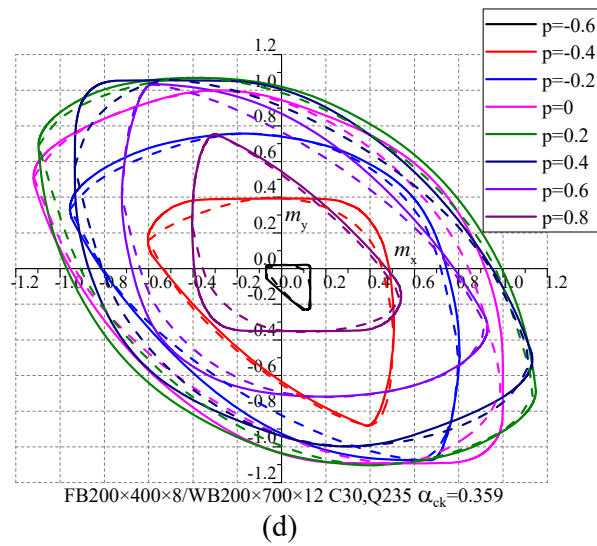
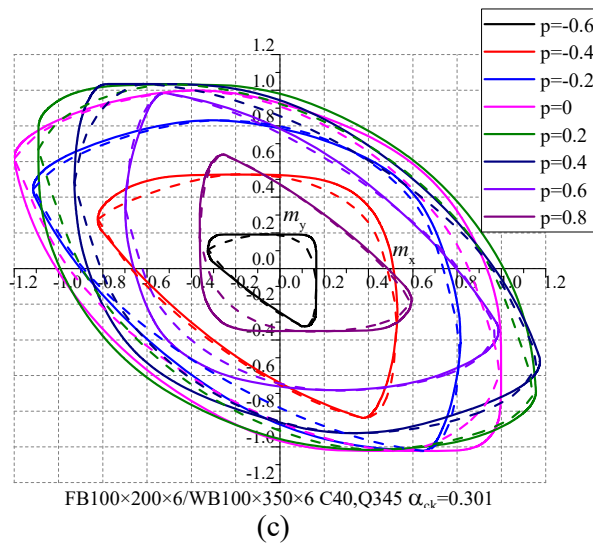
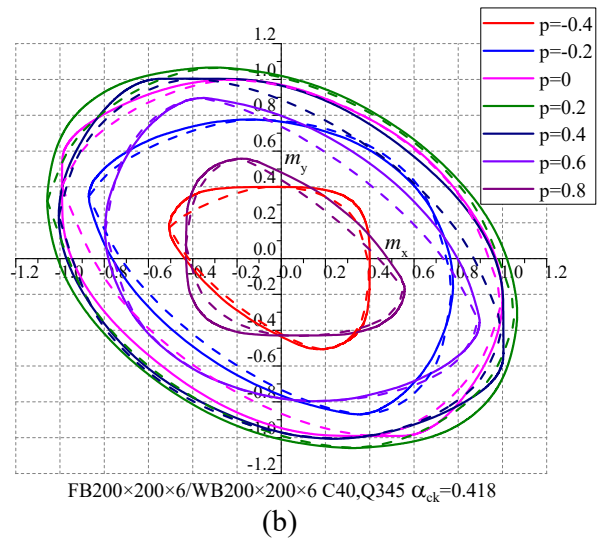
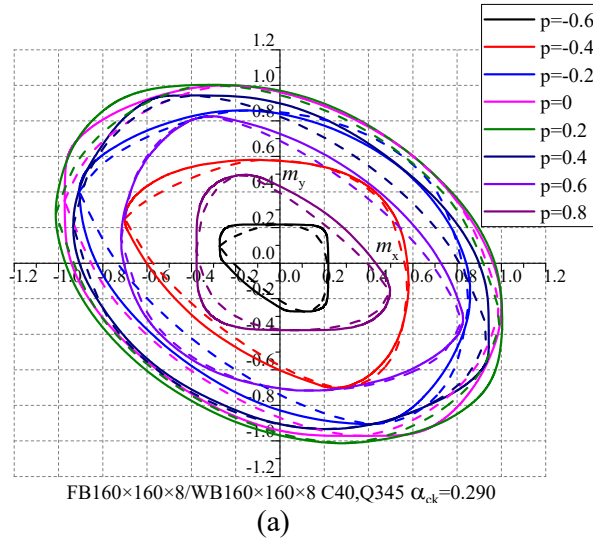
$$\left(\frac{m_{x4} - m_x}{m_{x4} - m_{x3}} \right)^{1.6 + \frac{2}{3}p} + \left(\frac{m_{y3} - m_y}{m_{y3} - m_{y4}} \right)^{1.6 + \frac{2}{3}p} = 1 \quad (28d)$$

Table 3. Parameters of Examples

Num	Flange box section/mm	Web box section/mm	f_{ck} (N/mm ²)	f_y (N/mm ²)	α_{ck}
1	160×160×8	160×160×8	26.8	345	0.290
2	200×200×6	200×200×6	26.8	345	0.418
3	100×200×6	100×350×6	26.8	345	0.301
4	200×400×8	200×700×12	20.1	235	0.359
5	200×400×8	250×450×10	38.5	235	0.568
6	250×350×6	200×400×8	20.1	235	0.462
7	100×250×6	100×250×6	38.5	235	0.471
8	200×400×8	200×400×10	38.5	235	0.539

Table 3 list 8 L-CFT sections with different values of f_{ck} and f_y , they are adopted to check the accuracy of Eq. 28. In Figure 10, solid lines show theoretical results based on full plasticity assumption, they are compared with Eq. 28 which are represented by dot lines, good agreements are achieved.

Eq. 28 can be used to calculate the ultimate yield surfaces of L-CFT of different parameters, it should be noted that the width-to-thickness of the section need to be limited to prevent the local plate buckling. Both flange and web box are required to satisfy $\left(\frac{b_1}{t_1}, \frac{h_1}{t_1}, \frac{b_2}{t_2}, \frac{h_2}{t_2} \right) \leq 60\sqrt{235/f_y}$.



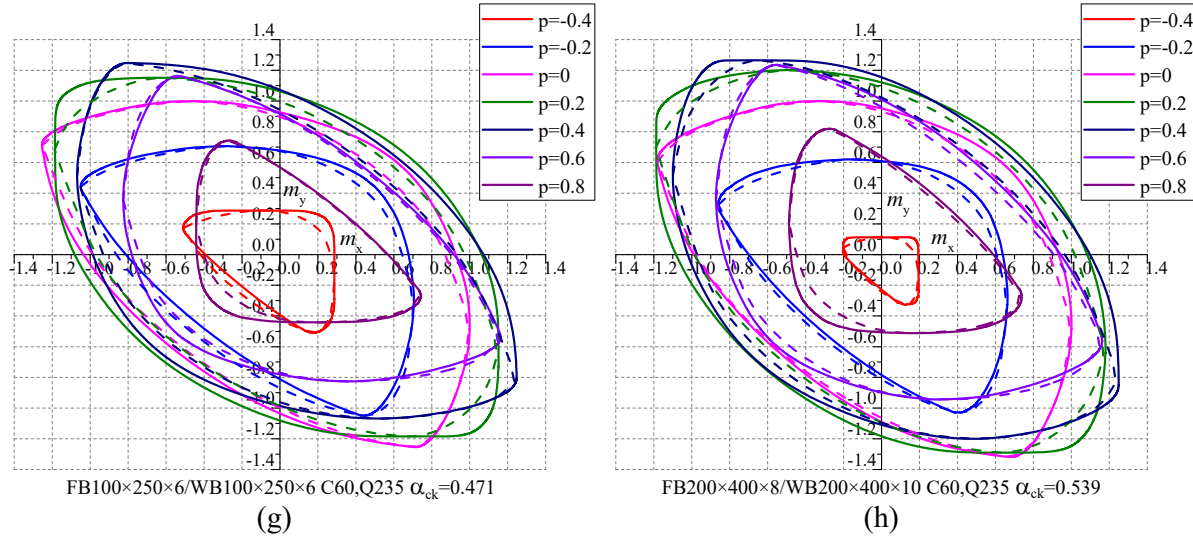


Figure 10. Comparison of Theoretical Results with Eq. 28
(Solid line: Theoretical Results, Dotted Line: Eq. 28)

4. CONCLUSION

The maximum yield strength of concrete filled L-shaped tube section under biaxial bending and axial force was studied. In the maximum strength state, the steel reaches its yielding strength while the concrete reaches its characteristic strength of compression with neglecting the part under tension.

First the plastic strengths under uniaxial compression and bending are investigated, the characteristics of the axial force-bending moment interaction curves are revealed, the rotational symmetry of the whole interaction curve is verified mathematically. Results show that when the L-CFT section is under uniaxial compression and bending around the x axis, there are 6 cases according to the positions of elastic centroid axis and plastic neutral axis under pure bending, $P-M_x$ and $P-M_{y,x}$ curves are approximated by multilinear expressions respectively using the values $(P, M_x, M_{y,x})$ of the key points in different positions of plastic neutral axis.

Under axial force and biaxial bending of L-CFT section, a series of $m_x - m_y$ curves under different axial force ratio p are presented. Examples show that the ultimate bending moment around x and y axis is maximum when the plastic neutral axis is parallel to x and y axis respectively, this characteristic is also verified mathematically. These maximum points are then used to help formulate the $p - m_x - m_y$ equations of the L-CFT section. According to the comparison of a large number of examples, the proposed formulas are accurate enough and on the safe side.

ACKNOWLEDGMENT

The authors are grateful to the financial support from the National Key Research and Development Program of China through the grant No. 2016YFC0701201.

REFERENCES

- [1] JGJ149-2006, "Technical Specification for Concrete Structures with Specially Shaped Columns". The Ministry of Housing and Urban-Rural Development of China: Beijing, 2006.
- [2] Hsu, C.T.T., "T-shaped Reinforced Concrete Members under Biaxial Bending and Axial Compression", *Aci Structural Journal*, 1989, Vol. 86, No. 4, pp. 460-468.
- [3] Hsu, C.T.T., "Biaxially Loaded L-shaped Reinforced Concrete Columns", *Journal of Structural Engineering*, 1985, Vol. 111, No. 12, pp. 2576-2595.
- [4] Sun, J.H., "Lateral Stiffness and Analysis of Frames Built of Special Shaped Columns", Zhejiang University: Hangzhou, 2003.
- [5] Zhao, Y.H., "Study on Bearing Capacity for SRC Special Shaped Columns", Xi'an University of Architecture and Technology: Xi'an, 2007.
- [6] Chen, W.F. and Atsuta, T., "Theory of Beam-columns", McGraw-Hill: New York, 1976.
- [7] Hajjar, J.F. and Gourley, B.C., "Representation of Concrete-filled Steel Tube Cross-section Strength", *Journal of Structural Engineering*, 1996, Vol. 122, No. 11, pp. 1327-1336.
- [8] CECS159-2004, "Technical Specification for Structures with Concrete Filled Rectangular Steel Tube Members". The Ministry of Housing and Urban-Rural Development of China: Beijing, 2004.
- [9] Chadwell, C.B. and Imbsen, R.A., "XTRACT: A Tool for Axial Force-ultimate Curvature Interactions", Structures Congress, ASCE, 2004.
- [10] Shen, Z.Y., Lei, M., Li, Y.Q. and Luo, J.H., "Experimental Study on Seismic Behavior of Concrete-filled L-shaped Steel Tube Columns", *Advances in Structural Engineering*, 2013, Vol. 16, No. 7, pp. 1235-1248.
- [11] Zuo, Z.L., Cai, J., Yang, C. and Chen, Q.J., "Eccentric Load Behavior of L-shaped CFT Stub Columns with Binding Bars", *Journal of Constructional Steel Research*, 2012, Vol. 72, No. 5, pp. 105-118.
- [12] Zhang, J.C., Shen, Z.Y., Lin, Z.Y., and Luo, J.H., "Experimental Research on Seismic Behavior of Concrete-filled L-section Steel Tubular Frames", *Journal of Building Structures*, 2010, Vol. 31, No. 8, pp. 1-7.
- [13] Wang, D. and Lv, X.L., "Experimental Study on Seismic Behavior of Concrete-filled Steel T-section and L-section Columns", *Journal of Building Structures*, 2005, Vol. 26, No. 4, pp. 39-44.
- [14] Lei, M., Shen, Z.Y., Li, Y.Q. and Luo, J.H., "Sectional Strength of Concrete-filled T-shaped Steel Tube Column Subjected to Axial Compression and Bending Moment", *Journal of Tongji University*, 2016, Vol. 44, No. 3, pp. 348-354.

SCIENTIFIC COMMITTEE

Chairman: František Wald

Scientific secretary: Michal Jandera

G.A. Altay (Turkey)	R. Landolfo (Italy)
I. Balaz (Slovakia)	N. Lopes (Portugal)
C. Baniatopoulos (Greece)	R. Leon (USA)
A. Bureau (France)	J.R. Liew (Singapore)
E.M. Batista (Brazil)	J. Loughlan (UK)
R. Beale (UK)	J. Macháček (Czech Republic)
R. Bjorhovde (USA)	M. Mahendran (Australia)
M.A. Bradford (Australia)	F. Mazzolani (Italy)
B. Brune (Germany)	E. Mirambell (Spain)
L. Calado (Portugal)	D. Nethercot (UK)
D. Camotim (Portugal)	J. Packer (Canada)
S.L. Chan (Hong Kong, China)	J. Paik (South Korea)
T.M. Chan (Hong Kong, China)	S. Pajunen (Finland)
R. Casciaro (Italy)	N. Rangelov (Bulgaria)
K.F. Chung (Hong Kong, China)	K.J.R. Rasmussen (Australia)
C. Chiorean (Romania)	E. Real (Spain)
M. D'Aniello (Italy)	B. Rossi (Belgium)
H. Degée (Belgium)	F. Roure (Spain)
J.-F. Démonceau (Belgium)	R. Sause (USA)
F. Dinu (Romania)	B.W. Schafer (USA)
D. Dubina (Romania)	L.S. Silva (Portugal)
L. Dunai (Hungary)	N. Silvestre (Portugal)
S. Easterling (USA)	H. Snijder (Netherlands)
A. Elghazouli (UK)	R. Stroetmann (Germany)
M. Fontana (Switzerland)	J.G. Teng (Hong Kong, China)
D. Frangopol (USA)	V. Ungureanu (Romania)
L. Gardner (UK)	H. Unterweger (Austria)
M. Garlock (USA)	B. Uy (Australia)
G. Garcea (Italy)	I. Vayas (Greece)
P. Gonçalves (Brazil)	P. Vellasco (Brazil)
F. Guarracino (Italy)	P. Vila Real (Portugal)
J. Hajjar (USA)	A. Wada (Japan)
G.J. Hancock (Australia)	N. Yardimci (Turkey)
M. Hjiiaj (France)	B. Young (Hong Kong, China)
B. Izzuddin (UK)	R. Zandonini (Italy)
Z. Kolakowski (Poland)	B. Zhao (France)
M. Kotelko (Poland)	R. Ziemian (USA)
U. Kuhlman (Germany)	A. Zingoni (South Africa)
D. Lam (UK)	Y.B. Yang (Taiwan, China)

ORGANISING COMMITTEE

K. Cábová
J. Dolejš
M. Eliášová
M. Jandera
J. Macháček

P. Ryjáček
Z. Sokol
M. Šorf
F. Wald
B. Židlický

COLLOQUIUM CONTACT

sdss2019.cz
info@sdss2019.cz



The International Colloquium on Stability and Ductility of Steel Structures

Prague 2019
11-13 September



FACULTY OF CIVIL
ENGINEERING
CTU IN PRAGUE

INTRODUCTION

The series of International Colloquia on Stability and Ductility of Steel Structures have been supported by the Structural Stability Research Council (SSRC) for more than forty years and its objective is to present the progress in theoretical, numerical and experimental research in the field of stability and ductility of steel and steel-concrete composite structures. Special emphasis is laid on new concepts and procedures concerning the analysis and design of steel structures and on the background, development and application of rules and recommendations either appearing in recently published Codes or Specifications or about to be included in their upcoming versions.

This International Colloquium series started in 1972 in Paris and its subsequent editions took place in different cities with the last five being held in: Timisoara, Romania (1999), Budapest, Hungary (2002), Lisbon, Portugal (2006), Rio de Janeiro, Brazil (2010) and Timisoara, Romania (2016).

The 2019 edition of SDSS is organized by the Czech Technical University in Prague. The university held the second edition of the Eurosteel conference in 1999 and first three editions of Applications of Structural Fire Engineering (ASFE) conference (2009, 2011 and 2013).

It is our pleasure to invite you to Prague again for the International Colloquium SDSS at the beginning of September 2019.

František Wald
Michal Jandera



DATE AND VENUE

11-13 September 2019

Czech Republic - Prague

Czech Technical University in Prague

Faculty of Civil Engineering

Thákurova 7, 166 29 Prague 6

KEY DATES

Call for abstracts and submission opening: **01.06.2018**

Abstract submission deadline: **31.10.2018**

Acceptance of abstracts and call for papers: **15.12.2018**

Submission of full papers: **15.02.2019**

Acceptance of papers: **01.05.2019**

Submission of final papers and registration: **15.05.2019**

SDSS 2019 opening: **11.09.2019**

REGISTRATION FEE

	Early bird registration by 1 June 2019	Standard registration after 1 June 2019
Conference participant regular	€ 500	€ 580
Conference participant student	€ 400	€ 450
Accompanying person	€ 120	€ 150
Kutná Hora trip after the closing session	€ 95	

No more than two papers can be presented by one registered participant. The conference participant fee covers an electronic copy of the Proceedings, admission to the technical sessions, lunches, coffee breaks, welcome reception and banquet dinner. The student registration fee applies to students of up to 35 years of age.

Welcome reception and conference banquet are included in the fee for accompanying persons.

The sightseeing trip to Kutná Hora can be purchased separately on request and will be organised for 10 participants as minimum. It is planned for the afternoon of the last day of the conference after the Closing Session.

ABSTRACT SUBMISSION

Abstract should be submitted to the e-mail address **michal.jandera@sdss2019.cz** by 31st October 2018. The abstract should summarise the content of the paper clearly and highlight its contribution to the current scope of knowledge and research.

PROCEEDINGS

The papers accepted by the SDSS 2019 Scientific Committee and presented at the colloquium will be published in electronic Proceedings distributed to the participants at registration and covered by SCOPUS.

MAIN TOPICS OF THE COLLOQUIUM

- Advanced structural analysis
- Bridges and footbridges
- Cold-formed members
- Connections
- Cyclic and blast loading
- Damage repair and assessment of steel structures
- Design codes and standards
- Dynamic behaviour and analysis
- Fatigue and fracture mechanics
- Fire engineering
- Frames
- High strength & stainless steel
- Innovative structural designs and applications
- Lightweight aluminium structures
- Lightweight fibre reinforced plastic composite structures
- Member behaviour: tension, compression, beams, beam-columns
- Off-shore structures
- Plate, shell and space structures
- Reliability and safety
- Robustness
- Seismic-resistant structures
- Stability of glass and hybrid structures
- Steel-concrete composite members and structures
- Thin-walled constructions
- Trusses, towers and masts
- Tubular constructions

**ORDER
FORM**

ISSN 1816-112X

**Advanced Steel Construction,
an international journal**Indexed by the Science Citation Index Expanded,
Materials Science Citation Index and ISI Alerting Services**From:****To:** Secretariat, Advanced Steel Construction, an international journal
Fax: (852) 2334-6389

I/ We would like to enter a subscription to the *International Journal of Advanced Steel Construction (IJASC)* published by The Hong Kong Institute of Steel Construction.

Please complete the form and send to:

International Journal of Advanced Steel Construction
c/o Department of Civil and Environmental Engineering
The Hong Kong Polytechnic University
Hungghom, Kowloon, Hong Kong

Fax: (852) 2334-6389 Email: ceslchan@polyu.edu.hkPublished by : The Hong Kong Institute of Steel Construction
Website: <http://www.hkisc.org/>**Please tick the appropriate box**

- ☐ Please enter my hard-copy subscription (**4 issues per year**).
☐ Please send me a complimentary copy of the *Advanced Steel Construction, an International Journal (IJASC)*.

Please tick the appropriate box(es)

	<u>Print</u>	<u>On-line is free</u>
Personal	<input type="checkbox"/> US\$ 125	
Institutional	<input type="checkbox"/> US\$ 280	

Total Amount US\$ _____

Methods of payment ☐ Please invoice me
(please tick the appropriate box(es)) ☐ Cheque enclosed for US\$ _____ payable to
Hong Kong Institute of Steel Construction Limited
(No personal cheque accepted)

Ship to

Name (Prof./ Dr./ Mr./ Ms.) _____
Address _____

City/ State/ Postal Code _____
Country _____
Email _____ Fax _____